THE UNIVERSITY OF SHEFFIELD

PHD THESIS

On the dynamics of robotic machining

Author:
Huseyin CELIKAG

Supervisors:
Prof. Neil D. SIMS
Dr. Erdem OZTURK

A thesis submitted in fulfilment of the requirements
for the degree of Doctor of Philosophy
in the

Department of Mechanical Engineering
The University of Sheffield

December 22, 2020

Summary

Machine tools could potentially be substituted with serial industrial robots to enable machining larger parts with high versatility and lower costs. However, robots tend to have poor pose accuracy and poor configuration dependent structural dynamics. Hence, configuration dependent stability boundaries and early onset of chatter are obstacles for robotic machining. Therefore, this thesis focuses on the effect of configuration dependent structural dynamics of serial industrial robots on the stability of self-excited vibrations in milling.

First, the static stiffness of a serial robot was modelled, simulated, identified and optimised based on the VJM (Virtual Joint Model) stiffness modelling technique. In this way, the extent of the configuration dependency of the robot static stiffness was investigated and form error minimisation was aimed for robotic milling.

Then, a robotic milling trial was designed to explore the idea of chatter avoidance by continuously configuring the robot around the axis of rotation of the tool while cutting across a straight trajectory. In low spindle speeds, the larger the configuration alteration was, the more the stability was affected in terms of lobe position shift. In high spindle speeds, the N=0 lobe coming from the structural robot mode alters the stability significantly based on the choice of the manipulator configuration. The optimised robot configuration was found to make it possible to control the N=0 lobe coming from the structural robot mode and hence, unveil stable regions and avoid chatter. However, the continuous configuration of the robot at low and high spindle speeds were found to be inconclusive.

The quantitative mismatch observed between regenerative stability predictions and tests suggested the possible presence of mode coupling chatter in robotic milling. Hence, the mode coupling chatter mechanism was adapted from the zero frequency and extended to multi frequency solution. Findings indicated that mode coupling chatter mechanism does not exist in milling.

Acknowledgements

I would like to acknowledge everyone who helped, contributed and supported me in any form and way throughout my PhD at The University of Sheffield and Advanced Manufacturing Research Center (AMRC).

I would like to express my sincerest gratitude to my academic supervisor, Prof. Neil D. Sims, for his insightful guidance, continuous motivation, support and patience throughout the project. His ideas and vision have given me inspiration and provided me invaluable knowledge that will shape and contribute my future career. It has been a privilege to work with him and learn from his rigorous ways of approaching problems. Therefore, I would like to thank you very much for all the contribution to my development.

I would like to share my deepest appreciation to my AMRC supervisor, Dr. Erdem Ozturk, for giving me cutting-edge ideas, essential directions and knowledgeable guidance throughout my PhD. I would specifically like to thank him greatly for his support during my time at AMRC with providing me all the assistance with the experimental execution. Your guidance has been very instructive all these years and I am very grateful I was given the opportunity to work with you.

I would like to thank to EPSRC for the funding provided for Industrial Doctorate Centre in Machining Science (EP/L0162557/1) and AMRC for the industrial financial sponsorship.

I would also like to deeply thank my parents, Mucahit and Nazan, and my sister, Meral, for all the support they provided me over the years. I am incredibly grateful to have you all by my side and this PhD thesis could have not been completed without your help. I would also like to thank my extended family and grandparents for always being there for me from Cyprus.

My work was greatly assisted by a few people I would like to acknowledge. Firstly, thank you to Jamie Booth who assisted me in designing, manufacturing and assembling of my experimental set-ups. Your help was very much appreciated. Secondly, I would like to thank Phil Bell for helping me with the machining trials at KTC, AMRC. Lastly, thank you Garry Hibbert for supporting me through complications arising during the cutting tests.

My Industrial Doctorate Centre (IDC) experience would have not been the same without my cohort, Chandy, Mate, Sam and Lisa. It has been a pleasure to work with all of you throughout these last few years. I am very glad I had the opportunity to get to know you and share valuable memories together.

Last but not least, a big thank you goes to my friends in Sheffield for making my time here extremely memorable. Thank you to Izgun, Halil, Erkan, Ozan and Kate for all the good times we shared and for supporting me throughout my PhD experience. I am very grateful to have you as my friends. I would also like to thank my friends from back home in Cyprus for supporting me even from a distance.

Contents

List of Figures

List of Tables

List of Abbreviations

CAD	**C**omputer **A**ided **D**esign
CCT	**C**onservative **C**ongruence **T**ransformation
CHM	**CH**emical **M**achining
CNC	**C**omputer **N**umerical **C**ontrol
DE	**D**ifferential **E**volution
DH	**D**enavit-**H**artenberg
mDH	**m**odified **D**enavit-**H**artenberg
DOC	**D**epth **O**f **C**ut
DOF	**D**egree **O**f **F**reedom
ECM	**E**lectro **C**hemical **M**achining
EDM	**E**lectrical **D**ischarge **M**achining
FE	**F**inite **E**lement
FEA	**F**inite **E**lement **A**nalysis
FRF	**F**requency **R**esponse **F**unction
KCI	**K**inetostatic **C**onditioning **I**ndex
LBM	**L**aser **B**eam **M**achining
MSA	**M**atrix **S**tructural **A**nalysis
NAVARO	**NA**ntes **VA**riable Actuation **RO**bot
PKM	**P**arallel **K**inematic **M**achine
POM	**P**oly**O**xy**M**ethylene
RPY	**R**oll **P**itch **Y**aw
RPM	**R**evolutions **P**er **M**inute
SADE	**S**elf **A**daptive **D**ifferential **E**volution
SCARA	**S**elective **C**ompliance **A**ssembly **R**obot **A**rm
SDOF	**S**ingle **D**egree **O**f **F**reedom
MDOF	**M**ulti **D**egree **O**f **F**reedom
SLD	**S**tability **L**obe **D**iagram
SS	**S**pindle **S**peed
TCP	**T**ool **C**enter **P**oint
VJM	**V**irtual **J**oint **M**odel

List of Symbols

a_i	Link length of link i
${}^{i-1}a_i$	Unit vector along Z-Axis of T_{i-1}
α_i	Link twist of link i
α, β, γ	RPY angles (roll, pitch, yaw)
α_{u1}, α_{u2}	Mode inclination angles for u_1 and u_2
$\dot{\alpha}, \dot{\beta}, \dot{\gamma}$	RPY (roll, pitch, yaw) angle rates
$\delta\alpha, \delta\beta, \delta\gamma$	Infinitesimal angular displacement along X, Y and Z-Axes
A	Cross sectional area
$A_F(.)$	Milling force coefficient matrix in frequency domain
$A_T(.)$	Milling force coefficient matrix in time domain
${}^{i-1}A_i$	Homogeneous transformation matrix (4×4)
b	Depth of cut
b_a	Axial location of the flute
b_{lim}	Depth of cut for marginal stability
$b_{c,low}$	Minimum depth of cut for marginal stability in low spindle speeds
$b_{c,high}$	Minimum depth of cut for marginal stability in high spindle speeds
b_w	Width of cut
$b_{w,lim}$	Width of cut for marginal stability
β_k	Gradient of the pitch with respect to axial location of k^{th} tooth
β_F	Force angle
c_u, c_x, c_y	Modal damping along u, X and Y-Axes respectively
C_c	Cartesian compliance matrix
C_θ	Joint compliance matrix
${}^{V}C_\theta$	Vector of joint compliance parameters
d_i	Link offset of link i
ϵ	Phase difference between current and previous waves
E	Young's modulus
E_b	Work done by the actuator
E_q	Work done in joint space
$Err_{\%}$	Maximum percentage error within 95.75% of the data
$f(.)$	Manipulator geometrical model
f_c	Chatter frequency
f_n	Natural frequency
f_r	Differential radial force
f_t	Differential tangential force
f_{tth}	Feed per tooth
f_x	Differential force in X direction
f_y	Differential force in Y direction
F_c	Cutting force
$F_f(t)$	Force in feed direction in time domain

$F_f(s)$	Force in feed direction in Laplace domain
$F_r(t)$	Dynamic radial force in time domain
$F_t(t)$	Dynamic tangential force in time domain
F_x, F_y, F_z	Force along X, Y and Z-Axes
$F_{x,k}(t)$	Dynamic force along X-Axis on k^{th} tooth in time domain
$F_x(t)$	Total dynamic force along X-Axis in time domain
$F_{y,k}(t)$	Dynamic force along Y-Axis on k^{th} tooth in time domain
$F_y(t)$	Total dynamic force along Y-Axis in time domain
$FRF(j\omega)$	Frequency Response Function in frequency domain
$FRF(s)$	Frequency Response Function in Laplace domain
$\mathcal{F}$	Fourier transform
$g(.)$	Heaviside (unit) step function
G	Real part of Frequency Response Function
γ_k	Helix angle of the k^{th} tooth
$h(t)$	Dynamic chip thickness in time domain
$h(s)$	Dynamic chip thickness in Laplace domain
h_0	Feed per revolution
$h_0(s)$	Feed per revolution in Laplace domain
H	Imaginary part of Frequency Response Function
$[\Psi(j\omega)]_{p,q}$	Doubly infinite harmonic transfer function
i	Real integer operator
I	Second moment of inertia
I_h	Hub inertia
$I_{3\times3}$	Identity matrix (3×3)
j	Imaginary number, $j = \sqrt{-1}$
$J(.)$	Geometric Jacobian
$J_A(.)$	Analytical Jacobian
$J_N(.)$	Normalised geometric Jacobian
k	Real integer operator representing the tooth number
κ	Ratio of the imaginary to real part of the eigenvalue
$\kappa_F(.)$	Condition number based on Frobenius norm
k_u, k_x, k_y	Modal stiffness along u, X and Y-Axes respectively
K	Number of teeth
K_c	Cartesian stiffness matrix
K_f	Complementary stiffness matrix
K_{fc}	Cutting constant in feed direction
K_{max}, K_{min}	Maximum and minimum principal stiffness
K_r	Ratio of tangential to radial cutting force coefficient
K_{rc}	Radial cutting force coefficient
K_{tc}	Tangential cutting force coefficient
K_θ	Joint stiffness matrix
${}^V K_\theta$	Vector of joint stiffness parameters
L	Characteristic length of the robot
λ	Eigenvalue of the characteristic equation
m	Point mass
m_u, m_x, m_y	Modal mass along u, X and Y-Axes respectively
M_p	Payload
M_x, M_y, M_z	Torque around X, Y and Z-Axes

n	Number of degrees of freedom
n_c	Number of manipulator configurations
n_w	Number of loading (wrench) applied to each manipulator configuration
${}^{i-1}n_i$	Unit vector along Y-Axis of T_{i-1}
N	Number of integer waves
ω	Angular frequency
ω_c	Angular chatter frequency
ω_T	Tooth passing frequency
$\omega_x, \omega_x, \omega_x$	Angular velocity around X, Y and Z-Axes
Ω	Spindle speed
Ω_{Best}	Spindle speed where stable region is located
$\phi_k(.)$	Instantaneous angular immersion of k^{th} flute
ϕ_{k0}	Position of the k^{th} flute across the circumference of the tool
ϕ_{st}	Start angle of radial tool immersion
ϕ_{ex}	Exit angle of radial tool immersion
Φ	Observation matrix
Φ^I	Left Moore-Penrose generalised inverse of observation matrix
ψ	Phase angle
P	Amplitude ratio between modes of vibration
P_m	Position vector, minimal representation
$\dot{P}_m$	End effector linear velocity, minimal representation
q_i	Joint variable of joint i
q_i^{Ac}	Static deflection of joint i
$q_{\theta,i}$	Joint angle of joint i
$q_{Off,i}$	Joint offset of joint i
$\dot{q}$	Joint velocity vector
r	Integer operator representing the spindle speed harmonics
r_{tool}	Tool radius
ρ	Mass density per unit volume
R_m	Rotation vector, minimal representation
$R_{Rot,x}$	Matrix for rotation around X-Axis (3×3)
$R_{Rot,y}$	Matrix for rotation around Y-Axis (3×3)
$R_{Rot,z}$	Matrix for rotation around Z-Axis (3×3)
${}^{i-1}R_i$	Rotation matrix (3×3)
$\dot{R}_m$	End effector rotational velocity, minimal representation
s	Laplace operator
${}^{i-1}s_i$	Unit vector along X-Axis of T_{i-1}
σ	Real part of Laplace operator
σ^{STD}	Standard deviation
τ	Torque vector in joint space
$tr(.)$	Trace of a matrix
θ	Vector of aggregation of joint variables, q and static deflection, q^{Ac}
Θ	Phase delay between current vibrations of modes of vibration
T	Time delay
$T_k(a)$	Time delay of k^{th} tooth at a depth of cut, a
T_i	i^{th} Coordinate frame
T_{Base}	Base frame
T_{TCP}	TCP frame

u_1, u_2	Modal directions
$v(t)$	Normal vibrations in time domain
V	Cutting velocity
w	Wrench vector in operational space
x_i, y_i, z_i	Cartesian axis coordinates of i^{th} coordinate frame
X_i, Y_i, Z_i	Cartesian axes of i^{th} coordinate frame
$x(t), y(t)$	Vibrations along X and Y-Axes in time domain
$x(s), y(s)$	Vibrations along X and Y-Axes in Laplace domain
$\dot{x}(t), \dot{y}(t)$	Velocity of vibrations along X and Y-Axes in time domain
$\ddot{x}(t), \ddot{y}(t)$	Acceleration of vibrations along X and Y axes in time domain
$\delta x, \delta y, \delta z$	Infinitesimal displacement along X, Y and Z-Axes
$\Delta x, \Delta y$	Variation of vibrations along X and Y-Axes
δX	TCP deflection
X_m	End effector pose, minimal representation (1×6)
$X(j\omega)$	Vibrations along X-Axis in frequency domain
$\dot{X}_m$	End effector linear and rotational velocity
$Y(j\omega)$	Vibrations along Y-Axis in frequency domain
$0_{3\times3}$	Zero matrix (3×3)
$\|\|(.)\|\|_F$	Weighted Frobenius norm

Dedicated to my family…

Chapter 1

Introduction

This thesis focusses on investigating effects of configuration dependent static stiffness and structural dynamics of serial industrial robots on the process stability when they are used for milling operations. Throughout this work, not only are their configuration dependent characteristics identified and modelled but also optimised by utilising the redundant degree of freedom around the axis of rotation of a milling tool. With the aim of improving limits of robotic machining operations, the thesis focuses on minimising form error, avoiding regenerative chatter vibrations and modelling and validating the mode coupling chatter mechanism in milling.

1.1 Introduction to modern manufacturing

Manufacturing is the process of making new parts and is crucial to contemporary industries in many ways. In fact, even before the industrial revolution, 2.6 millions years ago, the first manufacturing technique, cutting, was achieved by sharpening a piece of rock to create a cutting edge to cut the flesh of animals [1]. Nowadays, manufacturing can be described in terms of technologies and economics [2]. Technologically, it is the alteration of the geometry, property and appearance of a given raw material by physical and chemical processes to create parts and products. It could also be defined as the assembly of multiple parts into products. Economically, it is defined as converting materials into a higher value by means of one or multiple processing and/or assembly operations. Thus, on the whole, it can be regarded as the transformation of a raw material into a new, functional, valuable product. Manufacturing processes can be technologically classified in mainly five categories; joining, dividing, transformative, subtractive and additive technologies [3] as in Figure 1.1.

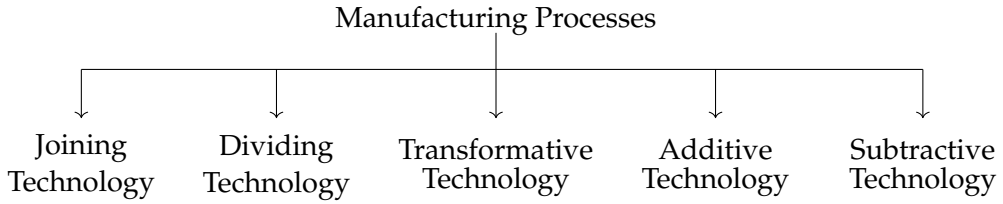

FIGURE 1.1: The technology based categorisation of manufacturing processes [4]

Joining technologies aim to connect one or more workpieces together to create the desired part such as riveting, fastening and assembly whereas dividing technologies aim

to partition a workpiece into two or multiple pieces such as sawing and disassembling. Transformative technologies are used to change the geometry of a workpiece by using another workpiece such as forging, shaping, casting [5], sheet forming [6]. On the other hand, additive technologies involve making parts by adding materials in layers such as Fused Deposition Modelling [7], Stereolithography [8], Electron Beam melting [9], Selective Laser Melting [10], Selective Laser Sintering [11] etc. [12–14]. Lastly, subtractive technologies, or in other words, machining processes, cover processes in which the final product is obtained by reducing the mass of a raw material by various techniques. Focusing on machining processes, according to [15], "*Machining is the removal of unwanted materials (machining allowance) from the workpiece so as to obtain a finished product of the desired size, shape, and surface quality*". It is the most widespread metal shaping process in the mechanical industry as emphasised by [16]. Machining can be further classified into traditional and nontraditional operations as in Figure 1.2.

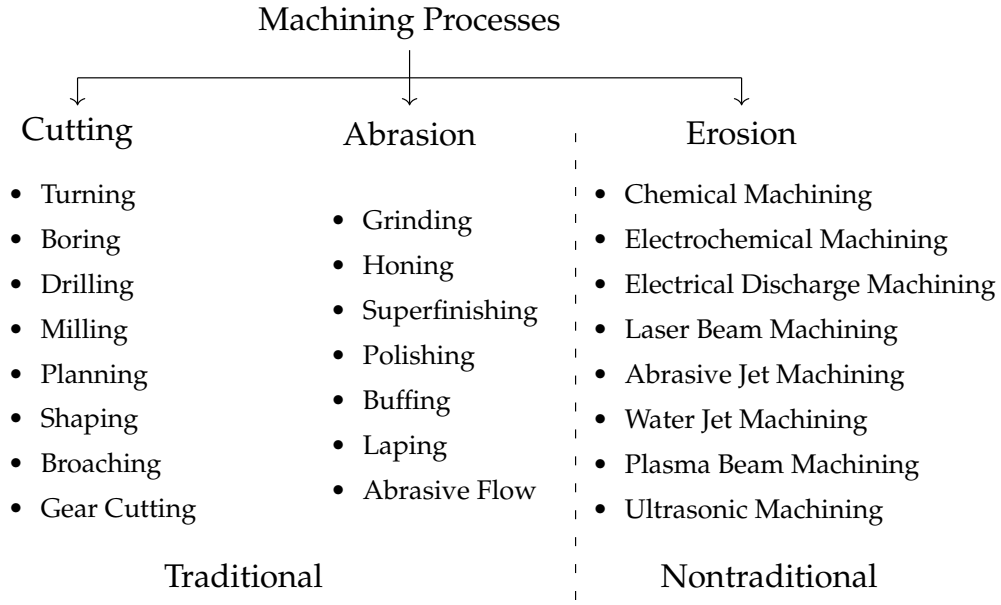

FIGURE 1.2: The classification of machining processes based on [15]

Traditional processes involve direct contact of the tool with the workpiece and require the tool to be much harder than the workpiece. Based on the geometrical definition of the cutting tool, traditional machining processes can be further divided into; Cutting and Abrasive machining. In cutting processes, such as turning, milling, boring, drilling etc., the cutting tool is geometrically defined and geometric properties could be utilised to improve machining process. In abrasive machining, the cutting tool can not be represented geometrically and material removal is acquired with abrasive particles on the surface of the tool as in grinding, honing, polishing etc. operations. On the other hand, nontraditional processes utilise non-contact material removal techniques with no defined cutting tool edge such as chemical machining (CHM), electrochemical machining (ECM), laser beam machining (LBM), electrical discharge machining (EDM) etc. In addition to traditional and nontraditional processes, there exists another classification of machining operations which is called hybrid processes. According to Lauwers et al. [17], "Hybrid manufacturing processes are based on the simultaneous and controlled interaction of process mechanisms and/or energy sources/tools having a significant effect on the process performance". Hybrid

processes are usually the combination of two or more traditional and/or nontraditional processes [18] such as vibration-assisted milling [19], vibration-assisted EDM milling [20], laser-assisted milling [21], laser-assisted water jet machining [22] etc..

All machining processes are controlled by computer numerical controlled (CNC) machines with high rigidity & precision to satisfy industry standards in dimensional accuracy & surface finish and are called (CNC) machine tools. In the next section, the motivation for utilising robots, in particular serial industrial robots as per the focus of the thesis, is discussed as a substitute for machine tools, revealing benefits they could bring and associated complications which need to be addressed.

1.2 The motivation for robots in machining

Advancements in technology and frequently & continuously changing customer demands due to market competition are causing unpredictable pressure in the manufacturing industry [23]. The pressure is embodied in the form of new products which have complex geometries, tight dimensional accuracies, variety of size and material properties, etc. This is to provide essential performance improvements to the end-product in terms of product & manufacturing cost, technical & design performance, manufacturability, quality, etc. or trade off between any of performance measures. Frequent introduction of new products, however, results in shortening of life span of the end-product and manufacturing facility. For this reason, adaptation becomes a necessity to prolong the life span of manufacturing facilities and to rapidly respond customer demands. In the pursuit of coping with market demands, a need for flexible production systems arises which should also entail reconfigurability of the system itself.

Currently, manufacturing sectors rely mostly on CNC machine tools for various machining operations. In spite of their capability to fulfil dimensional accuracy and surface finish requirements, limitations in versatility, workspace size and associated capital cost force investors to look for cheaper, flexible, reconfigurable solutions. When it comes to machining large aerospace components, the workspace of standard CNC machine tools are not large enough for the successful implementation of the machining process. Consequently, a larger CNC machine tool is required, which necessitates large capital investment. However, serial industrial robots (or manipulators as explain in Section 3.1), which are already being vastly employed in manufacturing industries could potentially be utilised to bridge the gap between reconfigurability and machining large aerospace components with low capital investment. They are relatively cheaper and have a much larger workspace than standard machine tools. Thus, serial industrial robots could be the perfect candidates that could fulfil the aforementioned limitations as a substitute to CNC machine tools.

Focusing on serial industrial manipulators, as per the scope of the thesis, they are able to bring automation, flexibility and reconfigurability into manufacturing facilities. In today's manufacturing systems, serial industrial manipulators are mainly used as material handling equipments. As opposed to prior process traditions where human involvement was a necessity, manipulators are currently employed to attain 24/7 operation, minimise occasions where human involvement might result in health concerns and fulfil better performance measures. In addition, due to their high versatility in conducting not only material handling but also vast range of other operations (such as painting, trimming, deburring, welding, ...etc.) and ability to carry out these operations in large work-volume,

serial industrial robots are perfect candidates for the functionality of a reconfigurable manufacturing system.

The idea of utilising serial industrial robots for machining applications emerged in early 90s as an alternative to machining with CNC machine tools [24, 25]. However, serial industrial robots tend to have intrinsic handicaps compared to CNC machine tools primarily due to their mechanical design & structure such as poor pose accuracy and dynamic characteristics. Considering the pose accuracy, which is one of vital measures in machining processes, serial industrial robots tend to fail to meet the requirements as a result of accumulated errors across their kinematic chain, as well as non-geometrical errors such as backlash, friction and wear at gears etc.. Due to their design purpose, serial industrial robots are better in carrying out repetitive tasks rather than tasks requiring high pose accuracy or path tracking. As opposed to machine tools, serial industrial robots have relatively poor dynamic characteristics which, as a whole, result in many complications such as; large form error, poor surface finish due to forced vibrations, early onset of chatter etc.. On the other hand, both machine tools and serial industrial robots tend to have configuration dependent dynamic properties due to the constantly varying position and orientation of their structural elements. In the next section, structural dynamic properties of machine tools are compared with that of serial industrial robots and their corresponding effects on machining dynamics are discussed.

1.3 The structural dynamics & machining dynamics

Machine tools consist of mainly three group of parts; mechanical structure, drives and control [26]. In combination, all parts contribute to structural dynamics of the machine tool at the tool tip where the cutting process takes place. The mechanical structure of machine tools consists of deformable components with various geometries and material properties. The numerous arrangement of these components are known to cause varying structural dynamics that is dependent on the tool position along the cutting trajectory [27–29]. The magnitude of the dynamic variation depends on the position and orientation of substructures (columns, beds, bridges, housings etc.) as well as the structure of the machine tool (being either serial or parallel kinematic structure). It is also known that structural modes of vibration of machine tools can be located at low and mid frequencies (as low as 15 Hz [30] up to almost 600 Hz [31]), of course, depending on its structure. Even though, structural modes are known to strongly depend on the tool pose, higher frequency tool and tool-holder modes are known to be local modes and not to exhibit strong position-dependent dynamics [32]. Henceforth, it is common practice and usually sufficient to conduct modal tests without altering the tool pose to characterise the tool and tool holder modes of vibration in machine tools.

Similar to machine tools, serial industrial robots possess deformable mechanical components that are driven by actuators while being controlled with a controller. Compared to machine tools, the serial kinematic chain of relatively flexible links and joints tend to result in poor dynamic properties at the tool tip [33]. Structural modes of vibration of serial industrial manipulators are usually located at low frequencies usually around 10-50 Hz and possess larger dynamic compliance compared to machine tools [34, 35]. In addition, the serial kinematic chain tends to reconfigure the position and orientation of links and joints at all times in order to satisfy the tool pose along the trajectories. The prominent consequence of this is the configuration dependent dynamic properties at the tool tip

[36]. Structural modes tend to show strong dependency to the manipulator configuration and the variation of the magnitude and frequency of structural modes depends on the configuration and the structure of the robot [37].

With regards to machining dynamics, the knowledge of the tool tip dynamics is particularly important in predicting the chatter phenomenon as it describes the dynamic behaviour of the tool under dynamic loading. Unstable chatter vibrations are detrimental for the tool, workpiece and sometimes for machine tools and are the causation of the poor surface finish, dimensional inaccuracies, tool wear and machine tool damage etc.. It is the instability of dynamic chip thickness being cut by the tool due to the vibration of the tool-workpiece interface as a result of cutting forces. Developments made over a century on the machine tool chatter research led to mathematical models to be developed considering the tool tip dynamics as well as process related machining parameters in an attempt to predict and avoid unstable vibrations. In that, stability lobe diagrams (SLD) were established for the most common type of chatter mechanism, regenerative chatter that describe stability boundaries based on the choice of depth of cut (DOC) and the spindle speed (SS) as illustrated in Figure 1.3.

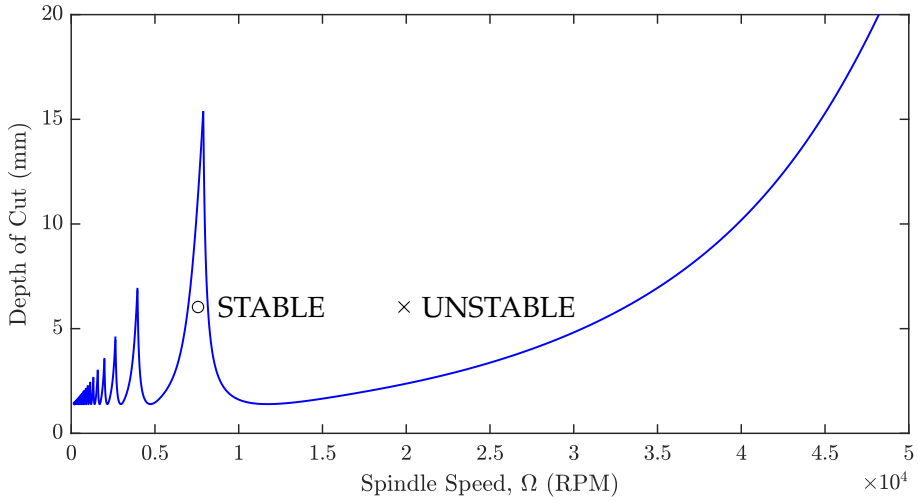

FIGURE 1.3: Stability lobe diagram (SLD)

Development of stability lobe diagrams enabled the machinist in machine shop floor to choose most productive machining parameters as per physical limitations of the machine tool allow while ensuring the product quality.

In this sense, the application of serial industrial manipulators to machining applications yields configuration dependent SLD similar to the position dependent SLD as in machine tools. Yet, limits of stable robotic machining operations are low compared to machine tools. However, while machine tools usually have a single configuration to reach a particular tool pose, serial manipulators are redundant to machining operations. For 5-axis machining operations, there exists a redundant degree of freedom around the axis of rotation of the tool that is inherent to serial industrial robots as per their ability to reach 6 DOF poses. The redundancy allows a number of manipulator configurations to satisfy a particular tool pose and hence, enables the opportunity to further vary and control the configuration dependent dynamics of the manipulator. Having underlined dynamic properties of serial

industrial robots applied in machining applications and their corresponding effect in the SLD, research directions are presented in the next section.

1.4 Brief overview of the research direction

Serial industrial manipulators applied to machining operations tend to have very similar dynamic characteristics to machine tools. They both have variations in their dynamic characteristics at the tool tip as a result of a particular arrangement of their structural elements to satisfy the tool pose. Yet, limits of stable robotic machining is still low making it very difficult to machine with robots. However, there exists an opportunity which arises as a result of the inherent redundant degree of freedom around the axis of rotation of tool in robotic machining applications whereas machine tools usually do not have such a redundancy. For this reason, the effect of configuration dependent structural dynamics and statics of serial industrial robots on self-excited vibrations (regenerative and mode coupling chatter) is investigated throughout the thesis. With the aim of improving stability limits of robotic milling, the redundancy is used to further vary and control configuration dependent dynamics of the manipulator. As such, regenerative stability boundaries are optimised at the vicinity of given machining parameters as well as chatter vibrations are avoided. Additionally, the role of mode coupling chatter in robotic milling operations is so far not clear. Consequently, mode coupling chatter theory in milling is analysed to develop further understanding and improve the stability of robotic milling. The aim and objectives of thesis are stated in more detail in the next chapter, in Chapter 2.

1.5 Thesis structure

The rest of the thesis is organised as below and the thesis layout is illustrated in Figure 1.4.

Chapter 2 presents an overview of robots in machining operations. It starts with detailing the cause of errors in robotic applications and proceeds to the modelling of manipulators. The current level of knowledge on manipulator static & dynamic behaviour as well as modelling and identification techniques are critically reviewed. Lastly, the overview of the chatter in robotic machining operations is presented by critically reviewing advancements in the field and the ambiguity appearing in the identified chatter mechanisms is reviewed.

In Chapter 3, the background theory of robotics and machine tool chatter is explained. First, the kinematics of serial manipulators is detailed in general and applied to the serial industrial manipulator ABB IRB 6640 205/2.75. The direct, inverse and differential kinematics are presented which play an important role in controlling the manipulator end effector pose, velocity and accelerations. Then, redundancies and singularities are covered to emphasise inherent characteristics of serial industrial manipulators in controlling their movements as opposed to machine tools. In the second part of the chapter, the theory of machine tool chatter mechanisms is explained. The theory includes the regenerative chatter mechanism in turning and milling as well as the mode coupling chatter mechanism in threading operation.

In Chapter 4, the static stiffness modelling of ABB IRB 6640 205/2.75 based on Virtual Joint Model (VJM) is detailed. A simulation is designed based on the preliminary experimental design to quantify the accuracy of virtual joint parameters to be identified in the experiment. Accordingly, the experimental work to identify and validate the static stiffness

model is explained and a static stiffness optimisation technique is presented with the aim of minimising form error in robotic machining operations.

A robotic milling trial was planned and implemented in Chapter 5. The kinematic performance of ABB IRB 6640 205/2.75 over the machining table is investigated to select redundancy parameters to be used to control the configuration of the manipulator during milling. Straight after that, the structural dynamics of the manipulator is investigated over the machining table and zero frequency regenerative stability boundaries are found out and validated. Redundancy parameters are utilised to continuously vary the manipulator configuration with the aim of suppressing chatter vibrations while cutting. Lastly, the relation between static stiffness predictions and minimum limiting stability at low and high spindle speeds is investigated.

On the other hand, in Chapter 6, the theory for mode coupling chatter in milling is explained and the zero frequency approach is extended to multi-frequency approach. The stability boundary of the mode coupling chatter in milling is illustrated in zero and multi frequency approaches and validated with cutting tests. Comparisons between regenerative and mode coupling chatter mechanisms are made and the type of the chatter mechanism observed in the robotic milling operation is validated.

Lastly, in Chapter 7, concluding remarks, limitations of the research and future research directions are discussed which is followed by appendices and references.

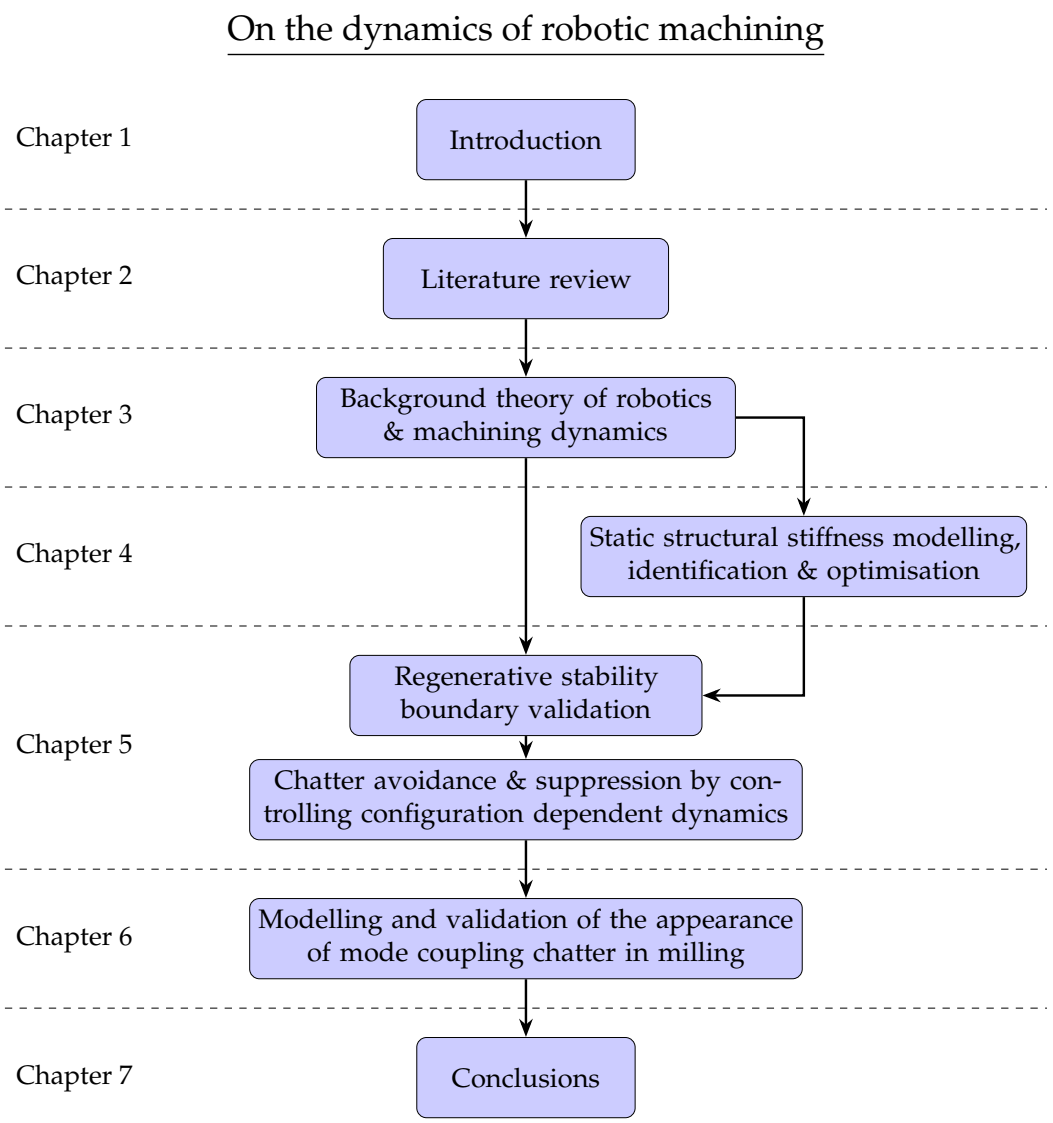

FIGURE 1.4: The thesis layout

Chapter 2

Robots in machining

In this chapter, the overview of the existing literature on machining with robots is presented. The topics outlined are the categorisation of errors in robotic machining applications, the manipulator structural modelling and identification and the chatter mechanisms appearing in robotic machining operations. The state of the art in robotic machining is covered to identify gaps in the knowledge and hence, propose areas where this thesis will make an original contribution to knowledge.

2.1 Introduction

The existence of industrial robots within the industry leans back to 1961 to the instalment of the first ever programmable robot called Unimate by the company known as Unimation to serve for die casting machine [38]. Ever since, the involvement of robots in the industry kept increasing due to their reliability, uniform quality delivery and versatility in carrying out various operations [39]. In today's manufacturing processes, while CNC machine tools are in common use for their excellence in manufacturing products with accurate dimensions and surface finish, their cost and small workspace are the main factors causing investors to seek alternative solutions. In this respect, the idea of substituting machine tools with industrial robots has emerged [24, 25]. This aim is to fully utilise benefits of robots to fulfil incapabilities of machine tools, in particular, low cost, large workspace, dexterity & versatility. Nevertheless, the robotic machining is suffering from poor dimensional accuracy, surface finish and productivity which need to be matched with industry standards. Currently, it is an issue to address these requirements due to various reasons which are the main focus of the thesis. These reasons consist of the relatively poor magnitude and configuration dependency of manipulator structural dynamics. In accordance with that, this chapter focusses on reviewing the state of art technologies developed to overcome aforementioned issues and make robotic machining more applicable in the manufacturing sector.

In this chapter, sources of error in robotic machining applications are categorised in Section 2.2. The modelling of robots in terms of structural static stiffness, as well as structural dynamics are discussed in Section 2.3 to investigate manipulator configuration dependent properties. Section 2.4 examines the chatter mechanisms in robotic machining applications and effects of configuration dependent structural dynamics of robots on the process stability. This is followed by a summary on the current state of art in robotic machining in Section 2.5. Lastly, gaps in the knowledge are discussed and clarified along with aims and objectives of the thesis in Section 2.6.

2.2 Overview of errors and application areas of robots

In machining, the performance of a machine tool is affected by errors that determine the quality of the end product, including, but not limited to, geometric and kinematic, thermal, static stiffness errors, dynamic (vibrations) as well as controller dynamics related errors etc. [40, 41]. Manipulators being utilised as machine tools for machining operations also suffer from similar sources of error as well as errors peculiar to the manipulator architectural structure. As described in [42], sources of error in robotic machining can be divided into three classifications; robot-dependent errors, process-dependent errors and environment-dependent errors.

- Robot-dependent errors are associated with the robot and can be divided into; geometrical and non-geometrical errors as in [43].
  - Geometrical errors arise due to the effect of geometrical imperfections of structural components on the accuracy of manipulator kinematic model. Examples to geometrical errors are; tolerance related errors, assembly (alignment) errors, backlash at gears (due to the looseness of reducers and gears [44]), bearing run-out errors and clearance errors in transmission mechanisms. Due to their nature, the magnitude of these errors could build up along the serial-parallel kinematic chain towards the end effector. Errors could appear as inaccuracies in the TCP pose and can possibly be configuration dependent. Luckily, geometric errors can be compensated to a great extent with kinematic calibration techniques and there are many methodologies developed for error identification, modelling and compensation [45–47].
  - Non-geometrical errors appear from deformation of the structure (transmission elements, links, joints) as well as wear, friction, hysteresis [48] and any other non-linear effects at servo motors [49]. Other factors include control issues arising at rapid TCP movements, wear at joints and thermal effects on motors, bearings and gears [50, 51]. These errors can be time and configuration dependent. Under a particular loading, majority of errors come from the compliance of the robot due to torques and stresses built up on links, gears at joints and servo drivers. It is possible to identify, model and calibrate errors coming from static compliance of the robot as in [52–54], however, this does not improve the TCP path deviations when abrupt change in the TCP motion occurs.
- Process dependent errors are related to the process loading and resultant deviations of the robot structure. The magnitude and direction of errors are directly related to the type and direction of the loading and hence, the operation carried out. Errors arising when handling a payload (static load) are easier to calibrate as their effect on the structure can be easily established as in [55]. In machining operations, however, the TCP is exposed to a dynamic cutting forces. These could result in forced and self-excited (chatter) vibrations in which the behaviour depends on machining parameters.
- Environmental errors are related to effects of environmental factors on the behaviour of the robot. These include vibrations transmitted from nearby machinery to the robot base in a machine shop-floor, mechanical and chemical properties of the floor where the robot is fixated, temperature variations [56], cell calibration [57] and many

more. These factors, in most cases, cannot be modelled and calibrated as they do not have fixed characteristics or values.

Majority of the quantifiable errors appearing in robotic machining applications can be concluded to come from the manipulator geometrical structure and process loading. Approximately 90% of TCP position errors comes from geometrical errors when the external loading is relatively small [43]. As a result, industrial manipulators tend to have relatively poor accuracy, usually in the range of $\pm$ 1 mm [39, 58]. Through appropriate kinematic compensation techniques, it is possible to improve the pose accuracy to 0.1-0.3 mm [59]. On the other hand, based on the fact that the design purpose of industrial manipulators is to perform repetitive tasks [60], they have much better repeatability compared to their pose accuracy, in the range of 0.1-0.03 mm [61, 62] depending on the size of the manipulator [63].

Exposed to dynamic loading (such as cutting forces), the magnitude of errors tends to increase significantly as a result of the relatively poor manipulator structural dynamics and can reach up to 1.5mm [64]. Consequently, the application of robots to machining operations necessitating high dimensional accuracy as well as surface finish has been limited [65]. Despite these drawbacks, machining with robots is currently being utilised in industry and some examples of robotic applications and operations are summarised in Table 2.1.

Machining Operation	Material	Robot
Milling	Steel	KUKA KR240 R2500 [66]
	Aluminum A6063S	Mitsubishi PA10 [67]
Boring	Titanium TC4	ABB IRB 6600-175/2.55 [68]
	High strength steel	ABB IRB 6600-175/2.55 [69]
Drilling	Titanium TA15	ABB IRB 6640-235/2.55 [70]
	Aluminum	ABB IRB 2400 [71]
Welding	Steel	General Electric P-50 [72]
	Mild steel	KUKA KR150 [73]
Waterjet	Rubber	N/A [74]
Grinding	Carbon steel	Scompi [75]
	Stainless steel 304L	Scompi [76]
	Aluminum 5083	Kuka [77]
Trimming & Deburring	CFRP	KUKA KR 500 [78]
	Iron, Aluminum	SCARA [79]
Polishing & Sanding	Aluminum 5083	KUKA [77]
	S45C	Motoman SV3 [80]
	Wood (Japanese Oak)	Kawasaki FS20N [81]

TABLE 2.1: Operations and materials used in robotic machining

2.3 Manipulator modelling for machining applications

In machining operations, controlling the behaviour of the manipulator is crucial in satisfying industry requirements. Identification and modelling of the accurate geometric, static stiffness, structural and controller dynamic models are essential in precisely predicting the manipulator behaviour within its workspace under cutting forces. In this respect, the overview of the literature in modelling and identification of the manipulator structural static stiffness and dynamics is given which are the main focus of the thesis. Thus, a better understanding on the configuration dependent static and dynamic characteristics of manipulators and their effect on chatter mechanisms in robotic machining operations is aimed to be developed.

2.3.1 Static stiffness modelling and identification

Structural stiffness modelling is used to represent configuration dependent quasi-static stiffness characteristics of the manipulator [82] to minimise and compensate compliance errors which are the main sources of non-geometric errors [83].

There are two types of compliance sources within the manipulator structure; passive and active compliance. Passive compliance comes from the geometric and material properties of the base, limbs, actuators, links, joints transmission elements [84, 85]. Passive compliance is usually configuration dependent due to geometric asymmetries as well as the interconnection of structural components resulting in non-uniform stiffness properties. Whereas, the compliance of the position control loop mechanism of actuators at joints is purely as a result of the resistance of the control system to position alterations as a consequence of external disturbances and it is hence called active compliance [86, 87]. This kind of compliance is not configuration dependent as it is entirely dependent on controller compliance. It usually accepted to have a constant flexibility around the axis of rotation of the joint [88, 89]. Combined together, active and passive compliance are dominant sources of deformation of the manipulator and tool under application of external loading.

The Cartesian stiffness for a typical serial industrial manipulator is usually less than 1 N/μm, while a standard CNC machine tool very often has stiffness greater than 50 N/μm [90]. For such a flexible structure, the knowledge and accurate representation of stiffness characteristics may bring the ability to meet higher accuracy and tolerance requirements on end products. The stiffness model can be beneficial for predicting the behaviour of the manipulator under external forces and compensating associated errors. This constitutes the reason for development of a manipulator stiffness model. In literature, there are three methods for estimating Cartesian stiffness of the manipulator at the end effector (or tool) and can be classified as; a) Finite Element Analysis (FEA) b) Matrix Structural Analysis (MSA) c) Virtual Joint Method (VJM).

2.3.1.1 Finite Element Analysis (FEA)

In Finite Element Analysis, the exact model of the robot is constructed in a CAD environment with true geometries, material properties and dimensions of its components [91]. The entire structure is broken down into small elements (truncation of actual geometry by discretisation with small elements) in which mathematical equations governing the underlying physics help in predicting every element's, and therefore the entire structure's behaviour. The stiffness matrix is computed at connecting node analytically by using

static equilibrium equations and conditions between finite elements. For a given loading condition, the mechanical behaviour of each element in equilibrium condition is formulated at each node and assembled into a global stiffness matrix. The global stiffness matrix defines the relationship between the loading applied to the deflection under predefined boundary conditions incorporating the behaviour of all finite elements. Thus, by using the global stiffness matrix, loading matrix and boundary conditions, nodal displacements are computed and assembled to predict global structural deformation. This methodology nowadays is encoded within finite element software packages such as Abaqus, ANSYS, COMSOL Multiphysics, etc. making the implementation of FEA more user friendly. With the availability of these software, static stiffness of manipulators, especially for parallel manipulators, was successfully modelled and validated in the literature.

Accordingly, the static rigidity of a new parallel platform mechanism, T3R1 was analysed using a FE software [92]. The mechanism was meshed with various types of finite elements such as solid, shell and spring elements expressed by different number of nodes and degrees of freedom, each to represent flexible and rigid components. The static stiffness of the robot was then characterised based on loading scenarios and solving the system of equations.

In [91], the FE model of a H4 parallel robot was developed in pursuit of evaluating its static stiffness. In contrast to [92], a simplified FE model of the robot was created with a simple beam model. This was due to the fact that forearms of the robot are bars and their exact behaviour could be described by beams with constant cross section with FEA. Experimental results were found to be similar in the order of magnitude with FEM simulation findings proving the accuracy of the FEA model.

In another work, an FE model of spatial 3-link manipulator with flexible links and joints was modelled [93]. System of equations considered coupling effects between rigid body motion, link flexibility (torsion and bending) and joint flexibility. Results from the numerical model showed that the torsional defection of links has a greater effect than link bending and joint flexibility on the position of the end effector.

Similarly, an FE model of a 3 link planar parallel robot was created based on the linear theory of kineto-elastodynamics to characterise its dynamics [94]. Axially-extendible quintic beam elements were used for each link and natural frequencies of the model were mapped to that of actual robot. It was shown that static stiffness of the robot could be easily obtained from equations developed at different robot configurations. It was noted that the configuration has a great influence on the deflection of the robot.

In [95], Euler- Bernoulli beam elements and shell elements were used to model the static stiffness of a planar parallel manipulator with an FE model for machining purposes. The static FEA was performed to compute displacements of the loaded manipulator and a mathematical optimisation was used to identify components having dominant influence on the overall structural stiffness of the manipulator. In this way, the design of the manipulator was optimised in terms of component dimensions to reduce the weight and improve its performance for machining applications. This showed that FEA is not only a tool for stiffness modelling but could also be used to design and optimise the manipulator architecture.

Dissimilar from other approaches, a static stiffness identification procedure was developed with a FE model for isolated manipulator links in [96]. The developed numerical procedure evaluates stiffness matrix of the manipulator links and takes into account its complex

shape, coupling between translational and rotational deflections and joint particularities. The obtained stiffness matrix was aimed to be used in lumped parameter models such as VJM that has lower computational requirements than FEA. Results obtained for an Orthoglide manipulator showed that the procedure was able to estimate the stiffness matrix of links with very high accuracy.

The literature suggests that FEA enables highly accurate and representative stiffness models for mainly parallel robots because of their easily modelled link geometry and size. On the other hand, as serial industrial manipulators have comparatively large components, FE models necessitate huge computational effort due to the large number of elements required to define the model. As the number of elements increases, the accuracy of the predicted model behaviour rises but with increased computational expense. For this reason, the FEA approach is mainly applied to small parallel robots and usually at the final design stage to assure the compatibility of the designed model with the actual manipulator [97, 98]. It should also be noted that the theoretical boundary conditions set between components within the model may not be realistic, which could easily impose inaccuracies on the modelled manipulator stiffness properties. In addition to that, FEA does not consider the active compliance of manipulators at joints as the model created is a continuum solid model assembled together. Knowing that the active compliance has a significant effect on the manipulator stiffness, ignoring the active compliance could be one of the drawbacks of FEA.

2.3.1.2 Matrix Structural Analysis (MSA)

Matrix Structural Analysis (MSA) is the historic ancestor of FEA. It stands on three aspects; mathematical models, matrix formulation of discrete equations and computing tools to do the numerical work [99]. In the FEA, the geometry is represented with continuum mathematical models and solved with more efficient matrix formulations as a result of the increased computational power. As opposed to FEA, the geometry of the structure is defined with large elements and discrete mathematical models in the MSA. Structures are defined in matrix formulations and solutions are obtained by computations under either human or computer controlled methods. FE elements being used are large and compliant (mostly shell, beam, truss, grid elements etc.) [100, 101]. The MSA can be thought as the simplified version of the FEA and the direct implication of this is the reduction of computational complexity of the problem and ease of understanding of the model behaviour. Thus, the MSA can be regarded as a tool to confirm credibility of FEA and obtain a quick understanding of the structure. In general, material properties of elements are defined in matrices, assembled in a global matrix and solved to obtain behaviour of the system, just as in the FEA, but with larger elements. Benefits of the MSA were also acknowledged and utilised in static stiffness modelling of manipulators. The ease of modelling links with large elements and relatively fast computation of the manipulator stiffness matrix made the MSA an attractive modelling tool.

In an attempt to calculate stiffness matrix of a Parallel Kinematic Machine (PKM) for machining applications, links were represented with large beam elements in [102]. The analytical stiffness model with perfectly rigid and flexible joints were computed and compared. The comparison of these MSA models with their corresponding FEA model as well as experiments showed that incorporation of flexible joints enhanced the model accuracy. This indicated that the MSA might suffer from inaccuracies due to oversimplification

compared to the FEA model, but acceptable accuracy could be established by increasing the model complexity by taking into account the joint flexibility.

In [103], truss elements were used to model the stiffness of a Stewart platform-based manipulator with a spindle via MSA for milling operations. The choice of FE element type simplified links as bodies enabling axial force transmission and hence allowing only translational deformations. The model was verified experimentally with fair accuracy. Stiffness maps of the manipulator were obtained within its workspace to show that the stiffness varies within the workspace. The choice of truss elements was suspected to be the reason for the relatively low accuracy in the predicted robot stiffness as they oversimplify stiffness characteristics of slender links.

Similarly, the stiffness of a Stewart platform was modelled by MSA in [104]. The manipulator was broken down into smaller and more identifiable substructures, the stiffness matrix of each substructure was built and then assembled to obtain the stiffness of the entire structure. This enabled the visualisation of the manipulator tangential, radial and axial stiffness distributions among its workspace and comparison with experimental results showed good match with model predictions.

In a more recent work, a unified MSA stiffness modelling technique was introduced which can be applied to various robot topologies with assorted structural component properties such as flexible links and rigid connections, passive and elastic joints etc. [105]. The unified model consists of aggregation of link stiffness characteristics at the end of each link (usually from a representative FEA model or analytical approximations for simple geometries), boundary constraints and connections between links imposed by various joint types. Thus, in its basis, the unified method does not take into account large FE elements as in the classical MSA method, but instead it utilises the accuracy of the FEA to represent compliance properties of these elements as a substitute. As a result, a more robust and accurate representation of the MSA manipulator stiffness could be obtained in which numerical solutions for NAVARO manipulator proved the effectiveness of the unified model.

On the whole, the Matrix Structural Analysis method enables relatively accurate stiffness modelling especially for parallel manipulators whose components can be defined by simple geometries such as uniform cross sectioned bars. Slender links of such manipulators are modelled by large FE elements, which distinguish the MSA from the FEA and provide reduction in computational complexity of the problem. Another benefit of the MSA is the ease of physical interpretation of findings, which help further understanding the manipulator behaviour and stiffness characteristics. With regards to the identification of MSA manipulator models, the model accuracy ultimately relies on material and geometrical parameters of FE elements representing manipulator links. These parameters could be either defined from a corresponding FEA model or identified by the static loading test.

2.3.1.3 Virtual Joint Method (VJM)

The Virtual Joint Method (VJM) is a "Lumped Parameter Model" where the description of the behaviour of the manipulator is simplified by discrete representation of the behaviour of each component. Stiffness properties of links and joints are defined in lumped locations. On this basis, the VJM is an extension of the original rigid model consisting of rigid links and joints. For stiffness modelling, the rigid model is relaxed to consider the localised joint elasticity to describe the deformation of the entire manipulator at the end effector. The main assumptions can be summarised as below;

- Manipulator links are rigid (inelastic).
- Torques developed at joints as a result of the manipulator weight and payload are acknowledged to be compensated by the controller.
- The main manipulator flexibility comes from the active position control loop flexibility of the actuator under external loading at joints.
- The control loop flexibility behaves linearly around the axis of rotation of the revolute joints along their natural motion axis and it is time invariant. Hence, it is represented by one-dimensional linear virtual torsional springs with constant stiffness at actuated joints [106].
- The external loading is small enough to ensure that the assumption of the linear control loop flexibility is satisfied.

The VJM approach is originated from Salisbury [107], in which the author aimed to actively control the Cartesian Stiffness of a manipulator end effector. Known as the "conventional stiffness model", the relationship between the Cartesian and joint stiffness was defined with the help of the Jacobian matrix. It was assumed that dominant source of compliance is due to the elasticity in the control loop mechanism at actuated joints and it can be simplified and represented as virtual linear torsional springs as in Figure 2.1. The same approach was applied to the planar and spatial parallel manipulators by Gosselin [108], where the stiffness matrix was realised in similar manner. Manipulator stiffness maps and the relation of the stiffness to singularities were analysed.

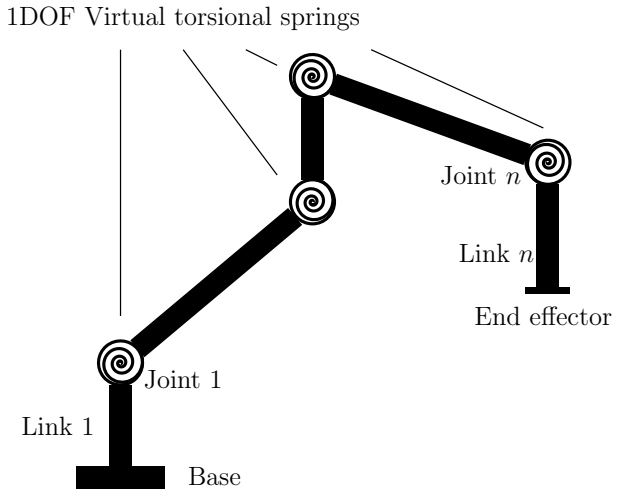

FIGURE 2.1: The VJM stiffness modelling of a serial robot based on conventional method

In [90], the insignificance of elasticity of links was underlined for a serial industrial robot, ABB IRB 6400, and dominant compliance was claimed to come from joint compliance. While assuming links to be rigid, the flexibility in joints was underlined to come from many sources, in addition to the control loop compliance. Hence, joint compliance was attributed to the overall elasticity at joints including active and passive components. The stiffness formulation derived followed the original approach introduced by Salisbury [107]. It was also underlined that the tool gravity was compensated via controller and therefore the manipulator is at unloaded equilibrium condition. The surface error before and after deformation compensation revealed that the magnitude of errors left behind are in the order of the pose accuracy of the robot.

Alternative approach was developed in [109] where as opposed to modelling Cartesian stiffness matrix, Cartesian compliance matrix was proposed for an industrial 6 axis serial robot. While the stiffness matrix requires computation of two inverse matrices as in [107, 108], utilising the compliance matrix requires only one. In this way, computational requirements can be reduced for potential application of online form error compensation techniques during machining. Comparison of model results with experimental findings revealed that model predictions underestimate Cartesian compliance of the manipulator, which could be seen as a proof of the low accuracy of the VJM. Similarly, researchers in [110] modelled the compliance model of a 5 axis serial machining robot. The compliance matrix formulation enabled representation of each compliance matrix entity in terms of joint compliance parameters and Jacobian matrix entities. Hence, the joint compliance parameter identification was facilitated by a great extent.

The conventional manipulator compliance modelling was extended in [111] by incorporating 2 more virtual linear torsional springs at joints in order to represent remaining rotational DOFs. The extended VJM model was aimed to take into account factors such as link and bearing flexibility of the serial manipulator RV130HSC. The comparison of experimental measurements, conventional stiffness model and the proposed model showed that a better approximation of the manipulator compliance could be achieved. The effect of link and bearing deformation around the joint's axis of rotation was found to be insignificant but this was not the case in other directions.

In following studies, "conventional stiffness model" is acknowledged to be only valid if the manipulator is not externally loaded. The conventional model was emphasised to misrepresent the manipulator stiffness under the external loading and result in non-conservative mapping between joint and operational spaces [112]. In this respect, an enhanced stiffness model known as "Conservative Congruence Transformation" (CCT) was introduced. It contains an additional stiffness component *Complementary stiffness matrix*, which takes into account the stiffness variation coming from the manipulator configuration alteration under the external loading [113]. Numerical simulations showed that introducing the *Complementary stiffness matrix* ensures symmetric mapping between joint and operational spaces, while preserving the positive definiteness of the manipulator stiffness matrix.

In [114], the stiffness model of a 6 axis industrial robot, Motoman SK 120 was identified and characterised with CCT. The *Complementary stiffness matrix*, was underlined to be essential for the accuracy and identification of the manipulator stiffness model. The *Complementary stiffness matrix* was observed to complicate the joint compliance identification due to the requirement of the derivative of manipulator Jacobian and non-linear least squares regression. Experimental findings showed that identified manipulator compliance matrix

entities were fairly linear. This indicated that the effect of *Complementary stiffness matrix* is relatively small and joint compliance parameters are, to a great extent, constant. It was shown that forces up to 10 kN are required to be externally applied in order to violate the positive definiteness of the stiffness matrix and linearity of compliance matrix entities.

In a similar work, the CCT stiffness modelling was utilised to identify stiffness characteristics and joint compliance parameters of an industrial 6 DOF Kuka KR240-2 robot in [115]. Dissimilar from [113, 114], Kinetostatic Conditioning Index (KCI) was used to search for non singular manipulator configurations, where the effect of *Complementary stiffness matrix* on the manipulator stiffness matrix is negligible. In this way, the CCT stiffness modelling was reduced to conventional stiffness modelling to ease the joint compliance identification process. The work also emphasised that the larger number of manipulator configuration used in the identification, the better the measurement noise would be minimised.

Extending the CCT stiffness modelling further, the flexibility of the gravity compensator of a heavy industrial serial robot, KUKA KR-270 TM was also modelled in [116, 117]. Modelling of the gravity compensator, however, required identification of its geometry and representative passive stiffness, which in turn introduced additional complexities into both numerical and experimental identification procedures. An approach to determine optimum manipulator configurations which are the least sensitive towards the measurement error was introduced but due to its numerical exhaustiveness, it was not computed. Even though joint stiffness parameters were identified relatively accurate, the compensator stiffness was observed to possess parameter identifiability problems because of its high stiffness. Similarly, the flexibility of the gravity compensator was also modelled with the same approach but for a parallelogram manipulator in [118] and a pneumatic gravity compensator for a serial robot in [119].

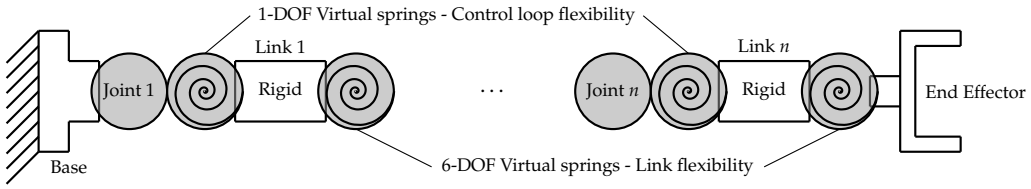

FIGURE 2.2: The VJM stiffness modelling considering the link flexibility adapted from [120]

Next enhancement was brought by introducing 6 DOF virtual springs to model the flexibility of each link of a serial manipulator in addition to 1 DOF linear torsional springs representing the control loop stiffness of joints as in Figure 2.2 [120]. The increased complexity of the model, however, resulted in the problem of elastostatic parameter identifiability. This was due to the significant effect of the noise on some of link compliance parameters whose magnitudes are not comparable to the impact of measurement noise. As a result, the experimental identification of elastostatic parameter may result in the compliance matrix losing its positive definiteness property, its symmetricity, and the accuracy of its entities. These entail the necessity of model reduction to avoid redundant and insignificant parameters to be identified. The comparison of the accuracy of the experimentally identified elastostatic parameters for Kuka KR-270 revealed that errors based on the compensated deflection of the manipulator were smaller for the model compared to the conventional stiffness model. For serial industrial robots, the proposed model was found to be the most accurate and advanced approach found in literature but at an expense to the numerically cumbersome model reduction as a result of consideration

of link flexibility and measurement errors. In addition, the model does not take into account the stiffness variation as a result of the manipulator configuration alteration under external loads, as in [113, 114].

Some scenarios exist where the VJM is applied to parallel manipulators. For example, in [82], over-constrained parallel manipulators, for which standard stiffness analysis cannot be performed, VJM stiffness modelling considering link and actuator flexibility by 6 DOF virtual springs and control loop flexibilities with 1 DOF virtual springs as in [120] was introduced. Dissimilar from serial industrial manipulators, the fact that parallel manipulators have multiple serial chains and various joints types such as passive, universal, parallelogram etc., each kinematic chain was treated individually. The stiffness of the entire manipulator was then obtained by the sum of stiffness of each serial chain. Compared to the commonly applied MSA stiffness modelling, the accuracy of the proposed VJM model and stiffness predictions was shown to be improved.

In [121], researchers developed an enhanced stiffness model for parallel manipulators with passive joints, which takes into account internal and external loadings on the manipulator. Kinematic chains under consideration were under-constrained and as opposed to [82]. The original VJM model was extended to include passive joints and additional 6 DOF virtual joints to represent stiffness of links. The proposed approach enables finding out the stability of the loaded configurations against buckling phenomenon which is important in the design stage for the evaluation of critical forces.

With regards to identification of the elastostatic (joint and link compliance) parameters in the VJM stiffness model, there are two approaches; Local and Global Method as described in [122]. Distinguishing features are the way external loading is applied and corresponding deflection is measured.

Local Method: In the local method, joint stiffness parameters are locally identified one at a time. This is done by locking joints of robot other than ones being measured, applying a static force to the link coming after the joint and measuring its angular displacement. This is to ensure that the applied loading cause angular displacement at only one joint at a time and not for the others simultaneously. In this way, equivalent linear torsional spring parameters for each joint could be estimated individually by the angular form of Hooke's Law.

In this respect, authors in [122] used a laser tracker to measure angular displacements of first and second joints of an industrial 6-axis robot. For the rest of joints, a locking equipment and electronic level were used to lock joints and measure their deflection. Each joint was loaded by dead weights and based on the position of the application of the force, the external torque on the joint was found. The relationship between torque and angular displacement, according to angular form of Hooke's Law, was used to obtain a measure for the virtual linear torsional spring. Similarly in [109], each joint was loaded one at a time by clamping the rest of the joints to ensure they were not moving. An external loading was then applied to the joint and its angular displacement was measured to find the corresponding joint compliance parameter of each joint.

It should be noted, in the local method, locking the joints does not guarantee that control loop flexibility being measured is unaffected by the deflection of other joints. The necessary pose adjustment for force application is also another issue to be considered for joints 4, 5 & 6 since they mainly contribute to the orientation of the end effector as in [123]. Another factor to acknowledge is that even though the local method aims to identify the control

loop flexibility, deflection of the links is also inherently measured as the loading is usually applied to the link. To summarise, the local method is onerous in being implemented in an industrial environment and requires extra equipment for locking the axes. The measured deflection would always be affected by the flexibility of other joints depending on the joint under consideration and the point of application of the loading as schematically shown in [122].

Global Method: In the global method, linear virtual torsional springs are identified by applying forces to the end effector and measuring the end effector deviation at specific manipulator configurations. On this basis, the global method aims to relate end effector deflections and applied loading to the linear virtual torsional springs with the help of Jacobian matrix. The identification of virtual springs requires the manipulator to be loaded multiple times and its deflection to be measured at different configurations. A minimisation algorithm is then used to identify the linear virtual springs at the same time to minimise errors coming from the deflection measurements.

In this approach, the applied loading at a given manipulator configuration is generally measured by a force sensor [66] or is comprised of previously measured static weights and torques as in [110, 114, 120]. On the other hand, the deflection of the end effector pose is usually measured with CMM [90, 110], laser trackers [114, 120], 3D Scanning Laser-Doppler Vibrometer (LDV) [66] etc.

In practice, however, the deflection of the end effector under the external loading is due to active and passive compliance of the manipulator structure as well as other factors such as assembly tolerances and backlash etc.. For conventional and CCT stiffness modelling with rigid link assumption [107, 108, 113, 114], all of these factors are included in the identified elastostatic parameters (linear virtual torsional springs). Except from the control loop flexiblity, these factors tend to vary at different manipulator configurations due to the geometric asymmetries of links, non-linearities due to the backlash within gears etc.. Hence, the repetition of the test at many manipulator configuration is not only essential to minimise the measurement noise but also to average out the effect of varying link flexibility, backlash, any tolerances on the identified elastostatic parameters (virtual springs). On the other hand, for the VJM models considering link flexibilities [82, 120, 121], the effect of varying link flexibility on linear virtual torsional springs are inherently eliminated allowing better modelling of the manipulator structural stiffness. To sum up, the global method is more pragmatic and accurate in identifying the elastostatic parameters of the model, allowing the consideration and identification of link flexibilities as well.

2.3.2 Static stiffness optimisation

The literature suggests that serial industrial manipulators have poor and configuration dependent static stiffness properties [65]. For a given time invariant load applied externally on the end effector, such as the static component of cutting forces, form errors tend to be relatively large and configuration dependent too. To compensate form error, mainly two approaches are being used; modification of the manipulator model by external encoder readings and modification of the robot control program by an error model (cutting trajectories) [124]. While the first option is an online compensation method, the second option is an offline method which enables cutting trajectory alteration based on predicted TCP deviation. In either way, both methods require TCP trajectory alteration to compensate the form error, where the larger the form error is, the larger is the TCP pose alteration needed.

A solution to minimise the severity of form errors is to optimise the configuration dependent manipulator stiffness. Improving the manipulator stiffness in the directions where cutting forces cause the most tool tip deviation has the potential to reduce form errors. In this respect, the degree of freedom around the axis of rotation of the tool could be utilised to control the manipulator configuration and hence, optimise its static stiffness. This should be attained while making sure the process is stable and the manipulator is away from any kinematic singularities. In literature, there is a substantial amount of work done in optimising the stiffness of industrial robots to improve the productivity of robotic machining.

In [125], the Stiffness Feasibility Ellipsoid was proposed for controlling Cartesian stiffness of the end effector based on the applied external force. The Stiffness Feasibility Ellipsoid describes feasible end effector stiffness characteristics along its principal dimensions. For the redundant manipulator, an optimisation algorithm was formulated to realise the desired Cartesian Stiffness matrix. The largest direction of the stiffness feasibility ellipsoid was aligned with the direction of the applied external loading while optimising the redundancy variable and hence, manipulator configuration. It should be noted that this approach is one-dimensional stiffness control based on the external force direction. It does not take into account the cross coupling and the magnitude of the force which could still impose a deflection in the direction in which the largest dimension of the ellipsoid is aligned.

In [126], the stiffness of a redundant cable driven anthropomorphic manipulator was modelled with the MSA, where shoulder, elbow and wrist stiffness matrices were assembled to realise the manipulator stiffness. The stiffness optimisation was achieved by computing the inverse kinematics of the manipulator by using the manipulator Jacobian. The eigenvalue of Cartesian stiffness matrix was used as the optimisation parameter as a scalar indication of manipulator stiffness. However, the proposed approach does not take into account any singularities and joint velocity limits, hence findings may not necessarily be applicable in practice. The eigenvalue of the stiffness matrix may not be an efficient approach to optimise the robot stiffness as eigenvectors may not be aligned with the DOF that needs to be optimised.

In [127], an off-line trajectory planner was used to determine optimal manipulator configurations for a tool trajectory for a platform with two manipulators. The optimisation was achieved by considering the redundancy arose as a result of utilising two manipulators, the trajectory and manipulator compliance. The methodology was based on a local optimisation method that approximates the next manipulator configuration by considering

the current configuration. To achieve a global optimisation, the null-space was searched to find the least compliant configurations starting from a random configuration. However, the fact that a local optimisation method was used to find the stiffest manipulator configuration from a completely random configuration does not guarantee that the optimisation would find the global stiffest configuration for the given tool pose. To clarify, what may seems as the stiffest configuration for a given tool pose might not be the same when the entire redundant degree of freedom was spanned.

For a robotic drilling application carried out by 6 DOF KUKA KR360-2 [128], the optimal manipulator posture was aimed to be determined in order to increase stiffness of the manipulator. A performance index that represents the volume of the compliance ellipsoid, whose primary dimensions correspond to the translational compliance of the tool tip, was optimised by a Jacobian-based local optimisation method. The redundant degree of freedom around the axis of rotation of the tool was slightly rotated and the new manipulator configuration and its corresponding performance index was computed iteratively. It should be noted that the performance index does not take into account the effect of cross compliance parameters, between the translational and rotational degrees of freedom which could still impose rotational errors on the tool path. Also, the computation of new joint angles of the robot raises concerns in the TCP pose accuracy and the stiffness index accuracy. Hence, the optimised configurations might not necessarily be configurations with highest stiffness in the considered force direction.

In [129], the manipulator configuration was optimised for machining operations based on the decoupling of the optimisation problem by position and orientation manipulator kinematics. Due to the fact that the manipulator configuration is dependent on the workpiece placement, first workpiece placement optimisation was carried out based on Kinetostatic Conditioning Index (KCI) (see Section 3.1.3 for the description). The stiffness index, same as in [128], was used to find optimal joint angle ranges for joints 2 and 3 to optimise the position of the workpiece, whereas the deformation index was used to determine optimal joint angles ranges for joints 4, 5 & 6. It should be noted that decoupling of the optimisation problem is not an effective way of optimising manipulator configurations as all joints have an effect on the manipulator stiffness. In contrast, the deformation index does not consider the effect of the loading magnitude, which inherently influences the optimisation problem.

Up until this point, the stiffness optimisation does not guarantee the exact tool tip pose as in [128] nor the optimal manipulator stiffness as in [125, 127, 129] nor practical constraints as in [126] at the same time. With the aim of investigating the tool tip direct compliance while ensuring guaranteed tool tip pose, the manipulator compliance optimisation was achieved in the author's conference publication in [130]. Briefly, the functional redundancy around the axis of rotation of the tool was discretised over the machining table to find all possible manipulator configurations by closed form inverse kinematics. Providing that the manipulator is away from singularities, the variations in the direct compliance parameters were investigated. The theory of the approach is detailed in Section 4.7 of this thesis. Note that, as the aim was to optimise the stiffness, the effect of the magnitude and direction of cutting forces on the deflection was not taken into consideration for form error minimisation and was out of the scope of the work.

For a robotic drilling operation in [131], the axial stiffness of the manipulator tool tip was obtained based on the stiffness ellipsoid rather than the compliance ellipsoid as in [128]. The TCP principal stiffness magnitude and directions were found and converted

to axial stiffness by assuming that unity external force is applied to TCP. The stiffness in axial direction was then optimised by utilising the functional redundancy around axis of rotation of the tool and the external axis while ensuring the tool tip pose, good manipulability and joint limit avoidance. It should be noted that for drilling applications, the assumption of unity force does not hold as axial forces are larger than radial forces hence, the approach may not deliver the optimal manipulator configuration with stiffest direction.

In [132], a number of critical points were defined on the end effector which were used to evaluate the deformation under cutting forces by using the sum of squared values of displacements assuming that torques coming from cutting process are negligible. As a result, the deformation ellipsoid was obtained and the largest eigenvector showing the largest deformation direction was used to create a deformation index. Then, the redundant degree of freedom around the axis of rotation was used to optimise the deformation index while ensuring exact tool tip pose, trajectory smoothness and avoiding joint limits and singularities. Note that the deformation index assumes constant norm for external forces and takes into account their direction but does not consider the actual magnitude of forces. In addition, the choice of the largest deformation direction could give the most compliant direction of the manipulator however, does not guarantee the minimisation of form errors in the required direction.

In [133, 134], the spindle configuration was optimised to achieve enhanced manipulator stiffness and minimum tool deflection. The previous work ([129]) was extended to optimise and design the spindle configuration and to minimise the tool defection by using a deformation model in [133]. Results indicate that the closer the tool tip is to the end effector flange, the less the tool tip deformation is due to the minimised torques at the end effector as a result of cutting forces. Whereas in [134], the installation angle of the spindle (spindle holder orientation) was first optimised by maximising manipulator stiffness and then the tool deflection was compensated to increase the accuracy of the robotic drilling task. The optimised installation angle was found to be 45° based on minimum singular value of the manipulator stiffness in translational directions.

It should also be underlined that the redundant degree of freedom around the axis of rotation of tool could also be utilised for optimising other aspects. These aspects include joint limit and singularity avoidance [4], minimising the joint rate and torque magnitude for machining operations [135], optimising the depth of cut while ensuring the milling process is regeneratively stable [136, 137].

To summarise this aspect of the literature, the manipulator stiffness and deformation optimisation techniques have been shown to be easily achievable by utilising the redundant degree of freedom around the axis of rotation of the tool. However, providing the cutting process is stable, optimising the stiffness of the manipulator is not sufficient to minimise form errors. This is due to the fact that the magnitude and directions of cutting forces and torques on the tool tip influence the magnitude of the TCP deformation. Therefore, deformation models are best suited to form error minimisation as they take into consideration the external loading. Nevertheless, in the literature, even though the direction of cutting forces were considered, their magnitudes were ignored. Hence, the manipulator configuration optimisation based on these deformation models does not guarantee the minimisation of form error. The deformation models can be improved by taking into account the magnitude and direction of the static part of cutting forces

and torques, which inherently depend on machining parameters. In this way, an off-line compensation methodology could be applied to effectively minimise any form errors.

2.3.3 Dynamic modelling and identification

In robotics, manipulator dynamics describes the relationship between end effector motion in terms of pose, velocity and acceleration to torques applied at joints to satisfy an accurate end effector trajectory tracking [138]. This is achieved, in general, by identifying, modelling and controlling of dynamics of links and joints. In practice, inverse dynamics, which provides joint torques and forces in terms of joint positions, velocities and accelerations [139], is the point of interest and solved in manipulator controller based on a particular manipulator dynamic model with Lagrangian, Newton-Euler method or virtual work principle [140]. Various types of models are present in the literature, which mainly describe inertial, frictional, centrifugal and gravitational effects of joints and links as well as static payloads on the end effector motion [141, 142]. Discrepancies between models appear in terms of the modelling method and underlying assumptions describing the model dynamics, such as rigid and flexible body assumptions of links and joints as in [93, 143, 144]. Nevertheless, manipulator dynamics is not the focus of this thesis, instead, manipulator quasi-static structural dynamics is the main point of interest, which describes the behaviour of the manipulator under externally applied dynamic loading for a particular manipulator configuration.

For machining operations, structural dynamics at the end effector (in particular, at the tool tip) is required to predict the behaviour of the structure under cutting forces. The behaviour of the system subject to the dynamic loading is in terms of dynamic displacement, velocity or acceleration in either time or frequency domains. In this respect, in [145, 146], in order to describe the dynamic behaviour of a one and two link flexible manipulator, the partial differential equations were established. Equations were solved based on the Lagrangian formulation. Even though the experimental and model results showed good agreement at the defined modes of vibrations, less significant modes of vibration and un-modelled dynamic particularities were observed to cause deviations, which could end up misrepresentation of the system.

As a more advanced approach, the numerical computation of partial differential equations, Finite Element Analysis (FEA), was utilised in latter studies for single link flexible manipulators as in [147, 148]. FE models of flexible manipulators showed improved performance relative to the models solved by analytical Lagrange formulations when compared with their experimentally identified dynamic behaviour. Nevertheless, developed FE models of single link flexible manipulators were simple models consisting of couple of elements and cannot be directly applied to serial industrial manipulators that are larger in size and complex structures.

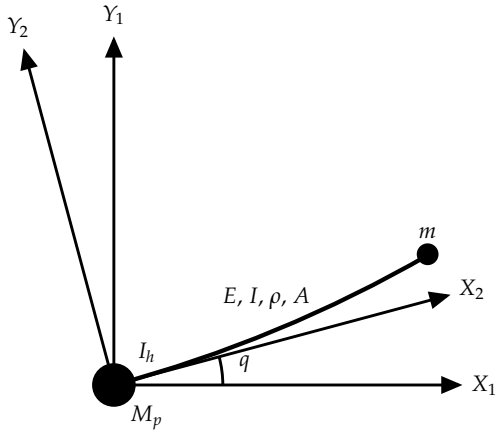

FIGURE 2.3: The description of a flexible single-link manipulator system [147]

In [149], a FEA model of a serial industrial manipulator, Staubli TX200, together with spindle and cutting tool were built in Abaqus to identify the modal mass of the first mode of vibration at the tool tip. Standard tetrahedron elements with various sizes were used to represent the structure. Findings showed that the first mode of vibration of the structure is at at a frequency approximately 44 Hz. Similarly, in order to model the configuration dependent low-frequency modes of vibration of a six axis serial robot, ABB IRB 1200, and obtain principal stiffness directions, the FEA model of the manipulator structural dynamics was established in ANSYS [150]. The model was built by tetrahedral elements and rigid connections were assumed between links and joints. In both approaches, control loop flexibilities of actuators were not taken into account and theoretical boundary conditions were used between links and joints. These facts indicate that even though the structural dynamics of individual components could be accurately represented, the structural dynamics of the assembly of components, the entire manipulator, could not be accurately computed at the tool tip by FEA.

The dynamic model of the anthropomorphic manipulator, Staubli 170 BH, was built based on the simplified FEA, Matrix Structural Method (MSA) in [136]. The serial chain of 3D Euler-Bernoulli beam elements were used to represent the flexibility of asymmetric links, whose stiffness properties were defined from its corresponding FEA model and linear virtual torsional springs were used to represent control loop flexibility. Assuming proportional damping, associated coefficients were calibrated with experimental modal testing and mode shapes and natural frequencies of the structure were obtained by Lagrange formulation. In this work, utilising a serial chain of beam elements with uniform cross section does not accurately represent the asymmetrical link geometry. Additionally, since the model was calibrated with a FEA model but not with any experimentally identified FRFs, the accuracy of the model is questionable.

Similarly, the dynamic model of the industrial manipulator ABB IRB 6660, was built by MSA in [137, 151]. In this case, a more complicated and accurate representation of links was obtained with the 3D Euler-Bernoulli beam elements and the first mode of vibration was verified in terms of its natural frequency with its corresponding FEA model. As before, linear virtual torsional springs were used to represent control loop flexibility, the proportional damping was assumed at the tool tip and the associated damping coefficients were calibrated with the experimental modal testing. In addition, in [137], geometrical and

material parameters of the spindle and tool were also calibrated with the experimental modal testing to fit the modelled modes of vibration to the experimentally identified FRFs. It is worth noting that, the verification of the first mode of vibration of links with its corresponding FEA model does not necessarily mean that the MSA model is accurate. The higher frequency modes of vibration were also not considered to fully validate the model. The frequency calibration to adjust the spindle, tool geometrical parameters and material properties through numerical optimisation could potentially result inaccurate representation of the structure. A numerical calibration could adjust the unknown parameters to fit the experimental data for a given manipulator configuration but it does not necessarily mean that findings are applicable across the workspace. Nevertheless, the control loop flexibility could easily be represented as well as the computational requirements could be alleviated to model the structural dynamics of manipulators with an acceptable accuracy in MSA compared to FEA models.

In order to further simplify the structural dynamic modelling and computational complexity, the lumped parameter modelling technique was used to represent mass and stiffness of components of industrial serial manipulators, KUKA KR210 and ABB IRB 6660, in [37, 152], respectively. The damping was assumed to be negligible, inertia matrix was obtained from either computer aided design (CAD) models or the manufacturer. On the other hand, stiffness matrix was obtained by estimating the static stiffness of the manipulator for a particular configuration by VJM stiffness modelling. The equation of motion was solved by Lagrange's method. Even though such an approach makes it easier to compute the structural dynamics, mass and stiffness matrices may not represent multiple modes of vibration of both the structural modes of vibration and local flexibilities, such as spindle shaft-tool holder and tool modes of vibrations. In addition, assumptions of symmetric mass and stiffness matrices are not valid assumptions considering the asymmetrical structure of the manipulator. In [153], the Lagrange formulation was used to model the tool tip dynamics of ABB IRB 6660, which were identified by modal testing. The prediction of tool tip dynamics however, was implemented with inverse distance weighted method in which the accuracy at high frequency modes of vibration was acceptable. It must be noted that low frequency modes of vibration were not considered.

In [154], a modal testing was implemented at the tool tip of COMAU NJ220 robot to obtain a more accurate representation of the dynamic behaviour compared to the modelling its dynamics through VJM, MSA or FEA. The direct FRFs at the tool tip were identified and represented with a the mass-spring-damper for process stability analysis. Eddy current dampers were then used to alter the structural dynamics. In the aforementioned work, the direct FRF in radial direction and the cross FRFs were not considered nor modelled, which cannot be neglected due to the effect of the poor dynamics of the flexible manipulator on the machining dynamics. In [34, 155], the direct FRFs in feed and radial as well as cross FRFs of FANUC-1000i and ABB IRB 6660 were identified with modal testing at the tool tip at a single manipulator configuration and shown that consideration of cross FRFs influences the stability of the process indicating that they are important in fully defining the dynamics of the structure.

Whereas, in [156], low frequency modes of vibration of the COMAU NS16 industrial robot were identified in direct and cross directions at a couple of manipulator configurations and shown to be configuration dependent. This finding underlines the fact that modal testing is only valid for a particular manipulator configuration and low frequency modes come from the manipulator structure. In [157], direct FRFs in low frequency spectrum

along the feed, radial and axial directions at the tool tip of KUKA KR240-2 were identified along the cutting trajectory. Their time response was studied while the spindle was turned on and off. Results indicated that low frequency modes of vibration depend on the manipulator configuration and by turning the spindle on, the frequencies due to imbalance were identified in order to better understand the frequency content of the manipulator dynamics. Similarly, the direct FRF in feed direction of ABB IRB 6660 was identified at low and high frequency spectrum with modal testing along the machining trajectory [35]. It was shown that low frequency modes of vibrations strongly depend on manipulator configuration whereas higher frequency mode of vibration coming from the spindle shaft-tool holder assembly show weak dependency. The slight variation of properties of the higher frequency mode of vibration was also validated along the cutting trajectory by modal testing at the tool tip of ABB IRB 6660 in [36]. In [153], instead of identifying the tool tip dynamics along the cutting trajectory, the manipulator configuration was altered around the axis of rotation of the tool, its functional redundancy. Findings showed that even though the tool tip position was the same, the high frequency modes of vibration could still get slightly altered as a result of the manipulator configuration alteration by the functional redundancy.

On the other hand, the direct and cross FRFs at the tool tip of a parallel (hexapod) robot were identified at various configurations within its workspace in [158, 159]. Low frequency modes of vibration were observed to be more rigid than that of serial industrial robots but the configuration dependent characteristics of its dynamics were observed to still be present for a parallel kinematic machine. This observation was due to the multiple serial kinematic chains supporting the end effector result in improved structural dynamics compared to a serial chain industrial manipulator.

To sum up, there exist FEA, MSA and lumped parameter modelling techniques to model the manipulator structural dynamics. Just as in static stiffness modelling, FEA delivers accurate predictions but suffers from high computational power requirements when it is applied to large manipulators. MSA could be utilised to reduce the computation load by utilising larger FE elements, however, virtual joints used do not only describe position control loop stiffness (during identification the link compliance and other non linear effects are also included) and the large FE elements are defined to represent links based on CAD models. As a result, a calibration is required, which still does not guarantee the accuracy of the model. The lumped parameter approach, in contrast, is the most simplistic way of representing the structural dynamics with a compromise of the overall prediction accuracy, which is the least among the rest. Considering all the bespoke techniques, the modelling and identification of a manipulator structural dynamic model is cumbersome and may lack of accuracy across the work volume for such large structures. The accuracy of identified dynamics could be enhanced greatly by conducting modal testing but findings are only valid for a specific manipulator configuration as opposed to the ability of FEA, MSA and lumped parameter models to predict the dynamics in different manipulator configurations.

2.4 Chatter in robotic machining

Unstable vibrations during machining processes (chatter) have been known to cause adverse effects including but not limited to tool wear, surface finish, dimensional accuracy, damage to the machine tool, etc. The machine tool chatter has been the interest of researchers leaning back to the 20th century [160]. The first ever attempts to explain characteristics of the chatter phenomenon were made by [161–163] but its behaviour was not fully understood at that stage. The first mathematical model of chatter vibrations (regenerative) that takes into account the spindle speed effect on the stability was developed in 1958 [164]. Later on, the machine tool chatter has been also covered by many authors and remarkable contributions were made to better understand the phenomenon as in [165–168]. The two major sources of self-excited chatter mechanisms in machining process have been identified to be regenerative and mode coupling chatter in machine tools [26], even though there also exist other chatter types as described in [169]. This section presents an overview of the previous work concerning regenerative and mode coupling chatter mechanisms in robotic machining operations.

2.4.1 Regenerative chatter

In machining, the machine tool instability is known to be dominated by a special type of self-excited vibrations called regenerative chatter [26]. Regenerative chatter emerges as a result of the instability of the dynamic chip thickness, which is the difference in the undulations (oscillations) imprinted on the surface of the chip on current and previous passes of the tool in turning, or tooth in milling (see Figure 2.4 for wave generation). Undulations are caused by the vibrations at the tool-workpiece interface which, depends on machine tool and workpiece structural dynamics. Provided that the amplitude of the dynamic chip thickness is large enough, the phase difference between current and previous undulations determine the stability of the process. The dynamic chip thickness causes dynamic variations in the cutting forces, which in turn affect proceeding undulations resulting in a closed-loop feedback mechanism. In case of instability, the system oscillates at a chatter frequency close to the natural frequency of the system, leaving behind poor surface finish on workpiece as well as potentially causing damage or wear on the tool.

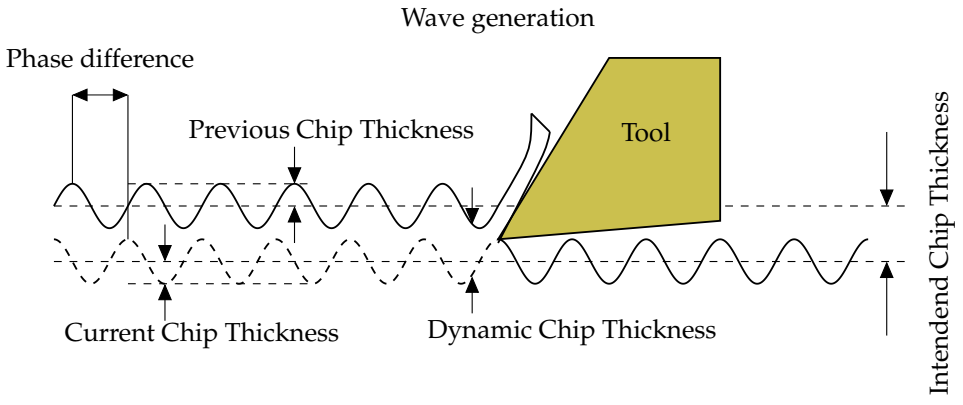

FIGURE 2.4: Wave generation in orthogonal cutting [26]

In robotic milling, regenerative chatter has been extensively explored compared to robotic

turning and boring operations. In a robotic boring operation [170], the stability of the process was modelled based on the regenerative chatter theory and cutting speed dependent force model. Analytical stability boundaries were obtained and verified experimentally and it was shown that the feed rate and depth of cut affect regenerative stability boundaries of the developed model.

A parallel kinematic robot was used for milling operations, in [159], the optimum feed direction was selected and alternative tool paths were determined in pursuit of achieving chatter free higher material removal rates. It was shown that the choice of feed direction affects the stability of the process due to the asymmetrical and configuration dependent tool tip dynamics of hexapod robot. Results indicated that the location and magnitude of the stability boundaries could vary based on the choice of feed direction and robot configuration.

While milling with articulated robots, the research interests were mostly towards stability optimisation and chatter suppression. In [136, 137], a dynamic model of a serial arm robot was used to predict and optimise the stability of a 5-axis robotic milling operation by utilising the kinematic redundancy. Experimental findings indicated that it is possible to increase limits of stable milling operation by utilising configuration dependent dynamics through varying the robot configuration around the axis of rotation of the tool. Manipulator optimal configurations which maximised the stability boundaries coming from the tool mode of vibration were selected to increase the productivity.

In [155], the effect of the cutting trajectory and workpiece clamping position on the process stability and surface finish was investigated. For a fixed set of machining parameters that ensures process stability, milling along different feed directions as well as workpiece location on the machining table were shown to have a significant influence on the process stability. This observation was concluded to be due to the asymmetrical and configuration dependent dynamics of the robot. It was also proven that cross-FRFs alter the process stability significantly in robotic milling.

In [34], the significance of the cross-FRFs was emphasized, especially at low frequency robot structural modes to underline the mode coupling effect on the process stability similar to [155]. At low spindle speeds, the stability was proven to strongly depend on the robot structural modes. At high spindle speeds, it was confirmed that the robotic milling system stability is dominated regeneratively and it depends on higher frequency modes of vibration rather than low frequency structural modes.

In an experimental study on high speed robotic milling in [35], the process stability was validated to be regenerative and dominated by the tool-spindle assembly mode at high spindle speeds. The lower frequency modes of the robot was concluded to be configuration dependent. Considerations such as static stiffness, trajectory following errors, forced vibrations and motion coupling were made to explain challenges of machining with industrial robots.

In an attempt to suppress chatter and increase stability limits for robotic milling, eddy current damper was designed and mounted onto the spindle in [154]. It was shown that tool-spindle assembly modes could be damped by using eddy current dampers and slight improvements in the stability boundaries were achieved and validated experimentally.

The literature depicts that robotic machining operations are also subject to the most common type of process instability; regenerative chatter, just as in machine tools. Poor

structural dynamics of manipulators results in low stability boundaries and makes machining with robots rather difficult. The stability limits are so low, in most cases, the minimum limiting stability boundary could be in the order of the pose accuracy as in [155, 159, 170]. As a result, difficulties could arise in retaining the required depth of cut during machining, as well as inaccuracies arising when the tool corner radius starts playing a larger role in chatter prediction models, which was fundamentally assumed to be negligible. Besides, the structural architecture of robots results in asymmetrical and configuration dependent structural dynamics. Consequently, configuration dependent stability characteristics are observed within the entire spindle speed spectrum, with most implications observed at stability lobes belonging to the highly coupled low frequency structural modes. When all combined, it is very challenging to accurately predict and ensure the stability of the process across the workspace of the robot. Nevertheless, the regenerative chatter theory was proven to apply to the robotic machining operations as in CNC machine tools.

2.4.2 Mode coupling chatter

Mode coupling chatter has firstly been considered for operations including thread turning and boring in which it has been recognised as one of the most powerful mechanisms of the self-excited vibrations alongside regenerative chatter [165, 166]. The mode coupling chatter was observed when thread cutting an asymmetrical boring bar milled flat on diametrically opposite sides having different principal stiffness directions as shown in Figure 2.5.

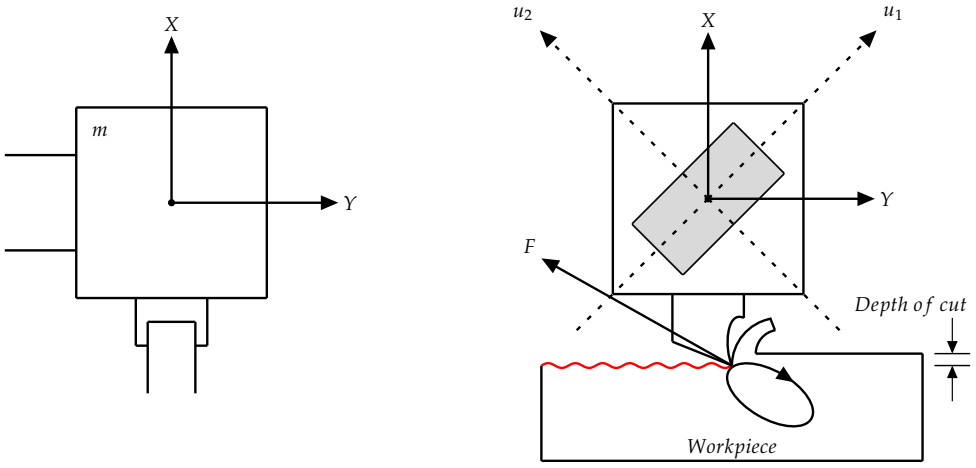

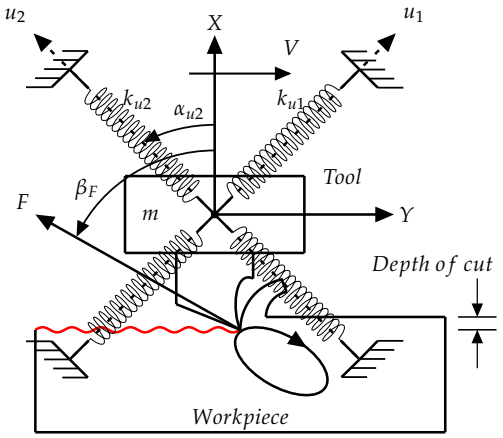

FIGURE 2.5: Mode coupling vibrations in 2 DoF asymmetrical boring bar [165]

There are complicated theories in order to describe the mode coupling chatter and the "scooping motion" arising as a result of the coupling of modes of vibration when successive cuts do not overlap [168]. In [168], for a simple vibratory system consisting of 2 uncoupled DOFs and no damping (as in Figure 2.5), the mathematical model of the mode coupling chatter mechanism was developed and explained. The state space equations of motion of coupled vibrations with dissimilar principal stiffness properties were developed for an excitation force that depends on the current vibrations of the system. For the considered dynamic system, the minimum cutting force coefficient was determined which depends on principal stiffness parameters and directional coefficients. It could also be used to analytically determine the stability boundary for width of cut. It was shown that the smaller the difference in principal stiffness parameters, the less probable the self induced vibrations are to occur. Also, the smallest principal stiffness was shown to be between normal and the force angle for instability to arise.

In [166], a machining scenario was considered where the tool always cuts a new surface (no regeneration) as in threading operation. As a result, the mode coupling chatter was proposed to result from the instability of the current oscillations, which is linearly related to the dynamic cutting force. The common features of the mode coupling chatter observed in mathematical models and experiments are; it occurs in minimum two degrees of freedom and the vibrations along the directions of modes of vibration are in different amplitudes and phases. The tool tip motion follows an elliptical pattern in clockwise direction where the first half-period resulting a width of cut along an elliptical pattern (force against motion) causes energy dissipation by the system. On the contrary, the tool tip encounters larger width of cut in its second half-period and the cutting force is in the direction of the tool tip motion delivering energy to the system. The surplus of energy between these cycles is what drive the mode coupling chatter [166, 168].

For the machining scenarios considered in [165, 166], an analytical stability boundary for the width of cut and two more parameters were derived in [171]. These parameters are "amplitude ratio" and "phase angle" between orthogonal modes of vibration which define the features of mode coupling chatter mechanism. In this respect, the spindle speed independent mode coupling chatter model was developed and the common features of mode coupling chatter were validated analytically for the first time. Additionally, it was proven that mode coupling chatter always happens above the limiting width of cut of

regenerative chatter for given particular machining parameters and configuration, even though they do not happen simultaneously.

In [172, 173], a state space model of mode coupling chatter mechanism in turning was developed. The developed model indicated that the chatter frequencies are the same at both modes of vibration as the tool vibrates in elliptical spiral motion. The mode coupling chatter depends on the natural frequencies of modes of vibration, the mode inclination and the cutting speed. In a robotic boring process [174], the state space model of the process was developed similarly but not identical to [172, 173]. The chatter mechanism was claimed to be affected by forced vibrations and a displacement feedback. After validating the model experimentally, a chatter suppression method that relies on application of a pressure foot mechanism was used to introduce additional damping to the robotic system during cutting.

In robotic milling operations, both regenerative and mode coupling chatter mechanisms were claimed to occur [175], whereas only regenerative chatter was observed in machine tools. The mode coupling chatter in robotic milling processes was claimed to be due to relatively poor structural dynamics compared to machine tools. The fact that mode coupling chatter was proven to depend on the process stiffness and difference in the principal stiffness of modes of vibration of the system as in [166], indicates that it is more prone to be pragmatically observed when machining with flexible machine tools. Consequently, severe vibrations observed when milling with articulated robots led to the consideration of the possibility of mode coupling chatter. The main assumptions include the adoption of the dynamic cutting force to be linearly proportional to tool vibrations as in the mode coupling chatter mechanism in turning and boring a thread.

A. Gasparetto modelled the mode coupling chatter in the state space for wood milling operation as a turning operation to simplify the problem [176, 177] as represented in Figure 2.6. Radial cutting force was assumed to be negligible and the mode coupling chatter stability was analysed and validated in two degrees of freedom (feed and axial directions). The chatter behaviour was found to be exactly the same as in [165, 166]. In [150], the mode coupling chatter model was utilised and a robotic milling path optimisation algorithm was proposed to avoid mode coupling chatter. Mode coupling chatter was observed at very high spindle speeds and validated based on low frequency characteristics and a stability diagram was proposed. In both of these approaches, however, the analysis presented was lacking the necessary comparisons to the regenerative chatter mechanism to make sure that the experimentally observed chatter behaviour does not match regenerative chatter. For a robotic milling operation, low frequency severe chatter at high spindle speed was claimed in [178], which does not depend on machining parameters (such as spindle speed, feed rate and width of cut) but is influenced from cutting direction and workpiece location. The process was proven to be stable in a regenerative point of view, hence mode coupling stability was modelled in state space by assuming forces in feed to be negligible as opposed to [176, 177]. Nevertheless, in [176–178], findings indicated that the factors affecting the process stability were analogous to the behaviour observed as in [165, 166]. In addition to that, the milling type was underlined to also influence the stability limits of the mode coupling chatter mechanism for the first time in [178].

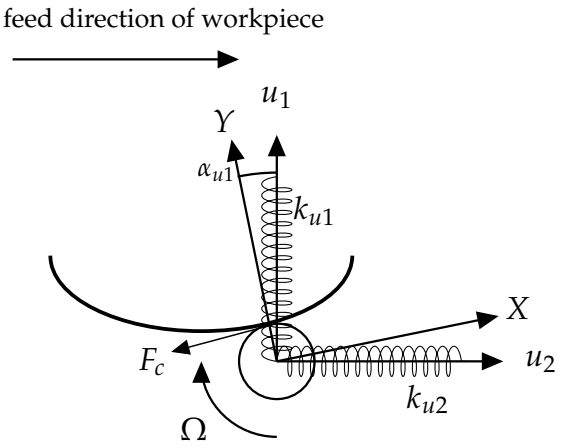

FIGURE 2.6: The model of the system that A. Gasparetto used for mode coupling chatter in milling [177]

In a another work, the mode coupling chatter was modelled in the state space, but this time incorporating the robot state space dynamic model based on CCT inertia and stiffness modelling [179]. The stability was modelled by ignoring oscillations along the axis of rotation of tool, thus in two degrees of freedom. In this work, mode coupling chatter avoidance was achieved by predicting the stability from the developed model and adjusting the cutting conditions by configuring the robot around the axis of rotation of the tool and also altering the orientation of the workpiece. In this way, dynamics of the system and force angle were varied to first predict and then avoid the mode coupling chatter. In [152], mode coupling chatter suppression strategy was presented based on using semi-active magnetotheological elastomer absorbers. The semi-active controller was used to identify the frequency of chatter and tune the absorber to acquire effective chatter suppression in pursuit of achieving better surface finish of the machined part.

In [37], a state space mode coupling model was developed for a robotic milling operation which includes CCT configuration dependent stiffness model. In its basis, the assumption made on the negligible force in feed direction in [176, 177] was relaxed by simply adjusting the tool frame and hence, three dimensional cutting force vector was considered in the model. The proposed technique utilises the CCT stiffness model, in particular the Complementary stiffness matrix, to alter the principal stiffness of the robot (K_{max}, K_{min}). The angle between the maximum principal stiffness and the average cutting force direction was controlled by modifying the feed rate of the tool to achieve chatter avoidance as shown in Figure 2.7. It was also shown that the configuration dependent stiffness of the robot influence the magnitude and directions of the principal stiffness and hence, mode coupling chatter stability limits. In addition to that, an online mode coupling chatter detection and avoidance algorithm was developed on the basis of controlling the feed rate to make sure the process is stable in [180] utilising the methodology developed in [37].

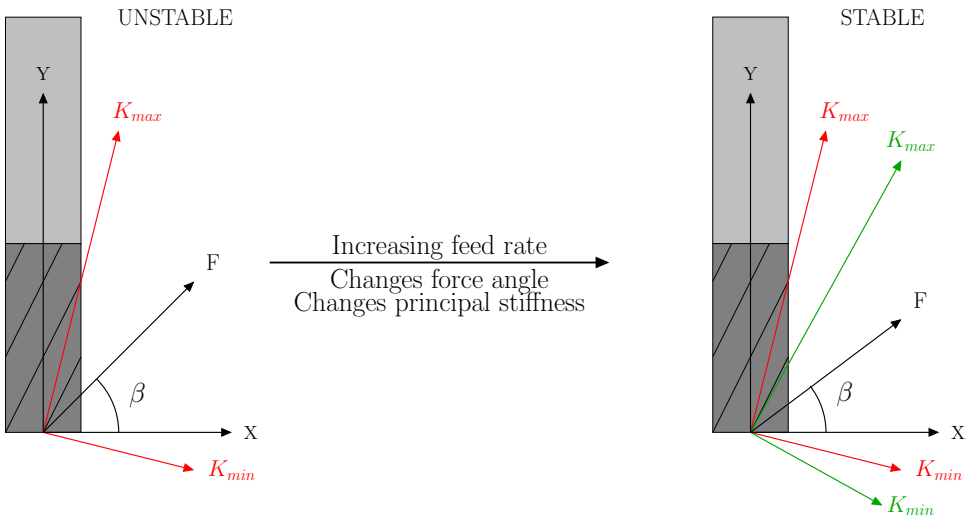

FIGURE 2.7: The mode coupling chatter avoidance technique achieved by altering the feed rate as in [37]

In [181], the mode coupling chatter model developed in [176, 177] was extended to cover three degrees of freedom with respect to principal stiffness directions of the robot architecture. In this way, the process stability was predicted for each robot configuration and chatter avoidance was aimed by changing feed direction even though this is very conservative and usually inapplicable when it comes to machining non-straight trajectories.

For highly varied helix end milling tools, the mode coupling chatter stability while milling with conventional machine tools was first defined in Zero Frequency Approach similar to that of regenerative chatter stability but ignoring the effect of the previous undulations left on the surface of the workpiece [182]. The highly varied helix of the end mill tool was shown as the main reason for the cancellation of the regenerative effect and the critical radial immersion for mode coupling chatter was computed. It was claimed that the mode coupling chatter does not happen in small radial immersions even though the stability mechanism was not experimentally validated. Nevertheless, the mode coupling stability equation is the first ever to be revealed for milling operations which takes into account the intermittent nature of the process.

To sum up, mode coupling chatter models were developed for thread turning and boring operations for machine tools, where a new surface is machined without the regenerative effect, the mode coupling chatter theory complies physically with the process in practice. The analytical solution for the depth of cut, phase angle and amplitude ratio were derived but models still lacking of consideration of the cross-FRF terms, multiple modes of vibration along the orthogonal directions and the prediction of chatter frequencies, which could facilitate identification of the chatter mechanism.

In milling, however, as a matter of fact, the mode coupling chatter models tend to possess inherent misrepresentation of the process coming from the nature of the cutting forces. For such an intermittent cutting operation, dynamic forces depend on undulations left by the previous tooth on the chip surface. Thus, the assumption of linearly varying tool vibrations is not a valid assumption as opposed to threading in turning or boring operations. Besides,

the machine-tool instability was concluded to be mode coupling chatter without making any effort to differentiate it from the regenerative chatter mechanism, except in [178]. Nevertheless, the stability predictions are missing the $N = 0$ lobe that dominates the stability in higher spindle speeds in [178]. For the considered machining parameters in the literature, there is a possibility for the system to regenerate at the robot structural modes causing low frequency instability which could potentially be misinterpreted as the mode coupling chatter. Without justifying the regenerative stability limits and distinguishing the two chatter mechanisms, it is very difficult to make sure what kind of instability mechanism dominates the process. Therefore, the mode coupling chatter in milling still lacks of analytically determined stability boundaries, if in reality, it exists at all.

2.5 Chapter summary

The literature suggests that limitations of robotic machining operations are significant and there are many complications which could be attributed to the poor pose accuracy, poor and configuration dependent structural properties. The aforementioned limitations motivate the accurate structural static stiffness and dynamics modelling, identification and optimisation of manipulators. Applying various chatter suppression, avoidance and depth of cut optimisation techniques could also increase the viability of robotic machining.

In this respect, various static stiffness modelling techniques exist to model and describe the configuration dependent stiffness characteristics of manipulators, such as FEA, MSA and VJM. Amongst these modelling techniques, the VJM is the most simplistic and easy to model but it is also the least accurate stiffness modelling technique. The assumption of rigid links but flexible joints is an oversimplification of flexibilities in the structure even though recent improvements enabled enhancement of its accuracy by consideration of link flexibilities. Nevertheless, the accuracy of the VJM model is quite satisfactory for form error compensation; the rest of errors are difficult to be compensated as their magnitudes are comparable to the manipulator pose accuracy. The identification of its parameters is more accurately and conveniently implemented when a global method is utilised; the entire deflection of the structure is modelled rather than only the control loop stiffness as in a local method.

The configuration dependent static stiffness as well as kinematic and functional redundancies allow stiffness optimisation and form error minimisation in robotic machining operations. Previous studies have aimed to optimise the manipulator stiffness by aligning the stiffest direction of the manipulator stiffness matrix with the force direction. However, the stiffness optimisation is not enough to minimise form errors, hence, cutting force dependent deformation optimisation techniques were applied, which were better suited to the problem. In this way, an improved form error minimisation was achieved even though current deformation optimisation still neglect the influence of the magnitude of cutting forces.

Serial and parallel robots were shown to possess poor and configuration dependent structural dynamics. The low-frequency modes of vibration are strongly cross coupled and configuration dependent, whereas high frequency modes of vibration that come from spindle shaft-tool holder are slightly affected by the manipulator configuration. With respect to the structural dynamic modelling, the FEA, MSA and lumped parameter modelling techniques exist to characterise the configuration dependent dynamic behaviour of industrial serial manipulators. The advantage of these models is that manipulator

structural dynamics can be predicted across the large workspace volume with a fair accuracy. However, even though dynamic models can be calibrated, predictions suffer from inaccuracies due to relatively large size of the manipulator. In an attempt to increase the accuracy of identification, the experimental modal testing at the tool tip could be conducted. The acquired dynamic response would be quite accurate and can be directly applied to predict process stability but it would describe the structural dynamics at a single manipulator configuration. The cross FRFs can also be easily identified with much greater accuracy than any other structural dynamic modelling techniques. Hence, based on the requirements, the compromise between accuracy and prediction capability over the entire robot workspace is necessary for modelling or identification of the structural dynamics of manipulators.

Regenerative stability boundaries tend to be quite low and configuration dependent at low spindle speeds due to the poor, low frequency, configuration dependent structural modes of vibration. Consideration of the cross-FRFs were also shown to be important in predicting the process stability in low spindle speeds. The relatively higher stability boundaries at high spindle speeds were shown to be dominated by higher frequency modes of vibration and slightly affected by the manipulator configuration. The chatter suppression and depth of cut optimisation techniques based on utilising the redundancy around the axis of rotation of the tool were considered to increase stability boundaries. Nevertheless the stability of robotic machining operations are still relatively low compared to that of conventional machine tools. Lastly, the mode coupling chatter was claimed to be observed in robotic milling. While low frequency vibrations were noted to be due to the mode coupling chatter, there was no evidence that distinguishes regenerative and mode coupling chatter mechanisms. This introduces an ambiguity in the nature of the chatter mechanism appearing in robotic milling operations and requires further clarification. Even though, the mode coupling chatter mechanism in milling was derived, stability boundaries and the presence of the chatter mechanism have not yet been validated experimentally.

2.6 The refined research questions

Having underlined the current state of art in robotic machining operations, the following research questions and gaps in the knowledge are identified.

1. Is it possible to optimise the Cartesian stiffness (static) of serial industrial robots whilst making sure the TCP pose requirements are satisfied?

   Earlier techniques for manipulator stiffness optimisation suffer from inaccuracies in the TCP pose as a result of the utilisation of Jacobian-based stiffness optimisation. The problem with the optimisation is the inexactness of the computed joint angles of optimised configurations. Computing inverse kinematics by taking inverse of Jacobian matrix is not ideal to make sure the accuracy of TCP poses along the cutting trajectory. Henceforth, there is a need to optimise the stiffness of the manipulator whilst at the same time ensuring accurate TCP pose requirements.

2. Is it possible to estimate and improve the regenerative chatter stability of milling with serial industrial robots by predicting and optimising their Cartesian stiffness (static)?

   The manipulator Cartesian stiffness (static) and structural dynamics are known to depend on configuration. The various arrangement of links and joints results in

their active and passive compliance, inertia, damping to affect the manipulator static stiffness and dynamics in various manners. For a linear system, the static stiffness can be associated to the modal stiffness which in turn is related to regenerative stability. Having estimated and optimised the static stiffness, a correlation is aimed to be found with the minimum limiting depth of cut of the regenerative stability boundary of robotic milling.

3. Is it possible to continuously alter manipulator structural dynamics and regenerative stability boundaries by reconfiguring the manipulator around the axis of rotation of the tool to achieve chatter avoidance or suppression during milling?

   Regenerative stability boundaries are known to be low and configuration dependent due to the poor and configuration dependent manipulator structural dynamics. Earlier attempts to increase the stability boundaries provided improvements however, the limiting depth of cut stayed still relatively low for industrialisation of robotic milling operations. In pursuit of searching for ways to further enhance regenerative stability boundaries, the configuration dependent dynamics could be exploited. Similar to the chatter suppression obtained by variable spindle speed technique as in [183, 184], the regenerative stability boundaries can be continuously altered during a robotic milling operation. The redundant DOF around the axis of rotation of the tool can be utilised to continuously alter the manipulator configuration and structural dynamics to achieve chatter suppression or avoidance for the given cutting parameters.

4. What is the role of mode coupling chatter in robotic milling, compared to traditional milling?

   The chatter mechanisms in robotic milling operations were claimed to be both associated with regenerative and mode coupling chatter in the existing literature. Robotic milling operations were shown to experience low frequency severe chatter vibrations at high spindle speeds which were noted to be due to the mode coupling chatter mechanism. However, almost all publications found in the current literature do not consider regenerative chatter mechanism extensively and distinguish both chatter mechanisms before concluding on the type of chatter mechanisms. In addition to that, even though zero frequency mode coupling chatter in milling frequency was formulated, it was not validated with experimental cutting tests. In this context, the development of a comprehensive mode coupling chatter model in milling operations, further analysis to distinguish both chatter mechanisms and experimental cutting tests are required to fully validate the type of the chatter mechanism in robotic milling.

The gaps in the knowledge and research questions are aimed to be addressed in this thesis in order to improve the feasibility and application of industrial robots to machining operations. The overarching aim of this thesis is to answer the above four research questions. This aim is achieved by focussing on the following specific objectives:

1. Perform an experimental static stiffness identification and modelling of an serial industrial robot
2. Use the identified static stiffness model to optimise the manipulator configuration and static stiffness

3. Perform a robotic milling trial to test the hypothesis of chatter suppression or avoidance by continuously altering manipulator configuration around the axis of tool rotation
4. Identify whether there is a correlation between the manipulator static stiffness and regenerative stability limiting depth of cut
5. Extend zero frequency mode coupling chatter stability theory in milling to modal directions and multi frequency approximation to investigate its characteristics with different approaches
6. Compute stability boundaries of mode coupling chatter mechanism in milling to validate its role with tests

Before describing progress against these objectives, the next chapter will first introduce the relevant theory.

Chapter 3

Background theory

In this chapter, some important terminology and background theory is provided on industrial robots. An introduction to robotics is given, within which the direct, inverse and differential kinematics of serial manipulators, types of redundancies and singularities are explained. Following that, the two main sources of self-excited vibrations, regenerative and mode-coupling chatter are defined for turning, boring, milling as well as thread cutting operations.

3.1 Theory of robotics

According to ISO 8373, a robot is defined as "actuated mechanism, programmable in two or more axes with a degree of autonomy, moving within its environment, to perform intended tasks" [185]. Hence, the term *robotics* is defined as "the science or study of the basic technologies associated with the theory and application of robotic systems". Based on ISO 8373, *Industrial* and *Service robots* are defined as [185];

- *Industrial Robot*: Automatically controlled, reprogrammable, multi-purpose manipulator, programmable in three or more axes, which can be either fixed in place or mobile for use in industrial automation.
- *Service Robot*: A robot that performs useful tasks for humans or equipment excluding industrial automation applications.

This thesis deals with industrial robots which constitute by the following elements as described in [186]:

- A mechanical structure of manipulator that consists of a sequence of rigid bodies (links) connected by means of articulations (joints); a manipulator is characterised by an arm that ensures mobility, a wrist that confers dexterity and an end effector that performs the task required of the robot.
- Actuators that set the manipulator in motion through actuation of joints; the motors employed are typically electric and hydraulic, or occasionally pneumatic.
- Sensors that measure the status of the manipulator (proprioceptive sensors) and, if necessary, the status of the environment (extroceptive sensors).
- A control system (computer) that enables control and supervision of the manipulator motion.

Industrial robots with the purpose of grasping or moving objects from one place to another are also called the "manipulators". Focusing on the mechanical structure of manipulators, the interconnection of links and joints creates a kinematic chain. Many different manipulators exist with different types of joints and a different sequence of how they are connected to each other. The translational degree of freedom is achieved between links with prismatic joints whereas revolute joints allow rotational movement. Some classifying manipulators are; Cartesian, cylindrical, spherical, SCARA (Selective Compliance Assembly Robot Arm) and anthropomorphic [39]. There are also three different topologies of manipulator kinematic chain; open, closed and hybrid kinematic chains. Then, a robot is said to be a serial manipulator if its kinematic chain is an open loop chain whereas it is said to be a parallel manipulator if it is a closed loop kinematic chain. A hybrid kinematic chain, on the other hand, is a combination of open and closed chains.

In this thesis, the focus is on 6-axis open kinematic chain (serial) industrial manipulators with an anthropomorphic structure and spherical wrist with all joints being revolute. The anthropomorphic mechanical arm is assigned to provide mobility in positioning the end effector across robot workspace. The spherical wrist refers to the arrangement of the last three revolute joints. The intersection of their axes occurs at a single point and is used to orientate the end effector. The representation of a 6-axis serial manipulator with anthropomorphic structure and spherical wrist, such as ABB IRB 6640 205/2.75, is illustrated as in Figure 3.1. The combination of arm and wrist enables decoupling of position and orientation of the end effector pose and facilitates the computation of inverse kinematics of serial manipulators [187].

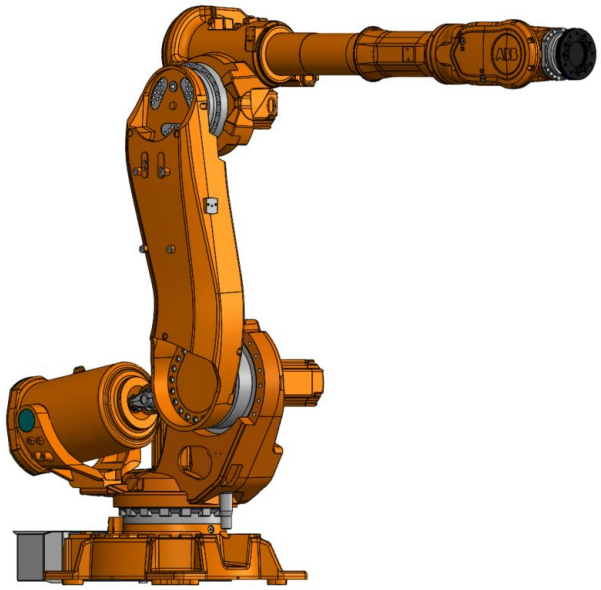

FIGURE 3.1: The serial industrial manipulator, ABB IRB 6640 205/2.75 [188]

3.1.1 Kinematics of serial industrial manipulators

Kinematics is the branch of mechanics that deals with the motion of bodies without taking forces and their effects on the motion into account. In robotics, the operations are defined by Cartesian coordinates and an appropriate orientation representation with respect to a reference frame. The space in which end effector pose is defined is called *operational space* [189], whereas the space where the application is specified is called *task space* [39]. The *joint space*, on the other hand, is the space where the joint variables are defined. A kinematic conversion between these spaces is required for the execution of tasks. Thus, kinematics designates the relationship between the joint variables in the joint space and the pose (position and orientation) of end effector in the operational space.

In order to achieve this, global and local coordinate frames are defined on the kinematic chain. By convention, a global reference frame called the *Base Frame* (T_{Base}) is defined where all other frames are referenced from. Then, based on the geometry of the manipulator, the coordinate frames are assigned on rigid links and the end effector. The geometry of a manipulator consists of geometrical features of its links and joints and is utilised to develop a geometrical model that describes the pose of end effector for a given set of joint variables with respect to *Base Frame*.

A systematic and standardised way of describing and modelling the geometry of a serial kinematic chain was first proposed by Denavit and Hartenberg with a notation which is known as *Denavit-Hartenberg (DH) notation* [190]. Two versions of *Denavit-Hartenberg notation* are present: *the standard and modified Denavit-Hartenberg notation*. The *standard Denavit-Hartenberg notation* is based on systematically defining position and orientation of two consecutive links in the serial kinematic chain for any serial manipulator. For an n axis manipulator with n number of joints, there are $n+1$ number of links, (i=1,...,n). Beginning from the base link, links are numbered from 0 to n where the 0^{th} and n^{th} links are the base and end effector whereas joints are numbered from 1 to n. Thus, two consecutive links, $i-1$ and i are connected to the joint i; actuation of the joint i drives the link i and subsequent links. The modified Denavit-Hartenberg (mDH) notation [191] was developed later in time for more tidier representation of the kinematic chain where the local coordinate frames are attached near to, instead of at the end of, each link. Nevertheless, in this thesis, the *standard Denavit-Hartenberg notation* was utilised to define the geometry of the serial industrial manipulator, ABB IRB 6640 205/2.75, due to its widespread use in robotics community.

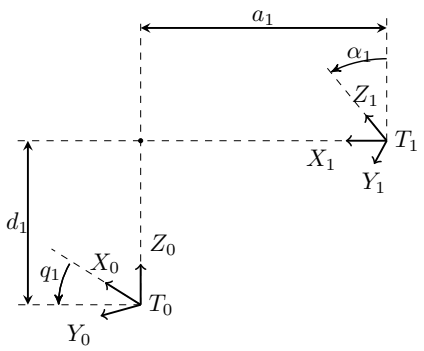

FIGURE 3.2: The coordinate transformation based on *standard Denavit-Hartenberg notation*

The *standard Denavit-Hartenberg notation* is based on attaching coordinate frames at the end of each link of a serial manipulator except for the base and the end effector. At the end of each link i, a local coordinate frame, T_i is defined where Z_i axis is aligned with the axis of rotation of joint $i+1$. The positive direction of the axis and therefore joint rotation or translation is found by the right hand rule for curve orientation. X_i axis is defined along the common normal to Z_{i-1} and Z_i with direction pointing from joint i to $i+1$. Y_i axis is defined based on the right hand rule and the origin of T_i is the intersection of corresponding X_i, Y_i and Z_i axes [186] as shown in Figure 3.2. Hence, no matter the physical relationship between links or the geometry of the serial kinematic chain, the coordinate transformation between consecutive links T_i to T_{i+1} can be expressed by the following four parameters [192]:

- q_i represents the joint variable which is the joint angle measured from the motor encoder, q_θ with respect to the joint offset, q_{Off}. The joint variable is the joint angle between two incident normals of a joint axis. It is the angle required to rotate the X_{i-1} axis into alignment with the X_i axis around the positive Z_{i-1} axis according to the right hand rule. The joint offset is a constant joint variable used to put the manipulator into a more convenient configuration.
- d_i is the link offset between two consecutive links and represents the translational distance between the two incident normals.
- a_i is the link length and describes the offset distance between two adjacent joint axes
- α_i is the link twist and represents the twist angle between two adjacent joint axes.

Following the *standard Denavit-Hartenberg notation*, modelling the geometry of serial industrial manipulators is straightforward. The serial industrial manipulator, ABB IRB 6640 205/2.75, with the nominal link offset and length dimensions is represented in Figure 3.3.

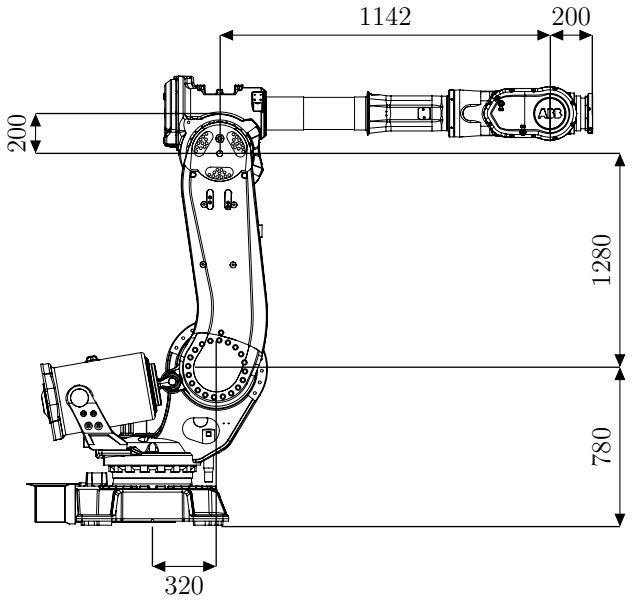

FIGURE 3.3: The dimensions of ABB IRB 6640 205/2.75 (mm) [188]

Thus, the nominal *Denavit-Hartenberg parameters* of the geometric model of ABB IRB 6640 205/2.75 can be summarised as seen in Table 3.1.

Link (i)	Link Length a_i (m)	Link Twist α_i (°)	Link Offset d_i (m)	Joint Variable q_i (°)
1	0.320	-90	0.780	$q_{\theta,1}$
2	1.280	0	0	$q_{\theta,2}$+$q_{Off,2}$
3	0.200	-90	0	$q_{\theta,3}$
4	0	-90	1.142	$q_{\theta,4}$+$q_{Off,4}$
5	0	90	0	$q_{\theta,5}$
6	0	0	0.200	$q_{\theta,6}$

TABLE 3.1: Nominal Denavit-Hartenberg parameters of ABB IRB 6640 205/2.75

Table 3.1 defines the geometry of ABB IRB 6640 205/2.75 from the zeroth coordinate frame, T_0, to the *End Effector Frame*, T_6 in terms of *standard Denavit-Hartenberg notation*. In this case, the second and forth joints tend to possess joint offsets, [$q_{Off,2}$, $q_{Off,4}$] that are [-90, 180]°, respectively. For industrial applications, in particular machining operations, additional equipment including spindle, tool holder and tool are installed onto the end effector. Hence, the geometry of the manipulator is extended to include additional equipment to define the tool center point frame, T_{TCP}. The additional transformation is defined from T_6 to T_{TCP} which can be modelled as rigid body transformation as illustrated in Figure 3.4.

An important point to note, the zeroth coordinate frame T_0, is usually attached to the first joint provided that Z_0 is aligned with the axis of rotation of the first joint [192]. Since it is common practice to locate the *Base Frame* at the floor and the location of the first joint along Z_0 does not alter kinematics of the manipulator, it is convenient to locate the first joint T_0 at the base T_{Base}.

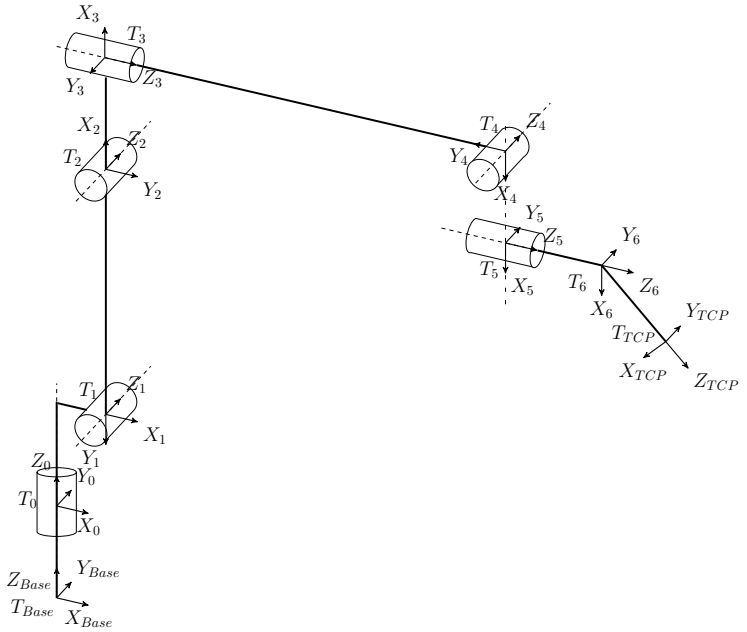

FIGURE 3.4: The geometric model of ABB IRB 6640 205/2.75

In robotics community, the Z_6 and Z_{TCP} axes are defined along the axis of rotation of the last joint and the direction of approach of the designated device. For machining operations, this designated device is the assembly of spindle, tool holder and tool. Hence, the direction of Z_{TCP} is aligned with the axis of rotation of the tool pointing out of the tool.

3.1.1.1 Direct (Forward) kinematics

The direct (forward) kinematics refers to computation of the position and orientation of the end effector, X_m, for a given set of joint variables q and the geometrical model $f(.)$ of a manipulator. For a set of joint variables, the end effector pose is uniquely defined and the resulting manipulator geometry is called configuration or posture. Thus, direct kinematics is the problem of mapping the joint space to operational space by solving Equation 3.1,

$$X_m = f(q) \tag{3.1}$$

In the above equation, X_m is the end effector pose composed of minimal representation of the position vector P_m and orientation R_m with respect to the *Base Frame*. P_m is a vector of Cartesian coordinates $[x, y, z]^T$ and R_m is a vector of elementary rotation angles $[\alpha, \beta, \gamma]^T$. R_m, however, is not uniquely defined and the parameters α, β and γ depend on the choice of representation of the orientation. The minimal representation of the end effector pose in vector format is as shown in Equation 3.2,

$$X_m = \begin{bmatrix} P_m \\ R_m \end{bmatrix} = \begin{bmatrix} x, y, z, \alpha, \beta, \gamma \end{bmatrix}^T \tag{3.2}$$

Referring back to Equation 3.1, the joint variable matrix q for the n-axis industrial serial manipulator is a vector of size $(n \times 1)$, where n is the number of joints or degrees of freedom in the joint space. For the industrial manipulator, 6-axis ABB IRB 6640 205/2.75 $(n = 6)$, there are six revolute joints and the joint variables are defined as,

$$q = [q_1, q_2, q_3, q_4, q_5, q_6]^T \tag{3.3}$$

The pose of any reference frame, such as the end effector frame, is usually represented with transformation matrices. The pose transformation, translation and/or rotation (pose), of a frame T_{i-1} to the frame T_i is expressed with a (4×4) *homogeneous transformation matrix* ${}^{i-1}A_i$, and can be represented as,

$${}^{i-1}A_i = \begin{bmatrix} {}^{i-1}s_i & {}^{i-1}n_i & {}^{i-1}a_i & {}^{i-1}P_i \end{bmatrix} = \begin{bmatrix} {}^{i-1}R_i & {}^{i-1}P_i \\ 0_{1\times3} & 1 \end{bmatrix} = \begin{bmatrix} s_x & n_x & a_x & x \\ s_y & n_y & a_y & y \\ s_z & n_z & a_z & z \\ 0 & 0 & 0 & 1 \end{bmatrix}. \tag{3.4}$$

The parameters ${}^{i-1}s_i$, ${}^{i-1}n_i$, ${}^{i-1}a_i$ correspond to the components of unit vectors along the axes X_i, Y_i, Z_i respectively. They are expressed in the frame T_{i-1}. ${}^{i-1}P_i$ and ${}^{i-1}R_i$ are the (3×1) position vector and (3×3) rotation matrix of frame T_i with respect to the frame T_{i-1}. The description of the rotation matrix ${}^{i-1}R_i$, is redundant as it has 9 elements to describe the orientation of a frame, which can be represented by three independent parameters. Such minimal representation of rotation is achieved by a set of three angles $R_m = [\alpha, \beta, \gamma]^T$ which are elementary rotations about the coordinate axis with a suitable sequence. Thus, there are 12 different combinations of sets of angles to represent the rotation matrix and

are called *Euler Angles*. In this thesis, *XYZ Euler angles* or *Roll-Pitch-Yaw angles* (RPY) were utilised to represent orientation of frames. On this basis, the angles $[\alpha, \beta, \gamma]$ are referred as *Roll-Pitch-Yaw angles*. Hence, the rotation matrix ${}^{i-1}R_i$ can be expressed in terms of the direction cosines [1] as,

$$ {}^{i-1}R_i = Rot_x(\alpha) \cdot Rot_y(\beta) \cdot Rot_z(\gamma) = \begin{bmatrix} c_\beta c_\gamma & -c_\beta s_\gamma & s_\beta \\ s_\alpha s_\beta c_\gamma + c_\alpha s_\gamma & -s_\alpha s_\beta s_\gamma + c_\alpha c_\gamma & -s_\alpha c_\beta \\ -c_\alpha s_\beta c_\gamma + s_\alpha s_\gamma & c_\alpha s_\beta s_\gamma + s_\alpha c_\gamma & c_\alpha c_\beta \end{bmatrix} \quad (3.5) $$

where $Rot_x(.)$, $Rot_y(.)$ and $Rot_z(.)$ are 3×3 rotation matrices and the angles $[\alpha, \beta, \gamma]$ are rotation angles around X, Y, Z axes respectively. Within homogeneous transformation matrices, the rotations around X, Y, Z axes are defined as,

$$ A_{Rot,x}(\alpha) = \begin{bmatrix} 1 & 0 & 0 & 0 \\ 0 & c_\alpha & -s_\alpha & 0 \\ 0 & s_\alpha & c_\alpha & 0 \\ 0 & 0 & 0 & 1 \end{bmatrix} \quad (3.6) \qquad A_{Rot,y}(\beta) = \begin{bmatrix} c_\beta & 0 & s_\beta & 0 \\ 0 & 1 & 0 & 0 \\ -s_\beta & 0 & c_\beta & 0 \\ 0 & 0 & 0 & 1 \end{bmatrix} \quad (3.7) $$

$$ A_{Rot,z}(\gamma) = \begin{bmatrix} c_\gamma & -s_\gamma & 0 & 0 \\ s_\gamma & c_\gamma & 0 & 0 \\ 0 & 0 & 1 & 0 \\ 0 & 0 & 0 & 1 \end{bmatrix} \quad (3.8) $$

whereas the translation of the reference frame is defined as,

$$ A_{Transl}(x, y, z) = \begin{bmatrix} 1 & 0 & 0 & x \\ 0 & 1 & 0 & y \\ 0 & 0 & 1 & z \\ 0 & 0 & 0 & 1 \end{bmatrix}. \quad (3.9) $$

The above equations summarise the general notation required to transform the position and orientation of a frame with respect to a reference frame. The *standard Denavit-Hartenberg notation* used to define the manipulator geometry is also related to transforming reference frames from one link to another. Therefore, the coordinate frame transformation can also be expressed with homogeneous transformation matrices. The transformation matrix defining the frame T_i relative to the frame T_{i-1} based on *standard Denavit-Hartenberg notation* is given by,

$$ {}^{i-1}A_i(q_i, d_i, a_i, \alpha_i) = A_{Rot,z}(q_i) \cdot A_{Transl}(0, 0, d_i) \cdot A_{Transl}(a_i, 0, 0) \cdot A_{Rot,x}(\alpha_i) \quad (3.10) $$

Hence, the expansion of the translation and rotations represented with homogeneous transformation matrices based on the *standard Denavit-Hartenberg notation* can be represented as,

$$ {}^{i-1}A_i(q_i, d_i, a_i, \alpha_i) = \begin{bmatrix} c_{q_i} & -s_{q_i} c_{\alpha_i} & s_{q_i} s_{\alpha_i} & a_i c_{q_i} \\ s_{q_i} & c_{q_i} c_{\alpha_i} & -c_{q_i} s_{\alpha_i} & a_i s_{q_i} \\ 0 & s_{\alpha_i} & c_{\alpha_i} & d_i \\ 0 & 0 & 0 & 1 \end{bmatrix} \quad (3.11) $$

Equation 3.11 above describes the pose of the coordinate frame attached on the end of each link T_i with respect to the coordinate frame attached on the previous link T_{i-1}. The kinematic chain of a serial manipulator can then be expressed as successive multiplication

[1] The abbreviations $s_{(.)}$ and $c_{(.)}$ represent $\sin(.)$ and $\cos(.)$ of an angle specified within the brackets

of homogeneous transformation matrices defining the pose of each link. Consequently, the pose of end effector frame T_6 of ABB IRB 6640 205/2.75 in relation to the robot frame T_0 can be obtained similar to Equation 3.2 but in the format, which is in the form of homogeneous transformation matrix, ${}^{0}A_6$.

$$X_m \equiv {}^{0}A_6 = \prod_{i=1}^{n=6} {}^{i-1}A_i(q_i, d_i, a_i, \alpha_i) \tag{3.12}$$

Thus, the direct kinematics of the manipulator from the robot frame T_0 to the end effector frame T_6 is computed. However, in reality, the location of the *Base Frame* may not be at T_0 and an end effector device could be attached on the robot. As a result, direct kinematics should be extended to cover the rigid body transformation of the location of the base and the dimensions of the end effector device. For machining operations, the attachment of spindle, tool holder and the tool requires a rigid transformation from the end effector to the tool center point (TCP) where the cutting would take place, defined as ${}^{Base}A_{TCP}$ as shown in Figure 3.5.

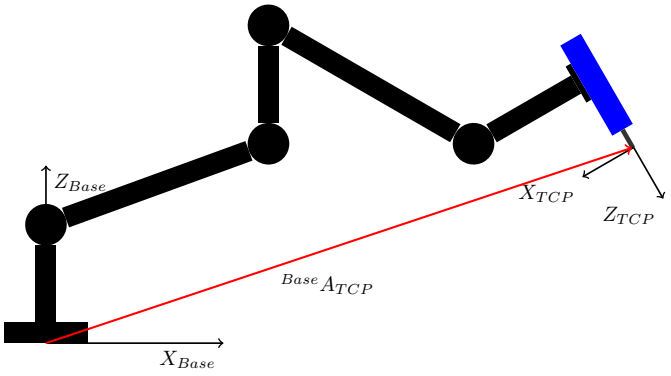

FIGURE 3.5: Transformation of coordinate frames from T_{Base} to T_{TCP}

As a whole, the direct kinematics of the manipulator is expressed as,

$${}^{Base}A_{TCP} = {}^{Base}A_0 \cdot \left[\prod_{i=1}^{n=6} {}^{i-1}A_i(q_i, d_i, a_i, \alpha_i) \right] \cdot {}^{6}A_{TCP} \tag{3.13}$$

where ${}^{Base}A_0$ and ${}^{6}A_{TCP}$ are the transformation matrices from T_{Base} to T_0 and T_6 to T_{TCP} respectively. It should be noted that Equations 3.1 and 3.12 both describe the pose of the end effector (or tool) in operational space but in different formats. The difference is while Equation 3.1 describes the degrees of freedom in a vector format with orientation described in an Euler Angle scheme, Equation 3.12 defines the same information within homogeneous matrix format. In that, the orientation is defined by the rotation matrix and position is defined by the position vector as in Equation 3.4. All in all, this concludes direct kinematics of serial manipulators, in particular ABB IRB 6640 205/2.75, which is essential for the scope of this thesis.

3.1.1.2 Inverse kinematics

In contrast to direct kinematics, inverse kinematics is the problem of computation of joint variables for a given end effector pose, X_m and manipulator geometrical model $f(.)$. Inverse kinematics problem is defined as,

$$q = f^{-1}(X_m). \tag{3.14}$$

The solution of the inverse kinematics problem is of fundamental importance as the motion specifications of tasks are defined in task space. Transformation of the motion specifications from task space to operation and joint space is required for their execution [186]. For a given TCP pose, as opposed to direct kinematics, inverse kinematics is not uniquely defined; there could happen to be more than one set of joint variables that could satisfy the manipulator configuration to reach the given pose. This is due to the structure of the manipulator and the number of non-null Denavit-Hartenberg parameters. However, the number solutions of the inverse kinematics problem is constrained with joint angle limits determined by the physical rotation capability of the actuators within joints.

For 6-axis industrial manipulators, such as ABB IRB 6640 205/2.75, with anthropomorphic structure and spherical wrist, a closed-form inverse kinematic solution is possible which relies on computation of joint variables based on the algebraical equations. The number of solutions to the problem depends on the TCP pose within the operational space and the joint limits. The solutions can be classified by the resulting configuration of the manipulator based on its arm and wrist. Some examples of the possible admissible manipulator configurations for a given TCP pose, excluding the redundancy arose as a result of the first joint, are shown as in Figure 3.6.

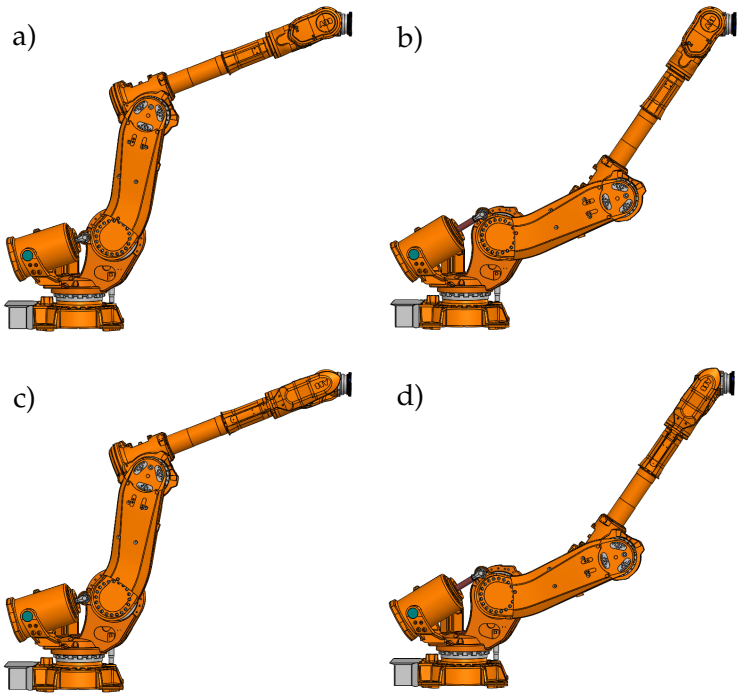

FIGURE 3.6: The admissible solutions of the inverse kinematics of ABB IRB 6640 205/2.75

Note that for a given robot configuration to reach a TCP pose, robot has a redundancy around the arm which was represented by Figure 3.6 "a" and "b" as well as a redundancy around the wrist which was represented by Figure 3.6 "a" and "c". In Figure 3.6 "d", both arm and wrist redundancy was illustrated with respect to robot configuration in Figure 3.6 "a".

The combination of anthropomorphic arm and spherical wrist makes it possible to decouple the position and orientation of the TCP pose for computation of the joint variables. The anthropomorphic arm is assigned to position the TCP whereas the spherical wrist is used to rotate the TCP to the required orientation. The intersection point of spherical wrist axes is used to decouple the position from the orientation as the spherical wrist does not contribute to position of the TCP pose. The most commonly utilised and accurate closed form inverse kinematics solution for anthropomorphic manipulators with spherical wrist can be found in [193, 194].

3.1.1.3 Differential kinematics

Differential (velocity) kinematics linearly maps the end effector linear and rotation velocities in operational space defined with X_m to the joint velocities $\dot{q}$ in joint space for a n-axis manipulator. In other words, it is the problem of expressing the end effector linear velocity and rotational velocity as a function of the joint velocity $\dot{q}$ by means of Equation 3.15 [186],

$$\dot{X}_m = \begin{bmatrix} \dot{P}_m \\ \dot{R}_m \end{bmatrix} = J(q)\dot{q} \tag{3.15}$$

where $J(q) \in \mathbb{R}^{6\times n}$ is the *Geometric Jacobian*. For Geometric Jacobian, the end effector linear velocity is $\dot{P}_m = [\dot{x}, \dot{y}, \dot{z}]^T$ and rotational velocity is represented by the angular velocity, $\dot{R}_m = [\omega_x, \omega_y, \omega_z]^T$. The direction of the angular velocity vector indicates the instantaneous axis of rotation of the rigid body. If the end effector orientation is represented in terms of minimal number of parameters as in Equation 3.2, the rotation velocity can then be described with the time derivative of the minimal representation of orientation with Euler Angles i.e. $\dot{R}_m = [\dot{\alpha}, \dot{\beta}, \dot{\gamma}]^T$. This type of Jacobian is called *Analytical Jacobian*. The only difference between the geometrical and analytical Jacobian is the representation of the orientation of the manipulator configuration. Considering the rotational velocity of the TCP expressed in terms of Roll-Pitch-Yaw angles as in Equation 3.5, then the relationship between angular and rotational velocity is defined as,

$$\begin{bmatrix} \omega_x \\ \omega_y \\ \omega_z \end{bmatrix} = \begin{bmatrix} 1 & 0 & s_\beta \\ 0 & c_\alpha & -c_\beta s_\alpha \\ 0 & s_\alpha & c_\beta c_\alpha \end{bmatrix} \begin{bmatrix} \dot{\alpha} \\ \dot{\beta} \\ \dot{\gamma} \end{bmatrix} = B(q) \begin{bmatrix} \dot{\alpha} \\ \dot{\beta} \\ \dot{\gamma} \end{bmatrix}. \tag{3.16}$$

The above relationship is obtained from the derivative of the time varying rotation matrix which relates the angular velocity indicating the instantaneous axis of rotation of a coordinate frame to the rotation at a given time. Thus, for a six-axis manipulator, the relationship between geometrical and analytical Jacobian, $J_A(q)$ can be expressed as,

$$J(q) = \begin{bmatrix} I_{3\times 3} & 0_{3\times 3} \\ 0_{3\times 3} & B(q)_{3\times 3} \end{bmatrix} J_A(q). \tag{3.17}$$

Geometric Jacobian is useful in transforming the forces and torques at the tool center point to the torques at the joints or vice versa in quasi-static conditions as;

$$\tau = J(q)^T w \tag{3.18}$$

where τ is $(n \times 1)$ torque vector in joint space defining the torques at each joint and w (6×1) is the wrench vector specifying the force and torque applied onto the tool center point (TCP), hence, $w = [F_x, F_y, F_z, M_x, M_y, M_z]^T$.

3.1.2 Redundancies

In Cartesian (operational) space, for a manipulator to realise a task, six degrees of freedom are required: three for positioning and three for orienting a reference frame with respect to a global frame. However, a robot manipulator might have more than six degrees of freedom in its joint space or tasks might need less degrees of freedom than that of robot is capable of reaching. Thus, a redundant degree of freedom could emerge which is not utilised for executing the tasks making the robot redundant for the operation. For industrial manipulators, there exist multiple types of redundancies.

- *Structural Redundancy* is revealed when a robot manipulator with open kinematic chain tends to have more degrees of freedom in its joint space compared to its operational space.
- *Kinematic Redundancy* arises when a manipulator has more number of degrees of freedom in its joint space than its task space.
- *Functional Redundancy* is a special kind of redundancy and appears when both joint and operational spaces have same degrees of freedom but the task defined tend to require less degrees of freedom than the operational space of the manipulator [186].

In general, a redundancy can be exploited to avoid any kinematic singularities, increase the reachable workspace, enhance the dexterity & versatility and improve other performance indices such as task based performance indices. From a machining point of view, industrial serial arm manipulators are both kinematically and functionally redundant for conventional machining operations such as milling, turning, drilling etc. In such cases, manipulators tend to be kinematically and functionally redundant, as the rotational degree of freedom around the axis of rotation of tool is irrelevant to the successful completion and fulfilment of the task as shown in Figure 3.7.

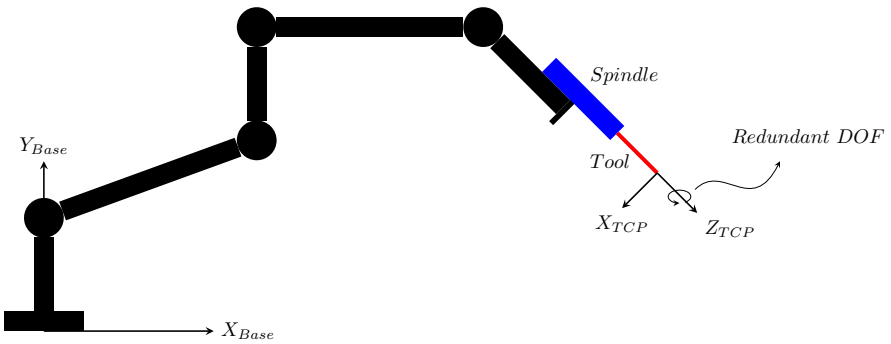

FIGURE 3.7: The redundant degree of freedom around the axis of rotation of the tool

Thus, the manipulator tends to theoretically have an infinite number of configurations that could satisfy the requirements of the task i.e. following a machining trajectory. Such an advantage could be used to avoid kinematic singularities and improve task based performance indices such as, in particular, static stiffness, controller dynamics, structural dynamics, stability boundaries etc. This will be a major area of interest in the present thesis.

3.1.3 Singularities

Serial manipulators may possess intrinsic singularities due to the relative location of joint axes along their kinematic chain. According to [186], singularities are important to find out due to the following reasons;

- They cause reduction in the mobility of the manipulator in operational space
- They result in an infinite number of manipulator configurations as solutions to the inverse kinematic problem
- Close to a singularity, large velocities in joint space are required to cause even small Cartesian velocities in the operational space

At singular configurations, a robot manipulator loses one or more degrees of freedom within its operational space. Such configurations are usually achieved when the axes of two prismatic joints become parallel, the axes of two revolute joints become collinear and the origin of end effector lies on a line that intersects all the joint axes [139].

Differential kinematics, *Jacobian*, of the manipulator is particularly crucial for trajectory planning problems. For a given end effector Cartesian velocity in operation space, joint velocities in joint space are computed in order to acquire the torque requirements needed to actuate joints based on Equation 3.15. In order to compute joint velocities, the inverse transformation of Jacobian matrix is required making trajectory planning dependent on the condition of the Jacobian. At singular configurations, Jacobian matrix becomes rank-deficient losing its number of linearly independent rows and columns. Thus, this results in the determinant of the Jacobian to be zero (singular) making the inverse transformation to be not invertible and resulting in ill conditioning of the Jacobian. If a manipulator is close but not at singularity, a small Cartesian velocity would require very high joint velocities and vice versa. At a singularity joint velocities become infinite.

In order to avoid singularities during manipulator motions and determine suitable manipulator configurations for execution of tasks, the manipulability and condition number are the most commonly used parameters. While both rely on the Jacobian matrix, manipulability has the potential to visualise end effector velocities on a six-dimensional ellipse called the velocity manipulability ellipsoid [186, 195]. The ellipsoid is computed by finding end effector velocities for a manipulator configuration for a set of joint velocities of unity norm.

$$\dot{q}^T \dot{q} = 1 \tag{3.19}$$

Substitution of the Jacobian as in Equation 3.15 results in the following relationship.

$$\dot{X}_m^T (J(q) J^T(q))^{-1} \dot{X}_m = 1 \tag{3.20}$$

Hence, end effector velocities resulting in unity joint velocities could be obtained which would end up on the surface of an ellipsoid in the end effector velocity space. The

directions and magnitudes of principal axes of the ellipsoid represent the directions and relative magnitude of the manipulator mobility in operational space. For the sake of simplicity, in this thesis, velocity manipulability ellipsoid hasn't been utilised as there is no need to for detailed kinematic performance analysis. Instead, a single scalar parameter that would indicate the closeness of the manipulator to any singularity is enough to be determined to make sure the manipulator is away from any singularities.

In this context, the condition number of a matrix gives a scalar index that could be used to assess the kinematic performance of the manipulator configuration. The condition number is the ratio of the largest eigenvalue to smallest eigenvalue of a matrix provided that the matrix is positive-definite. The minimum condition number of a manipulator Jacobian defines the design robustness against manufacturing, assembly and joint encoder errors [196]. The fact that 2-norm condition number of Jacobian matrix is cumbersome due to singular values (eigenvalues) of the matrix are not an analytic function at whole set of joint variables, the condition number based on Frobenius norm is preferably applied as in [196]. Hence, throughout this thesis, the condition number based on Frobenius norm of the homogeneous Jacobian of 6-axis serial industrial manipulator is utilised for kinematic analysis and can be defined as;

$$\kappa_F(J_N) = ||J_N||_F||J_N^{-1}||_F \tag{3.21}$$

where

$$||J_N||_F \equiv \sqrt{\frac{1}{6}tr(J_N J_N^T)} \tag{3.22}$$

with a weighted norm of the matrix as in [196].

It should be noted that, for 6-axis serial industrial manipulators, Jacobian does not have dimensional homogeneity in its entities. Thus, the characteristic length, L, of the given manipulator needs to be computed to normalise Jacobian matrix. For a given manipulator, the characteristic length of the manipulator would be the ratio of the specified reach distance to the reach distance of its homogeneous counterpart postured to have minimum Frobenius norm [196]. The homogeneous manipulator would be the same manipulator but link lengths and offsets are simply length ratios. The homogeneous (normalised) Jacobian would be [197];

$$J_N = \begin{bmatrix} \frac{1}{L} & \frac{1}{L} & \frac{1}{L} & 0 & 0 & 0 \\ \frac{1}{L} & \frac{1}{L} & \frac{1}{L} & 0 & 0 & 0 \\ \frac{1}{L} & \frac{1}{L} & \frac{1}{L} & 0 & 0 & 0 \\ 0 & 0 & 0 & 1 & 1 & 1 \\ 0 & 0 & 0 & 1 & 1 & 1 \\ 0 & 0 & 0 & 1 & 1 & 1 \end{bmatrix} \times J \tag{3.23}$$

Hence, the measure of distance to a singularity is evaluated with *Kinetostatic Conditioning Index*, *KCI*, which is defined as;

$$KCI(\%) = \frac{1}{\kappa_F(J_N)} \times 100 \tag{3.24}$$

Kinetostatic Conditioning Index being 100% means the manipulator is able to move in all directions with an isotropic mobility. On the other hand, the closer the *KCI* to zero means the robot is in a neighbourhood of a singularity. Hence, it can be used to quantify distance to any singularity for a given manipulator configuration and can be

useful in many ways for robotic applications. As such, KCI can be utilised to find out singular manipulator configurations to minimise the effect of the *Complementary stiffness matrix* in the identification of static stiffness of the manipulator by VJM as in Chapter 4. Configurations where the manipulator is less prone to the effect of loading on its end effector pose can be found to simplify the CCT stiffness model to conventional stiffness model for easier identification of the virtual torsional stiffness parameters. In addition, KCI can also be utilised to examine the kinematic performance of the robot along the cutting trajectories in machining operations to make sure the manipulator is away from any singularities and avoid any reduction in linear and angular feed rates as in Chapter 5. The manipulator configurations that are close to a singularity can be determined before machining operations and the functional redundancy of the manipulator could further be used to avoid singularities while benefiting the advantages it brings as much as possible.

3.2 Machine-tool dynamics

Machine tools tend to experience forced and self-excited vibrations due to the nature of the cutting operations [26]. Forced vibrations are inherent in the nature of milling operations as a result of the periodic engagement of the teeth. They could also arise due to cutting forces created from unbalance in tool-tool holder assembly, non-symmetric teeth or a run-out in the rotating components. Thus, in practice, forced vibrations are always present in the operations due to the existence of aforementioned imperfections in the machine tool system. However, the presence of self-excited vibrations are more destructive to the quality of the end product (dimensional and surface finish) as well as to the machine tool system compared to forced vibrations. The main reason of the self-excited vibrations is the instability in the dynamic chip thickness generation. Thus, self-excited vibrations have the potential to grow quickly and damage the machine tool, equipment and end product.

Self-excited vibrations could appear in two different types namely mode coupling and regenerative chatter which are classified based on the dynamic chip thickness generation mechanisms [198]. In the following sections, self-excited vibrations, regenerative and mode coupling chatter mechanisms, will be described in detail.

3.2.1 Regenerative chatter

Regenerative vibrations are the most common type of self-excited instability in cutting operations [199]. The regenerative stability depends on the stability of the dynamic chip thickness which is due to the difference between the vibrations left on the previously and newly cut chip surface by the virtue of the tool propagating across the workpiece for material removal. The stability of the dynamic chip thickness generation mechanism strongly depends on the phase difference between waves left by the tool on the previously cut surface and current vibrations [26]. Based on the phase difference, the chatter vibrations may grow resulting in instability, poor surface finish and dimensional accuracy. In the following sections, the regenerative chatter mechanism in turning and milling operations will be explained.

3.2.1.1 Turning and boring operations

In turning operations, the workpiece is held in the chuck of a lathe machine and rotated with a spindle to remove material by feeding a single point cutting tool into the workpiece. In orthogonal turning conditions, it is assumed that a flat faced tool is fed perpendicular to the axis of rotation of the cylindrical workpiece as described in [26]. The tool and the workpiece are flexible bodies and thus, the point of contact of the tool with the workpiece tends to be flexible too. In the first revolution of the tool or workpiece, a vibration-free surface is cut but the cutting forces result in vibration of the system leaving behind a wavy surface. In the second revolution, the chip being cut would have a wavy surface on both sides of the chip owing to the vibrations left by current and previous revolution of the tool. This creates uneven dynamic chip thickness which varies with time, vibration frequency and the speed of rotation of the workpiece as shown in Figure 3.8.

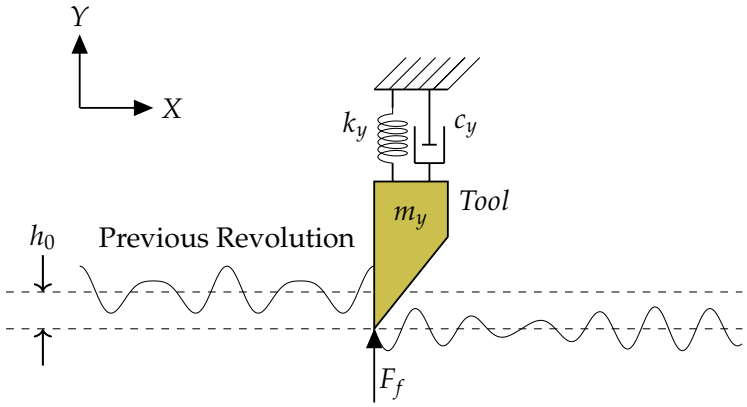

FIGURE 3.8: The representation of the waves left by the previous and current revolution for turning and boring operations for a SDOF system [200]

Following the derivations in [26], for orthogonal cutting, the dynamic chip thickness, $h(t)$, in general form is,

$$h(t) = h_0 - (y(t) - y(t-T)) \tag{3.25}$$

where h_0 is the feed per revolution (feed rate), $y(t)$ and $y(t-T)$ are the current and previous normal vibrations at time, t and at time equal to a spindle speed period, T, before. In feed direction, assume that the system exhibits a single degree of freedom (SDOF) behaviour at the tool-workpiece point of contact along surface normal. Such a system can be regarded as a simple oscillator that can be defined with a spring-mass-damper system vibrating in only one direction. Then, equation of motion of the system is expressed as,

$$m_y\ddot{y}(t) + c_y\dot{y}(t) + k_y y(t) = F_f(t) = K_{fc} b_w h(t) \tag{3.26}$$

where the parameters m_y, c_y and k_y represent the modal mass, damping and stiffness of the system, F_f is force at feed (normal) direction, K_{fc} is cutting constant in feed direction and b_w is width of cut. The dynamic chip thickness in Equation 3.25 can be expressed in Laplace domain as;

$$h(s) = h_0(s) + y(s)(e^{-sT} - 1) \tag{3.27}$$

where $s = \sigma + j\omega$, σ is a real number, ω is the angular frequency, $h(s)$ is the Laplace transform of $h(t)$, $h_0(s) = \frac{h_0}{s}$ is the Laplace transform of a static feed per revolution and $y(s)$ is the Laplace transform of $y(t)$. The dynamic chip thickness results in a dynamic cutting force as in Equation 3.28.

$$F_f(s) = K_{fc} b_w h(s) \tag{3.28}$$

The dynamic cutting force excites the system creating current vibrations as below;

$$y(s) = F_f(s) FRF(s) = K_{fc} b_w h(s) FRF(s) \tag{3.29}$$

where the Frequency Response Function of the system in Laplace Domain, $FRF(s)$, is

$$FRF(s) = \frac{y(s)}{F_f(s)} = \frac{1}{m_y s^2 + c_y s + k_y} \tag{3.30}$$

Substituting Equation 3.29 into Equation 3.27 and rearranging to give the open loop transfer function in Laplace domain yields,

$$\frac{h(s)}{h_0(s)} = \frac{1}{1 + (1 - e^{-sT})K_{fc}b_w FRF(s)} \tag{3.31}$$

The block diagram of regenerative chatter mechanism based on above equations is depicted in Figure3.9.

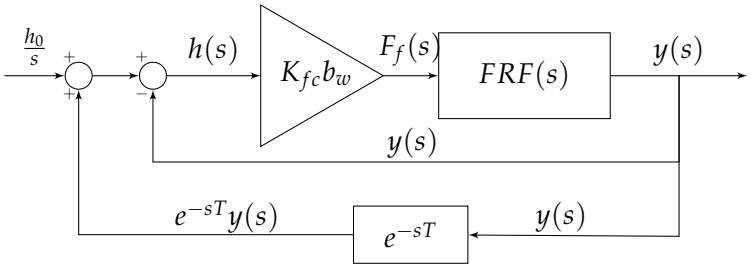

FIGURE 3.9: Block diagram of chatter dynamics [26]

Roots of the close loop transfer function of the open loop transfer function in Equation 3.31 determine the stability of the system and are found by considering the characteristic equation, which is,

$$1 + (1 - e^{-sT})K_{fc}b_w FRF(s) = 0 \tag{3.32}$$

Considering the marginal stability by setting the real part to zero $\sigma = 0$, the root of the characteristic equation can be represented as $s = j\omega_c$ where ω_c is the chatter frequency in radians (note that the chatter frequency in hertz, $f_c = \frac{\omega_c}{2\pi}$ (Hz)). Hence, Equation 3.32 turns into,

$$1 + (1 - e^{-j\omega_c T})K_{fc}b_{w,lim} FRF(j\omega_c) = 0 \tag{3.33}$$

where $b_{w,lim}$ is the width of cut for marginal stability. Separating the real and imaginary parts of Frequency Response Function, $FRF(j\omega) = G + jH$ and Equation 3.33 yield,

$$1 + K_{fc}b_{w,lim}[G(1 - \cos(\omega_c T)) - H\sin(\omega_c T)] = 0 \tag{3.34a}$$
$$j(K_{fc}b_{w,lim}[G\sin(\omega_c T) + H(1 - \cos(\omega_c T))]) = 0 \tag{3.34b}$$

setting the imaginary part to zero returns the spindle speeds for each possible chatter frequency by,

$$\tan(\psi) = \frac{H(\omega_c)}{G(\omega_c)} = \frac{\sin(\omega_c T)}{\cos(\omega_c T) - 1} \tag{3.35}$$

where ψ represents the phase of the frequency response function of the system in radians. Expanding Equation 3.35, with trigonometric identity functions results,

$$\omega_c T = 2\pi N + 3\pi + 2\psi \tag{3.36a}$$
$$\omega_c T = 2\pi N + \epsilon \tag{3.36b}$$

where N is the integer number of waves and ϵ is the phase difference between the previous and current waves on the chip surface. For a given chatter frequency and integer number

of waves, the spindle speed period is found and thus the spindle speed, Ω (rev/min) by,

$$\Omega = \frac{60}{T} \tag{3.37}$$

Considering the real part of Equation 3.34a and substituting Equation 3.35 yields the width of cut for marginal stability, $b_{w,lim}$, as,

$$b_{w,lim} = \frac{-1}{2K_{fc}G(\omega_c)} \tag{3.38}$$

The cutting force, however, doesn't usually act along the surface normal in practice and the system usually possesses multi degrees of freedom (MDOF) in the plane the cutting force acts. For a simplified case, the cutting force, F_c, is shown to act with an angle, β_F, to the normal and two modes of vibration in orthogonal directions, u_1 and u_2 are shown in Figure 3.10.

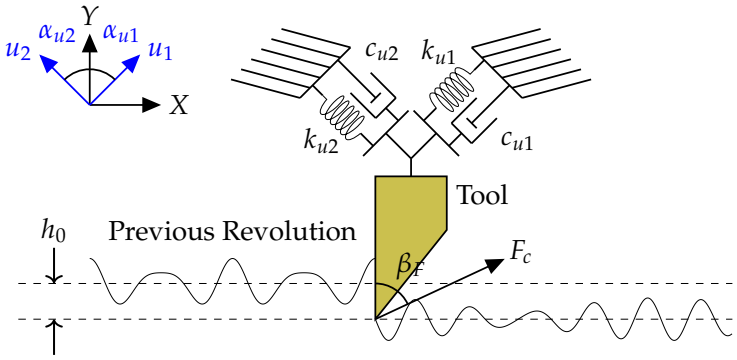

FIGURE 3.10: The representation of 2 DOF system for turning and boring operations [200]

Here, the oriented frequency response function, FRF_{orient}, of the system is computed based on the mode inclination angles of two orthogonal modes, α_{u1} and α_{u2}, as well as the cutting force direction to the normal, β_F, to compute the dynamics at the surface normal,

$$FRF_{orient}(s) = \mu_1 FRF_{u1}(s) + \mu_2 FRF_{u2}(s) \tag{3.39}$$

where FRF_{u1} and FRF_{u2} are the frequency response function of orthogonal modes u_1 and u_2 and μ_1 and μ_2 are their components on the frequency response function at the surface normal respectively. In this case, $FRF_{orient}(s)$ replaces $FRF(s)$ in Equation 3.33 and the rest is computed in the same manner. The coefficients μ_1 and μ_2 are given as in [26, 171],

$$\mu_1 = \cos(\beta_F - \alpha_{u1})\cos(\alpha_{u1}) \tag{3.40a}$$
$$\mu_2 = \cos(\beta_F + \alpha_{u2})\cos(\alpha_{u2}) \tag{3.40b}$$

3.2.1.2 Milling operation

In milling operations, a rotating tool with one or more teeth is held on the spindle and the tool or workpiece are fed towards each other for material removal. Milling is an intermittent cutting process and involves periodic engagement of the teeth into the workpiece to tear away the material in the form of chips. Chips created tend to have varying chip thickness as a result of the feed and rotation of the cutter. In addition to this, the chip thickness is affected by vibrations at the point of tool-workpiece contact. As teeth engage with the workpiece, dynamic cutting forces result in deflection at the surface normal and the subsequent teeth engagement causes the thickness of the chip to vary depending on the phase difference between current and previous vibrations.

In milling operations, the regenerative chatter mechanism was modelled in frequency domain such as Zero and Multi Frequency Approach [201–203] as well as in time domain such as Semi-discretization and Full-discretization Method [204, 205] respectively. There also exist numerous chatter suppression techniques such as utilisation of special tool geometries, active and passive damping and control techniques etc. as described in [206]. Defining the regenerative chatter mechanism in milling, the cutter is approximately defined by two degrees of freedom orthogonal to each other. Thus, the dynamics of the 2-DOF milling operation can be represented as in Figure 3.11a.

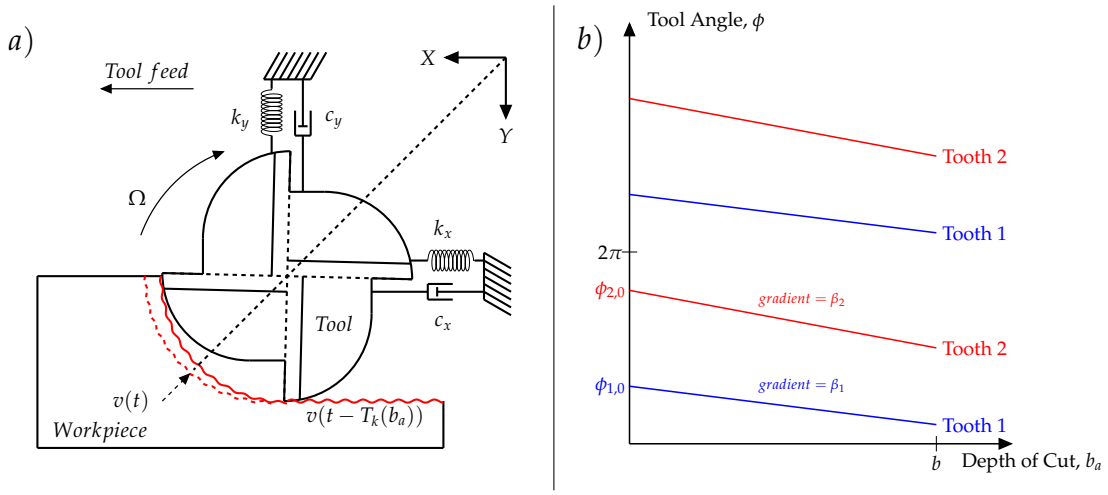

FIGURE 3.11: a) The representation of the waves left by the previous and current revolution for milling operation for a 2 DOF system b) The variation of tool angles across the depth of cut for an irregular end mill tool [203]

The derivation of regenerative chatter mechanism in milling for tools with variable pitch and helix angles was adapted based from [203] but extended to 2-DOFs. Taking the feed rate along the X-axis, the dynamic chip thickness, $h(\phi_k(a,t))$ can be summarised as,

$$h(\phi_k(b_a,t)) = (h_0 - v(t) + v(t - T_k(b_a)))g(\phi_k(b_a,t)). \tag{3.41}$$

The static part of the chip thickness is represented as $h_0 = f_{tth}\sin(\phi_k(b_a,t))$ where f_{tth} is feed rate per tooth, $\phi_k(b_a,t)$ is the instantaneous angular immersion of tooth k at a given time t for a cutter with K number of tooth with axial location, b_a. The $v(t)$ and $v(t - T_k(b_a))$ represent current and previous radial vibrations at present and at a time equal to the time

delay between successive tooth passes at axial location, b_a, $T_k(b_a)$ as,

$$v(t) = -x(t)\sin(\phi_k(b_a,t)) - y(t)\cos(\phi_k(b_a,t)) \quad (3.42a)$$

$$v(t-T_k(b_a)) = -x(t-T_k(b_a))\sin(\phi_k(b_a,t)) - y(t-T_k(a))\cos(\phi_k(b_a,t)) \quad (3.42b)$$

Thus, current and previous vibrations along X-axis and Y-axis are $x(t)$ & $y(t)$ and $x(t - T_k(b_a))$ & $y(t - T_k(b_a))$ respectively. The function $g(\phi_k(b_a,t))$ is a Heaviside (unit) step function that determines the engagement of tooth based on instantaneous angular immersion of tooth by,

$$g(\phi_k(b_a,t)) = \begin{cases} 1 & \phi_{st} < \phi_k(b_a,t) < \phi_{ex}, \\ 0 & otherwise \end{cases} \quad (3.43)$$

where ϕ_{st} and ϕ_{ex} are start and exit immersion angles of the tooth respectively. The stability of the dynamic chip load regeneration is not affected from the static part of the chip thickness $h_0(\phi_k(b_a,t))$, hence it is omitted from Equation 3.41. This yields,

$$h(\phi_k(b_a,t)) = (\Delta x\sin(\phi_k(b_a,t)) + \Delta y\cos(\phi_k(b_a,t)))g(\phi_k(b_a,t)). \quad (3.44)$$

where $\Delta x = x(t - T_k(b_a)) - x(t)$ and $\Delta y = y(t - T_k(b_a)) - y(t)$. Considering the spindle is rotating at a spindle speed Ω (rad/s), the instantaneous angular immersion for each tooth becomes;

$$\phi_k(b_a,t) = \Omega t + \phi_{k0} + \beta_k b_a \quad (3.45)$$

where ϕ_{k0} is the position of tooth across the circumference of the tool at its end, β_k is the gradient of the pitch with respect to the axial location of the tooth, b_a [203]. Therefore, for the k^{th} tooth with a helix angle γ_k and radius r_{tool}, β_k is;

$$\beta_k = \frac{\tan(\gamma_k)}{r_{tool}} \quad (3.46)$$

The dynamic tangential ($F_{t,k}(b_a,t)$) and radial ($F_{r,k}(b_a,t)$) cutting force are directly proportional to the dynamic chip thickness $h(\phi_k(b_a,t))$ for a given infinitesimal axial location b_a along the tool and their corresponding cutting force coefficients (K_{tc} and K_{rc}). The differential dynamic tangential and radial cutting forces are represented as follows;

$$f_{t,k}(b_a,t) = K_{tc}h(\phi_k(b_a,t))db_a \quad (3.47)$$

$$f_{r,k}(b_a,t) = K_rK_{tc}h(\phi_k(b_a,t))db_a \quad (3.48)$$

where K_r is $K_r = K_{tc}$ / K_{rc} and the coefficients are constant for each tooth on the cutter. The differential dynamic tangential and radial cutting forces can be decomposed into their force components in X and Y directions as;

$$f_{x,k}(b_a,t) = -f_{t,k}(b_a,t)\cos(\phi_k(b_a,t)) - f_{r,k}(b_a,t)\sin(\phi_k(b_a,t)) \quad (3.49)$$

$$f_{y,k}(b_a,t) = +f_{t,k}(b_a,t)\sin(\phi_k(b_a,t)) - f_{r,k}(b_a,t)\cos(\phi_k(b_a,t)) \quad (3.50)$$

Therefore, the total cutting force in X and Y directions becomes;

$$\begin{bmatrix} F_x(t) \\ F_y(t) \end{bmatrix} = \frac{1}{2}K_{tc}\sum_{k=1}^{K}\int_{b_a=0}^{b}[A_T(\phi_k(b_a,t))]\begin{bmatrix} x(t)-x(t-T_k(b_a)) \\ y(t)-y(t-T_k(b_a)) \end{bmatrix}db_a \quad (3.51)$$

In here, the matrix $A_T(\phi(b_a,t))$ is called the directional dynamic milling force coefficient matrix and the elements of the matrix are represented as;

$$\sum_{k=1}^{K}\int_{b_a=0}^{b}[A_T(\phi_k(b_a,t))]db_a = \sum_{k=1}^{K}\int_{b_a=0}^{b}\begin{bmatrix}a_{xx}(\phi_k(b_a,t)) & a_{xy}(\phi_k(b_a,t))\\ a_{yx}(\phi_k(b_a,t)) & a_{yy}(\phi_k(b_a,t))\end{bmatrix}da \tag{3.52}$$

where

$$a_{xx}(\phi_k(b_a,t)) = -g(\phi_k(b_a,t))[\sin(2\phi_k(b_a,t)) + K_r(1-\cos(2\phi_k(b_a,t)))] \tag{3.53a}$$
$$a_{xy}(\phi_k(b_a,t)) = -g(\phi_k(b_a,t))[(1+\cos(2\phi_k(b_a,t))) + K_r\sin(2\phi_k(b_a,t))] \tag{3.53b}$$
$$a_{yx}(\phi_k(b_a,t)) = +g(\phi_k(b_a,t))[(1-\cos(2\phi_k(b_a,t))) - K_r\sin(2\phi_k(b_a,t))] \tag{3.53c}$$
$$a_{yy}(\phi_k(b_a,t)) = +g(\phi_k(b_a,t))[\sin(2\phi_k(b_a,t)) - K_r(1+\cos(2\phi_k(b_a,t)))] \tag{3.53d}$$

Taking the Fourier Transform of Equation 3.51, converts the cutting forces in time domain into frequency domain as;

$$\begin{bmatrix}F_x(j\omega)\\ F_y(j\omega)\end{bmatrix} = \frac{1}{2}K_{tc}\sum_{k=1}^{K}\int_{b_a=0}^{b}\mathcal{F}\Big([A_T(\phi_k(b_a,t))]\begin{bmatrix}x(t)-x(t-T_k(b_a))\\ y(t)-y(t-T_k(b_a))\end{bmatrix}\Big)db_a \tag{3.54}$$

Fourier Expansion of directional dynamic milling force coefficient matrix ($[A_T(\phi_k(b_a,t))]$) becomes;

$$[A_T(\phi_k(b_a,t))] = \sum_{r=-\infty}^{\infty} e^{jr(\phi_{k0}+\beta_k b_a)}[A_F(r)]e^{jr\Omega t} \tag{3.55}$$

where r is number of harmonics and $[A_F(r)]$ is

$$[A_F(r)] = \frac{1}{2\pi}\int_{\phi_{st}}^{\phi_{ex}} A_T(\phi)e^{-jr\phi}d\phi \tag{3.56}$$

As in [203], Equation 3.54 turns into the following;

$$\begin{bmatrix}F_x(j\omega)\\ F_y(j\omega)\end{bmatrix} = \frac{1}{2}K_{tc}\sum_{k=1}^{K}\int_{b_a=0}^{b}\sum_{r=-\infty}^{\infty} e^{jr(\phi_{k0}+\beta_k b_a)}[A_F(r)]\mathcal{F}\Big(\begin{bmatrix}x(t)-x(t-T_k(b_a))\\ y(t)-y(t-T_k(b_a))\end{bmatrix}e^{jr\Omega t}\Big)db_a \tag{3.57}$$

With the application of the shift theorem as in [203], Equation 3.57 turns into;

$$\begin{bmatrix}F_x(j\omega)\\ F_y(j\omega)\end{bmatrix} = \frac{1}{2}K_{tc}\sum_{k=1}^{K}\int_{b_a=0}^{b}\sum_{r=-\infty}^{\infty} e^{jr(\phi_{k0}+\beta_k b_a)}[A_F(r)](1-e^{-T_k(b_a)(j\omega-jr\Omega)})\begin{bmatrix}X(j\omega-jr\Omega)\\ Y(j\omega-jr\Omega)\end{bmatrix}db_a \tag{3.58}$$

Assuming linear time-invariant combined tool-workpiece structural dynamics ($FRF(j\omega)$, where $\frac{X(j\omega)}{F(j\omega)} = FRF(j\omega)$), then Equation 3.57 becomes;

$$\begin{bmatrix}X(j\omega)\\ Y(j\omega)\end{bmatrix} = \frac{1}{2}K_{tc}\sum_{k=1}^{K}\int_{b_a=0}^{b}\sum_{r=-\infty}^{\infty} e^{jr(\phi_{k0}+\beta_k b_a)}[A_F(r)] \\ (1-e^{-T_k(b_a)(j\omega-jr\Omega)})[FRF(j\omega)]\begin{bmatrix}X(j\omega-jr\Omega)\\ Y(j\omega-jr\Omega)\end{bmatrix}db_a \tag{3.59}$$

where $FRF(j\omega)$ is,

$$FRF(j\omega) = \begin{bmatrix} FRF_{xx}(j\omega) & FRF_{xy}(j\omega) \\ FRF_{yx}(j\omega) & FRF_{yy}(j\omega) \end{bmatrix} \tag{3.60}$$

and $[A_F(r)]$ is

$$[A_F(r)] = \begin{bmatrix} A_{xx}(r) & A_{xy}(r) \\ A_{yx}(r) & A_{yy}(r) \end{bmatrix} \tag{3.61}$$

with each element of $[A_F(r)]$ in frequency domain is computed by taking the Fourier Transform of Equations 3.53.

The stability of equation 3.59 can be solved using two approaches based on the approximation of the directional dynamic milling force coefficient matrix; Zero Order and Multi Frequency Solution.

In "Zero Order Solution", the static part of the directional dynamic milling force coefficient matrix $[A_F(r)]$ is considered ($r = 0$). Then, for regular pitch vertical fluted conventional end milling cutters, Equation 3.59 is reduced to;

$$\begin{bmatrix} X(j\omega) \\ Y(j\omega) \end{bmatrix} = \frac{1}{2} K_{tc} \sum_{k=1}^{K} \int_{b_a=0}^{b} (1 - e^{-j\omega T})[A_F(0)][FRF(j\omega)] \begin{bmatrix} X(j\omega) \\ Y(j\omega) \end{bmatrix} db_a \tag{3.62}$$

where T is the time delay between the subsequent teeth which is constant and independent of the axial location. Thus, Equation 3.62 can be further simplified to,

$$\begin{bmatrix} X(j\omega) \\ Y(j\omega) \end{bmatrix} = \frac{K}{2} b K_{tc} (1 - e^{-j\omega T}) \begin{bmatrix} A_{xx}(0) & A_{xy}(0) \\ A_{yx}(0) & A_{yy}(0) \end{bmatrix} \begin{bmatrix} FRF_{xx}(j\omega) & FRF_{xy}(j\omega) \\ FRF_{yx}(j\omega) & FRF_{yy}(j\omega) \end{bmatrix} \begin{bmatrix} X(j\omega) \\ Y(j\omega) \end{bmatrix} \tag{3.63}$$

If the critical process stability is considered, the roots of the characteristic equation are obtained from the determinant of Equation 3.63 as;

$$\det \left(I - \frac{K}{2} b K_{tc} (1 - e^{-j\omega T}) \begin{bmatrix} A_{xx}(0) & A_{xy}(0) \\ A_{yx}(0) & A_{yy}(0) \end{bmatrix} \begin{bmatrix} FRF_{xx}(j\omega) & FRF_{xy}(j\omega) \\ FRF_{yx}(j\omega) & FRF_{yy}(j\omega) \end{bmatrix} \right) = 0 \tag{3.64}$$

where the static part of the directional dynamic milling force coefficient matrix is given by;

$$A_{xx}(0) = \frac{1}{2} (\cos(2\phi) - 2K_r\phi + K_r \sin(2\phi)) \Big|_{\phi_{st}}^{\phi_{ex}} \tag{3.65a}$$

$$A_{xy}(0) = \frac{1}{2} (-\sin(2\phi) - 2\phi + K_r \cos(2\phi)) \Big|_{\phi_{st}}^{\phi_{ex}} \tag{3.65b}$$

$$A_{yx}(0) = \frac{1}{2} (-\sin(2\phi) + 2\phi + K_r \cos(2\phi)) \Big|_{\phi_{st}}^{\phi_{ex}} \tag{3.65c}$$

$$A_{yy}(0) = \frac{1}{2} (-\cos(2\phi) - 2K_r\phi - K_r \sin(2\phi)) \Big|_{\phi_{st}}^{\phi_{ex}} \tag{3.65d}$$

The eigenvalue of the characteristic equation, Equation 3.64 is,

$$\lambda = -\frac{K}{2} b K_{tc} (1 - e^{-j\omega T}) \tag{3.66}$$

Let Φ be,

$$\Phi = \begin{bmatrix} \Phi_{1,1} & \Phi_{1,2} \\ \Phi_{2,1} & \Phi_{2,2} \end{bmatrix} \tag{3.67}$$

where $\Phi_{1,1}$, $\Phi_{1,2}$, $\Phi_{2,1}$ and $\Phi_{2,2}$ include the product of $[A_F(n)]$ and $[FRF(j\omega)]$ matrices. Then,

$$\Phi_{1,1} = A_{xx}(0) FRF_{xx}(j\omega) + A_{xy}(0) FRF_{yx}(j\omega) \tag{3.68a}$$
$$\Phi_{1,2} = A_{xx}(0) FRF_{xy}(j\omega) + A_{xy}(0) FRF_{yy}(j\omega) \tag{3.68b}$$
$$\Phi_{2,1} = A_{yx}(0) FRF_{xx}(j\omega) + A_{yy}(0) FRF_{yx}(j\omega) \tag{3.68c}$$
$$\Phi_{2,2} = A_{yx}(0) FRF_{xy}(j\omega) + A_{yy}(0) FRF_{yy}(j\omega) \tag{3.68d}$$

Consequently, the determinant in Equation 3.64 gives the following;

$$(\Phi_{1,1}\Phi_{2,2} - \Phi_{1,2}\Phi_{2,1})\lambda^2 + \lambda(\Phi_{1,1} + \Phi_{2,2}) + 1 = 0 \tag{3.69}$$

A quadratic equation is obtained and can be easily solved to get its solutions, $\lambda_{1,2}$,

$$\lambda_{1,2} = \frac{-(\Phi_{1,1} + \Phi_{2,2}) \pm \sqrt{(\Phi_{1,1} + \Phi_{2,2})^2 - 4(\Phi_{1,1}\Phi_{2,2} - \Phi_{1,2}\Phi_{2,1})}}{2(\Phi_{1,1}\Phi_{2,2} - \Phi_{1,2}\Phi_{2,1})} = \lambda_{Re} + j\lambda_{Im} \tag{3.70}$$

Both solutions for $\lambda_{1,2}$ are complex numbers due to the nature of $FRF(j\omega)$. Substituting, λ into Equation 3.66 gives the limiting depth of cut, b_{lim},

$$b_{lim} = -\frac{1}{K K_{tc}} \left[\frac{\lambda_{Re}(1 - \cos(\omega_c T)) + \lambda_{Im} \sin(\omega_c T)}{1 - \cos(\omega_c T)} + j \frac{\lambda_{Im}(1 - \cos(\omega_c T)) + \lambda_{Re} \sin(\omega_c T)}{1 - \cos(\omega_c T)} \right] \tag{3.71}$$

The limiting depth of cut is a physical quantity and therefore is a real number. Thus, equating the imaginary part to zero yields,

$$\lambda_{Im}(1 - \cos(\omega_c T)) + \lambda_{Re} \sin(\omega_c T) = 0 \tag{3.72}$$

which can be put into the following form,

$$\kappa = \frac{\lambda_{Im}}{\lambda_{Re}} = \frac{\sin(\omega_c T)}{1 - \cos(\omega_c T)} \tag{3.73}$$

Expanding Equation 3.73 gives,

$$\kappa = \tan(\psi) = \cot((\omega_c T)/2) = \tan(\pi/2 - (\omega_c T)/2) \tag{3.74}$$

where ψ is the phase angle of the eigenvalues of the characteristic equation. Thus, the above equation gives the relationship between the phase angle of the corresponding solution to the phase distance in one tooth period [26]. For an integer number of full-vibration waves, N, Equation 3.74 can be expressed as,

$$\omega_c T = \pi - 2\psi + 2\pi N = \epsilon + 2\pi N \tag{3.75}$$

where ϵ defines the phase shift between the current and previous waves imprinted on the both surfaces of the chip. Hence, the fact that right hand side of the above equation is known enables computation of the left hand side where T is unknown.

$$T = \frac{1}{\omega_c}(\pi - 2\psi + 2\pi N) \tag{3.76}$$

The time delay, T, between the current and previous vibrations is used to determine the spindle speed which is responsible for the phase difference between the vibrations of the given system. The spindle speed is found out by,

$$\Omega = \frac{60}{KT}(RPM) \tag{3.77}$$

Considering the real part of Equation 3.71 and substituting Equation 3.73 makes it possible to compute the stability boundary of depth of cut in a more compact form as,

$$b_{lim} = -\frac{1}{KK_{tc}}\lambda_{Re}[1 + \kappa^2] \tag{3.78}$$

In the "Multi Frequency Solution", the directional dynamic milling force coefficients are computed with a non-zero harmonic number, r, in order to better approximate the force profile. This is usually essential in low radial immersion milling operations due to the intermittent nature of cutting forces [202]. This, in turn, necessitates consideration of higher frequency components of the waveforms in order to better approximate the directional dynamic milling force coefficients. As a result, a higher order harmonics is required for increased accuracy even though computational time and complexity would be the major trade off. Following [203] and rewriting ω=ω+$p\Omega$, Equation 3.59 can be expressed as;

$$\begin{bmatrix} X(j\omega + jp\Omega) \\ Y(j\omega + jp\Omega) \end{bmatrix} = \frac{1}{2}K_{tc}\sum_{k=1}^{K}\int_{b_a=0}^{b}\sum_{r=-\infty}^{\infty} e^{jr(\phi_{k0}+\beta_k b_a)}[A_F(r)] \\ (1 - e^{-T_k(b_a)(j\omega - jr\Omega + jp\Omega)})[FRF(j\omega + jp\Omega)]\begin{bmatrix} X(j\omega - jr\Omega + jp\Omega) \\ Y(j\omega - jr\Omega + jp\Omega) \end{bmatrix} db_a \tag{3.79}$$

Let the harmonic number to be $r = p - q$, then,

$$\begin{bmatrix} X(j\omega + jp\Omega) \\ Y(j\omega + jp\Omega) \end{bmatrix} = \frac{1}{2}K_{tc}\sum_{k=1}^{K}\int_{b_a=0}^{b}\sum_{p-q=-\infty}^{\infty} e^{j(p-q)(\phi_{k0}+\beta_k b_a)}[A_F(p-q)] \\ (1 - e^{-T_k(b_a)(j\omega + jq\Omega)})[FRF(j\omega + jp\Omega)]\begin{bmatrix} X(j\omega + jq\Omega) \\ Y(j\omega + jq\Omega) \end{bmatrix} db_a \tag{3.80}$$

If p represents rows and q represents the columns of a matrix where $p = -\infty, \ldots, \infty$ and $q = -\infty, \ldots, \infty$, then Equation 3.80 can be expressed in a more compact way after reverting $r = p - q$ format as;

$$\begin{bmatrix} X(j\omega) \\ Y(j\omega) \end{bmatrix}_p = \begin{bmatrix} X(j\omega + jp\Omega) \\ Y(j\omega + jp\Omega) \end{bmatrix} \tag{3.81}$$

$$[FRF(j\omega)]_{p,p} = [FRF(j\omega + jp\Omega)] \tag{3.82}$$

$$[\Psi(j\omega)]_{p,q} = \frac{1}{2} K_{tc} \sum_{k=1}^{K} \int_{b_a=0}^{b} e^{jr(\phi_{k0}+\beta_k b_a)} (1 - e^{-T_k(b_a)(j\omega - jq\Omega)}) [A_F(r)] db_a \tag{3.83}$$

Therefore,

$$\begin{bmatrix} X(j\omega) \\ Y(j\omega) \end{bmatrix}_p = [FRF(j\omega)]_{p,p} \sum_{q=-\infty}^{\infty} [\Psi(j\omega)]_{p,q} \begin{bmatrix} X(j\omega) \\ Y(j\omega) \end{bmatrix}_q \tag{3.84}$$

The $[FRF(j\omega)]_{p,p}[\Psi(j\omega)]_{p,q}$ can be visualised as doubly infinite harmonic transfer function between the vibrations in the frequency domain and itself. The stability of the system can be obtained by computing Generalised Nyquist Stability Criterion as in [203, 207]. The system is stable if the $\det([I] - [FRF(j\omega)]_{p,p} \sum_{q=-\infty}^{\infty} [\Psi(j\omega)]_{p,q})$ is non zero and does not circulate the origin in clockwise direction.

In summary, the regenerative chatter mechanism is developed for milling operations for cutters with variable pitch and helix in Zero and Multi frequency approaches. Note that, developed equations can be further simplified to cover the cutters with regular & variable pitch as well as zero, regular and variable helix angles and applied to determine the stability of the milling process. In this thesis, the behaviour of the process stability based on the regenerative chatter mechanism will be investigated when milling with a serial industrial robot in Chapter 5. The formulations developed above will be utilised to determine the stability boundary predictions in Zero Frequency approach to predict and validate stability of robotic milling tests.

3.2.2 Mode coupling chatter

Mode coupling chatter is a special type chatter and is known to happen without regeneration - the surface being cut is always a new surface and absent from any vibrations left by the cutter. As such, the system is observed to vibrate simultaneously in at least two degrees of freedom with different amplitudes and with a difference in phase [176].

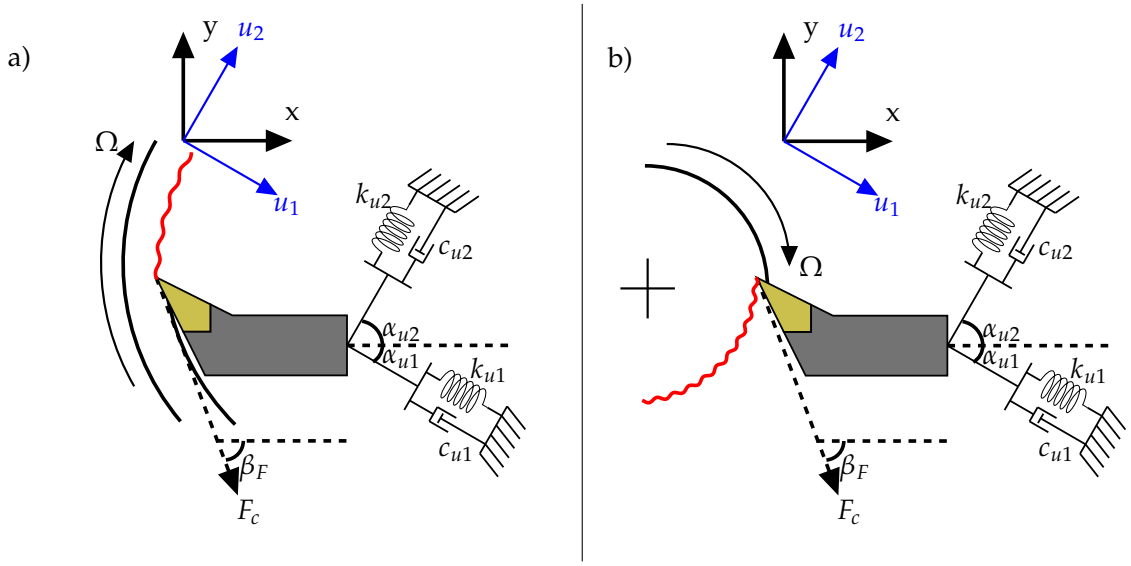

FIGURE 3.12: Mode coupling vibrations in 2 DOF of a) Boring operation b) Turning operation

For axial turning and boring operations with a large feed, such as in thread cutting operations, the surface being machined is not cut in the subsequent revolution of the workpiece. Hence, the dynamic chip thickness only depends on current vibrations as opposed to regenerative chatter. In addition to this, mode coupling chatter requires the degrees of freedom of the system at the point of contact between the tool and the workpiece to possess different dynamic properties. Thus, the following assumptions should hold at all times for mode coupling chatter to be feasible [165, 166];

- The surface being cut is a new surface absent from any surface waves left by the previous revolution of the workpiece; the chip regeneration.
- The system should have different dynamic properties in at least two orthogonal degrees of freedom

The workpiece having different second moment of inertia across its cross section and/or the tool having asymmetrical dynamic properties could trigger mode coupling chatter provided that above assumptions are satisfied. The following theory of mode coupling chatter mechanism is adapted based on [171]. Assuming the point of contact dynamics can be approximated with two orthogonal modes as in Figure 3.12 for turning or boring operation, with a large feed so that the tool is always cutting a new surface, equations of motions along the orthogonal modal directions, u_1 and u_2 are;

$$m_{u1}\ddot{u}_1(t) + c_{u1}\dot{u}_1(t) + k_{u1}u_1(t) = -K_c b_w(u_1(t)\cos(\alpha_{u1}) + u_2(t)\sin(\alpha_{u1}))\cos(\beta_F - \alpha_{u1}) \tag{3.85a}$$

$$m_{u2}\ddot{u}_2(t) + c_{u2}\dot{u}_2(t) + k_{u2}u_2(t) = K_c b_w(u_1(t)\cos(\alpha_{u1}) + u_2(t)\sin(\alpha_{u1}))\sin(\beta_F - \alpha_{u1}) \tag{3.85b}$$

Assuming that the modes of vibration, u_1 and u_2, oscillate in a harmonic motion but with a phase delay between them, Θ, the modal displacements, velocities and accelerations can be visualised as;

$$\begin{aligned} u_1(t) &= A_1 e^{(\sigma+i\omega)t} & u_2(t) &= A_2 e^{(\sigma t + i(\omega t - \Theta))} \\ \dot{u}_1(t) &= A_1(\sigma + i\omega)e^{(\sigma+i\omega)t} & \dot{u}_2(t) &= A_2(\sigma + i\omega)e^{(\sigma t + i(\omega t - \Theta))} \\ \ddot{u}_1(t) &= A_1(\sigma^2 - \omega^2)e^{(\sigma+i\omega)t} & \ddot{u}_2(t) &= A_2(\sigma^2 - \omega^2)e^{(\sigma t + i(\omega t - \Theta))} \end{aligned}$$

where A_1 and A_2 are the amplitudes of modal vibrations u_1 and u_2 respectively. Substituting the modal displacements, velocities and accelerations into Equation 3.85 yields,

$$(m_{u1}(\sigma^2 - \omega^2) + c_{u1}(\sigma + i\omega) + k_{u1})A_1 e^{(\sigma+i\omega)t} = -K_c b_w(A_1 e^{(\sigma+i\omega)t}\cos(\alpha_{u1}) + A_2 e^{(\sigma t + i(\omega t - \Theta))}\sin(\alpha_{u1}))\cos(\beta_F - \alpha_{u1}) \tag{3.86a}$$

$$(m_{u2}(\sigma^2 - \omega^2) + c_{u2}(\sigma + i\omega) + k_{u2})A_2 e^{(\sigma t + i(\omega t - \Theta))} = K_c b_w(A_1 e^{(\sigma+i\omega)t}\cos(\alpha_{u1}) + A_2 e^{(\sigma t + i(\omega t - \Theta))}\sin(\alpha_{u1}))\sin(\beta_F - \alpha_{u1}) \tag{3.86b}$$

Introducing P as the ratio of amplitudes of the modes where $P = \frac{A_1}{A_2}$ and dividing both sides of Equation 3.86 with $e^{i\Theta}$ give,

$$\begin{aligned}(m_{u1}(\sigma+i\omega)^2+c_{u1}(\sigma+i\omega)+k_{u1})P = \\ -K_c b_w(P\cos(\alpha_{u1})+e^{i\Theta}\sin(\alpha_{u1}))\cos(\beta_F-\alpha_{u1})\end{aligned} \tag{3.87a}$$

$$\begin{aligned}(m_{u2}(\sigma+i\omega)^2+c_{u2}(\sigma+i\omega)+k_{u2}) = \\ K_c b_w(Pe^{i\Theta}\cos(\alpha_{u1})+\sin(\alpha_{u1}))\sin(\beta_F-\alpha_{u1})\end{aligned} \tag{3.87b}$$

Collecting the real and imaginary parts of Equation 3.87 constitutes 4 set of equations as;

$$\begin{aligned}(m_{u1}(\sigma^2-\omega^2)+c_{u1}\sigma+k_{u1})P = \\ -K_c b_w(P\cos(\alpha_{u1})+\cos(\Theta)\sin(\alpha_{u1}))\cos(\beta_F-\alpha_{u1})\end{aligned} \tag{3.88a}$$

$$(2m_{u1}\sigma+c_{u1})P\omega = K_c b_w\sin(\Theta)\sin(\alpha_{u1})\cos(\beta_F-\alpha_{u1}) \tag{3.88b}$$

$$\begin{aligned}m_{u2}(\sigma^2-\omega^2)+c_{u2}\sigma+k_{u2} = \\ K_c b_w(P\cos(\Theta)\cos(\alpha_{u1})+\sin(\alpha_{u1}))\sin(\beta_F-\alpha_{u1})\end{aligned} \tag{3.88c}$$

$$(2m_{u2}\sigma+c_{u2})\omega = K_c b_w P\sin(\Theta)\cos(\alpha_{u1})\sin(\beta_F-\alpha_{u1}) \tag{3.88d}$$

where σ, P, Θ, b_w and ω are unknowns. For a vibratory system, the marginal stability is achieved when $\sigma = 0$. Setting the $\sigma = 0$ and dividing Equations 3.88b to 3.88d results,

$$\frac{\sin(\alpha_{u1})\cos(\beta_F-\alpha_{u1})}{P\cos(\alpha_{u1})\sin(\beta_F-\alpha_{u1})} = \frac{c_{u1}\omega_c P}{c_{u2}\omega_c} \tag{3.89}$$

where ω_c is chatter frequency. Here, there appears to be only one unknown which is P, hence, making it the subject of equation gives,

$$P = \sqrt{\frac{c_{u2}\sin(\alpha_{u1})\cos(\beta_F-\alpha_{u1})}{c_{u1}\cos(\alpha_{u1})\sin(\beta_F-\alpha_{u1})}} \tag{3.90}$$

Similarly, dividing Equation 3.88c by 3.88a results in,

$$\frac{(P\cos(\Theta)\cos(\alpha_{u1})+\sin(\alpha_{u1}))\sin(\beta_F-\alpha_{u1})}{-(P\cos(\alpha_{u1})+\cos(\Theta)\sin(\alpha_{u1}))\cos(\beta_F-\alpha_{u1})} = \frac{k_{u2}-m_{u2}\omega_c^2}{(k_{u1}-m_{u1}\omega_c^2)P} \tag{3.91}$$

For any possible chatter frequency, ω_c, the phase delay Θ, is obtained as,

$$\cos(\Theta) = -\frac{\Theta_{num}}{\Theta_{den}} \tag{3.92}$$

where Θ_{num} and Θ_{den} are defined as,

$$\Theta_{num} = (k_{u1}-m_{u1}\omega_c^2)P\sin(\alpha_{u1})\sin(\beta_F-\alpha_{u1})+(k_{u2}-m_{u2}\omega_c^2)P\cos(\alpha_{u1})\cos(\beta_F-\alpha_{u1})$$

$$\Theta_{den} = (k_{u1}-m_{u1}\omega_c^2)P^2\cos(\alpha_{u1})\sin(\beta_F-\alpha_{u1})+(k_{u2}-m_{u2}\omega_c^2)\sin(\alpha_{u1})\cos(\beta_F-\alpha_{u1})$$

Hence, sweeping through the possible chatter frequencies, ω_c, and finding out the corresponding phase delay, Θ, between modes of vibrations make it possible to compute the last unknown, the limiting width of cut $b_{w,lim}$, with the following two independent equations,

$$b_{w,lim} = \frac{c_{u1}\omega_c P}{K_c \sin(\Theta)\sin(\alpha_{u1})\cos(\beta_F - \alpha_{u1})} \tag{3.93a}$$

$$b_{w,lim} = \frac{k_{u2} - m_{u2}\omega_c^2}{K_c(P\cos(\Theta)\cos(\alpha_{u1}) + \sin(\alpha_{u1}))\sin(\beta_F - \alpha_{u1})} \tag{3.93b}$$

The chatter frequencies resulting in same values of positive real width of cut, $b_{w,lim}$, from both equations are searched and gathered. Therefore, the intersection of Equations 3.93a and 3.93b defines the stability boundary of the mode coupling chatter in turning and/or boring operations. Note that in this mode coupling chatter mechanism, the process damping and therefore the effect of spindle speed on the cutting force are ignored.

Based on the above mechanism, the mode coupling chatter is spindle speed independent and could only occur when the direction of the lower natural frequency mode happens to be between the displacement and force direction [171]. When the system chatters, the cutting edge moves in an ellipse delivering energy into the system which is the fundamental reason behind the mode coupling chatter mechanism. It can be seen that the mode coupling chatter could still happen when modes of vibrations are orthogonal to each other and there is no cross coupling between them. Hence, the mode coupling chatter should not be confused with the presence or significance of the cross-FRF terms.

It should be noted that, the above formulation of the mode coupling chatter mechanism in thread cutting operations does not consider the cross-FRF terms. In addition, the mode coupling chatter formulation cannot accommodate multiple modes of vibration in orthogonal axes. For this reason, this mathematical model of the mode coupling chatter mechanism cannot be applied straight away in an industrial environment and is still lacking crucial aspects that play an important role in the stability boundary predictions. Nevertheless, the mode coupling chatter mechanism in thread cutting operations is presented to better understand its causation mechanism and behaviour. In this way, the behaviour of the mode coupling chatter mechanism can be analysed to distinguish it from the regenerative chatter mechanism. Having distinguished the chatter mechanism, the mode coupling chatter claims observed in robotic milling operations in the existing literature can be enlightened. The understanding developed in the mode coupling chatter mechanism in thread cutting operations will be applied to to derive mode coupling chatter mechanism in milling operations in Chapter 6 in order to validate the chatter mechanism appearing in the robotic milling trials as described in Chapter 5.

3.3 Chapter summary

In this chapter, the theory for "robotics" and "machine tool dynamics" were defined. Firstly, terminology and definitions in robotics were established. The geometrical modelling and kinematics of serial manipulators were introduced. Then, direct and inverse kinematics of serial manipulators were defined to allow computation of TCP pose from joint variables and vice versa. Following that, differential kinematics was introduced, which was essential in describing stiffness characteristics and the closeness of a manipulator configuration

to any singularity. Additionally, types of redundancy, the causation of singularities and quantification of how close the manipulator is to a singularity were discussed. This was to emphasise the existence of redundancies for a serial robot and define a scalar parameter to make sure the manipulator is away from any singularities.

In the second half of the chapter, the regenerative chatter mechanism in turning/ boring as well as milling operations were defined. The regenerative chatter mechanism in milling was extended to 2 DOF to enable determination of stability boundary predictions for a 2 DOF system. Finally, the mode coupling chatter mechanism in thread cutting operations was introduced to better understand its behaviour. This was to clarify the ambiguity in the identified chatter mechanism in robotic milling applications in the existing literature. In this way, the knowledge acquired can be applied to distinguish and validate regenerative and mode coupling chatter mechanisms.

Chapter 4

Structural stiffness modelling, identification and optimisation

In this chapter, Virtual Joint Model approach is used to model, identify and optimise the static stiffness of a serial industrial robot. The theory of stiffness modelling with Virtual Joint Model is presented and equations are arranged for experimental identification of joint stiffness parameters. However, the experimental identification of stiffness parameters are challenging and their accuracy is dependent on measurement noise. Consequently, a preliminary analysis is performed using a numerical simulation to illustrate potential experimental challenges and design a suitably robust experimental regime. Detailed experiments are then performed in order to fully characterise and validate the corresponding stiffness model. Following this, the stiffness model is used to optimise robot stiffness by utilising the redundant degree of freedom around the rotation axis of the tool.

4.1 Introduction

In this chapter, modelling, identification and optimisation of static stiffness of the serial industrial manipulator ABB IRB 6640 205/2.75 based on Virtual Joint Model (VJM) is discussed. The choice of the stiffness modelling technique was primarily based on the simplicity of the model and low computational effort required to estimate manipulator stiffness. However, the VJM is the least accurate static stiffness modelling technique compared to more complicated models such as FEA and MSA.

As discussed in literature, the VJM can be classified into three based on the underlying assumptions;

- Conventional stiffness model [107, 108]
- Conservative Congruence Transformation (CCT) without link flexibility [113–115]
- Conventional stiffness model with link flexibility [120]

In all approaches, the control loop stiffness of actuators is represented with linear torsional springs and the manipulator is assumed to be in equilibrium. Thus, torques at joints as a result of gravitational effects are assumed to be balanced.

In *conventional stiffness model*, the base and links are assumed to be rigid. Stiffness model doesn't take into account the stiffness alteration as a result of configuration change when an external loading applied. Hence, it is the most simplistic stiffness model.

The *Conservative Congruence Transformation without link flexibility* is an extension of conventional stiffness model. Stiffness alteration (as a result of the externally applied static load) is taken into account when estimating manipulator stiffness.

Finally, the *conventional stiffness model with link flexibility* is an extension of conventional stiffness model but additionally considers link compliance which improves the accuracy of model predictions. However, the consideration of link flexibility introduces parameter identifiability issues and could complicate the identification process [120].

In Conservative Congruence Transformation without link flexibility, neglecting 6-DOF flexibility of the link would result in underestimation of stiffness characteristics of the manipulator. Hence, it is an oversimplified stiffness model and suffers from inaccuracies. Nevertheless, it is accurate enough to demonstrate configuration dependent stiffness properties of serial manipulators as per the existing literature. For this reason, Conservative Congruence Transformation (CCT) was chosen to be applied to model stiffness of serial industrial manipulator, ABB IRB 6640 205/2.75. The identification procedure was also chosen to be global method since it is more pragmatic when experimentally identifying the virtual joint compliance parameters than the local method.

The rest of the chapter is organised as follows; the underlying theory for VJM and joint compliance parameter identification is presented in Section 4.2. Preliminary experimental set-up design is outlined in Section 4.3. The factors affecting the joint compliance identification accuracy are identified and discussed in Section 4.4. In Section 4.5, a simulation is designed to quantify joint compliance parameter identification accuracy. The experimental work for kinematic calibration and joint compliance parameter identification are described in Section 4.6. Lastly, Cartesian compliance of the manipulator is optimised by utilising its kinematic and functional redundancies in Section 4.7. The chapter is summarised in Section 4.8 and a summary of the contributions to the knowledge is given in Section 4.9.

4.2 Theory of stiffness modelling with Virtual Joint Model

Virtual Joint Method (VJM) is extension of original Lumped Parameter Model in which links and joints are modelled as rigid bodies. In Virtual Joint Method, however, the assumption of rigid joints is relaxed and flexibility of joints is represented with virtual springs (linear torsional springs). Joint flexibility is assumed to mainly come from the control loop compliance of actuators.

Kinematics of serial industrial manipulators presented in Chapter 3 is based on the Lumped Parameter Model with rigid transformations between reference frames as described in Equations 3.10 and 3.13. Hence, in order to take into account flexibility of joints, the theory need to be modified too. Extending forward kinematics requires consideration of joint flexibility with an additional parameter to reflect the angular deflection of joints around their axis of rotation. The VJM model based on CCT without link flexibility is illustrated schematically in Figure 4.1.

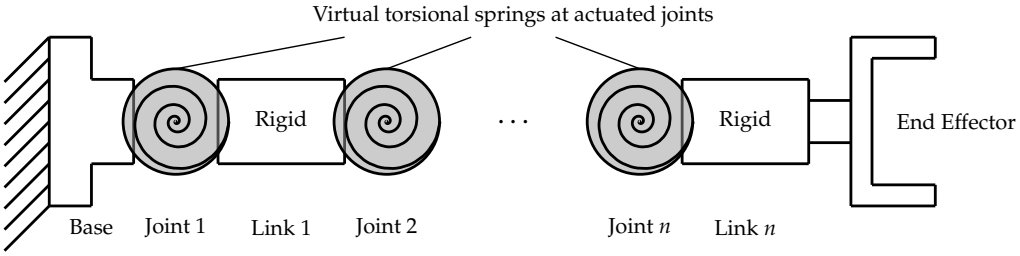

FIGURE 4.1: The Virtual Joint Model of a serial industrial manipulator adapted from [120]

The serial kinematic chain with flexible joints and rigid links is defined under the following assumptions according to [120];

- A rigid link between the manipulator base plate and first actuated joint that is described by a constant homogeneous transformation matrix, ${}^{Base}A_0$
- A number of flexible actuating joints and rigid links described by homogeneous transformation matrices ${}^{i-1}A_i(\theta_i, d_i, a_i, \alpha_i)$ where θ_i corresponds to aggregation of actuated joint variables q_i and virtual joint variables which represent joint deflections q_i^{Ac}; $\theta_i = q_i + q_i^{Ac}$ of the i^{th} joint under consideration
- A rigid link between the end effector and the tool that is described by a constant homogeneous transformation matrix, ${}^{n}A_{TCP}$

Actuated joint variables (joint angles or null encoder readings), q, is aggregated into $q = [q_1, q_2, ..., q_n]^T$. Whereas, virtual joint variables, q_i^{Ac}, is aggregated into $q^{Ac} = [q_1^{Ac}, q_2^{Ac}, ..., q_n^{Ac}]^T$ and represent the angular deflection of each virtual joint under the static external loading. Therefore, the aggregation of joint variables, $\theta = q + q^{Ac}$, would represent the overall joint variable after application of external loading.

The new kinematic chain of the industrial manipulator based on VJM model with flexible joints is expressed in terms of aggregated joint and virtual joint variables, as below;

$$ {}^{Base}A_{TCP} = {}^{Base}A_0 \cdot \left[\prod_{i=1}^{n=6} {}^{i-1}A_i(\theta_i, d_i, a_i, \alpha_i) \right] \cdot {}^{6}A_{TCP} \tag{4.1} $$

Having the new kinematic chain explained, the theory behind static stiffness modelling is then adapted from [120] and explained. Considering a scenario where the serial manipulator is in a quasi-static configuration, deflection of joints under its weight (gravitational forces and torques) is assumed to be compensated through the controller. Thus, the manipulator structure can be said to be in equilibrium. Then, the relationship between external torques at joints and their corresponding angular deflections can be represented with Hooke's law in joint space;

$$\delta\tau = K_\theta \cdot \delta\theta \tag{4.2}$$

where τ is the aggregated vector of virtual torques at each joints, $\tau = [\tau_1, \tau_2, ..., \tau_n]^T$ and the K_θ represents the joint stiffness matrix consisting of the control loop stiffness parameters (virtual joint stiffness) of each joint across its diagonal as,

$$K_\theta = \begin{bmatrix} K_{\theta,1} & 0 & 0 & 0 & 0 & 0 \\ 0 & K_{\theta,2} & 0 & 0 & 0 & 0 \\ 0 & 0 & K_{\theta,3} & 0 & 0 & 0 \\ 0 & 0 & 0 & K_{\theta,4} & 0 & 0 \\ 0 & 0 & 0 & 0 & K_{\theta,5} & 0 \\ 0 & 0 & 0 & 0 & 0 & K_{\theta,6} \end{bmatrix} \tag{4.3}$$

In static condition, applying the principle of virtual work, the sum of the work done in joint space, E_q, under the application of external wrench, w, is,

$$E_w = w^T J(\theta)\theta \tag{4.4}$$

On the other hand, the virtual work done by the actuator to balance the work done by the external wrench, E_b, is,

$$E_b = \tau^T\theta \tag{4.5}$$

Thus, in an equilibrium, the work done by external wrench is equal to the work done by the actuator to balance external disturbance. Hence,

$$w^T J(\theta)\theta = \tau^T\theta \tag{4.6}$$

This yields the following relationship in quasi-static equilibrium conditions,

$$\tau = J(\theta)^T w \tag{4.7}$$

as directly relatable to Equation 3.18. Similarly, application of the wrench, w, tends to result in translational and angular displacement at the TCP. The relationship between infinitesimal translational and angular displacement at the TCP and wrench is defined by the manipulator (Cartesian) stiffness matrix, K_c, as,

$$\delta w = K_c \delta X \tag{4.8}$$

Taking partial differentiation of Equation 4.7 with respect to aggregated joint variables θ, the following relationship is obtained,

$$\frac{\delta\tau}{\delta\theta} = \frac{\delta J(\theta)^T}{\delta\theta} w + J(\theta)^T \frac{\delta w}{\delta X}\frac{\delta X}{\delta\theta} \tag{4.9}$$

Substituting Equations 3.15, 4.2 and 4.8 into Equation 4.9 yields the following relationship,

$$K_\theta = \frac{\delta J(\theta)^T}{\delta \theta} w + J(\theta)^T K_c J(\theta) \tag{4.10}$$

The relationship derived in Equation 4.10 is called Conservative Congruence Transformation (CCT). When there is no externally applied wrench, the wrench vector w is equal to zero and the above equation is simplified to conventional stiffness relationship which is the active stiffness control formulation [114],

$$K_\theta = J(\theta)^T K_c J(\theta) \tag{4.11}$$

This could also be the case if a robot manipulator has a configuration independent Jacobian such as for Cartesian gantry robots [113]. However, if an external wrench is applied, the manipulator Jacobian matrix changes due to configuration alteration as a result of the manipulator deflection. The associated term representing changing stiffness of the manipulator due to altered manipulator configuration as per deflection of the end effector is called *Complementary stiffness matrix*, K_f. Complementary stiffness matrix is defined as follows;

$$K_f = \frac{\delta J(\theta)^T}{\delta \theta} w \tag{4.12}$$

Equation 4.10 can be rearranged to give Cartesian stiffness matrix of the manipulator,

$$K_c = J(\theta)^{-T} \big(K_\theta - K_f\big) J(\theta)^{-1} \tag{4.13}$$

Substituting Equation 4.8 into Equation 4.13 enables estimation and identification of the desired joint stiffness matrix by application of a wrench vector and measuring the TCP translational and angular deflections, δX, as;

$$w = J(\theta)^{-T} \big(K_\theta - K_f\big) J(\theta)^{-1} \delta X \tag{4.14}$$

Comparing the Conservative Congruence Transformation (CCT) in Equation 4.10 with conventional stiffness model in Equation 4.11, it is obvious that Complementary stiffness matrix requires additional steps to be carried out but ensures symmetric mapping between the joint and operational spaces. Hence, Conservative Congruence Transformation is a more accurate representation of stiffness mapping between the joint and operational space of the manipulator, compared to conventional stiffness model.

For experimental identification of the manipulator joint stiffness matrix, K_θ, Equation 4.14 is solved for a known wrench and measured manipulator deflections for a given manipulator configuration. However, the presence of Complementary stiffness matrix makes it difficult to evaluate Equation 4.14 due to the fact that it requires computation of derivative of Jacobian matrix with respect to changing aggregation of joint variables. Therefore, a more pragmatic way of approaching this problem is established by searching manipulator configurations where Complementary stiffness matrix is so small that it could be neglected from Equation 4.14. This reduces the stiffness model based on Conservative Congruence Transformation to conventional stiffness model at selective configurations for identification of the joint stiffness matrix.

For a given wrench, a negligible Complementary stiffness matrix occurs when manipulator configurations result in a negligible change in the Jacobian matrix which is analogous to

manipulator non-singular configurations. In other words, the effect of Complementary stiffness matrix on Cartesian stiffness matrix is larger when the manipulator is at singular configurations as proven in [115]. Hence, the Kinetostatic Performance Index (KCI) can be utilised to find out non-singular manipulator configurations by using Equation 3.24 to minimise Complementary stiffness matrix. Under these conditions, Conservative Congruence Transformation model is reduced to manipulator conventional stiffness model as in Equation 4.11. In this sense, Equation 4.14 is simplified to the following,

$$w = J(\theta)^{-T} K_\theta J(\theta)^{-1} \delta X = K_c \delta X \tag{4.15}$$

Rearranging above equation for easier computation without taking inverse of the Jacobian matrix gives,

$$\delta X = J(\theta) C_\theta J(\theta)^T w = C_c w \tag{4.16}$$

where $C_\theta = K_\theta^{-1}$ represents joint compliance matrix (control loop compliance of each joint) and C_c is Cartesian compliance. Equation 4.16 can also be represented as,

$$\begin{bmatrix} \delta x \\ \delta y \\ \delta z \\ \delta \alpha \\ \delta \beta \\ \delta \gamma \end{bmatrix} = \begin{bmatrix} c_{xx} & c_{xy} & c_{xz} & c_{x\alpha} & c_{x\beta} & c_{x\gamma} \\ c_{yx} & c_{yy} & c_{yz} & c_{y\alpha} & c_{y\beta} & c_{y\gamma} \\ c_{zx} & c_{zy} & c_{zz} & c_{z\alpha} & c_{z\beta} & c_{z\gamma} \\ c_{\alpha x} & c_{\alpha y} & c_{\alpha z} & c_{\alpha\alpha} & c_{\alpha\beta} & c_{\alpha\gamma} \\ c_{\beta x} & c_{\beta y} & c_{\beta z} & c_{\beta\alpha} & c_{\beta\beta} & c_{\beta\gamma} \\ c_{\gamma x} & c_{\gamma y} & c_{\gamma z} & c_{\gamma\alpha} & c_{\gamma\beta} & c_{\gamma\gamma} \end{bmatrix} \begin{bmatrix} F_x \\ F_y \\ F_z \\ M_x \\ M_y \\ M_z \end{bmatrix} \tag{4.17}$$

Rewriting joint stiffness and compliance matrices into six dimensional vectors yields,

$$^V K_\theta = \begin{bmatrix} K_{\theta,1} \\ K_{\theta,2} \\ K_{\theta,3} \\ K_{\theta,4} \\ K_{\theta,5} \\ K_{\theta,6} \end{bmatrix} \quad \& \quad ^V C_\theta = \begin{bmatrix} C_{\theta,1} \\ C_{\theta,2} \\ C_{\theta,3} \\ C_{\theta,4} \\ C_{\theta,5} \\ C_{\theta,6} \end{bmatrix} \tag{4.18}$$

Then, Equation 4.16 can be represented in a more compact way as,

$$\delta X = \begin{bmatrix} \sum_{j=1}^{n} \left(^V C_{\theta,j} \cdot J^{1j} \sum_{i=1}^{n} J^{ij} \cdot w_i \right) \\ \sum_{j=1}^{n} \left(^V C_{\theta,j} \cdot J^{2j} \sum_{i=1}^{n} J^{ij} \cdot w_i \right) \\ \sum_{j=1}^{n} \left(^V C_{\theta,j} \cdot J^{3j} \sum_{i=1}^{n} J^{ij} \cdot w_i \right) \\ \sum_{j=1}^{n} \left(^V C_{\theta,j} \cdot J^{4j} \sum_{i=1}^{n} J^{ij} \cdot w_i \right) \\ \sum_{j=1}^{n} \left(^V C_{\theta,j} \cdot J^{5j} \sum_{i=1}^{n} J^{ij} \cdot w_i \right) \\ \sum_{j=1}^{n} \left(^V C_{\theta,j} \cdot J^{6j} \sum_{i=1}^{n} J^{ij} \cdot w_i \right) \end{bmatrix} = \begin{bmatrix} \delta x \\ \delta y \\ \delta z \\ \delta \alpha \\ \delta \beta \\ \delta \gamma \end{bmatrix} \tag{4.19}$$

where the integer i represents the row and j represents the column of the corresponding matrix. Joint compliance terms within Equation 4.19 can be factorised to give the following relationship,

$$\delta X = \Phi \cdot ^V C_\theta \tag{4.20}$$

where Φ is called observation matrix as in [115]. The expansion of observation matrix, Φ is as below,

$$\Phi = \begin{bmatrix} J^{11}\sum_{i=1}^{n=6} J^{i1}w^i & J^{12}\sum_{i=1}^{n=6} J^{i2}w^i & J^{13}\sum_{i=1}^{n=6} J^{i3}w^i & J^{14}\sum_{i=1}^{n=6} J^{i4}w^i & J^{15}\sum_{i=1}^{n=6} J^{i5}w^i & J^{16}\sum_{i=1}^{n=6} J^{i6}w^i \\ J^{21}\sum_{i=1}^{n=6} J^{i1}w^i & J^{22}\sum_{i=1}^{n=6} J^{i2}w^i & J^{23}\sum_{i=1}^{n=6} J^{i3}w^i & J^{24}\sum_{i=1}^{n=6} J^{i4}w^i & J^{25}\sum_{i=1}^{n=6} J^{i5}w^i & J^{26}\sum_{i=1}^{n=6} J^{i6}w^i \\ J^{31}\sum_{i=1}^{n=6} J^{i1}w^i & J^{32}\sum_{i=1}^{n=6} J^{i2}w^i & J^{33}\sum_{i=1}^{n=6} J^{i3}w^i & J^{34}\sum_{i=1}^{n=6} J^{i4}w^i & J^{35}\sum_{i=1}^{n=6} J^{i5}w^i & J^{36}\sum_{i=1}^{n=6} J^{i6}w^i \\ J^{41}\sum_{i=1}^{n=6} J^{i1}w^i & J^{42}\sum_{i=1}^{n=6} J^{i2}w^i & J^{43}\sum_{i=1}^{n=6} J^{i3}w^i & J^{44}\sum_{i=1}^{n=6} J^{i4}w^i & J^{45}\sum_{i=1}^{n=6} J^{i5}w^i & J^{46}\sum_{i=1}^{n=6} J^{i6}w^i \\ J^{51}\sum_{i=1}^{n=6} J^{i1}w^i & J^{52}\sum_{i=1}^{n=6} J^{i2}w^i & J^{53}\sum_{i=1}^{n=6} J^{i3}w^i & J^{54}\sum_{i=1}^{n=6} J^{i4}w^i & J^{55}\sum_{i=1}^{n=6} J^{i5}w^i & J^{56}\sum_{i=1}^{n=6} J^{i6}w^i \\ J^{61}\sum_{i=1}^{n=6} J^{i1}w^i & J^{62}\sum_{i=1}^{n=6} J^{i2}w^i & J^{63}\sum_{i=1}^{n=6} J^{i3}w^i & J^{64}\sum_{i=1}^{n=6} J^{i4}w^i & J^{65}\sum_{i=1}^{n=6} J^{i5}w^i & J^{66}\sum_{i=1}^{n=6} J^{i6}w^i \end{bmatrix} \tag{4.21}$$

Observation matrix, Φ, relates end effector deflections to unknown joint compliance parameters under external wrench applied to the manipulator. It should be noted that Equations 4.19 and 4.20 can be solved to give the joint compliance parameters for a single test (wrench application) on a single configuration of a 6-axis manipulator. For this particular case, the deflection vector, δX, becomes (6×1) whereas the observation matrix is (6×6).

However, for elastostatic parameter calibration or joint compliance (or stiffness) identification purposes, several manipulator configurations as well as a number of loading tests on a single configuration are usually considered. The main purpose of this is to minimise measurement noise induced to Equation 4.20. Measurement noise can be attributed to mostly come from the TCP deflection measurements taken by laser tracker, inaccuracy of the applied load and imperfect manipulator kinematic model. For this reason, the system of equations are created by stacking Equation 4.20 for each test (single wrench applied to a particular manipulator configuration) together creating an overdetermined system. Assuming n_c to be the number of configurations and n_w to be the number of wrench applied to each manipulator configuration, then the displacement vector, δX becomes $(nn_cn_w \times 1)$ whereas the observation matrix, Φ, becomes $(nn_cn_w \times 6)$. This creates an overdetermined system for $(n \times 1)$ joint compliance matrix, ${}^{V}C_\theta$ as there are more than n number of equations to solve for n joint compliance parameters. As observation matrix Φ, is not a square matrix any more, it can not be inverted straight away to find joint compliance parameters thus a minimisation technique needs to be applied.

According to [113, 115], the values of joint compliance parameters that minimise the error within Equation 4.20 can be computed by,

$$ {}^{V}C_\theta = \Phi^{-1} \cdot \delta X = \Phi^{I} \cdot \delta X \tag{4.22}$$

where Φ^I is left Moore-Penrose generalised inverse of the observation matrix. However, since Equation 4.20 is an ordinary overdetermined system for a number of tests implemented, joint compliance parameters could also be found by well-established regression analysis. Thus, relying on the assumption that joint compliance parameters are constant values, linear least-square method was applied to solve the overdetermined system instead of utilising left Moore-Penrose generalised inverse of the observation matrix. Either way,

no matter which approach is utilised, both deliver the same joint compliance parameters that minimise error in the overdetermined system of equations.

All in all, above formulations constitute the manipulator stiffness model and joint compliance parameter identification procedure for a serial manipulator. The stiffness modelling takes into account the manipulator end effector movement by application of an external force (Complementary stiffness matrix). Joint stiffness identification formulations, however, consider minimisation of the Complementary stiffness matrix to simplify the overdetermined problem and ease identification. In the next section, a preliminary experimental set-up design of joint compliance parameter identification is outlined. It also serves as the backbone of the simulation implemented to quantify the identification accuracy of joint compliance parameters.

4.3 Preliminary experimental design

Having defined the theory, the main focus was experimental identification of joint compliance parameters of ABB IRB 6640 205/2.75. The manipulator loading and deflection measurement strategies and techniques in the existing literature were examined to draft a preliminary experimental design. In this respect, the preliminary experimental design was concluded to combine the loading methodologies used in [110, 120] while deflection measurements to be taken by a laser tracker. Figures 4.2 and 4.3 schematically illustrate the preliminary experimental design.

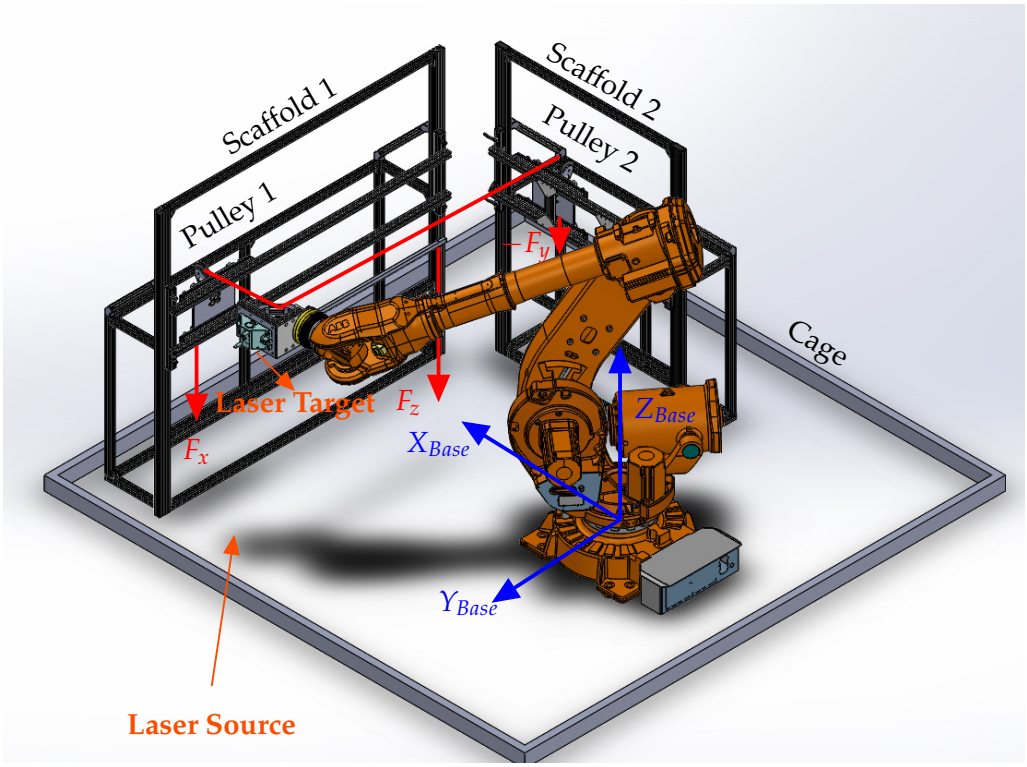

FIGURE 4.2: The preliminary experimental design in *Solidworks*^{TM}

Two scaffolds were aimed to be used for applying static forces aligned with *Base frame* as in [110]. Similarly, an *end effector device* would be designed to be attached onto the end effector (as depicted in Appendix A). The device would be used to apply a force and torque around the end effector as in [120].

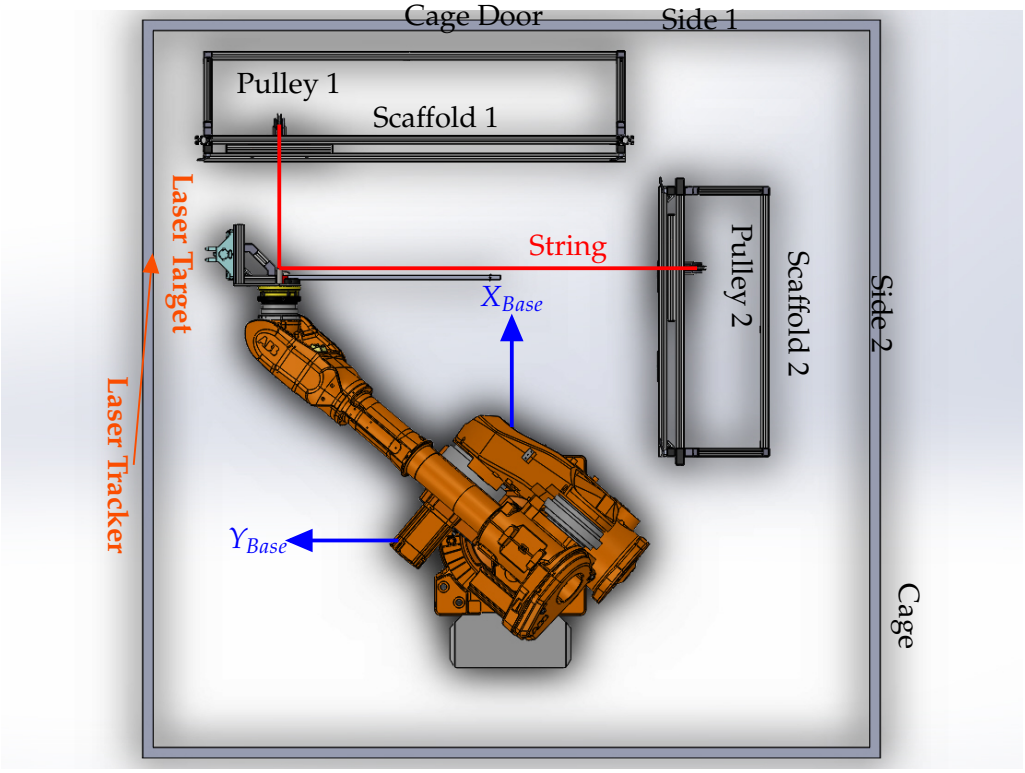

FIGURE 4.3: The top view of the preliminary experimental design in *Solidworks*^{TM}

The forces along positive X_{Base} and negative Y_{Base} would be applied via scaffolds placed within the robot cage with the help of strings, pulleys and dead weights. One end of the string would be attached to the hook on end effector device and the other end to weight baskets which would be hung via pulleys. The scaffolds would be designed such that the position of pulleys could be adjusted to make sure the force applied to the TCP would be aligned with the *Base Frame*.

End effector device would be designed to allow application of the force along negative Z_{Base} direction and a torque by hanging the dead weights. The applied torque could be a vector, $[M_x, M_y, M_z]$, with end effector orientation defining components of the torque with respect to *Base Frame*.

The end effector deflection would be measured with an industrial laser tracker, Leica AT401, which is able to measure position and orientation of an object with the help of a special device (laser target) called T-Mac (Tracker-Machine control sensor). T-Mac is 6 DOF tracking device and would be attached onto the end effector device to track and measure the TCP pose based on the *Base Frame*.

4.4 Factors affecting the joint compliance identification accuracy

Factors affecting the identification accuracy of joint compliance parameters to be experimentally identified are listed as below.

- Manipulator geometric model: Nominal DH parameters as in Table 3.1 do not represent the actual geometric model of ABB IRB 6640 205/2.75 in practice. The modelled and actual pose of TCP does not match for a given set of joint variables. This, in turn, affects the identification accuracy as the geometric model is fundamentally crucial in computing Jacobian matrix which appears in observation matrix as in Equation 4.21.
- Joint variables: Defining manipulator configurations in operational space results in joint variables (irrational number) that need to be truncated to be applied in practice. Truncation of joint variables imposes inaccuracies in the modelled and actual TCP pose and hence, on the Jacobian matrix which is a crucial parameter for joint compliance identification.
- Laser tracker sensitivity: The laser tracker sensitivity plays an important role in the accuracy of measured deflections and hence, joint compliance parameters. The laser tracker absolute distance and angular sensitivity are $\pm 10 \mu m$ and $\pm 15 \pm 6 \mu m/m$ respectively [208].
- Uncertainty in applied loading: The inaccuracy of weights, the misalignment of strings with the *Base Frame*, the string not being inextensible and the friction on pulleys are the main factors causing uncertainties in applied loading. Such uncertainties in the applied loading could easily affect the accuracy of joint compliance parameters.
- Complementary stiffness matrix: In order for CCT to be equivalent to conventional stiffness model, manipulator configurations need to be found out where Complementary stiffness matrix is negligible. The lower the condition number based on Frobenius norm (or higher the KCI), the smaller Complementary stiffness matrix is. In this way, inaccuracies coming from the reduction of CCT to conventional stiffness modelling can be reduced.
- Manipulator configuration: The more flexible the manipulator configuration is, the less noise to deflection ratio is obtained. Similarly, the more manipulator configurations are considered, the larger the observation matrix is and hence, better the identification accuracy gets. However, higher number of manipulator configuration comes with a compromise which is experiment duration. Therefore, a sweet point needs to be found that assures the accuracy of joint compliance parameters while ensuring pragmatic experiment duration.
- Loading: The direction and magnitude of applied loading plays an important role. Additionally, the loading procedure and number of loading applied to each manipulator configuration are also known to enhance the identification accuracy.

These factors were addressed in the numerical simulation and experiment to minimise their effect on the accuracy of joint compliance parameter identification.

4.5 Joint compliance identification - simulation

4.5.1 Introduction

A numerical simulation was designed to replicate the preliminary experimental design. The intention was to quantify the accuracy of joint compliance parameters that would be experimentally identified. The aim of the simulation was to analyse factors affecting the joint compliance parameter identification and optimise procedures to be implemented experimentally for enhanced identification accuracy.

The following parameters were analysed in the simulation;

- Loading procedure
- Choice of the manipulator configurations
- Number of manipulator configurations
- Number of loading to be applied at each manipulator configuration

Theoretical end effector deflections (translational and angular) under the applied theoretical loading were simulated as per Equation 4.16 with initially defined theoretical joint compliance parameters. The simulated deflection and loading were then used to identify the initially defined theoretical joint compliance parameters with Equation 4.22. In theory, for a system of equations unaffected from any experimental inaccuracies and uncertainties, identified joint compliance parameters are the same as the initially defined theoretical joint compliance parameters. However, inaccuracies coming form various sources (which are discussed in Section 4.4) influences the system of equations in practice. Therefore, the simulation was used to imitate inaccuracies and uncertainties arising from various sources in a virtual environment and to optimise the accuracy of joint compliance parameters of ABB IRB 6640 205/2.75, which are aimed to be identified in the experiment.

Note that, since there was no exemplary joint stiffness parameters found in literature for ABB IRB 6640 205/2.75, the joint stiffness parameters of ABB IRB 6660 as in [209] were used in the simulation.

4.5.2 Mitigating the factors affecting the joint compliance identification accuracy

The factors affecting the accuracy of the joint compliance parameter identification in Section 4.4 were mitigated by the following strategies;

- Manipulator geometric model: The manipulator geometric model would be calibrated numerically by experimentally measured TCP poses to mitigate inaccuracies coming from the nominal geometric model.
- Joint variables: Integer joint variables would be defined in joint space to mitigate associated truncation errors.
- Laser tracker sensitivity: The sensitivity of the laser tracker is the most limiting factor due to its comparable size to robot deflection. For this reason, measurement noise would be assumed to be normally distributed with zero mean and standard deviation being 10 times the laser tracker sensitivity ($\pm 100 \mu m$ in absolute distance and angular accuracy) in the simulation. This is to consider the laser tracker's

sensitivity dependency to remoteness of TCP pose and vibrations from nearby machines.

- Uncertainty in applied loading: Loads to be applied would be measured by a highly sensitive balance and applied with respect to *Base Frame* by aligning scaffolds using robot movements. Nevertheless, there could still be slight inaccuracies due to misalignment of loading with *Base Frame*. For this reason, the uncertainty in applied loading would be assumed to be normally distributed with zero mean and standard deviation of $\sqrt{5}$ N in the simulation.
- Complementary stiffness matrix: In the simulation, the condition number based on Frobenius norm was set to 10. This is to minimise the effect of Complementary stiffness matrix on the joint compliance parameter identification for filtered manipulator configurations.
- Manipulator configuration: The effect of the number and choice of manipulator configurations on the accuracy of joint compliance parameter identification would be investigated in Section 4.5.5 in the simulation.
- Loading: Given the fact that the loading direction was constrained with the set-up, a maximum weight of 80 kg would be applied with dead weights. This is for the sake of not exceeding the torque limitations of actuators in practice. The effect of loading procedure and the number of loading applied to each manipulator configuration on the joint compliance parameter identification would be investigated in Section 4.5.5.

Note that the robot TCP was configured to a restricted work volume to make sure the TMAC visibility by the laser tracker and application of loads with scaffolds. The constrained work volume was between the following diagonal corners of the rectangular prism: (0.8,1.3,1), (1.1,0,1.5).

4.5.3 Description of the simulation

The simulation procedure implemented in $Matlab^{TM}$ environment is described below;

1. Selection of the manipulator configurations based on user defined joint variables and computation of TCP pose by forward kinematics.
2. Refinement of the manipulator configurations based on constraints such as; TMAC visibility to the laser tracker and scaffold work volume restrictions.
3. Computation of the Jacobian (Equation 3.15), Cartesian compliance matrix and the condition number based on Frobenius norm (Equation 3.21) to make sure the Complementary stiffness matrix (Equation 4.12) is small enough to be neglected.
4. Computation of the wrench vector with respect to the *Base Frame* based on TCP orientation for the considered loading procedure.
5. Computation of the theoretical TCP deflection for each loading (application of the wrench vector) at each manipulator configuration (Equation 4.16).
6. Incorporation of inaccuracies coming from laser tracker and loading. Inaccuracies were added to theoretically computed TCP deflections and theoretical wrench vector.
7. Computation of the observation matrix (Equation 4.21) and then, identification of the initially defined joint compliance parameters from noisy data.

8. Repetition of steps 6-7 for statistical analysis with different normally distributed noise applied to theoretical TCP deflections and wrench vectors.
9. Computation of the identification accuracy.

The flow chart explaining the simulation is shown in Figure 4.4;

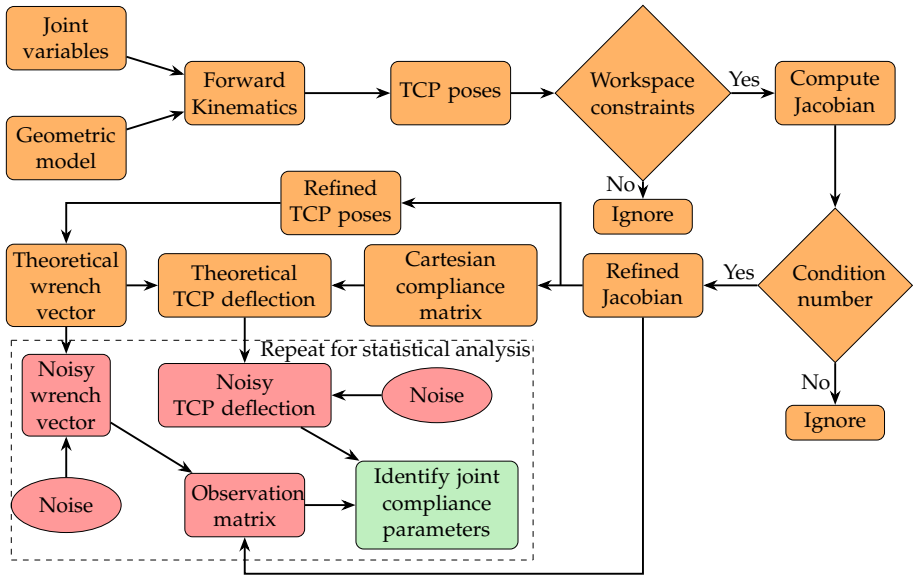

FIGURE 4.4: The simulation flow chart. Colours represent: Orange → Generation of fictitious data, Pink → Noisy data and Green → Post-processing to identify joint compliance parameters

4.5.4 Statistical analysis

The factors defined in Section 4.4 affect the identification accuracy in dissimilar magnitudes. For this reason, with the aim of quantifying the variation in identified joint compliance parameters, the simulation was repeated 500 times. Every time the simulation was repeated, a new random set of noise from the normal distribution was applied to theoretical TCP deflections and wrench vectors while keeping rest of simulation parameters same. The simulation was repeated for 500 times, the mean of identified joint compliance parameters and their standard deviation were found out and recorded.

Having assumed measurement noise from the laser tracker and applied loading to be normally distributed, identified joint compliance parameters were also assumed to be normally distributed. Instead of showing every distribution of 500 tests, a scalar parameter that would show the limiting identification accuracy would be more applicable for visualisation of findings. For normal distributions, it is known that the expectation of having values two standard deviation from the mean of distribution account for 95% of the data set. Therefore, Equation 4.23 was used to quantify the maximum percentage error that 95% of identified joint compliance parameters would have with respect to their corresponding theoretical values.

$$Err_{\%} = \max\left(\frac{2\sigma_i^{STD}}{{}^{V}C_{\theta,i}}\right) \times 100 \tag{4.23}$$

where $i = 1, ..., n$ and σ_i^{STD} is the standard deviation of the identified i^{th} joint compliance parameter after repetition. The maximum percentage error among identified joint compliance parameters was accepted as the identification accuracy. The smaller the $Err_{\%}$ is, the more accurate identified joint compliance parameters are.

4.5.5 Parameter selection

Having defined a measure of identification accuracy for joint compliance parameters, $Err_{\%}$, the parameters affecting the identification accuracy were investigated as described in Section 4.5.1. Determining these parameters, however, was not straight forward since there could be infinite possible combinations to consider. For the sake of simplifying the parameter selection and practicality in the experiment, the loading was applied with dead weights of 5 kg increments along all axes with maximum weight to be suspended was limited to 80 kg. This makes 17 unique sets of loading to be applied along each axis in 5 kg resolution. In addition to that, the following loading procedures were considered,

1. Incremental loading: Incrementally loading from 0 kg up to 80 kg.
2. Incremental unloading: Incrementally unloading from 80 kg down to 0 kg.
3. Random loading: Random loading with minimum being 0 kg and maximum 80 kg.

Note that, wrench vectors additionally take into account the weight of the baskets as well as the weight of end effector device together with the TMAC in the simulation.

For the same arbitrarily chosen refined manipulator configurations, the number of manipulator configurations and number of loading to be applied to each configuration were altered for each loading procedure and the identification accuracy, $Err_{\%}$, was computed. The results are depicted as in Figure 4.5.

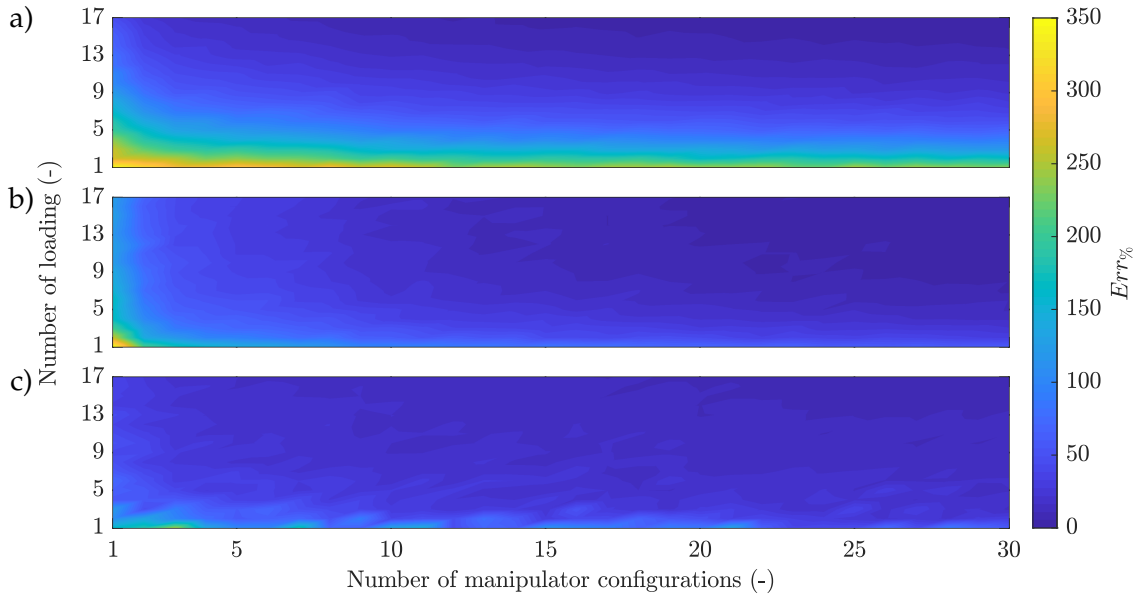

FIGURE 4.5: The effect of the number of loading and manipulator configurations on the identification accuracy for the loading procedures a) Incremental loading b) Incremental unloading c) Random loading

Figure 4.5 depicts that increasing the number of loading applied to each manipulator configuration as well as number of configurations enhanced the identification accuracy, $Err_{\%}$, for all loading procedures. This is due to the fact that, the observation matrix as in Equation 4.21 tends to get larger in size and larger number of equations are established to estimate joint compliance parameters. This, in turn, results in better minimisation of the noise within equations.

Having the maximum weight to be suspended via the end effector device and scaffolds was set to 80 kg (Section 4.4), the number of loading applied to each manipulator configuration was set to 17 (maximum). In this way, the comparison between the loading procedure types was simplified. Thus, the identification accuracy, $Err_{\%}$, with respect to the number of manipulator configurations was compared for each loading procedure and was depicted in Figure 4.6.

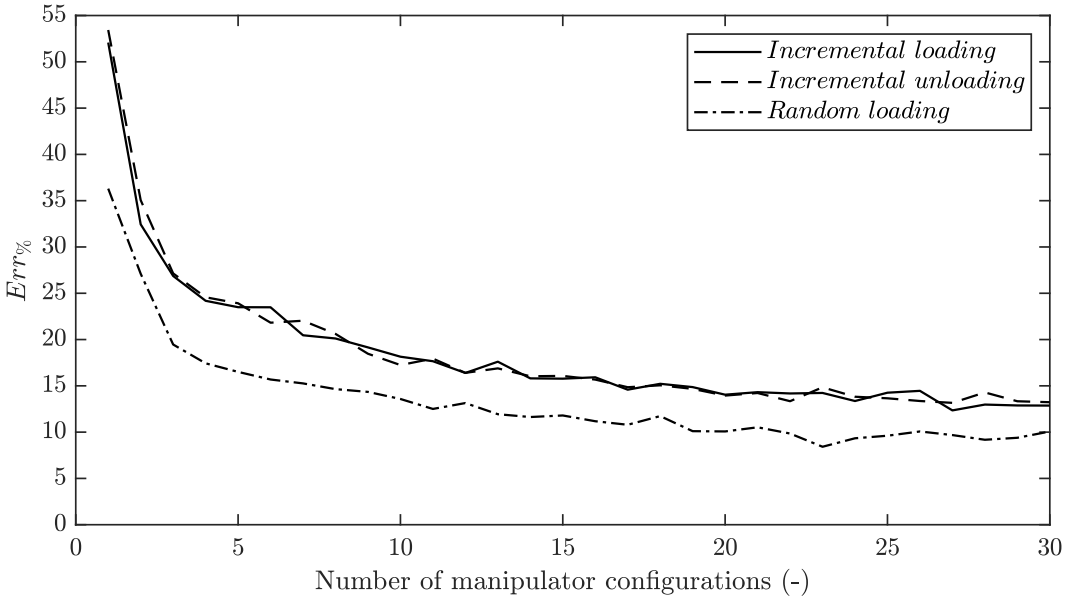

FIGURE 4.6: The identification accuracy with respect to number of manipulator configurations for the considered loading procedures

The results showed that incremental loading and unloading performed almost the same. This is because the order of equations within observation matrix are altered rather than equations themselves, thus the identification accuracy is almost same. The remaining variation in the identification accuracy is due to the slightly dissimilar normally distributed noise. On the other hand, random loading was observed to perform better for any number of manipulator configurations. In incremental loading and unloading, since the weights were loaded or unloaded in 5 kg increments, some of the rows of observation matrix became multiple or a factor of others, hence it represented the same relationship. On the other hand, in random loading, the rows of observation matrix became dissimilar from each other and a better minimisation of error through least-squares was achieved. For this reason, the random loading procedure was selected to be used in the experiment.

Application of 17 sets of loading to each manipulator configuration and measuring its deflection could take quite a time in practice. For the sake of establishing a trade of between the identification accuracy and experiment duration, the number of configurations to be

used in the experiment was chosen to be 23. The identification accuracy for 23 manipulator configurations with 17 sets of random loading would be approximately 8.4%. Such an identification accuracy would mean 95% of the identified joint compliance parameters would have a maximum of 8.4% deviation from its mean. The choice of manipulator configurations was observed to have a minor influence on the identification accuracy in the simulation. Hence, they were chosen based on the set of manipulator configurations used within the simulation that resulted 8.4% identification accuracy. The identification procedure was, in fact, limited by measurement noise in the TCP pose measurements by the laser tracker rather than the manipulator configuration itself. This was because of the main factor playing an important role in the identification accuracy was the deflection to noise ratio considering the fact that maximum loading applied along each axis was set to 80 kg. The random loading applied to each configuration is given in Appendix B.

4.5.6 Discussion

Due to the lack of knowledge about the manipulator characteristic length, the Jacobian could not be normalised and hence, the condition number based on Frobenius norm of Jacobian might not represent true kinematic performance of the manipulator. As a result the choice of the manipulator configurations might not have assured minimised Complementary stiffness matrix in the simulation. The main implication of this was the additional inaccuracy introduced to identified joint compliance parameters as a result of the increased unsymmetrical mapping between the joint and operational space of VJM model. This is, of course, correct provided that CCT model truly represents stiffness characteristics of the manipulator. Hence, errors coming from Complementary stiffness matrix were acknowledged. The revision of manipulator configurations revealed later on that, the manipulator was away from singularities. For this reason, errors coming from not minimised Complementary stiffness matrix were expected to be relatively small.

The sensitivity of the laser tracker and inaccuracies coming from applied loading were modelled as normally distributed noise in the simulation for sensitivity analysis and investigation of their effect on the identification accuracy. In practice, however, inaccuracies coming from the laser tracker and loading may not behave as a distribution. For this reason, having assumed that inaccuracies can be characterised by a normal distribution, care needs to be taken while choosing their corresponding standard deviation. In that, a sensible value was chosen to be used in the simulation for deflection and loading standard deviations based on the judgement and considerations made on the experimental set-up and equipments. The chosen standard deviations were estimate rather than exact magnitude of errors in the experiment, hence results should not be regarded as an accurate indicator of the identification accuracy.

All in all, the simulation was designed to quantify the identification accuracy of joint compliance parameters based on analysing factors affecting the identification accuracy and considering the preliminary experimental design. The backbone of simulation is the assumption of rigid links and flexible joints while the joint flexibility being characterised as virtual linear torsional spring that defines VJM. The fact that such an assumption makes VJM an overly simplified stiffness modelling method means the simulation results must be seen as informative rather than indicative.

4.6 Joint compliance identification - experiment

4.6.1 Introduction

In the simulation, the factors affecting the joint compliance identification accuracy were investigated and optimal experimental parameters were determined and used as a guide to plan the experiment. The main aim of the experiment was to identify joint compliance parameters of ABB IRB 6640 205/2.75 to construct a representative stiffness model based on VJM. The objectives of the experiment are listed below.

- Calibrate the kinematic model
- Identify manipulator joint compliance parameters
- Validate the stiffness model based on VJM

The flow chart detailing the main steps for joint compliance parameter identification is illustrated in Figure 4.7. The flow chart can be directly related to Equation 4.22 which describes how the joint compliance parameters are computed.

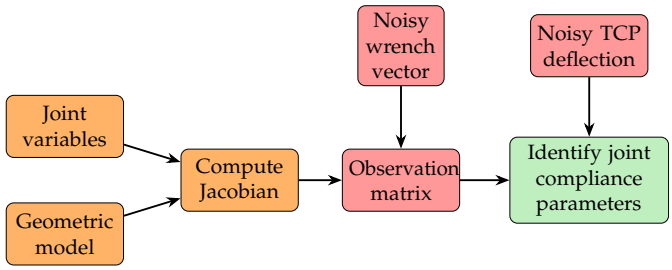

FIGURE 4.7: The flow chart illustrating joint compliance parameter identification

4.6.2 Experimental Set-up

The experimental set-up for joint compliance identification is shown in Figure 4.8.

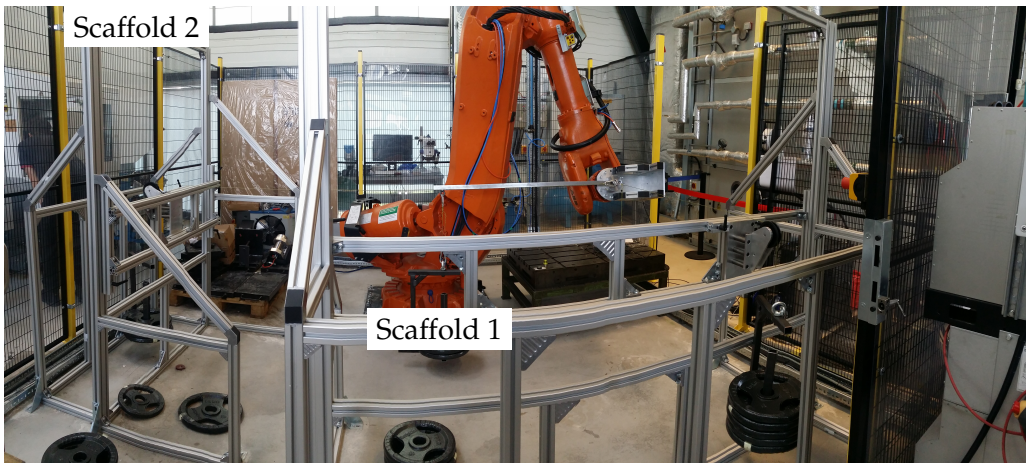

FIGURE 4.8: The experimental set-up for joint compliance identification of ABB IRB 6640 205/2.75

The experimental set-up was consisted of two scaffolds, an end effector device, Leica AT401 laser tracker as well as strings, weights and weight baskets.

The robot cage inner dimensions are approximately 2.4 m in length (from robot base to Side 1 along X_{Base} as in Figure 4.3) and 3.4 m in width (from one side to another along Y_{Base}). Both scaffolds were assembled outside of the robot cage (see Appendix C for the bill of materials of both scaffolds). Scaffold 1 was positioned 100 mm from Side 1 and 1120 mm from Side 2. Scaffold 2 was positioned 700 mm from Side 1 and 480 mm from Side 2. In this way, both scaffolds were installed to concrete floor so that the robot could be configured within the given work volume during joint stiffness identification. Both scaffolds were aligned with *Base Frame* by jogging robot along its *Base Frame* axes and comparing their alignment.

The laser tracker was placed outside of the cage as shown in Figure 4.9. The cage wall was removed to allow undisrupted visibility of reflectors and TMAC by the laser tracker.

VJM requires robot deflections to be measured with respect to *Base Frame*. For this reason, *Base Frame* of the robot was identified by the laser tracker. First, reflectors were placed onto the robot base and their poses were measured by the laser tracker to identify the plane which robot was installed. Then, a reflector was placed on the link between Joint 2 & 3 and Joint 1 was rotated incrementally. Measuring the pose of reflector and fitting a circle would give the direction of Z_{Base}. Similarly, Joint 2 was rotated incrementally after setting joint angle for Joint 1 to 0° and the direction of Y_{Base} was identified. Having directions of Y_{Base} and Z_{Base} identified, direction of X_{Base} was easy to find as it is orthogonal Y_{Base} and Z_{Base}. Lastly, the origin of identified frames were positioned onto the identified plane where the robot was installed to obtain *Base Frame* of the robot, T_{Base}. In that T_{Base} was positioned where Z_{Base} intersected the identified plane.

In order to define the pose of TMAC with respect to *Base Frame*, first robot was configured to the following joint angles $q = [0, 0, 0, 0, 0, 0]^\circ$. Then, the surface of turntable (Joint 6) was measured by placing reflectors and recording their pose with respect to the laser tracker. This defines surface of the end effector of robot. To define the local end effector frame, a reflector was attached onto the turntable and first Joint 6 was rotated incrementally while measuring pose of the reflector. By fitting a circle, the direction of Z_6 was identified. Similarly, having set the joint angle of Joint 6 to 0°, Joint 5 was rotated incrementally and the direction of Y_6 was identified. Similar to the *Base Frame* identification, X_6 was found due to its orthogonality and end effector frame T_6 was positioned on the turntable surface where Z_6 intersected with the turntable surface.

Having the end effector frame defined, the end effector device was installed together with the TMAC onto the robot while keeping the robot at the following joint angles $q = [0, 0, 0, 0, 0, 0]^\circ$. Obtaining a measurement pose from TMAC (6 DOF) enabled identifying the pose of TMAC with respect to the end effector frame T_6. In this way, full kinematics of ABB IRB 6640 205/2.75 could be identified in Section 4.6.3 to minimise inaccuracies coming from the nominal geometric model of robot as well as improve joint stiffness identification accuracy in Section 4.6.4. Due to the fact that Geometric Jacobian defines end effector velocities with respect to *Base Frame*, the laser tracker was set to take all measurements based on *Base Frame*. Additionally, measured robot deflections were modified to reflect deflections at end effector rather than at TMAC by utilising the identified local end effector frame with respect to TMAC measurements.

4.6.3 Kinematic calibration

The manipulator geometric model constructed with nominal DH parameters does not result in the same TCP pose as per the controller of the ABB IRB 6640 205/2.75. The mismatch of the modelled and actual TCP pose means that the geometric model with nominal DH parameters does not represent the actual manipulator geometry. Hence, the inaccurate geometric model could possibly yield inaccuracies in the computed Jacobian matrix during identification of joint compliance parameters. For this reason, the geometric model of the manipulator was aimed to be calibrated to acquire an accurate manipulator kinematics and VJM model. The flow chart highlights the effect of calibrating the geometrical model on the joint compliance parameter identification in Figure 4.9. The red arrows show the propagation of kinematic errors in the identification of joint compliance parameters.

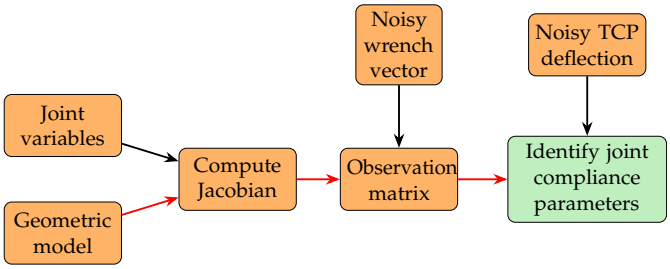

FIGURE 4.9: The flow chart showing the effect of kinematic calibration on the joint compliance parameter identification

In the experiment, six TCP poses were commanded by user defined six sets of joint variables in joint space. The six TCP poses were measured at six different manipulator configurations with the laser tracker with respect to the identified *Base Frame* while the manipulator was unloaded as in Figure 4.10. Then, a multi parameter optimisation tool and population based stochastic search technique, Self Adaptive Differential Evolution (SADE), was used to optimise nominal DH parameters of the manipulator, Table 3.1.

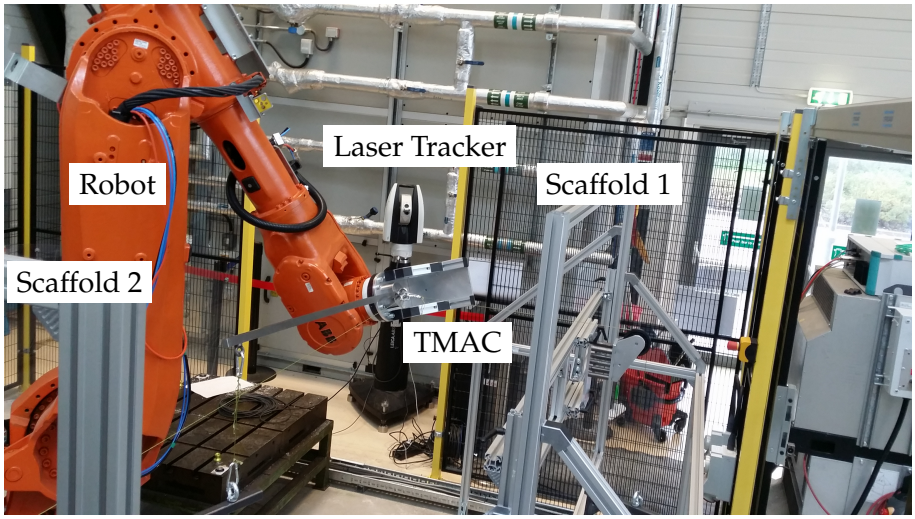

FIGURE 4.10: A snap while taking TCP pose measurements for kinematic model calibration

Accordingly, SADE was applied to calibrate the geometric model and optimise the six nominal DH parameters responsible only for link lengths and offsets of the manipulator. Calibrating only the link lengths and offsets was to make sure that the decoupling of position and orientation of the TCP pose of manipulator kinematics was sustained. Within the six TCP poses, five of them used for calibrating the kinematic model while keeping one for validation purposes. Details of the SADE, cost function, evolution of the parameters being calibrated through a number of generations and configuration are given in the Appendix D.

The calibrated DH parameters of the geometric model of ABB IRB 6640 205/2.75 are given in Table 4.1.

Link (i)	Link Length a_i (m)	Link Twist α_i (°)	Link Offset d_i (m)	Joint Variable q_i (°)
1	0.3242	-90	0.7682	$q_{\theta,1}$
2	1.2844	0	0	$q_{\theta,2}$+$q_{Off,2}$
3	0.1784	-90	0	$q_{\theta,3}$
4	0	-90	1.1454	$q_{\theta,4}$+$q_{Off,4}$
5	0	90	0	$q_{\theta,5}$
6	0	0	0.1996	$q_{\theta,6}$

TABLE 4.1: The calibrated DH parameters of ABB IRB 6640 ABB IRB 6640 205/2.75

Having calibrated the geometric model, forward kinematics of both nominal and calibrated models were computed based on the user defined six sets of joint variables. The modelled TCP poses for both nominal and calibrated models were compared with experimentally measured six TCP poses. Hence, the position and orientation (in terms of RPY angles) errors are shown as in Table 4.2.

Model	TCP Pose	x (mm)	y (mm)	z (mm)	α (°)	β (°)	γ (°)
Nominal	1	22.35	-3.53	-17.30	-0.20	-1.32	0.47
	2	18.24	4.51	-27.29	-2.81	0.68	2.77
	3	5.36	5.84	-31.79	-1.93	0.11	1.40
	4	2.17	4.19	-26.43	-1.08	-0.74	-0.17
	5	5.19	15.36	-26.20	-1.89	0.40	0.71
	6 (Validation)	-1.98	4.56	-28.56	-1.19	-0.39	-0.21
Calibrated	1	-1.07	0.27	0.49	-0.20	-1.32	0.47
	2	0.57	0.17	-2.07	-2.81	0.68	2.77
	3	-0.28	0.21	-2.86	-1.93	0.11	1.40
	4	-2.45	-3.46	2.04	-1.08	-0.74	-0.17
	5	-1.08	3.14	0.92	-1.89	0.40	0.71
	6 (Validation)	-0.84	2.31	2.10	-1.19	-0.39	-0.21

TABLE 4.2: The position and orientation errors of nominal and calibrated kinematic models with respect to the measurements taken with the laser tracker

Note that robot was configured to q=$[110, -40, 46, 44, -88, -120]^\circ$ for validation TCP pose. Results showed that position errors were reduced significantly by calibrating the nominal model with TCP pose measurements taken with the laser tracker. The orientation errors stayed the same due to the fact that the magnitude of link lengths and offsets does not influence the TCP orientation.

4.6.4 Identification of joint compliance parameters

As described in Section 4.5.5, the manipulator was randomly loaded with 17 sets of loading applied to each of 23 manipulator configurations and end effector deflection was measured in order to identify joint compliance parameters. However, during the experiment, only 11 manipulator configurations could have been used for joint compliance parameter identification due to the experimental complications (the joint variables for manipulator configurations are given in Appendix E). This would give 12.5% identification accuracy as seen in Figure 4.6. Based on 11 manipulator configurations, the joint compliance parameters of ABB IRB 6640 205/2.75 were computed and compared with that of ABB IRB 6660 as in Table 4.3.

Joint Compliance Parameters	ABB IRB 6660 [209]	ABB IRB 6640 205/2.75
$C_{\theta,1}$ (rad/Nm) $\times 10^{-6}$	1.00	0.66
$C_{\theta,2}$ (rad/Nm) $\times 10^{-6}$	0.50	0.51
$C_{\theta,3}$ (rad/Nm) $\times 10^{-6}$	0.50	0.48
$C_{\theta,4}$ (rad/Nm) $\times 10^{-5}$	0.22	0.18
$C_{\theta,5}$ (rad/Nm) $\times 10^{-5}$	0.33	0.42
$C_{\theta,6}$ (rad/Nm) $\times 10^{-5}$	0.33	0.20

TABLE 4.3: Experimentally identified joint compliance parameters of ABB IRB 6640 205/2.75 and comparison with that of ABB IRB 6660 [209]

The comparison between the joint compliance parameters of the two manipulators in Table 4.3 depicted that the parameters are at the same order of magnitude. This supports the credibility of simulation implemented to quantify the identification accuracy. In order to assess the performance and validity of identified joint compliance parameters and the manipulator VJM model, a linearity test was implemented in Section 4.6.5. The Figure 4.11 shows the experimental set-up and loading of the manipulator during the experiment.

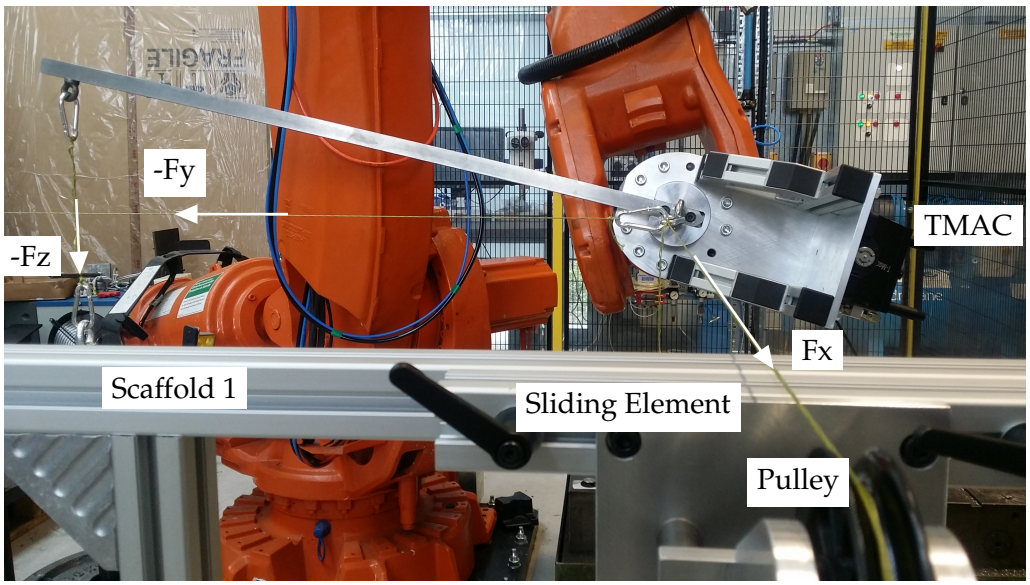

FIGURE 4.11: The application of loading to the end effector device with string and pulleys

4.6.5 The linearity test - VJM model validation

The purpose of linearity test was to validate the identified stiffness model and investigate the linearity of force-deflection relationship at manipulator end effector. This is to justify whether the assumption made on the negligible Complementary stiffness matrix is valid or not. By comparing predicted and measured force-deflection relationship trends, the VJM model and its performance were validated and evaluated respectively. In this sense, the manipulator was loaded incrementally in a single direction at a time at two configurations. The corresponding joint variables of the configurations and their KCI are given in Table 4.4.

Joint Variable (°)	q_1	q_2	q_3	q_4	q_5	q_6	KCI %
Configuration A (CA)	40	5	50	40	-85	-30	56.3
Configuration B (CB)	40	5	60	40	-85	-30	55.4

TABLE 4.4: The manipulator configurations used for the linearity test

The manipulator was incrementally loaded along the positive X_{Base} and $-Y_{Base}$ twice by 5 kg increments up to 100 kg in order to minimise errors due to backlash at joints. Hence, the second loading set was considered for the validation of the VJM model. The laser tracker taking TCP pose measurements from TMAC attached to the end effector device during the experiment is shown in Figure 4.12. The deflection-force relationship obtained from the linearity test for both configurations and loading directions were illustrated as in Figures 4.13 and 4.14.

The gradient of deflection-force relationships obtained from the linearity test gives direct and cross Cartesian compliance parameters. It could be seen that, for the deflection obtained well above sensitivity of the laser tracker, the deflection-loading relationships were fairly linear (Figure 4.13 a, c, f and Figure 4.14 a, c, f). The rest of the deflection-loading relationships, however, showed significant fluctuations which were due to the fact that measured manipulator deflection was in the magnitude of sensitivity of the laser tracker. For this reason, the deflection measured was susceptible to laser tracker measurement errors.

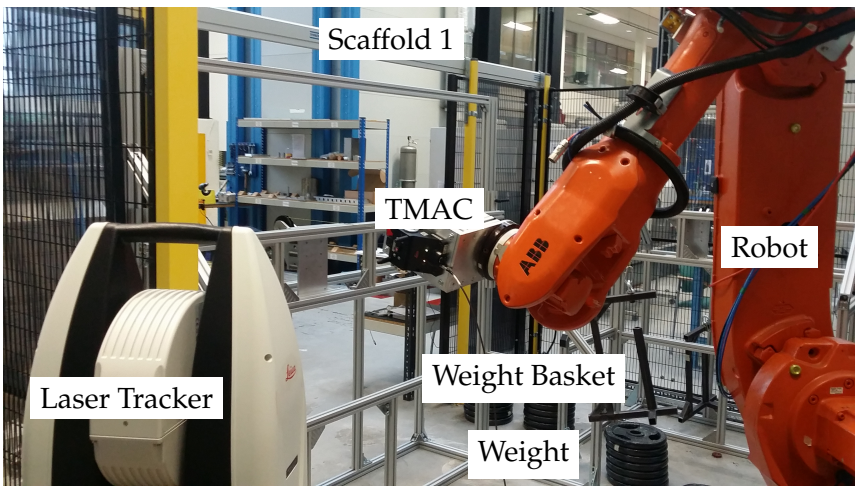

FIGURE 4.12: The laser tracker taking TCP pose measurements of the manipulator

Considering the linearity of deflection-loading relationships (Figure 4.13 a, c, f and Figure 4.14 a, c, f), the manipulator compliance (gradient) could be estimated to be constant for the loading range applied. The linear behaviour of deflection-force relationships imply that manipulator compliance does not significantly change with the applied loading. Hence the effect of changing configuration on manipulator compliance, in other words, Complementary stiffness matrix is negligible. The insignificance of the magnitude of Complementary stiffness matrix has also been reported for serial industrial manipulators in literature such as in [114, 133]. Thus, the validity of reduction of CCT model to conventional stiffness model which was used for the identification of joint compliance parameters was proven. The kinematic performance of the manipulator (KCI) for the given configurations were also shown to be high enough to accept the negligibility of Complementary stiffness matrix as shown in Table 4.4. The work done in literature also supports that the higher the KCI, the smaller and more negligible the effect of Complementary stiffness matrix on Cartesian stiffness as discussed in [115].

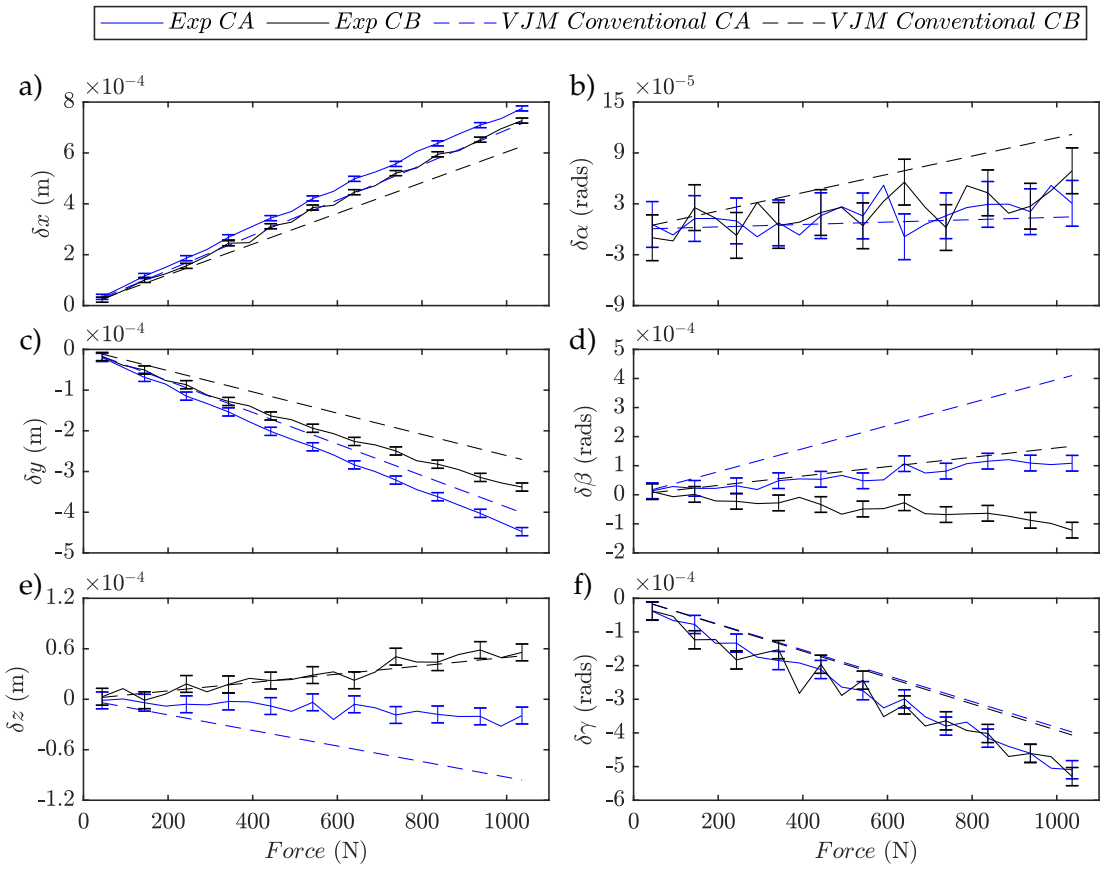

FIGURE 4.13: The force-deflection relationship comparison while loading along positive X_{Base} between the experimental linearity test and the representative VJM conventional compliance model

Having justified the negligible effect of configuration alteration, Cartesian compliance parameters of the manipulator were approximated from measured deflection-loading relationships. This was done by fitting a linear polynomial in least-squares sense and computing its gradient. The same compliance parameters were then modelled with VJM model for the given configurations as in Equation 4.11 and compared in Table 4.5. The

percentage difference of modelled parameters with respect to identified compliance parameters is also shown to give an insight to the performance of the robot compliance model. The deflection-force relationships of manipulator configurations were also modelled based on the VJM conventional compliance model and presented in Figures 4.13 and 4.14 respectively.

Compliance Parameter	VJM Model		Linearity Test		Percentage Difference	
	CA	CB	CA	CB	CA	CB
Loading along positive X_{Base}						
$c_{xx}\ (m/N) \times 10^{-7}$	6.91	6.04	7.49	7.09	-7.82%	-14.74%
$c_{yx}\ (m/N) \times 10^{-7}$	-3.87	-2.61	-4.26	-3.24	-8.99%	-19.45%
$c_{\gamma x}\ (rads/N) \times 10^{-7}$	-3.83	-3.92	-4.72	-4.64	-18.8%	-15.42%
Loading along negative Y_{Base}						
$c_{xy}\ (m/N) \times 10^{-7}$	-3.87	-2.61	-4.03	-3.29	15.07%	15.30%
$c_{yy}\ (m/N) \times 10^{-7}$	13.48	11.87	11.71	10.30	-3.84%	-20.66%
$c_{\gamma y}\ (rads/N) \times 10^{-7}$	13.81	12.90	12.73	10.29	8.51%	25.32%

TABLE 4.5: The comparison of modelled and identified Cartesian compliance parameters

The percentage difference was observed to be mostly negative between Cartesian compliance parameters being predicted and identified through the linearity test. This could be potentially attributed to the oversimplified representation of the manipulator stiffness underestimating Cartesian compliance parameters. However, it shouldn't be forgotten that Cartesian compliance parameters are composed of Jacobian entities and joint compliance entities as in Equations 4.16 and 4.17. Hence, the predicted percentage error for identified joint compliance parameters are cumulative when comparing Cartesian compliance parameters which might be the reason for the relatively large percentage difference.

The effect of large magnitudes of percentage difference on deflection of the manipulator, however, might be insignificant when large forces, as in machining operations, are applied to the structure due to their small magnitude. Thus, the errors between measured and predicted deflection of the manipulator while it was loaded with the maximum weight ($\approx$ 1036 N) were computed in Table 4.6.

Deflection	Error		Error	
	CA	CB	CA	CB
	Loading along $+X_{Base}$		Loading along $-Y_{Base}$	
$\delta x\ (m) \times 10^{-3}$	0.06	0.10	0.04	0.08
$\delta y\ (m) \times 10^{-3}$	-0.05	-0.07	0.19	0.15
$\delta z\ (m) \times 10^{-3}$	0.08	0.00	-0.02	0.01
$\delta\alpha\ (rads) \times 10^{-3}$	0.02	-0.04	-0.22	-0.32
$\delta\beta\ (rads) \times 10^{-3}$	-0.30	-0.29	-0.07	-0.12
$\delta\gamma\ (rads) \times 10^{-3}$	-0.11	-0.12	0.19	0.28

TABLE 4.6: The comparison of measured and modelled deflection of the manipulator while being loaded with maximum weight

The order of magnitude of errors between the measured and predicted deflection in Table 4.6 depicted that VJM model is able to predict the deflection of the manipulator under

a load of approximately 1036 N quite accurately. Bearing in mind that static (or mean) machining forces are not usually as large as 1000 N (except for cutting hard to machine materials such as titanium), errors would be even smaller and less significant compared to the pose accuracy of the manipulator. For this reason, VJM model can be said to be satisfactorily accurate and valid based on the linearity test.

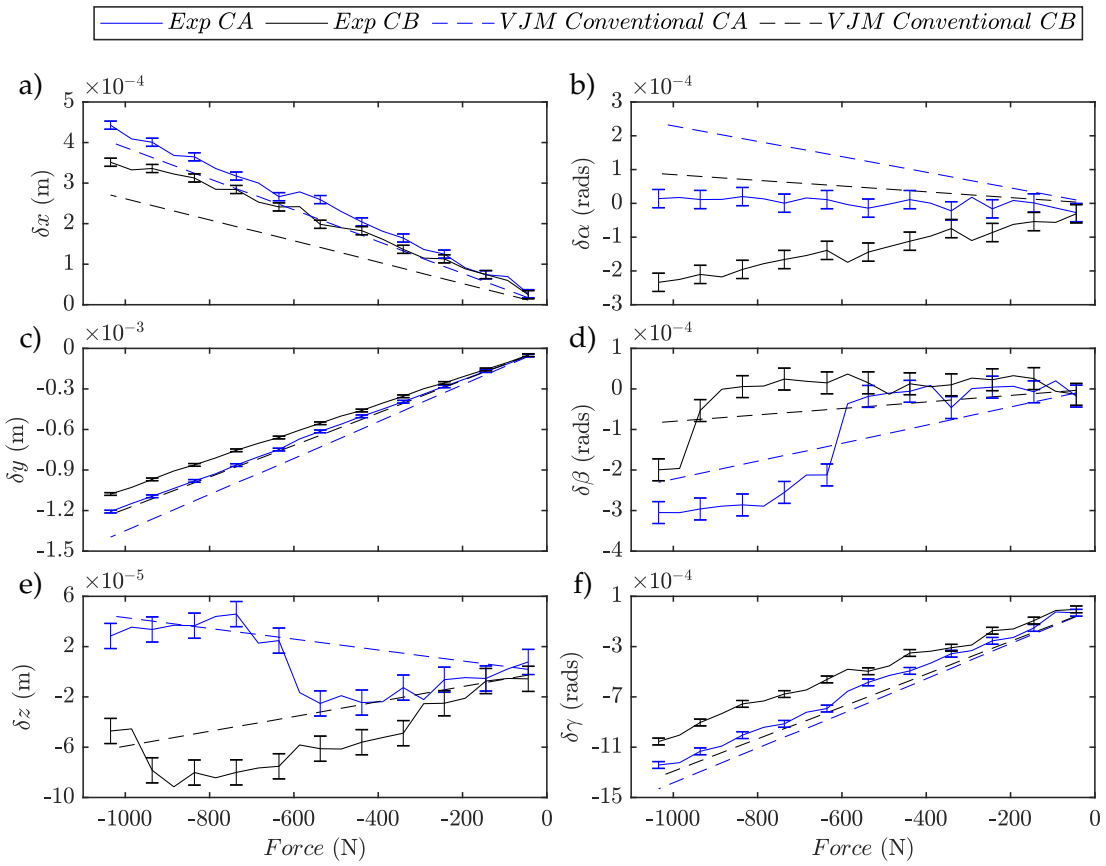

FIGURE 4.14: The force-deflection relationship comparison while loading along $-Y_{Base}$ between the experimental linearity test and the representative VJM conventional compliance model

Note that errors bars for absolute distance was taken to be $\pm 10\mu m$ whereas $\pm 27\mu m$ for angular sensitivity assuming TMAC was positioned approximately 2m from laser tracker.

4.6.6 Discussion

Before identifying joint compliance parameters of the manipulator stiffness model, the manipulator nominal geometric model was calibrated with SADE in order to minimise errors coming from its geometric structure. The optimisation was designed to preserve the decoupling between the position and orientation of the TCP pose. Such an assumption limits the accuracy of calibrated geometric model as the orientation of joints and links might not be perfectly orthogonal or aligned with each other but ensures the computation of closed form inverse kinematics problem. Nevertheless, it is possible to increase the number of parameters being calibrated within the manipulator kinematic model if inverse kinematics was not the point of interest.

Another factor to consider is that, SADE is a numerical optimisation technique and hence, the optimised parameters might not necessarily be the true dimensions of manipulator components in reality. For this reason, as many as possible experimental measurements needed to be fed into the optimisation algorithm for increased credibility of the parameters being optimised. In this case, one could argue that the number of TCP measurements taken for kinematic calibration might not be enough. Considering the fact that DH convention is a simple geometric modelling technique with minimal number of parameters to represent the manipulator architecture, the accuracy of kinematic calibration of such a model is limited. Nevertheless, even though the number of TCP pose measurements might not be enough, a more accurate geometric model was obtained to reduce inaccuracies in the joint compliance identification procedure compared to the nominal dimensions.

While identifying joint compliance parameters and throughout the linearity test, the static weight of the end effector device was not compensated through the robot controller. The uncompensated weight of the end effector device could potentially introduce inaccuracies to identified joint compliance parameters and linearity test. However, revisiting the underlying assumption in VJM stiffness modelling that necessitates the manipulator equilibrium at static conditions, the resultant torques at joints should be zero. Introducing an external loading due to the weight of the end effector device does not violate this assumption since the manipulator would still be in equilibrium (the manipulator does not collapse). The unknown external loading is compensated through static deflection of the structure (including joints) thus, resultant torques at joints become equal to zero. For this reason, the effect of uncompensated weight of the end effector device on VJM stiffness modelling and identification was assumed to be negligible.

Lastly, the joint compliance parameter identification and validation through the linearity test did not cover various manipulator configurations across entire workspace. The end effector device pose had to enable application of loading and measurement of deflection through the laser tracker. For this reason, the accuracy of VJM model might suffer from inaccuracies. This is because the model wasn't taught the parameter space outside of the envelope within which the identification and validation were carried out. The fact that the machining table is located within the work volume where joint compliance parameters were identified however, means that the VJM stiffness modelling can be satisfactorily utilised for form error compensation for robotic milling operations in future. Even though two manipulator configurations were used for the linearity test, the number of loading applied to each configuration at each loading direction gave a substantial amount of test data for successful validation of the stiffness model.

4.7 Cartesian compliance optimisation

4.7.1 Introduction

In machining operations, poor and varying static stiffness of serial industrial manipulators may result in relatively large and configuration dependent form errors even though the stability of the process is ensured. Although online and offline form error compensation techniques are available, manipulator deflections under dynamic cutting forces are large enough to yield poor surface finish and dimensional inaccuracy. Hence, the end-product quality can not meet requirements of the industry. For this reason, accurate modelling of stiffness of serial manipulators is only the part of the solution for the improved compensation of form errors. Besides, controlling manipulator stiffness to acquire as uniform as possible stiffness properties across the cutting trajectory as well as optimising its Cartesian stiffness (or compliance) are possible measures that could be utilised for improved form error compensation.

A uniform manipulator Cartesian stiffness across cutting trajectories has the potential to facilitate the form error compensation by minimising TCP pose alterations required to make up for the deflections. Hence, the effectiveness of compensation algorithms could be enhanced for better dimensional accuracy and surface finish. On the other hand, Cartesian stiffness (or compliance) optimisation has the ability to minimise deflections of the manipulator TCP across the cutting trajectory. In both cases, manipulator configurations could be controlled by utilising the kinematic and functional redundancy of the manipulator around the axis of rotation of the tool.

In this section, the Cartesian compliance optimisation is considered with the aim of minimising the TCP compliance of the VJM model of the ABB IRB 6640 205/2.75. The Cartesian compliance parameters, c_{xx} and c_{yy}, were optimised by utilising the functional and kinematic redundancy of the manipulator around the axis of rotation of the tool to selectively choose the manipulator configurations over the machining table.

4.7.2 Methodology

The proposed methodology for optimising compliance of the manipulator VJM model stands on the employment of the functional and kinematic redundancy of the manipulator. In this respect, the machining table surface having a fixed height of 0.6 m was divided into a mesh of points. The points were set to have a even spacing of 1 cm between each other and the tool orientation was set to be perpendicular to the machining bed surface, Z_{TCP} pointing along negative Z_{Base} direction. Due to the fact that the redundant degree of freedom around Z_{TCP} coincides with the $-Z_{Base}$, the redundancy could be represented by γ based on Roll-Pitch-Yaw convention. Hence, defining the position of the tool TCP and its orientation to be perpendicular to the machining surface yielded a set of 5 DOF poses. The rest of the steps are summarised below,

1. The redundant degree of freedom, γ, was discretised and varied sequentially to create a number of 6 DOF poses between $0 - 2\pi$.
2. For each 6 DOF pose, the manipulator configuration was computed by solving its closed form inverse kinematics.

3. For each manipulator configuration, Jacobian, $J(q)$, the Cartesian compliance matrix, C_c and the Kinetostatic Conditioning Index (KCI) were computed based on Equations 3.15, 4.16 and 3.24 respectively.
4. Based on the choice of compliance parameters within Equation 4.17, manipulator configurations that have an optimum compliance at every 5 DOF TCP pose were found out and assigned for the cutting trajectory.

Consequently, a map of the optimum Cartesian compliance parameter of the manipulator TCP over the surface of the machining table was acquired to investigate the variation of compliance of the manipulator TCP. This summarises the methodology for Cartesian compliance optimisation. The machining table surface was chosen to examine TCP compliance characteristics of the VJM model of ABB IRB 6640 205/2.75, however, the aforementioned methodology could be applied to any TCP cutting trajectory.

The experimentally identified, validated and calibrated VJM model of ABB IRB 6640 205/2.75 was used for Cartesian compliance parameter optimisation. However, the calibrated geometric model of the manipulator in Section 4.6.3 does not include the spindle, tool holder and tool dimensions. For this reason, a dummy tool with the following pose with respect to the last joint was used to represent the spindle, tool holder and the tool;

$$ {}^{6}A_{TCP} = \begin{bmatrix} 0.7071 & 0 & 0.7071 & 0.2 \\ 0 & 1 & 0 & 0 \\ -0.7071 & 0 & 0.7071 & 0.5 \\ 0 & 0 & 0 & 1 \end{bmatrix} \tag{4.24} $$

The tool was assumed to be rigid as per the assumptions of VJM. With the dummy tool installed, the characteristic length of the manipulator was computed with Self Adaptive Differential Algorithm (SADE) according to [196]. The characteristic length was found by normalising the robot structure until globally minimum condition number based on Frobenious norm (Equation 3.21) was obtained. Hence, together with the dummy tool, the characteristic length of ABB IRB 6640 205/2.75 was found out to be 0.6216 m.

For a milling operation, cutting through a straight trajectory along X_{Base} and Y_{Base} axes with tool oriented perpendicular to the machining table surface, the cutting forces on the tool along X_{Base} and Y_{Base} are usually larger than the axial forces whereas torques are usually negligible [200]. In addition to that, the direct compliance parameters of the manipulator are known to be larger than the cross-compliance parameters as in Table 4.5. Hence, the described methodology was followed to optimise the direct compliance parameters c_{xx} and c_{yy} Cartesian compliance parameters of VJM model of ABB IRB 6640 205/2.75 over the machining table.

The Cartesian compliance parameters, c_{xx} and c_{yy}, are expressed in the following form when Equation 4.16 is expanded.

$$ c_{xx} = J_{11}^2 C_{\theta,1} + J_{12}^2 C_{\theta,2} + J_{13}^2 C_{\theta,3} + J_{14}^2 C_{\theta,4} + J_{15}^2 C_{\theta,5} + J_{16}^2 C_{\theta,6} \tag{4.25a} $$

$$ c_{yy} = J_{21}^2 C_{\theta,1} + J_{22}^2 C_{\theta,2} + J_{23}^2 C_{\theta,3} + J_{24}^2 C_{\theta,4} + J_{25}^2 C_{\theta,5} + J_{26}^2 C_{\theta,6} \tag{4.25b} $$

Equations 4.25a and 4.25b clearly depict that each Cartesian compliance parameter is composed of joint compliance parameters and Jacobian matrix entities. Each Jacobian entity, whose magnitude is determined by the manipulator configuration, defines the associated

contribution of the joint compliance parameter to Cartesian compliance parameter, c_{xx} and c_{yy}. The Jacobian entities, hence, can be visualised as the fraction of the effect of joint compliance on Cartesian compliance parameter. Each corresponding fraction associated with the joint compliance parameter can be monitored to develop deeper understanding on the behaviour of manipulator TCP compliance over the machining table surface.

4.7.3 Cartesian compliance parameter optimisation - c_{xx}

The Cartesian compliance parameter c_{xx} is responsible for TCP deflections along X_{Base} for cutting forces applied along X_{Base} only. First, c_{xx} was maximised and the corresponding KCI was computed in order to investigate its behaviour over the machining table as illustrated in Figure 4.15.

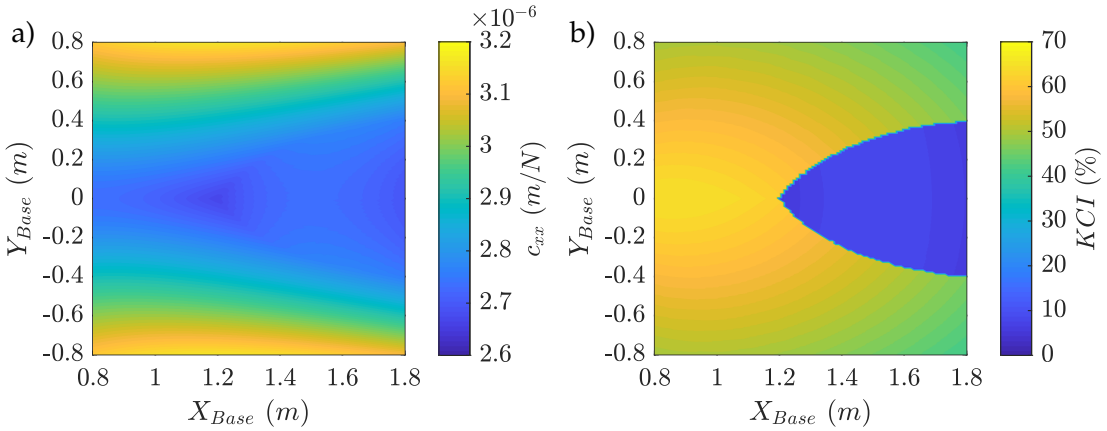

FIGURE 4.15: a) The maximum c_{xx} b) The corresponding KCI of the VJM model over the machining table

The results showed that the maximised parameter c_{xx} gets larger when the TCP is located away from X_{Base} ($Y_{Base} = 0$) compared to when the TCP is located along or close to X_{Base}. Across the middle of the machining table, along the X_{Base}, c_{xx} was observed to diminish further on the borders of "c" shaped area which also revealed itself in the corresponding KCI performance in Figure 4.15b too. On the other hand, the corresponding KCI indicated that closer to *Base Frame*, the manipulator was more dexterous whereas manipulator configurations got singular in the middle of the machining table and further along the X_{Base}.

In order to better understand the behaviour of the maximised c_{xx}, Jacobian entities (fractions) associated with each VJM joint compliance parameters were computed and illustrated as in Figure 4.16. The findings depict that Jacobian entities (fractions) associated with joint compliance of Joints 1, 3 and 5 have a larger magnitude thus, they result the largest effect on the maximised c_{xx} compared to the rest. This was due to the position and orientation of joints and hence, the transmission ratio of the force along X_{Base} to cause torque at the corresponding joints. In Figures 4.16 b, c, d, e and f, the "c" shaped area where the fractions showed a discontinuation which was analogous to the findings in the Figure 4.15.

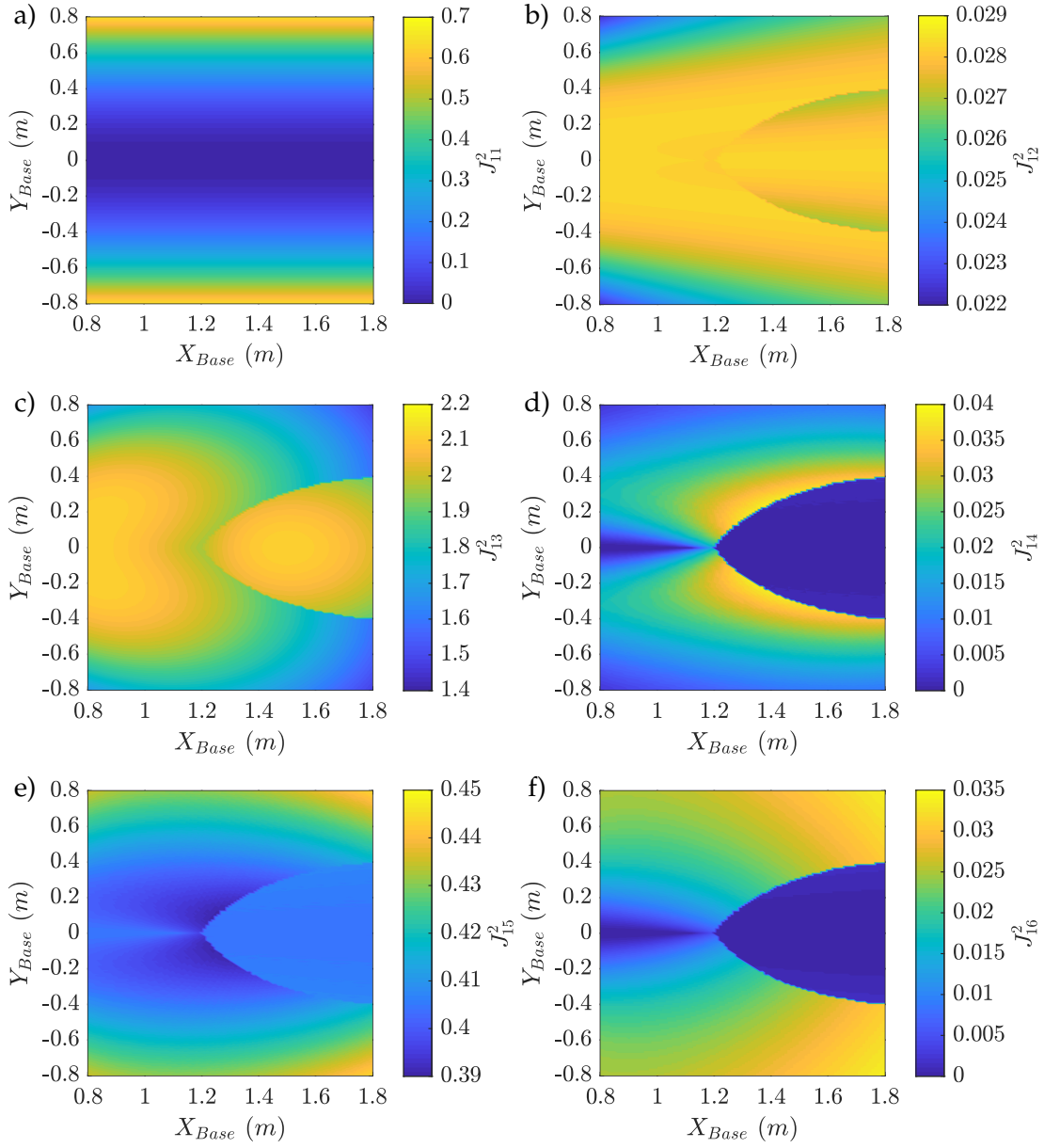

FIGURE 4.16: The Jacobian entities of a) Joint 1 b) Joint 2 c) Joint 3 d) Joint 4 e) Joint 5 f) Joint 6

At the circumference of this area, the manipulator makes a sudden configuration alteration to maximise c_{xx} and hence, there observed to be a change in the magnitude of Jacobian entities. The magnitude of Jacobian entities for Joints 4 and 6 being almost zero means, the movement around these joints are restricted. This explains the "c" shaped area in Figure 4.15 being as a consequence of the incapability of some of the joints to cause TCP movement along X_{Base} as a result of current TCP position and orientation.

On the other hand, singular configurations indicated by the KCI performance of the manipulator could be explained by the fractions associated with the joint compliance parameters of Joints 4 and 6. The Figures 4.16d and e showed that the joints were completely incapable of causing TCP movement along X_{Base}. This means that the manipulator is very close to a singularity due to the reduction in the magnitude of corresponding Jacobian matrix

entities and hence, this was reflected in the KCI performance. Such an incapability is due to the alignment of the Joints 4 and 6.

Next, c_{xx} was minimised and the corresponding KCI was shown in Figure 4.17.

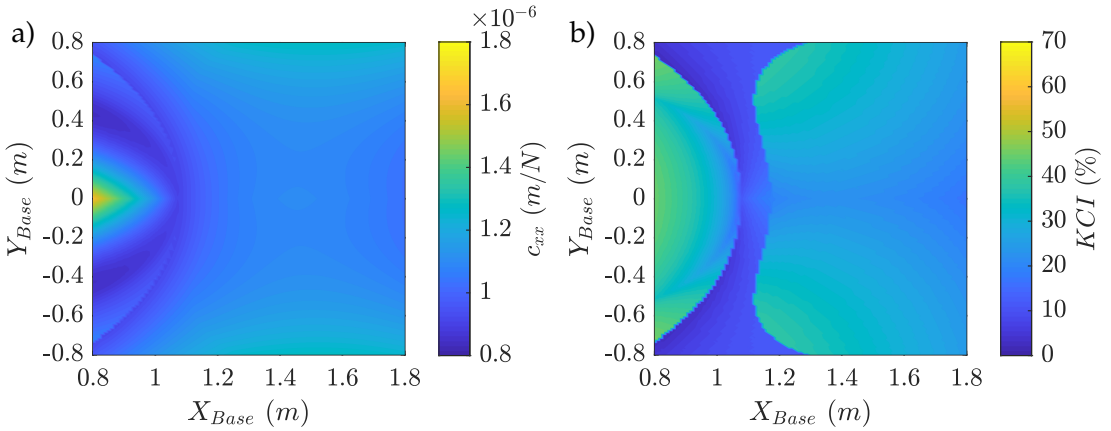

FIGURE 4.17: a) The minimum c_{xx} b) The corresponding KCI of the VJM model over the machining table

The findings showed that when the TCP was close to *Base Frame*, the manipulator had the lowest and most minimised c_{xx}. Outside the region, the minimised c_{xx} was observed to converge and stay uniform across the rest of the machining table. The corresponding KCI indicated that a corridor of singular manipulator configurations was present just outside of the aforementioned region in Figure 4.17a. Thereafter the region, the dexterity of optimised manipulator configurations also settled down and stayed mostly uniform across the rest of the machining table.

The ratio of maximised to minimised c_{xx} was taken to investigate the capability of the parameter being improved over the machining table and shown in Figure 4.18.

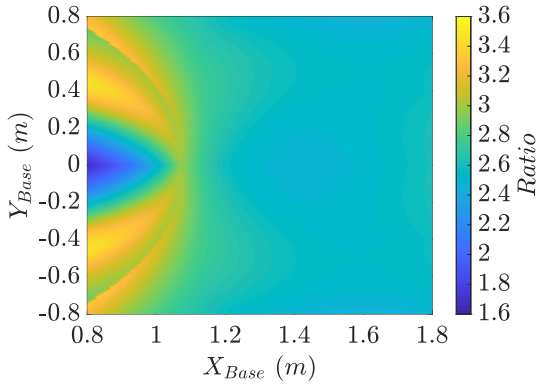

FIGURE 4.18: The ratio of maximum to minimum c_{xx} over the machining table

A maximum of 246% and a minimum of 69% c_{xx} parameter optimisation was observed at the region close to the manipulator *Base Frame*. On the other hand, the parameter optimisation of c_{xx} was around 160% and uniform after 1.1 m along X_{Base}.

4.7.4 Cartesian compliance parameter optimisation - c_{yy}

The Cartesian compliance parameter c_{yy} is responsible for TCP deflections along Y_{Base} for cutting forces applied along Y_{Base} only. As before, c_{yy} was maximised and the corresponding KCI was found out over the machining table as shown in Figure 4.19.

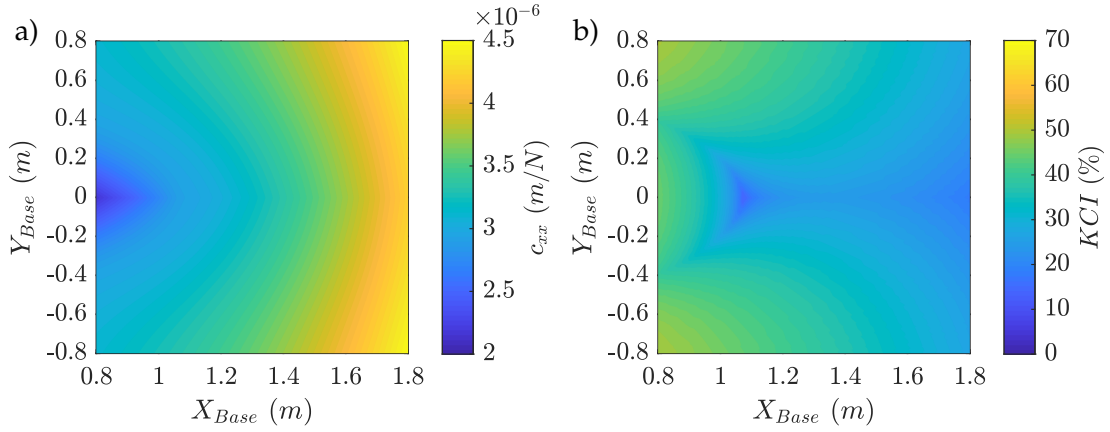

FIGURE 4.19: a) The maximum c_{yy} b) The corresponding KCI of the VJM model over the machining table

The maximised c_{yy} parameter was observed to increase radially away from the *Base Frame*. Corresponding KCI values showed singular configurations at an arc like boundary around the minimum c_{yy} values. In addition to that, optimised manipulator configurations were observed to get more and more singular as the TCP poses located further away from *Base Frame*.

Similarly, c_{yy} was minimised and the corresponding KCI was shown in Figure 4.20.

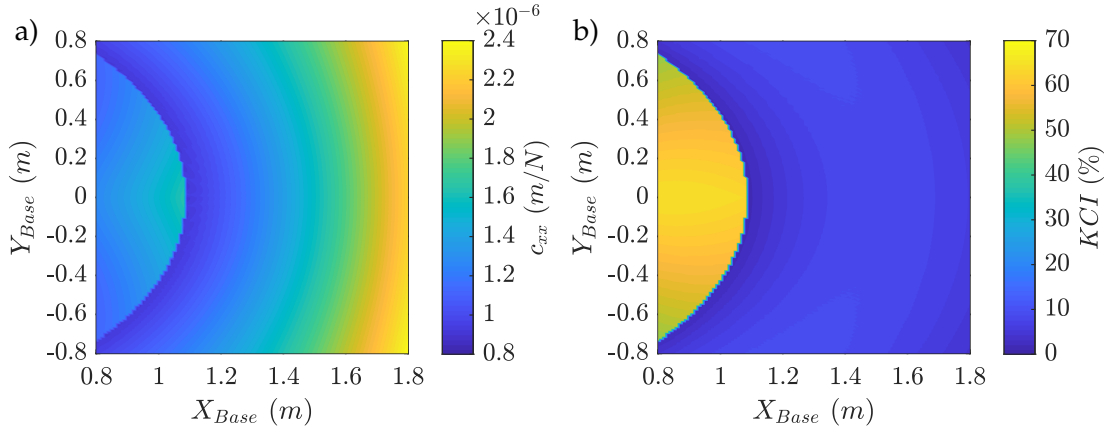

FIGURE 4.20: a) The minimum c_{yy} b) The corresponding KCI of the VJM model over the machining table

Analogous to Figure 4.19, c_{yy} was observed to increase radially away from *Base Frame*. A segment like region was spotted where c_{yy} plunged just outside but relatively higher in the inside. Corresponding KCI values were relatively higher within the segment in Figure

4.20a indicating dexterous manipulator configurations but lower outside it pointing out the optimised configurations were very close to singularity.

The ratio of maximised to minimised c_{yy} was taken in order to investigate the capability of the parameter being improved over the machining table and shown in Figure 4.21.

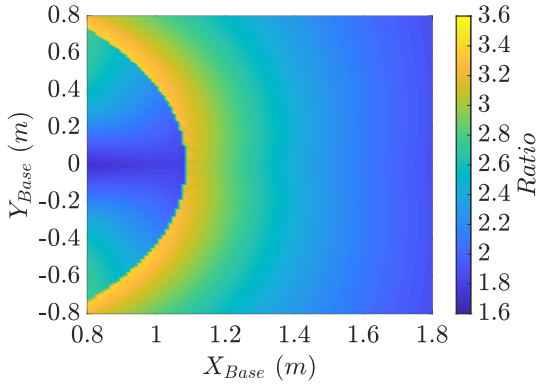

FIGURE 4.21: The ratio of maximum to minimum c_{yy} over the machining table

A maximum of 241% and a minimum of 70% c_{yy} parameter optimisation were shown to be possible over the machining table. The improvement was observed to diminish as the TCP pose got located further along the X_{Base}.

4.7.5 Discussion

It was shown that it is possible to optimise Cartesian compliance parameters c_{xx} and c_{yy} by utilising the functional and kinematic redundancy of the manipulator around the axis of rotation of the tool one at a time. In this way, the extent which static compliance parameters of the manipulator varied over the marching table was investigated. The findings showed that static as well as dynamic characteristics of the manipulator alter based on the manipulator configuration.

The industrial application of a single parameter Cartesian compliance optimisation may include robotic waterjet cutting and robotic milling operations with low radial immersion where forces normal to the feed direction are relatively small and thus, can be ignored. The developed optimisation scheme is not only applicable in machining operations but also in any environment where the robot is subject to a force in a single direction. Such an application could be robot supporting a component as a flexible support mechanism. Robotic assisted machining is another area where optimisation scheme can be utilised as a support with controllable stiffness to minimise the form error of machining thin wall workpieces in aerospace sector. Results showed that compliance parameters and hence, form errors could be minimised more than twice compared to the worst case scenario. Such an improvement is promising however, contact dynamics between robot and thin wall workpiece needs to be carefully analysed.

However, in robotic milling, optimising single parameter at a time does not make sure minimisation of form errors. In the absence of the cutting force profile, a cost function could have been defined that enables multiple compliance parameter optimisation at the same time making sure the manipulator is away from any singularities. In case of the

presence of the cutting force profile, instead of optimising the manipulator compliance (or stiffness), the manipulator deformation (deflection) index can be utilised to make sure minimisation of form errors but, both were out of the scope of the thesis.

4.8 Chapter summary

In this chapter, Virtual Joint Modelling (VJM) technique was adapted, applied to identify, model and optimise static stiffness (or compliance) characteristics of the serial industrial manipulator, ABB IRB 6640 205/2.75.

First, Conservative Congruence Transformation (CCT) without link flexibility was chosen to be most suitable VJM technique for the scope of the thesis. This was due to its simplistic but effective representation of manipulator stiffness as well as its least exhaustive computational requirement for modelling and identification. The theory behind the CCT was introduced defining the relationship between joint and Cartesian stiffness (and compliance) matrices for stiffness modelling and identification. For joint compliance parameter identification, manipulator configuration dependent stiffness term, Complementary stiffness matrix, was minimised and neglected by refining manipulator configurations. The CCT was reduced to conventional stiffness modelling at selective manipulator configuration for joint compliance parameter identification. In this way, the complicated nature of the joint compliance identification procedure was simplified into a tidier form.

Following that, the preliminary experimental design was outlined and virtually simulated for joint compliance parameter identification. The aim was to quantify the identification accuracy of joint compliance parameters, analyse factors affecting the identification accuracy and hence, to optimise procedures to be implemented in the experiment. The identification accuracy was underlined to be affected from many factors but mostly from the sensitivity of the laser tracker and uncertainties in the loading applied. In order to minimise errors, mainly, the loading procedure, number of loading and configuration were investigated. Findings depicted that the random loading procedure with maximum number of loading applied to each manipulator configuration yielded the best identification accuracy. The random loading procedure was found to minimise measurement noise more effectively than others by regression analysis. Hence, a practically non-exhaustive number of configurations was chosen to be 23 that would deliver less than 10% expected error in the joint compliance parameters to be identified in the experiment. The manipulator configurations were chosen based on the ones utilised in the simulation due to their minor influence on the identification accuracy.

In the experimental section, after describing the experimental set-up, the manipulator geometric model was calibrated. Thus, the effect of inaccuracies arising due to the mismatch of numerical and actual manipulator geometrical model on the identified joint compliance parameters was minimised. Then, joint compliance parameters were identified. However due to the experimental complications, the number of configurations used was 11 rather than 23. As per the simulation, the predicted identification error was increased to 12.5%. Even though, the predicted identification accuracy could not be validated straight away, the performance of the identified VJM model was validated. This was done by quantifying the measured and predicted Cartesian compliance parameters and deflection of the manipulator with the linearity test.

Finally, VJM model was used to optimise direct Cartesian compliance parameters, c_{xx} and c_{yy}, over the machining table surface. In this way, form error is aimed to be minimised by utilising the kinematic and functional redundancy around the axis of rotation of the tool to ease its compensation. Findings showed that the considered Cartesian compliance parameters could be improved significantly to avoid excessive static deflection of the manipulator TCP under cutting forces. Besides, it was proven that manipulator static compliance varies largely across its workspace and can be controlled by managing the manipulator configuration. The optimisation also indicated that along with the compliance, the manipulator dynamics would also depend on the manipulator configuration which has already been underlined in the literature. Managing the manipulator configurations, dynamics of the manipulator could also be controlled by utilising its kinematic and functional redundancy and hence, the stability of robotic machining operations which will be investigated in the next chapter.

4.9 Summary of contributions to knowledge

Compared to the previous literature, the work described in this chapter has made the following contributions to knowledge:

- The static stiffness of an serial arm robot has been quantified via an extensive numerical and experimental routine. It has been shown that a rigorous treatment of experimental errors is required in order to achieve satisfactory identification accuracy by a numerical simulation. Similar numerical analysis was developed and published in [115] for a number of manipulator configurations but applying the same loading by taking into account various sources of inaccuracies. In comparison, both numerical simulation models address the same problem; the identification accuracy of the joint compliance parameters. However, the developed numerical simulation is more realistic given the magnitude of the applied loading and its dependency to the TCP pose.
- The redundancy around the axis of tool rotation enables the optimisation of aspects related to the performance of manipulators such as kinematic performance (singularity avoidance), stiffness optimisation, form error minimisation, joint avoidance etc. [4, 132, 135]. It has been numerically shown that static compliance optimisation can be achieved satisfactorily to optimise the manipulator stiffness for machining industrial robots. The approach makes sure exact TCP pose requirements are satisfied while at the same time analysing kinematic performance of the manipulator over the machining table. The procedure and numerical simulations were also published in the following conference paper;

  H. Celikag, N. D. Sims, and E. Ozturk. *"Cartesian Stiffness Optimization for Serial Arm Robots"* In. vol. 77. Procedia CIRP. 2018, pp. 566-569. [130]

These contributions demonstrate that whilst serial industrial manipulators are more compliant than traditional CNC machine tools, there is scope to optimise their configuration in order to improve their performance during machining. However, it is well known that during machining operations the dynamic behaviour can be of great importance. Static stiffness analysis can offer some qualitative insight into the dynamic behaviour of a structure, but in order to explore the machining capabilities of robots in more detail, a dynamic analysis is also required. This will be the subject of the next chapter.

Chapter 5

Robotic machining trial

In this chapter, a robotic milling trial is designed to investigate the effect of configuration dependent structural dynamics on process stability characteristics. The main focus is continuous deployment of the kinematic and functional redundancy to improve process stability. However, configuration dependent structural dynamics is very difficult to model accurately. Consequently, an experimental approach is taken to investigate the effect of continuously changing structural dynamics on process stability. Following this, the relationship between stability boundaries and static stiffness predictions is investigated.

5.1 Introduction

Machining with serial industrial robots suffer from early onset of chatter and configuration dependent process stability due to the robot's poor and configuration dependent structural dynamics. In this respect, the chapter aims to investigate the effect of varying structural dynamics of manipulator on process stability in pursuit of increasing limits of stable robotic milling operations. The stability boundaries are expected to vary depending on the manipulator configuration. Having chosen suitable set of cutting parameters, chatter avoidance and/or suppression are intended. Such an effect on the process stability can be associated to chatter suppression achieved by continuous spindle speed variation as in [183, 184]. Instead of varying the spindle speed, stability boundaries were aimed to be altered by controlling the manipulator configuration hence, its structural dynamics. Besides, in the existing literature, different chatter types were claimed to happen when machining with serial industrial robots. While regenerative chatter vibrations were observed in [34, 136, 137, 155], mode coupling chatter was claimed to appear in [37, 176, 178, 182]. Thus, a further insight is aimed to be developed to validate the ambiguity in the chatter mechanism in robotic milling operations.

The aim of the machining trial was to deploy continuously varying structural dynamics by utilising the kinematic and functional redundancy around the axis of rotation of the tool. This was to achieve chatter stabilisation and/or suppression while milling with the serial industrial robot, ABB IRB 6640 205/2.75.

In this respect, the following objectives are defined for the robotic milling trial;

1. Examine kinematic performance of the robot over the machining bed surface to locate singularities and to determine a set of redundancy parameters to control manipulator configuration dependent structural dynamics.

2. Impact test the robot at different locations over the workpiece while configured to chosen redundancy parameters to identify and characterise the dynamic behaviour of the robot.
3. Obtain quasi-static regenerative stability predictions at the impact tested manipulator configurations.
4. Validate quasi-static regenerative stability predictions while robot is configured to the chosen redundancy parameters at low and high spindle speed regimes.
5. Investigate the conformity of chatter characteristics to the regenerative chatter mechanism and distinguish any mismatch.
6. Continuously alter between redundancy parameters to vary configuration of the robot during milling to test the hypothesis of chatter stabilisation and/or suppression by control of manipulator dynamics.

The rest of the chapter is organised as follows; the properties and adequacy of workpiece material to be used in the machining operation are discussed in Section 5.2. Section 5.3 describes extended kinematics of the manipulator through attachment of the spindle, tool holder and tool. In Section 5.4, manipulator kinematic performance is analysed to select different manipulator configurations to control its dynamics during milling. In Section 5.5, the experimental set-up, equipment and machining parameters are listed. The dynamic identification equipment and methodology are presented in Section 5.6 and identified frequency response functions at low and high frequency spectrum are investigated. In Section 5.7, MDOF state space models of the FRFs are identified and in Section 5.8, chatter identification methods are described. The influence of cross-FRFs on stability predictions are analysed in Section 5.9. The quasi-static zero frequency regenerative stability boundaries are computed and validated by experimental tests in Section 5.10. In Section 5.11, the chatter stabilisation by controlling configuration dependent manipulator dynamics is examined in low and high spindle speeds by cutting tests. The relation of static stiffness to regenerative stability boundaries is discussed in Section 5.12. Finally, the chapter is discussed in Section 5.13, summarised in Section 5.14 and the contribution made to the knowledge is described in Section 5.15.

5.2 Workpiece material - Acetal polymer

Machining with serial industrial robots is expected to result in low regenerative chatter stability boundaries for a given material compared to CNC machine tools. The literature suggests that at high spindle speeds, the limiting depth of cut could reach to approximately 0.1-0.7 mm when milling aluminium for slotting and 83% radial immersion respectively [35, 155]. Such magnitudes of limiting depth of cut are in the order of magnitude of pose accuracy of serial industrial robots, hence could cause complications in the process stability identification. Thus, a soft material needs to be selected for validating and enhancing the stability of robotic milling. After reviewing the literature to find a suitable material, polyacetal (acetal polymer) was chosen as a workpiece material for the robotic machining trial as depicted in Figure 5.8. Polyacetal is a family of thermoplastics and also known as Polyoxymethylene (POM). POM has a semi-crystalline structure with high stiffness, mechanical strength over wide temperature range, toughness, hardness, dimensional stability characteristics and machinability [210] (further information on the mechanical properties and characteristics of acetal polymer can be found in [211, 212]).

In order for mechanistic modelling of cutting forces to be applied to acetal copolymer, the chip formation mechanism should work the same as machining metals. In that, the chip formation by shearing should take place at a thin plane extending from the tip of the tool to the surface of workpiece [213, 214]. Machining plastics, however, was proven to behave similar to machining metals for very limited range of machining parameters. The maximum depth of cut where chip formation could be accepted to happen along a thin plane is too small for robotic milling operations (considering its pose accuracy). Beyond these parameters, chip formation was observed to create discontinuous chips. The presence of discontinuous chip formation could introduce inaccuracy to the mechanistic modelling of cutting forces based on the assumptions in [213, 214]. These inaccuracies are incorporated within identified cutting force coefficients being identified with conventional identification methods [215]. Nevertheless, the cutting force coefficients identified for the acetal polymer (K_{tc}=142.2MPa and K_{rc}=18.9MPa) in [216, 217] were observed to be satisfactorily used to predict stability boundaries with an excellent agreement with experimental findings. Acknowledging possible inaccuracies coming from the application of conventional cutting force identification model to machining acetal polymer, from chatter stability point of view, the system behaved similar to metal cutting. This proved that acetal polymer could be used as a workpiece material and regenerative chatter point of view, the system behaves similar to metal cutting. All in all, an end milling tool with a rake angle of 10° and helix angle of 35-35-35° was chosen with same geometry as the tool used as in [216, 217]. This was to make sure the cutting force coefficients identified could be utilised for regenerative chatter stability predictions in the robotic milling trial.

5.3 Kinematics with spindle & tool

Manipulator geometric architecture plays an important role in kinematic performance of any manipulator. Modifications made on the robot structure, such as connecting a new or different end effector tool (grasping mechanism, spindle, paint sprayer etc.) do also have an effect on its kinematic performance. For this reason, in order to find out the dexterous areas where the manipulator is far away from any singularities, the spindle, tool holder and tool dimensions need to be incorporated into robot geometric model. The spindle attached on the robot, is GMN HV-P 150 - 30000/26 high-speed spindle. Its tool holder collet pose was measured with a laser tracker from the surface of turning disk plate of Joint 6 (end effector as in Figure 3.1) and is given as below;

$$ {}^{6}A_{7} = \begin{bmatrix} 0.7073 & 2.9132 \times 10^{-4} & 0.7070 & 0.0776 \\ -4.1190 \times 10^{-4} & 1 & 0 & -9.3 \times 10^{-4} \\ -0.7070 & -2.9119 \times 10^{-4} & 0.7073 & 0.4386 \\ 0 & 0 & 0 & 1 \end{bmatrix} \tag{5.1} $$

Above matrix is a homogeneous transformation matrix defined based on Equation 3.4. In the machining trial, Regofix tool holder equipped with a ProMicron sensory ring with HSKA63 interface. The tool was fitted to the tool holder with a Regofix PGU 9500 clamping system. The tool and tool holder length were then measured with a tool setter. The tool and tool holder offset together was found to be 171.553 mm from the clamping surface as shown in Figure 5.1.

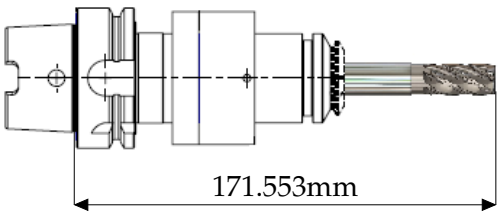

FIGURE 5.1: The schematic of the tool holder and tool

Hence, the TCP pose (spindle, tool holder and tool), ${}^{6}A_{TCP} = {}^{6}A_{7} \times {}^{7}A_{TCP}$, where ${}^{7}A_{TCP}$ is simply translation along Z_{TCP}, was defined to the controller of the robot as below.

$$ {}^{6}A_{TCP} = \begin{bmatrix} 0.7073 & 2.9132 \times 10^{-4} & 0.7070 & 0.1989 \\ -4.1190 \times 10^{-4} & 1 & 0 & -9.3 \times 10^{-4} \\ -0.7070 & -2.9119 \times 10^{-4} & 0.7073 & 0.5599 \\ 0 & 0 & 0 & 1 \end{bmatrix} \tag{5.2} $$

Having the kinematic structure of ABB IRB 6640 identified in Chapter 4, the manipulator kinematic structure with the spindle, tool holder and tool could be obtained easily as ${}^{0}A_{TCP} = {}^{0}A_{6} \times {}^{6}A_{TCP}$.

5.4 Workpiece placement & redundancy parameter selection

In this section, kinematic performance of ABB IRB 6640 205/2.75 was analysed over the machining table in order to locate singular regions and manipulator configurations. Having located the singularities, manipulator configurations were aimed to be selected to avoid singularities and hence, TCP feed rate reductions. The same procedure for kinematic performance analysis was repeated as in Section 4.7. However, instead of placing the machining table along positive X_{Base}, it was moved to the diagonal as in Figure 5.2. The machining bed surface (with its dimensions being 101.5 $\times$ 75 $\times$ 50 cm) was raised to 0.6 m in order to take into account the dynamometer and thickness of workpiece plates. The Z_{TCP} was set such that the tool is perpendicular to the surface pointing along negative Z_{Base}, as before.

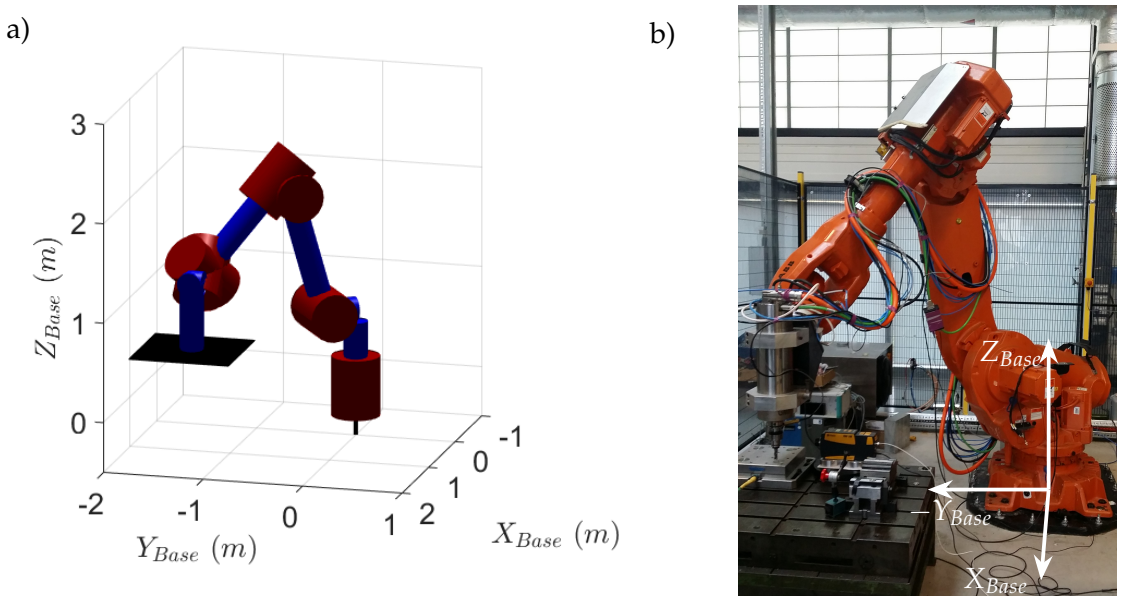

FIGURE 5.2: The position of machining table with respect to robot in the a) Simulation b) Machining trial

Computation of KCI requires finding out the characteristic length of ABB IRB 6640 205/2.75 with the spindle, tool holder and tool attached. As before, the characteristic length of ABB IRB 6640 205/2.75 was computed with Self Adaptive Differential Algorithm (SADE) following the methodology developed in [196]. The findings showed that the characteristic length of ABB IRB 6640 with spindle, tool holder and tool mounted was 0.6359 m.

Over the considered machining table surface, the minimum and maximum KCI of the robot were found out and plotted over the machining table, as shown in Figure 5.3.

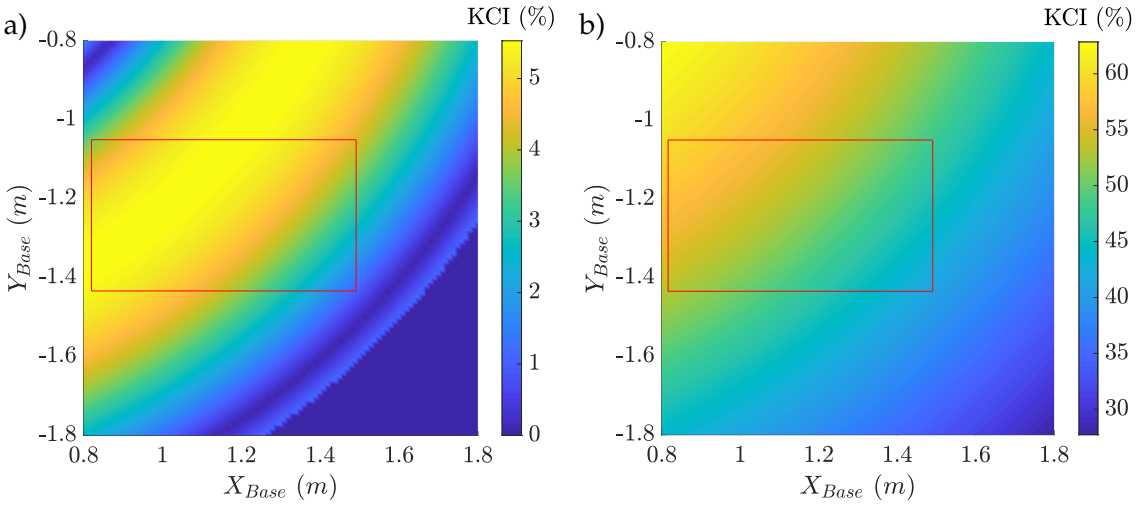

FIGURE 5.3: The KCI of the robot on the machining bed a) Minimum KCI b) Maximum KCI

The minimum KCI in Figure 5.3a shows the locations where singularities are over the machining table. The singularities appeared both close and away from the robot base as observed by the dark blue regions at the corners in Figure 5.3a. Close to the robot base, singular configurations appeared due to robot trying to collapse over itself to reach given TCP poses resulting in impractical configurations. Whereas, away from the robot base, a number of unreachable and hence, singular configurations started emerging as a result of kinematic limitations.

On the other hand, the maximum KCI showed the locations where robot had its most dexterous configurations over the machining bed in Figure 5.3b. The manipulator was found to have its most dexterous configurations close to its base where an infinitesimal changes in joint angles could achieve large Cartesian speeds. The least dexterous regions were found to be away from the robot base due to the reduced kinematic capabilities of the manipulator and difficulty in reaching this region of the workspace.

A common characteristic observed from Figure 5.3 was that the kinematic performance of the robot followed a radial path with respect to the robot base frame. This was due to the fact that first joint has no influence on kinematic performance of the robot as mentioned in [196].

All in all, the least singular region as shown by the red rectangle in Figure 5.3a and b was aimed to be the working volume in the machining trial to avoid any singularities. Note that, even though the robot might be close to a singularity in singular regions, the singularity might not be in the direction that the robot would move in the machining operation. In this respect, an exemplary tool trajectory within the region determined with red square was selected. Having defined all the cutting trajectories to run along X_{Base}, the exemplary trajectory was set to have y_{Base} of -1.24 m to further investigate the manipulator kinematic performance. The exemplary trajectory actually coincided with the cutting trajectory along the length of the workpiece where $P3$ and $P4$ are located as shown in Figure 5.9.

Along the chosen trajectory, KCI of each manipulator configuration having all possible values of the redundancy parameter, γ, was computed and is shown as in Figure 5.4.

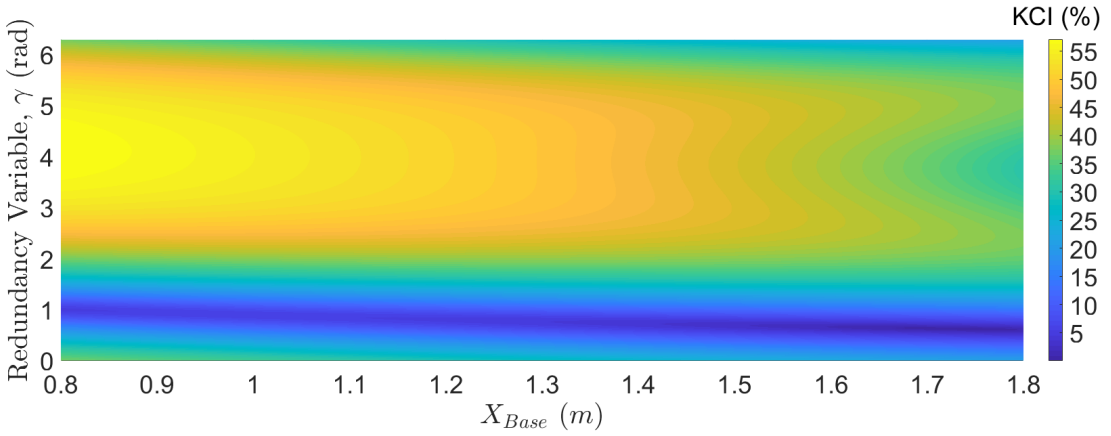

FIGURE 5.4: The KCI of the robot along an exemplary trajectory

Figure 5.4 shows that there was a singular region along the trajectory if the redundancy variable, γ, was to be set between [0-$\frac{1}{2}\pi$]. For this reason, in pursuit of controllably varying structural dynamics of the robot by utilising the redundancy variable, four redundancy variables were selected. The selected redundancy variables are γ=[$2\pi, 1.5\pi, \pi, 0.5\pi$] and the corresponding manipulator configurations were referred as C1, C2, C3 and C4. The manipulator kinematic performance while following the cutting trajectories with constant redundancy variable along X_{Base} (between 0.9-1.4 m) is demonstrated in Figure 5.5 for each chosen redundancy variable.

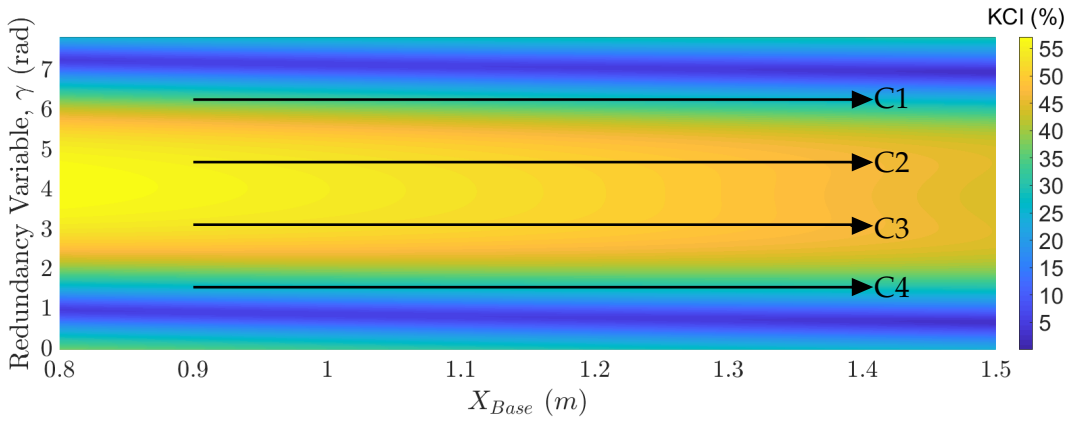

FIGURE 5.5: The manipulator KCI while having the constant redundancy variable

In spite of the fact that C1 & C4 were close to the singular region, the singularity could only be reached if redundancy variable was altered. Hence, the translational movement of the robot was not affected by the presence of the nearby singularity in this case. In this way, all chosen redundancy parameters were assured not to coincide with a singularity during milling. Note that, the trajectories shown for every redundancy parameter were the trajectories followed by the robot in Section 5.10 along the length of the workpiece where P3 and P4 are located.

In order to vary manipulator structural dynamics, the chosen redundancy variables were aimed to be continuously altered while cutting. The exemplary trajectory followed and the manipulator kinematic performance while along the X_{Base} are shown in Figure 5.6.

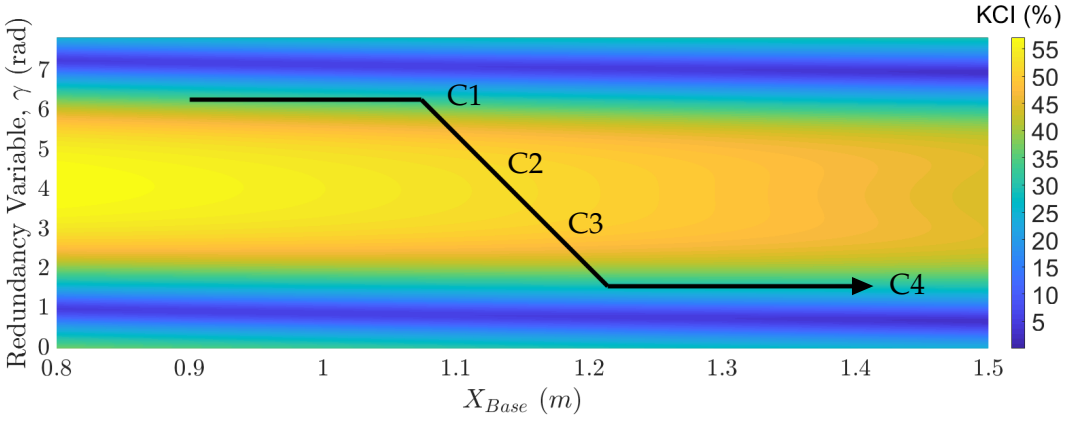

FIGURE 5.6: The manipulator KCI while altering between the chosen redundancy variables

Varying the manipulator configuration from C1 to C4 could avoid singular regions and hence, enable controlling the manipulator configuration around the axis of rotation of the tool. The exemplary cutting trajectory in Figure 5.6 actually represents the cutting trajectory in Section 5.11 along the length of the workpiece. For clarity, the resultant configurations of the robot having the redundancy parameters C1, C2, C3 and C4 are demonstrated in Figure 5.7.

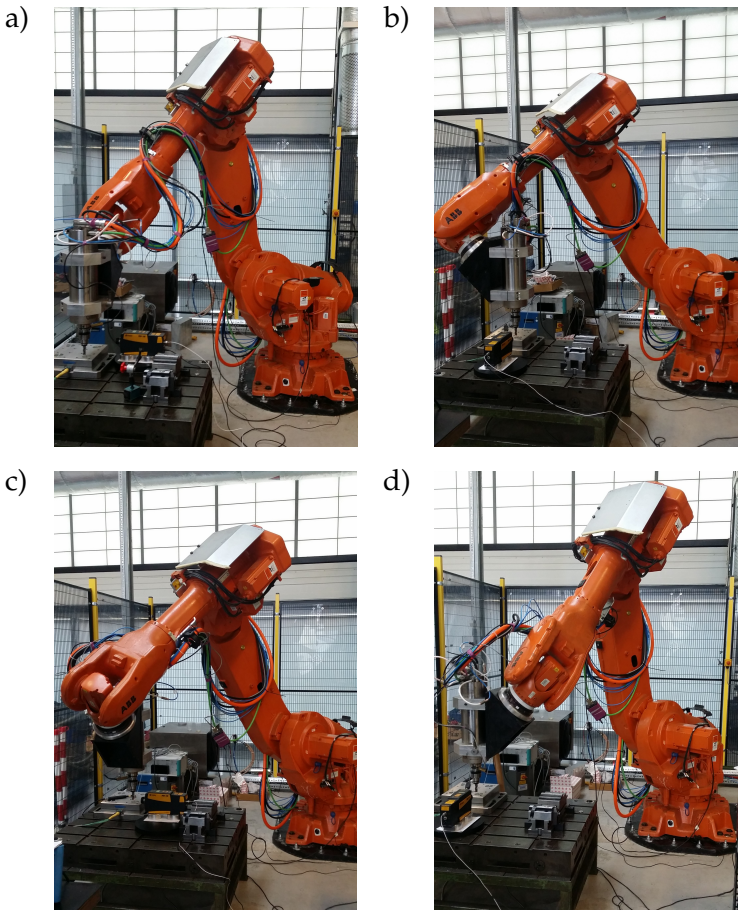

FIGURE 5.7: The configurations of the robot for a given exemplary 5 Dof pose with the redundancy parameter a) γ=2π, b) γ=1.5π, c) γ=π, d) γ=0.5π

It should be noted that even though the manipulator was configured to stay away from singularities as much as possible, this does not mean that Cartesian feed rates defined in the controller were always sustained during the cutting tests. Constantly changing kinematic performance of the manipulator could cause fluctuations in the Cartesian feed rates as well as the controller not being able to keep up with manipulator dynamics as a result of changing manipulator configuration.

This summarises the methodology followed to analyse kinematic performance of the robot over the machining table and cutting trajectories. Thus, the location of the dynomometer over the machining table was identified while ensuring cutting trajectories were unaffected by any singularities. The chosen redundancy parameters made sure the robot was well away from any singularity while following a straight cut along X_{Base}. Transition between the redundancy parameters (in the specified order) also enabled smooth orientation of the TCP around the axis of rotation of the tool.

5.5 Experimental set-up

In order to identify chatter within the process, a tri-axis accelerometer was mounted onto the spindle, a microphone was installed close to cutting trajectories and a hall effect sensor was mounted onto the spindle holder. Having the position of the dynamometer determined in Section 5.4, it was clamped over the machining table and aligned with *Base Frame*. Then, the workpiece was attached onto the dynamometer. The equipments used and set-up of the machining trial are shown in Figure 5.8.

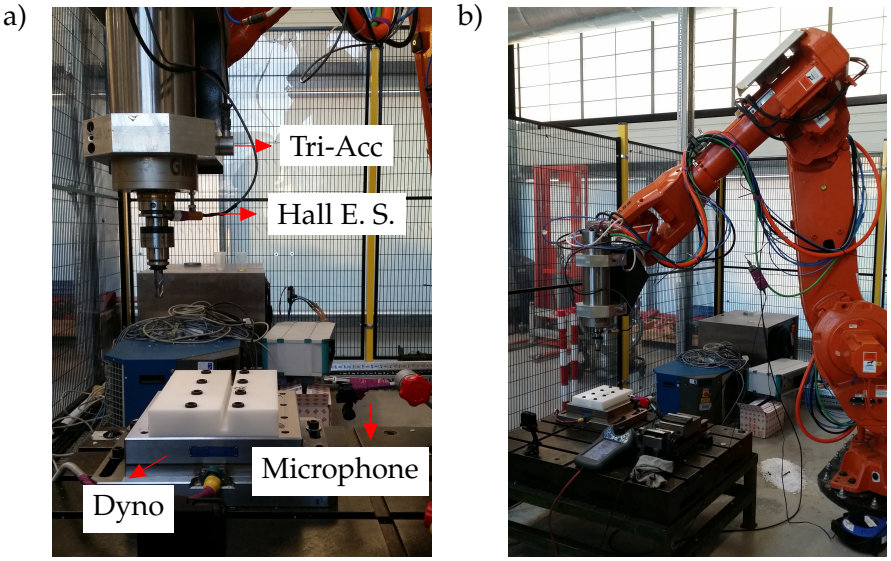

FIGURE 5.8: The experimental set-up of the machining trial a) Front View b) Isometric View

The hall effect sensor was used to track the spindle revolution and synchronise measurements by taking one per tool revolution data. The hall effect sensor is a device that measures the magnitude of a magnetic field. In the machining trial, it was set to point out a key way on the tool holder. The change in shape of the tool holder as a result of appearance of the key way every revolution of the tool gave rise to a change in the

magnetic field. In this way, the position of the key way on the tool holder was tracked at every revolution for spindle speed measurement purposes.

The machining parameters used in the trial are summarised below;

Machining Parameters	Type	Down-milling
	Radial Immersion	50%
	Feed per tooth	0.15 $mm/tooth$
Tool	Type	End Mill
	Manufacturer	Technicut
	Tool Number	TCD6537
	Material	Solid Carbide
	Pitch	0° - 120° - 240°
	Helix Angle	35° - 35°- 35°
	Rake Angle	10°
	Number of teeth	3
	Diameter	16 mm
	Overhang Length	51.5 mm
Workpiece	Material	Acetal Copolymer
	Types	Square Plate
		Rectangle Plate
	Tangential CFC (K_{tc})	142.2 MPa [217]
	Radial CFC (K_{rc})	18.9 MPa [217]

TABLE 5.1: The machining parameters used throughout the machining test

The details of the equipment used in the machining test are listed in Table 5.2.

Dynamometer	Type	Plate
	Manufacturer	Kistler 9255C
Tri-Axis Accelerometer	Manufacturer	PCB Piezotronics
	Model	M604B31
	Frequency Range	0.5-5000 Hz
Hall Effect Sensor	Manufacturer	ZF NPN
Microphone	Manufacturer	PCB Piezotronics
	Model	377B20

TABLE 5.2: The equipments and specifications

Dimensions of the workpiece and tool trajectories are depicted in Appendices H and F respectively. This summarises the set up of the machining parameters and equipments used in the robotic milling trial. In every cut, the tool was ensured to be perpendicular to the surface of the workpiece and feeds were along $+X_{Base}$. Next, dynamics of the structure was identified for stability predictions.

5.6 Dynamic identification of the structure - modal testing

In machining operations, cutting takes place at the tool tip which makes it more suitable for tap (impact) testing to be used for structural dynamics identification. In this work, manipulator structural dynamics was identified in the form of Frequency Response Function (FRF) which describes the response of dynamic compliance of the structure across frequency spectrum. In this case, point FRFs were acquired at various manipulator configurations and directions to characterise structural behaviour across frequency spectrum and analyse the process stability.

Serial manipulators are known to have relatively poor (compared to machine tools) and configuration dependent dynamics due to their ever-changing posture. Thus, entire frequency spectrum of FRF needs to be identified to capture all modes of vibration. Since, frequency excitation mainly depends on the impact hammer used, two different hammers were used to excite low and high frequency spectrum of FRF in the impact testing; a Dytran 5803A impulse sledgehammer and Kistler 9722A500 impulse hammer.

A Dytran 5803A impulse sledgehammer was used to excite low frequency spectrum of the FRF whereas Kistler 9722A500 hammer was used to excite higher frequency spectrum. The specifications used in the impact testing is shown in Table 5.3.

	Dytran 5803A	Kistler 9722A500
Frequency Range (Hz)	1-200	1-10000
Frequency Resolution (Hz)	0.1	0.5
Sampling Rate (Hz)	10000	51200
Tip	Soft (Orange)	Nylon
Sensitivity (mV/N)	0.227	11.630

TABLE 5.3: The parameters used for impact hammers in the impact (tap) testing

For measuring the response of the structure, PDV-100 portable digital vibrometer (laser vibration velocity sensor) was used. The sensitivity of PDV-100 laser vibrometer is 7980 mV/(m/s).

In machine tools, due to the very high rigidity of the structure, usually direct-FRFs are enough to be identified for chatter stability analysis. However, industrial robots tend to have relatively poor structural dynamics compared to machine tools and the structure can easily get coupled when subject to cutting forces. For this reason, it is crucial to identify cross-FRFs in addition to direct-FRFs at tool tip when machining with robots. In pursuit of identifying direct and cross-FRFs of ABB IRB 6640, 4 locations (5 DOF poses) on the workpiece were defined which are referred as $P1$, $P2$, $P3$ and $P4$. At every location, the robot was configured to chosen configurations C1, C2, C3 and C4 as illustrated in Figure 5.9. Note that, *Work Object Frame* (with axes X_{Wobj}, Y_{Wobj}, Z_{Wobj}) was set such that it was 8 mm (tool radius) away from both sides of the workpiece orthogonal to the corner. Additionally, it was aligned with *Base Frame* to an extent capabilities of the robot allowed. An example of identified homogeneous transformation matrices of *Work Object Frames* for square and rectangle workpieces are represented in Appendix G.

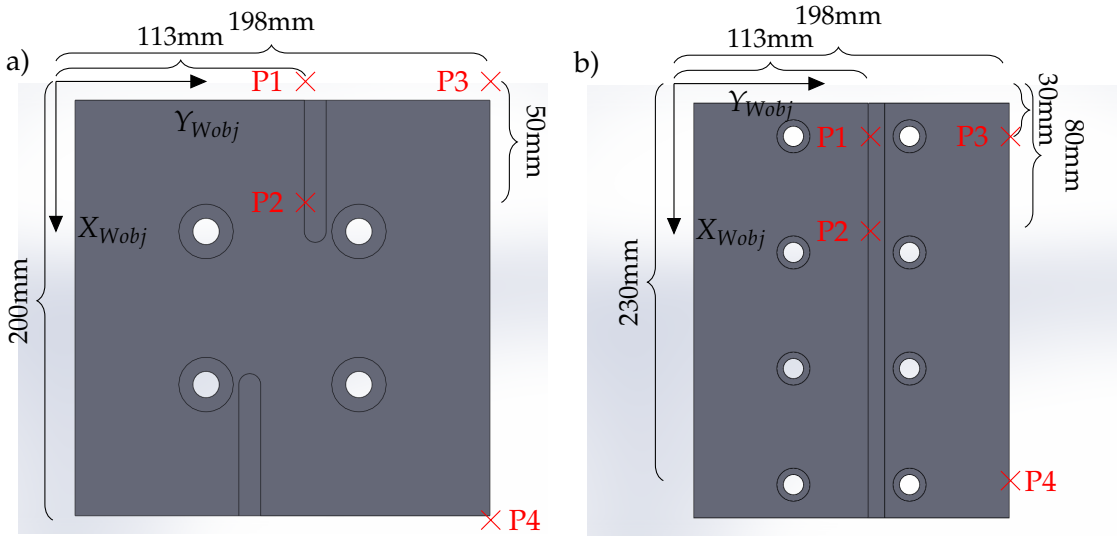

FIGURE 5.9: Top view of Acetal Co-polymer workpieces in CAD a) Square b) Rectangle

The structure was excited at different locations on the robot due to the size difference of impact hammers. Kistler 9722A500 impact hammer was used to excite at the tool tip whereas the structure was excited at the spindle holder with Dytran 5803A impulse sledgehammer. This was because the size of the Dytran 5803A impulse sledgehammer did not allow exciting the structure at tool tip (primarily due to not damage the tool & spindle). The spindle holder faces where the structure was excited are demonstrated with the white arrows as in Figure 5.10a;

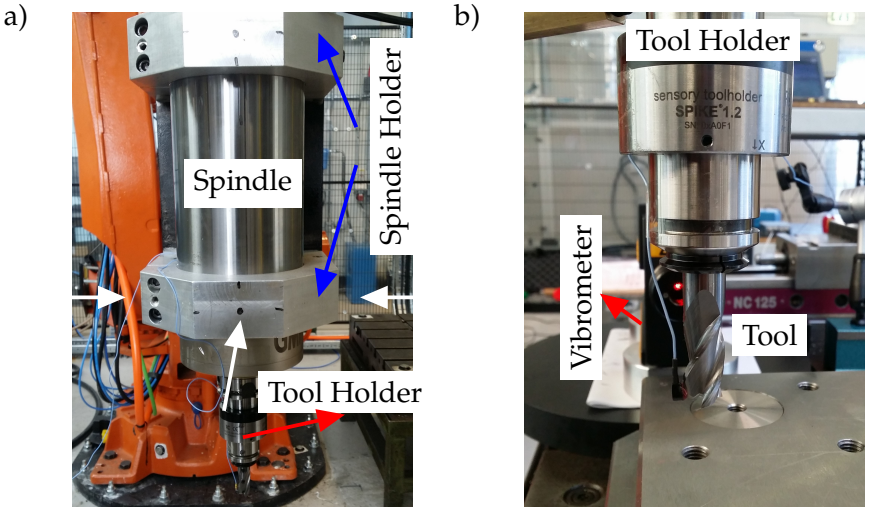

FIGURE 5.10: a) White arrows show the locations excited with Dytran 5803A sledgehammer b) PDV-100 portable digital vibrometer pointing towards the tool tip

For measurement of the response and exciting the structure, *BaseFrame* was used as a reference. An exemplary set of FRFs were chosen demonstrate excitation frequencies of

both hammers. The magnitude of FRF and coherence for the FRF identified by Dytran 5803A and Kistler 9722A500 are shown in Figure 5.11 and 5.12 respectively.

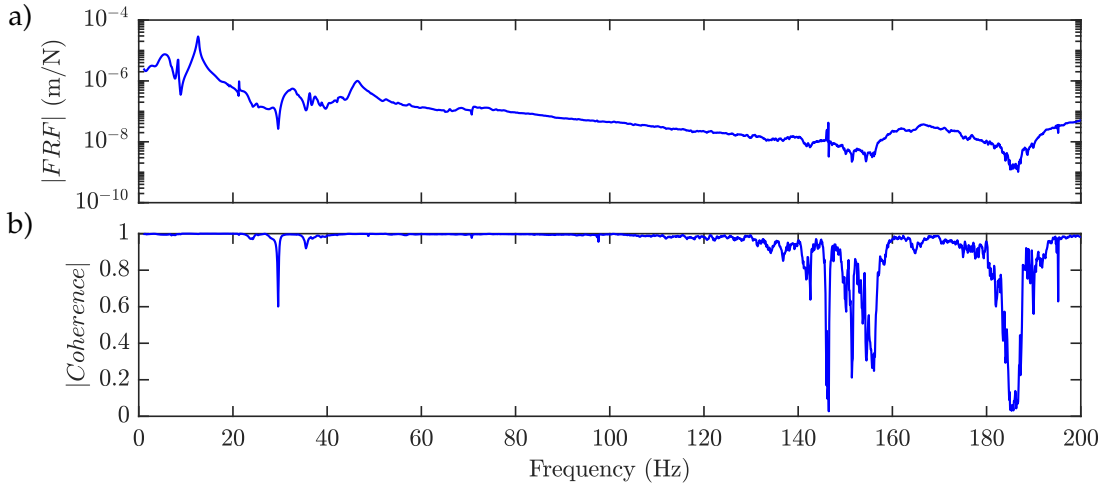

FIGURE 5.11: Exemplary FRF and coherence obtained by Dytran 5803A impulse sledgehammer

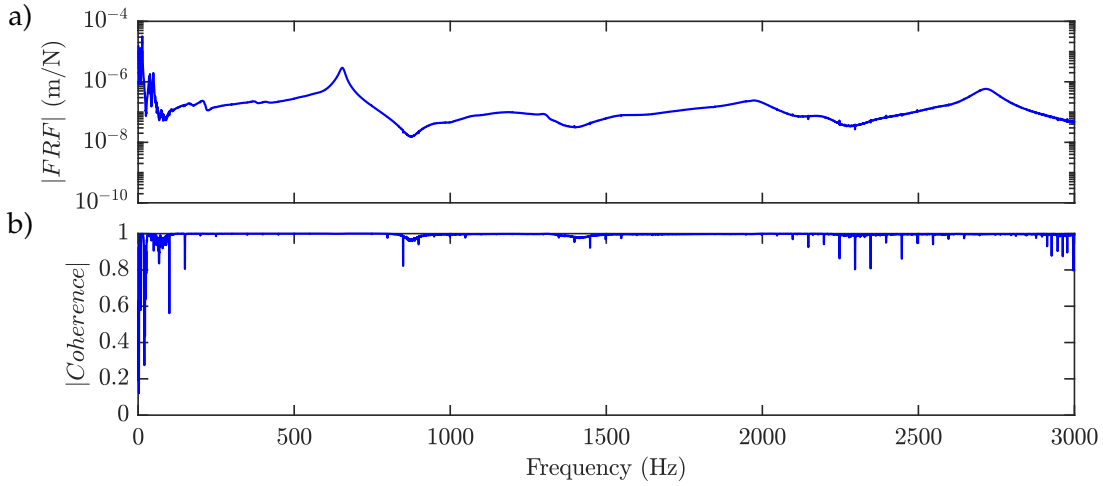

FIGURE 5.12: Exemplary FRF and coherence obtained by Kistler 9722A500 impact hammer

The magnitude of coherence shows that Dytran 5803A impulse sledgehammer was effective in exciting low frequency spectrum whereas Kistler 9722A500 impact hammer was effective in exciting the high frequency spectrum of the FRF. The magnitude of coherence close or equal to 1 indicated that both input and output signals are linearly correlated. There were minimal noise and possibly non-linearity between the two signals. In this respect, the pros and cons of impact hammers are summarised below;

- Kistler 9722A500 impact hammer was able to excite high frequency spectrum (above 150 Hz) of tool tip FRF effectively whereas low frequency spectrum had low coherence which meant that the identified FRF was not that reliable. The frequency resolution of FRFs identified was 0.5 Hz hence, FRFs were coarsely defined.

- Dytran 5803A impulse sledgehammer was effective in exciting low frequency spectrum (between 1 - 150 Hz) of FRF whereas higher frequencies could not be excited due to the size and tip of the hammer. FRFs identified were not a tool tip FRFs as the excitation was applied to spindle holder and response measured from the tool tip. The frequency resolution of FRFs was 0.1 Hz hence, they were defined relatively finer.

Based on the presented pros and cons, identified FRFs from both hammers were used in quasi-static regenerative stability predictions. Note that, FRFs identified by Dytran 5803A impulse sledgehammer weren't collocated FRFs at the tool tip. Low frequency modes of vibration are known to come from structural modes of vibration and the connection between spindle holder and tool interface was quite rigid. Thus, the connection between spindle holder and tool interface was assumed to have negligible effect on the low frequency response of the structure. FRFs identified by Dytran 5803A impulse sledgehammer were assumed to be tool tip FRFs.

5.6.1 Low-frequency FRF - structure response

Dytran 5803A impulse sledgehammer was used to examine low frequency spectrum of the dynamic response of the structure. The experimental direct and cross FRFs identified at $P1$ with redundancy variable, γ=2π, was shown in Figure 5.13.

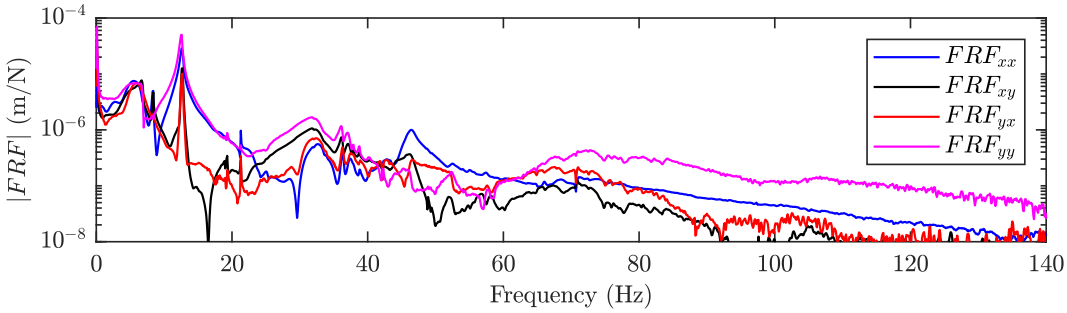

FIGURE 5.13: The low frequency spectrum FRF at $P1$ while γ=2π

The most notable feature of FRFs was that all significant modes were located well below 60 Hz whereas most dominant ones were located at even lower frequencies; below 20 Hz. An interesting feature observed was the magnitude of cross FRFs; it was found out to be similar or close to that of direct FRFs in the frequency range considered. This meant that structure was highly coupled at low frequency structural modes.

The effect of translating tool tip around workpiece on manipulator dynamics was investigated while keeping the redundancy variable, γ, the same. In this respect, experimental direct FRFs at tap tested locations were plotted in Figure 5.14 with redundancy variable kept at γ=π.

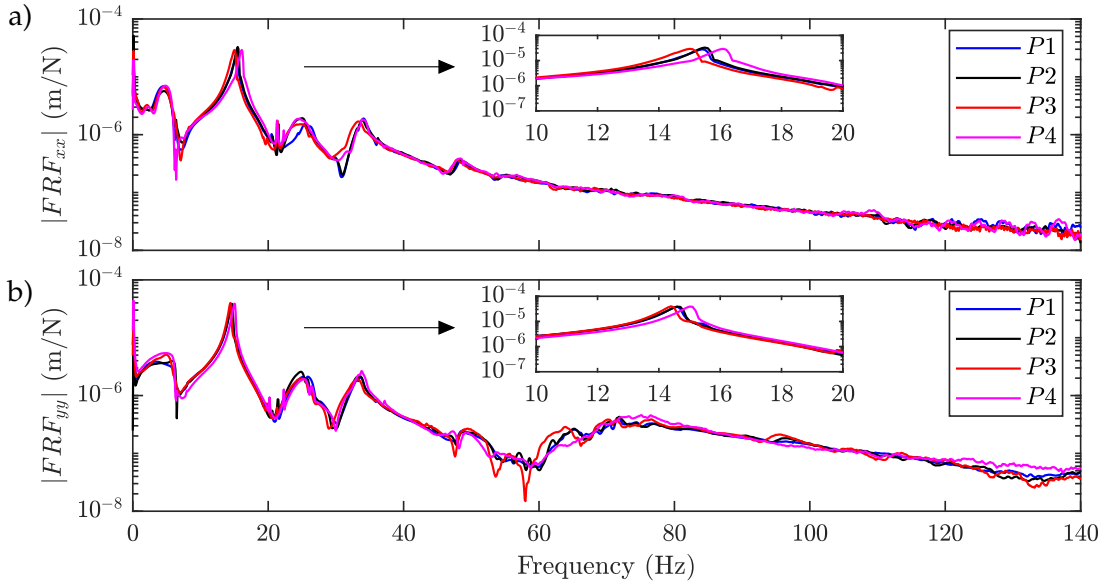

FIGURE 5.14: The low frequency spectrum FRF at tap tested locations while $\gamma=\pi$

Considering the most dominant (flexible) mode at both FRF_{xx} and FRF_{yy}, keeping the redundancy variable the same but translating tool tip across a workspace as small as the size of workpiece caused slight natural frequency shift and magnitude variations. The inherent manipulator configuration alteration was the primary reason for perturbations in direct FRFs. It should also be noted that the magnitude of perturbations could depend on the choice of the redundancy variable and tool tip translation.

The effect of configuration alteration as a result of varying redundancy variable, γ, was explored on a single tap test location (5 DOF). In this respect, experimental direct FRFs at $P1$ were plotted as an example in Figure 5.15 for all of the chosen redundancy variables.

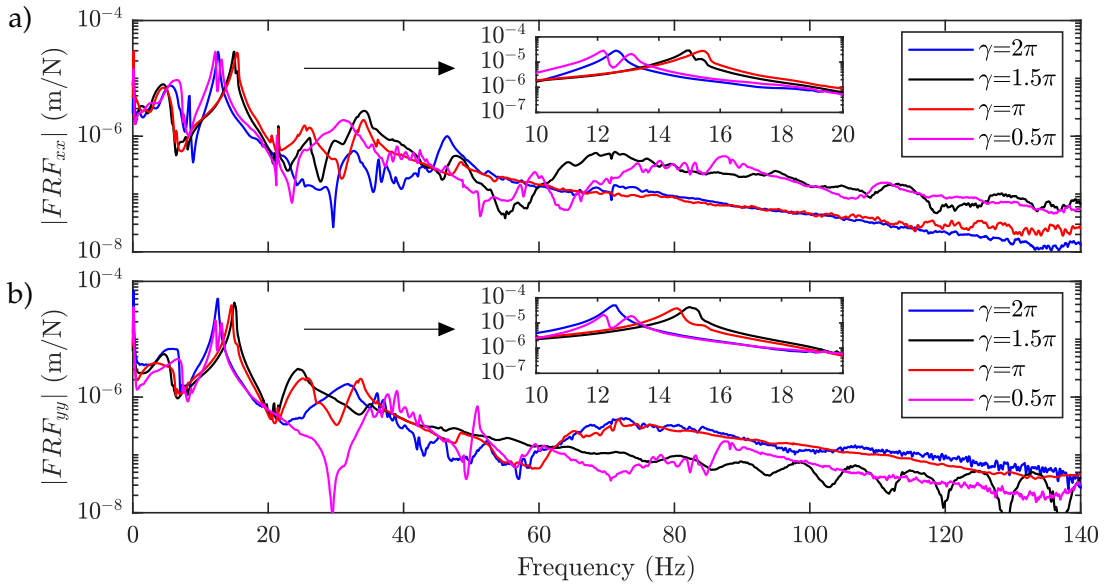

FIGURE 5.15: The low frequency spectrum FRF at $P1$ with the chosen redundancy variable, γ

Considering the most flexible mode of vibration, the alteration of redundancy variable (and therefore the configuration such as in Figure 5.7) results a significant frequency shift and magnitude. A more significant change in the manipulator configuration was obtained by altering the redundancy variable compared to the configuration change acquired by translating tool tip while keeping the redundancy variable constant. Hence, the extent of the variation in the most dominant mode suggested that low frequency modes are manipulator structural modes which agrees with the literature.

All in all, findings implied that the redundancy variable could be used to further vary manipulator structural dynamics (besides the dynamic variation obtained as a result of tool translation) during machining which supported the main aim of the machining trial.

5.6.2 High-frequency FRF - tool holder-spindle shaft response

FRFs covering higher frequencies were identified Kistler 9722A500 impact hammer to characterise the higher frequency tool holder-spindle shaft and tool modes of vibration. In this respect, the direct and cross FRFs were plotted at $P1$ while γ=2π.

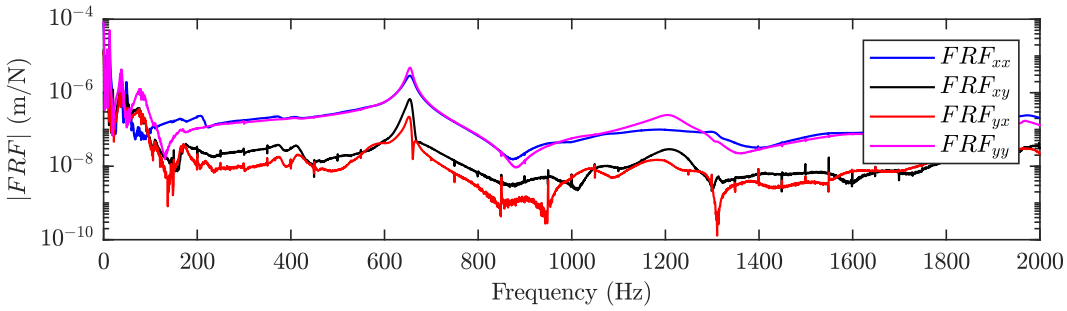

FIGURE 5.16: The high frequency spectrum FRF at $P1$ while γ=2π

The tool holder-spindle shaft shaft mode was observed to be the most flexible mode upon the considered high frequency spectrum of FRFs and was located around 654 Hz whereas tool modes were at 1204 and 1976 Hz. At high frequencies, the structure exhibited less coupling in cross directions and hence, stiffer dynamic behaviour as opposed to the low frequency behaviour as in Figure 5.13.

The effect of translating tool tip around workpiece on high frequency spectrum of the direct FRFs was investigated while keeping the redundancy variable, γ, constant. The experimental direct FRFs at tap test location were shown in Figure 5.17 while the redundancy variable was kept γ=2π.

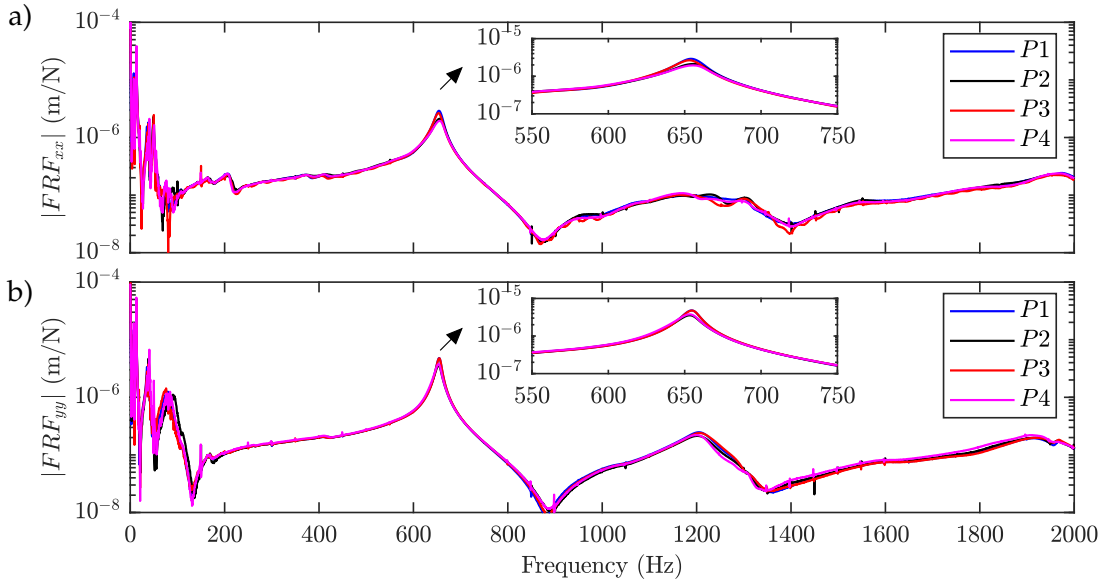

FIGURE 5.17: The high frequency spectrum FRF at tap tested locations while γ=2π

Considering the most flexible mode due to its expected dominance in regenerative stability predictions at high spindle speeds, the translation of tool resulted in almost insignificant variations in its magnitude and frequency. This might be due to the fact that high frequency modes of vibration were being local modes on the structure and hence, they get hardly affected by the manipulator configuration alteration.

Next, the effect of configuration alteration on high frequency spectrum of direct FRFs was explored by varying the redundancy variable, γ, on a single tap tested pose. In this way, experimental direct FRFs at $P3$ were plotted as an example in Figure 5.18 for all the redundancy variables.

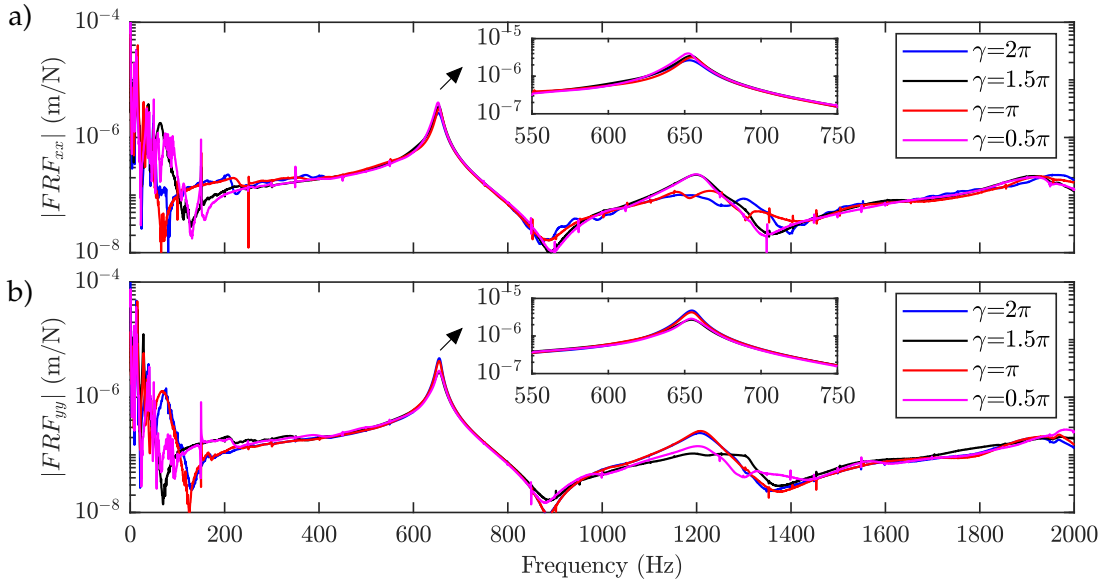

FIGURE 5.18: The high frequency spectrum FRF at $P3$ with the chosen redundancy variable, γ

The configuration alteration as a result of varying the redundancy parameter at a single tap testing pose, resulted in slight variations in magnitude and frequency in the most flexible mode of vibration. This could be attributed to the greater extent of manipulator configuration change (and therefore variation in structural dynamics) acquired by varying the redundancy parameter compared to the Figure 5.17.

To sum up, higher modes of vibration were found to be affected more when the manipulator configuration was altered by controlling the redundancy variable compared to the inherent configuration change as a result of the tool tip translation. Nevertheless, higher modes were proved to be still affected by the manipulator configuration even though the effect wasn't as striking as that of low frequency structural modes.

5.7 Identification of state space model of MDOF system

Stability boundaries for regenerative chatter mechanism can be computed by utilising either a state space model of structural dynamics or experimental FRFs. However, computation of stability boundaries of mode coupling chatter mechanism in milling can only be achieved by using a state space model (which will be covered in Chapter 6). In order to compare both mechanism in a fair way, the state space model of robot structural dynamics was identified and used for stability analysis throughout the thesis. In this respect, an experimental modal identification toolbox, Structural Dynamics Toolbox (SDT) [218], was utilised to derive the state space model and modal properties of modes of vibration from experimental FRFs. The main assumptions were as follows;

1. The mode model was assumed to be "normal mode". The structure was assumed to behave like linear elastic structure with modal damping, hence, the normal mode model has a symmetric pole structure.
2. "Multi Input Multi Output" or "MIMO" reciprocity was assumed which implies that cross FRFs (FRF_{xy} & FRF_{yx}) were assumed to behave the same.

In the identification at low frequency spectrum, dominant structural modes below 40 Hz were identified and modelled. The experimental and modelled direct-FRFs at $P1$ for redundancy variable γ=π at low frequency spectrum are shown as in Figure 5.19.

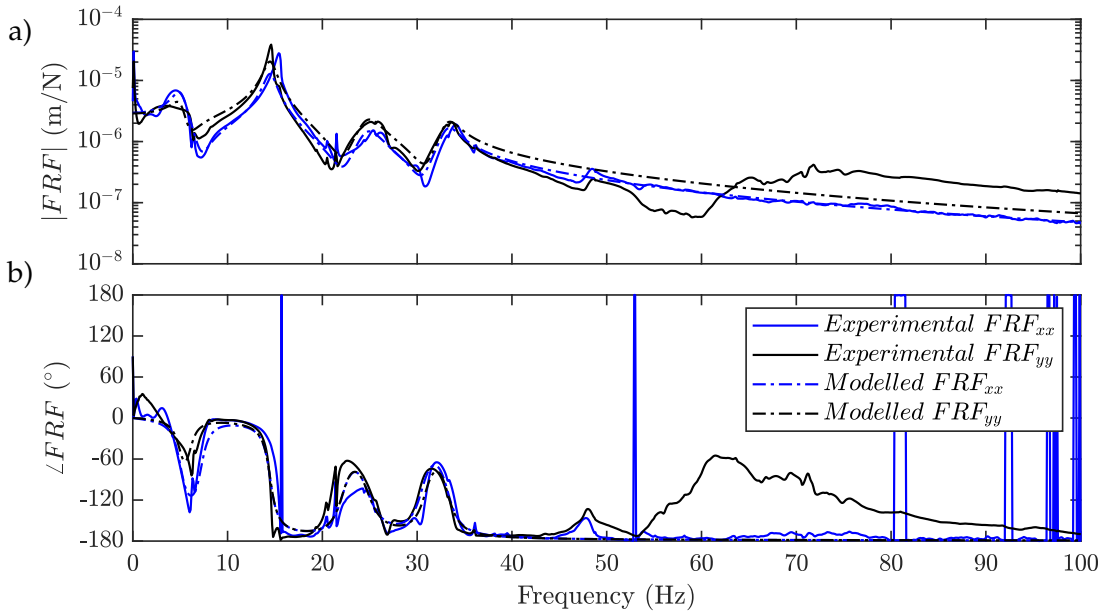

FIGURE 5.19: The experimental and modelled direct FRFs at low frequency spectrum a) Magnitude b) Phase

Both experimental and modelled direct-FRFs showed good agreement with each other in general. It was found to be slight mismatch especially at the peaks of modes of vibration where linear approximations start not fitting to non-linear dynamics of the robot.

Similarly, the experimental and modelled cross-FRFs at $P1$ for redundancy variable $\gamma=\pi$ at low frequency spectrum are shown as in Figure 5.20.

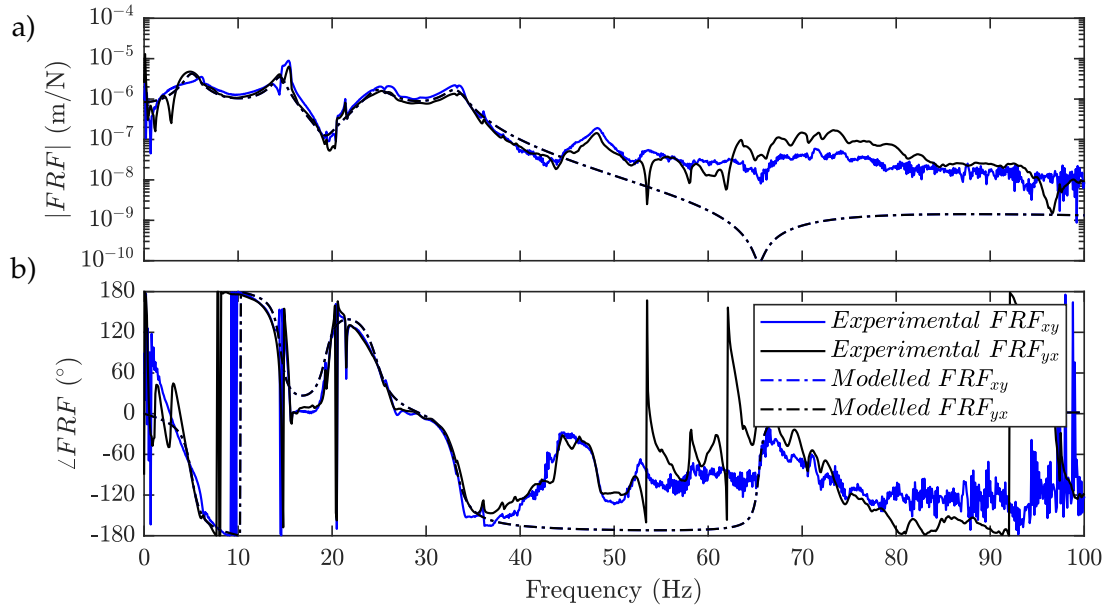

FIGURE 5.20: The experimental and modelled cross FRFs at low frequency spectrum a) Magnitude b) Phase

The comparison revealed that MIMO reciprocity may not be the case especially for structural robot modes of vibration due to the non-linear coupling between the orthogonal directions of FRFs. The non-identical cross-FRFs were also an indication of the asymmetry of manipulator structure. Nevertheless, the assumption held for most of the frequency spectrum of cross FRFs. The modelled cross FRFs were observed to fit to experimental FRFs with a good accuracy below 40 Hz.

The experimental FRFs at high frequency spectrum showed that tool holder-spindle shaft mode was the most dominant mode and behaved very similar to a single degree of freedom (SDOF) system. For this reason, only tool holder-spindle shaft mode was identified and modelled ignoring higher frequency modes of vibrations for the sake of simplicity. The identification and modelling for a SDOF mode are quite well established and results showed an excellent match. Therefore, the comparison between experimental and modelled tool holder-spindle shaft mode of vibrations wasn't shown here. Yet, it should be acknowledged that all modes of vibration needed to be taken into account for a full regenerative stability diagram if one requires a more detailed stability analysis.

5.8 Identification of chatter within the process

For identification of chatter within the process, the following methodology was followed;

1. Steady state region of the milling process in time domain was identified.
2. In steady state region, Fast Fourier Transform (FFT) of acceleration data, voltage output from hall effect sensor, sound pressure from microphone were computed.
3. The precise spindle speed and its harmonics were identified from Fast Fourier Transform (FFT) of acceleration, hall effect sensor and microphone data.
4. The chatter frequencies were identified in frequency domain using acceleration and microphone data based on comparing the relative magnitude of a suspected chatter frequency to the third harmonic of spindle speed (tooth passing frequency, $\omega_T = \frac{3\Omega}{60}$ Hz).

In low spindle speeds, two exemplary data sets are compared to clarify and explain the identification of chatter by using FFT of acceleration data only. The microphone data was noisy for low frequency sound measurements, hence accelerometer data was shown. Accordingly, two scenarios are shown in Figure 5.21.

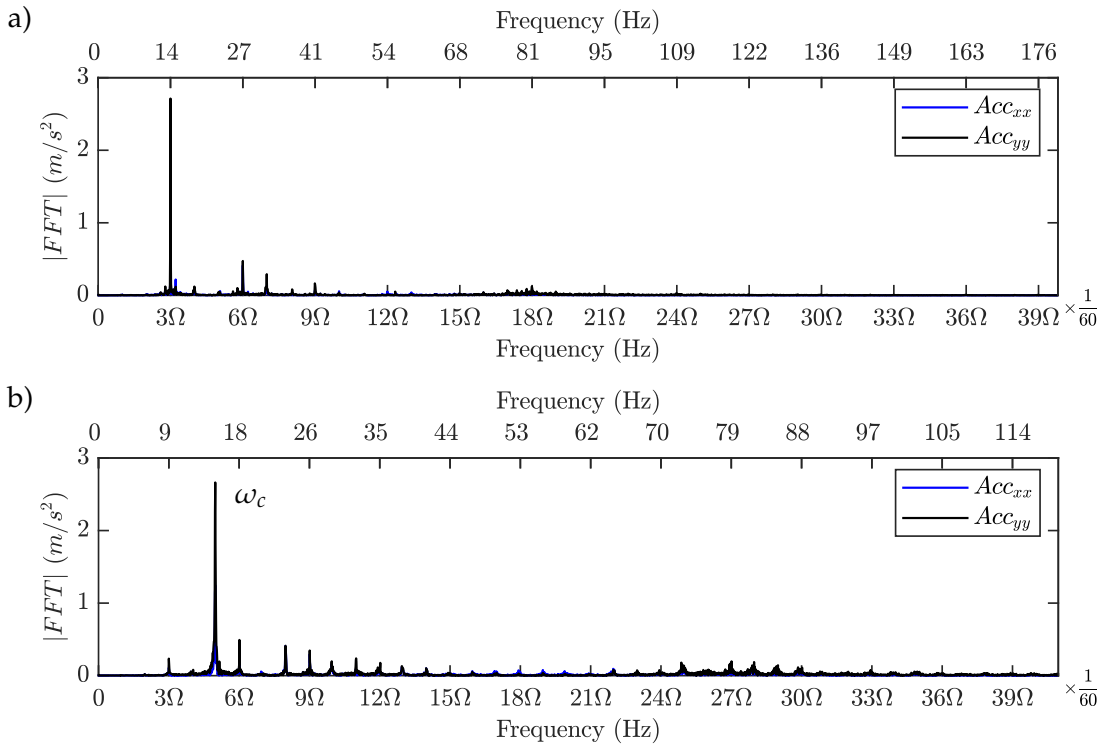

FIGURE 5.21: The FFT of acceleration signals for two cutting scenarios a) Stable b) Unstable

In Figure 5.21a, spindle speed was identified to be 271.3 RPM. The frequency content of both acceleration data showed that the dominant frequency was around the third harmonic of spindle pass frequency. Hence, the stability of process was concluded to be stable as there were not any other frequencies competing with excitation frequency of the system. In Figure 5.21b, spindle speed was identified to be 175.8 RPM however, the

dominant frequency was found not to coincide with any of the harmonics of excitation frequency. This meant that the dominant frequency in the process was not coming from the periodic excitation of spindle, hence the process was concluded to be unstable.

In high spindle speed tests, the same procedure was repeated. The FFT of acceleration data of two exemplary scenarios are shown in Figure 5.22.

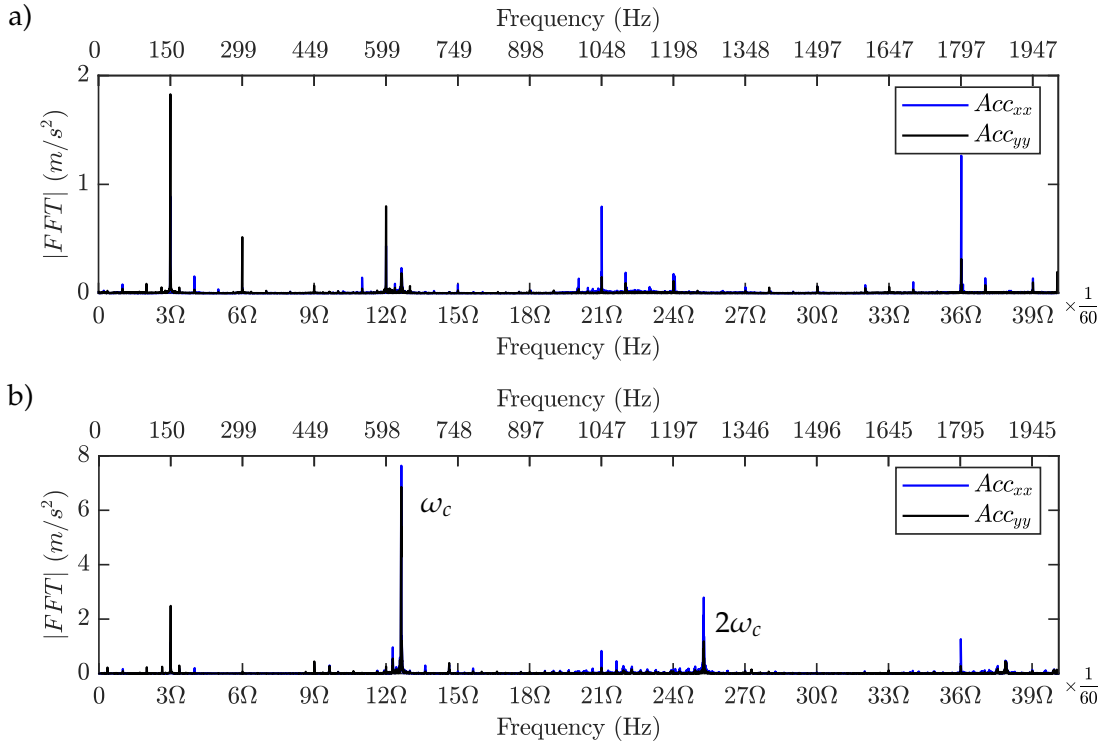

FIGURE 5.22: The FFT of acceleration signals for two cutting scenarios a) Stable b) Unstable

For the case represented in Figure 5.22a, spindle speed was identified to be 2995 RPM where the third harmonic of spindle frequency, tooth passing frequency, was observed to have the highest magnitude. A closer look into the frequency spectrum revealed that the rest of peaks correspond to harmonics of spindle speed due to the periodic nature of forcing frequency (spindle frequency). This meant that the process was stable in Figure 5.22a. On the contrary, spindle speed was identified to be 2992 RPM in Figure 5.22b. In here, the magnitude of the third harmonic of spindle frequency, tooth passing frequency, was observed to be much lower than the peak at 630 Hz. This peak was found not to comply with forcing frequency (spindle) harmonics and was found to be located close to the tool-spindle shaft mode (around 650 Hz). All these indications strongly pointed out that the peak was a chatter frequency at tool-spindle shaft mode.

Similarly, the FFT of microphone data for the cases in Figure 5.22 was analysed and presented as in Figure 5.23 below.

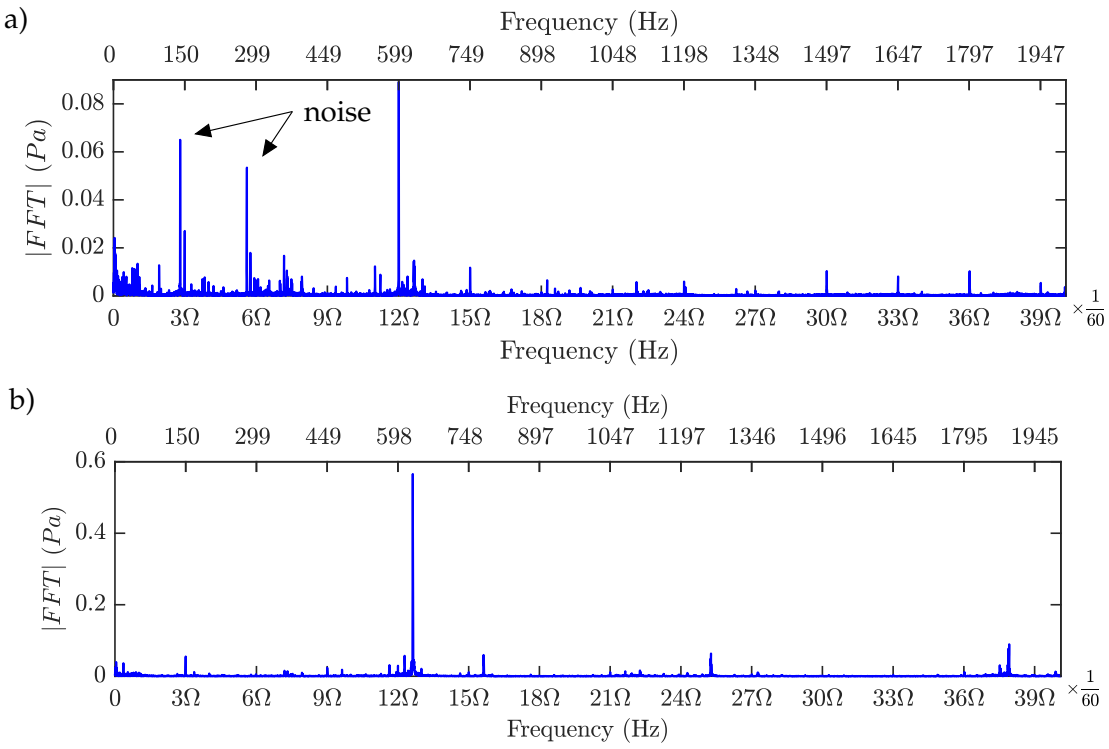

FIGURE 5.23: The FFT of microphone signals for two cutting scenarios a) Stable b) Unstable

FFT of microphone data was found to collect noise coming from nearby machines in the workshop floor as well as from the cutting process. The peak at 140 Hz and its harmonic at 280 Hz were identified to be noise coming from the nearby machine as they appeared in all of the collected microphone data. Ignoring peaks at 140 and 280 Hz, FFT of the microphone data showed exactly the same findings as in Figure 5.22; stable operation due to the dominance of harmonics of forcing frequency in Figure 5.22a whereas chatter frequency and its harmonics were observed in Figure 5.22b.

Likewise, for the rest of the operations, stable and unstable operation characteristics from both acceleration and microphone signals were identified and the stability of the process was concluded. This summarises the methodology followed to identify the stability of milling operations.

5.9 Influence of cross-FRFs on quasi-static zero frequency stability predictions

Structural modes of the robot were shown to have strong cross coupling at low frequencies owing to its asymmetrical and slender architectural structure as in Figure 5.13. The strong cross coupling between modes of vibration could potentially have an influence on the behaviour of the chatter mechanism.

In this respect, the effect of cross-FRFs on zero order quasi-static regenerative stability predictions was investigated for the machining parameters given in Table 5.1. The stability predictions obtained from structural modes of vibration of the robot are presented with and without cross-FRFs at low spindle speed regime in Figure 5.24.

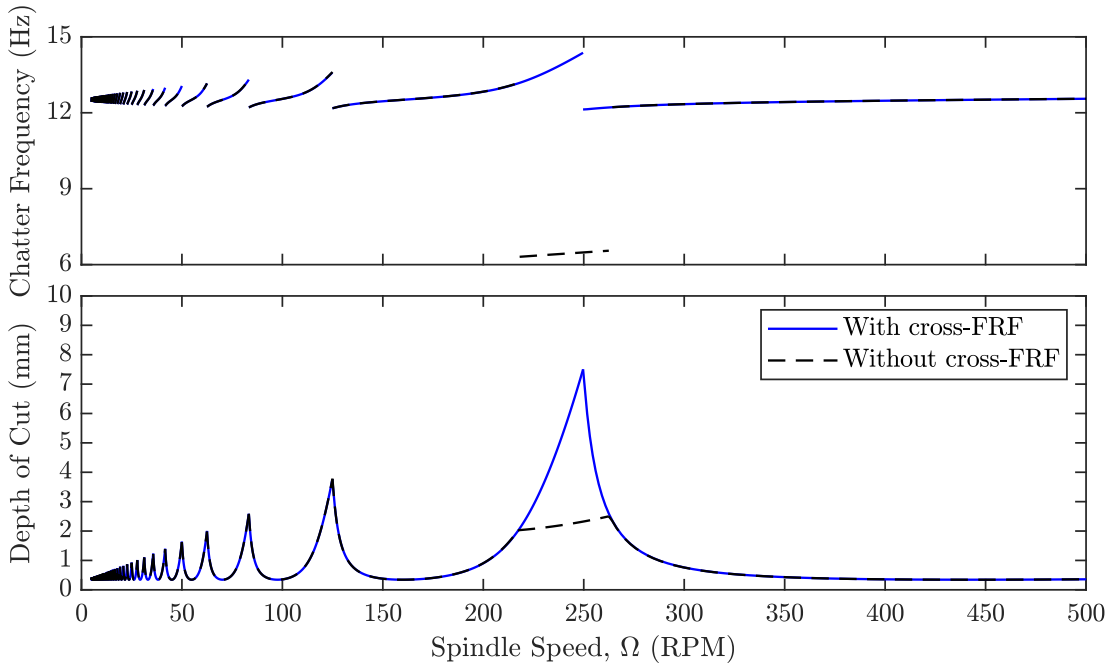

FIGURE 5.24: The low-spindle speed stability predictions at $P1$ when γ=2π

The accuracy of the stability prediction was observed to be highly affected by the cross coupling between the structural modes of vibration at low spindle speeds. Omitting cross-FRFs from the stability analysis was observed to cut-off the stability region located around 200-300 RPM with the stability boundary resulted from the mode of vibration around 6 Hz. On the other hand, consideration of cross-FRF terms indicated that the stability was not actually affected by the stability boundary appearing due to the mode of vibration at 6 Hz. Therefore, it was deduced that due to highly coupled low frequency structural modes, cross-FRFs needed to be taken into account while computing zero order quasi-static regenerative stability predictions.

On the other hand, the tool holder-spindle shaft mode of vibration was observed to show much less cross-coupling as shown in Figure 5.16. Nevertheless, the effect of cross-FRFs on stability predictions were investigated as in Figure 5.25.

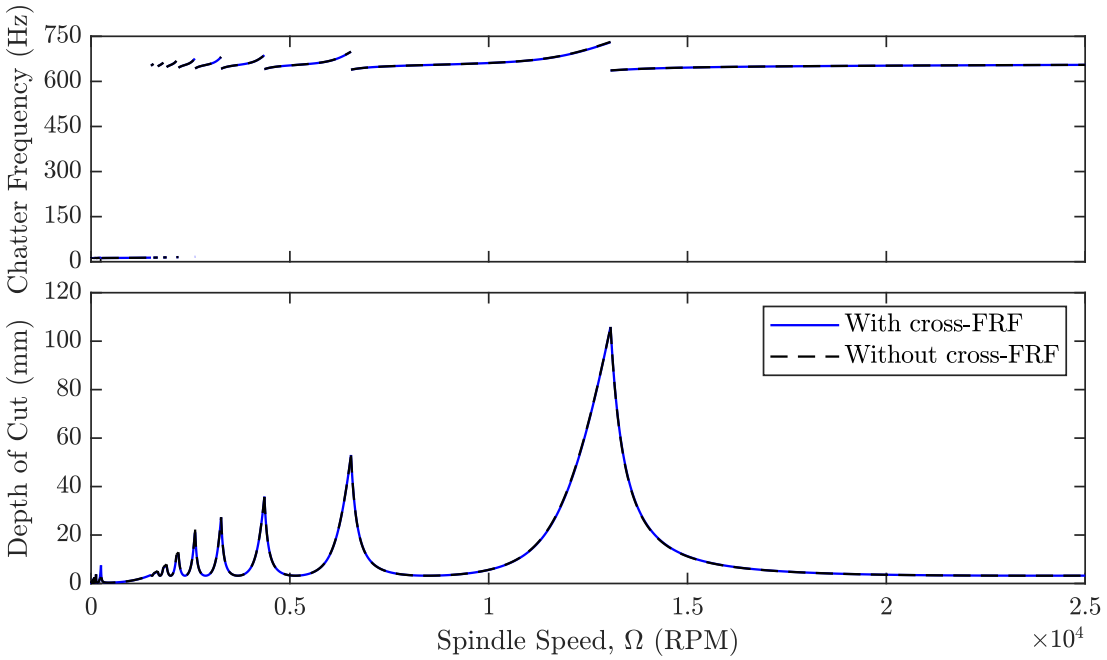

FIGURE 5.25: The high spindle speed stability predictions at $P1$ when γ=2π

The comparison between stability predictions with and without cross-FRFs revealed that there was not a considerable change in the predicted process stability, hence, its effect on stability predictions could be concluded to be insignificant.

All in all, it was proven that, the accuracy of stability predictions was affected by cross-FRFs of the manipulator structural modes at low frequencies. However, stability predictions were shown to be largely unaffected by the cross coupling of the higher frequency tool holder-spindle shaft mode of vibration. This could be attributed to the tool holder-spindle shaft mode of vibration having relatively low cross coupling.

5.10 Quasi-static zero frequency regenerative stability predictions & validation

The quasi-static zero frequency regenerative stability predictions (predictions while the structure is assumed to be instantaneously stationary) at $P1$, $P2$, $P3$ and $P4$ were obtained for all redundancy variables with the state space model of FRFs. This was to investigate the effect of varying structural dynamics as a result of tool translation on the process stability. Workpieces were machined along the designed trajectories by keeping the redundancy variable constant (tool tip motion involves only translation along positive X_{Base}). The predictions were analysed in two different spindle speed regions namely low spindle speed and high spindle speed regions. In these regions, the effect of structural and tool-spindle shaft modes on the regenerative stability was examined.

5.10.1 Low spindle speed region

The low cutting speeds are usually used to machine difficult-to-cut materials. Spindle speeds are slowed down when machining materials with low machinability in order not to cause high temperatures at the cutting zone and excessive tool wear. In this case, stability predictions were obtained and validated for redundancy variables, γ=[1.5π, π] at all tap testing locations to show the stability variation as robot followed the trajectory. In this respect, the quasi-static stability prediction when the redundancy variable was set to γ=1.5π is shown in Figure 5.26.

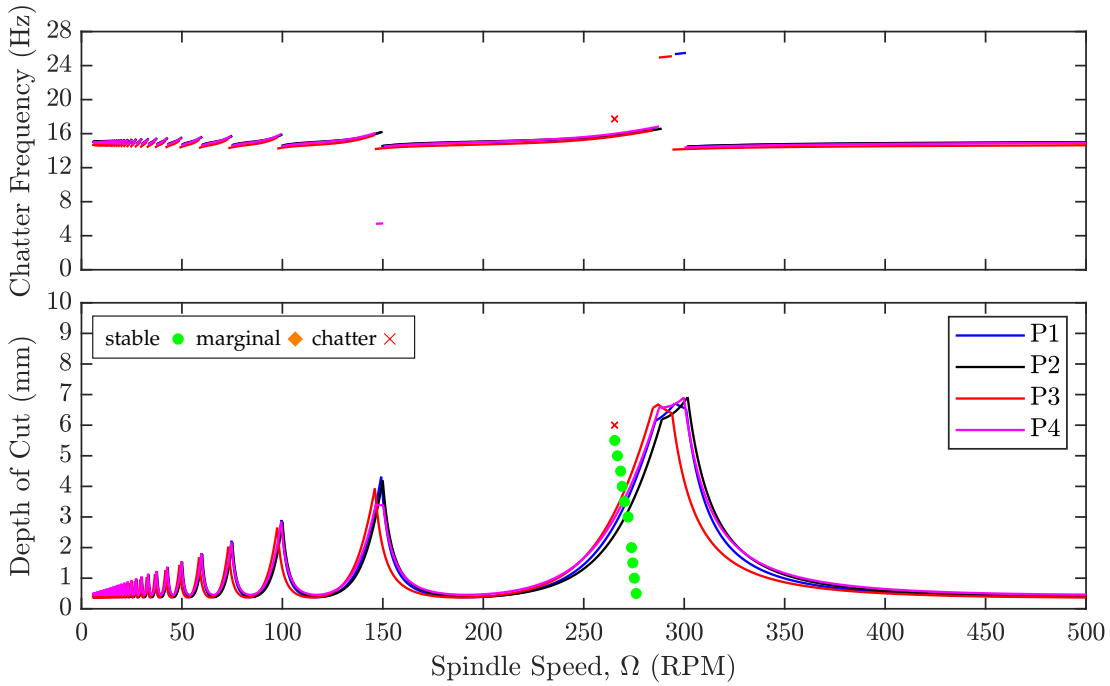

FIGURE 5.26: The low-spindle speed regenerative stability predictions at all tap tested poses when γ=1.5π

Predictions depicted that the stability is not affected significantly when the tool tip was translated to tap testing locations which was analogous to Figure 5.14. The presence of the lobe was validated by keeping spindle speed the same but increasing the depth of cut

even though spindle speed variation was observed. This was because the spindle was not able to compensate external torques created by the cutting process. The experimentally identified lobe seemed to be present at slightly lower spindles speeds than predictions.

Similarly, the redundancy variable was set to $\gamma=\pi$, and stability predictions were validated for a larger set of spindle speeds and depth of cuts as in Figure 5.27.

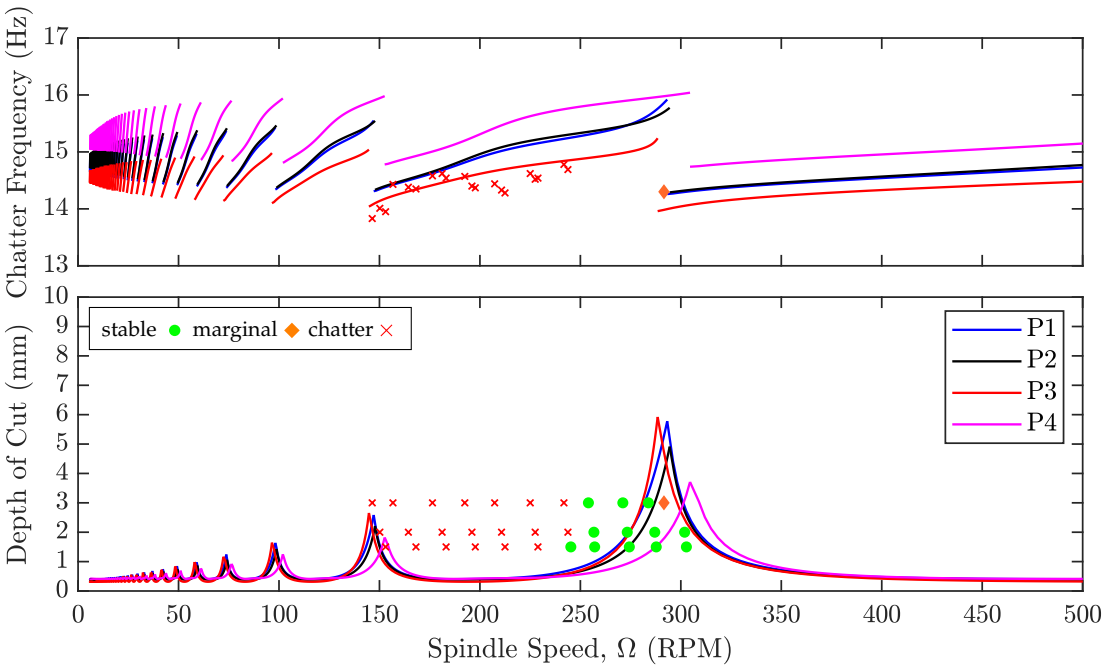

FIGURE 5.27: The low-spindle speed regenerative stability predictions at all tap tested poses when $\gamma=\pi$

In this case, stability predictions were observed to change to a greater extent compared to Figure 5.26. There was a larger shift in natural frequencies of structural modes of vibration because of a different choice of the redundancy parameter. Experimental findings depicted that the stability lobe was located at slightly lower spindle speeds than the predictions as in Figure 5.26.

On the whole, at lower spindle speeds, the dominance of structural modes of the robot was observed where tool holder-spindle shaft modes were damped out by the process. The predictions showed that depth of cut for stable cutting zones are quite low simply due to flexible robot modes. Predicted and validated lobe locations in Figures 5.26 & 5.27 did not perfectly match to each other. This could be due to the influence of the tool-workpiece interaction on flexible robot modes, the effect of the manipulator pose accuracy on the tool radial and axial immersion, inaccuracies in cutting force coefficients and the effect of inaccuracies in the state space model identification on the stability predictions. Also note that, large forced vibration amplitudes were observed at low-spindle speed tests for both chatter and stable cases which caused unacceptable surface finish on the workpiece.

5.10.2 High spindle speed region

Quasi-static stability predictions were validated in the high spindle speed region at all tap testing 5 DOF poses while keeping the redundancy variable the same. In that, predictions depicted the stability alteration due to the inherent configuration variation of the robot as the tool tip translated to each tap testing pose. For this reason, N=0 stability boundaries coming from low frequency structural modes are shown separately (dashed lines) to emphasise their behaviour. However, it should be noted that the process stability is dominated by the stability boundary having the lowest depth of cut for a given spindle speed in the SLD diagram.

The quasi-static stability predictions when the redundancy variable was set to γ=2π are shown in Figure 5.28.

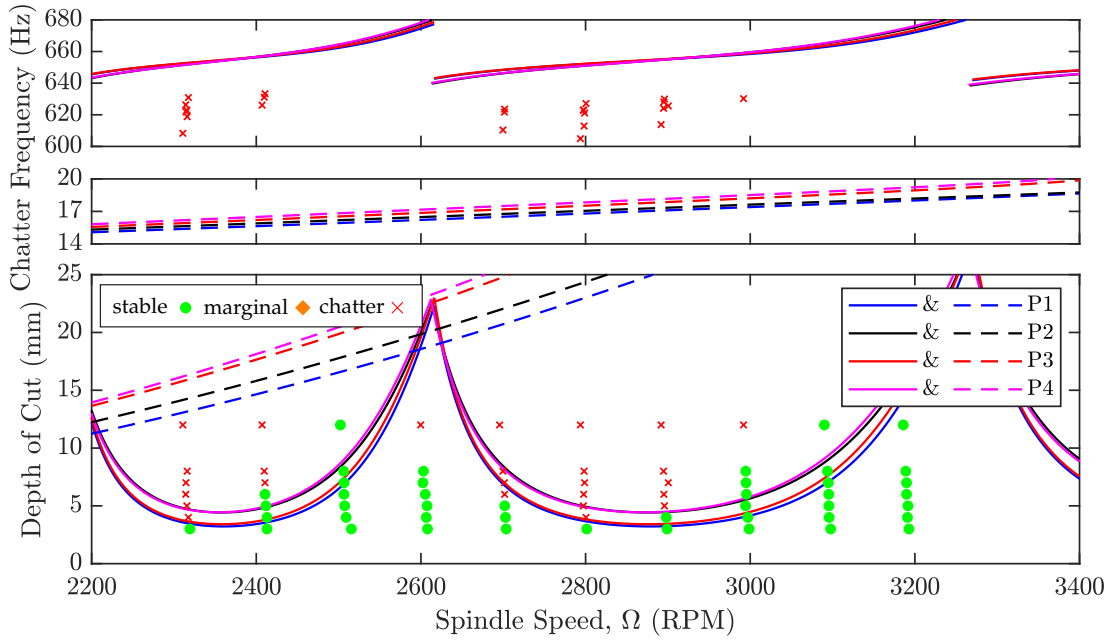

FIGURE 5.28: The high spindle speed regenerative stability predictions at all tap tested poses when γ=2π; solid lines: tool holder-spindle shaft mode & dashed lines: structural robot mode

Stability predictions indicated that two modes of vibrations dominated the considered spindle speed region; structural robot mode and tool holder-spindle shaft mode. Predictions from the robot structural mode were observed to vary due to the mode being affected by the robot configuration variation as the tool translated across tool path. On the other hand, lobes coming from tool holder-spindle shaft mode were observed to be at the same location even though the limiting stability was found to vary. This was analogous to the slight magnitude alteration of the tool holder-spindle shaft mode that was identified as in Figure 5.17.

Cutting tests were conducted to validate the presence of the lobes. Findings showed that there was a quantitative mismatch between the location of lobes predicted and experimentally validated (approximately 100 RPM difference). The mismatch could be due to cutting process influencing natural frequency of the tool holder-spindle shaft mode. Such a significant shift in the lobe location is not usually observed in machine tools but

the flexibility of robot could have amplified the effect. It should also be noted that chatter frequencies identified were close to the natural frequency of the tool holder-spindle shaft mode, therefore, the process stability wasn't affected by structural modes for chosen machining parameters and redundancy parameter.

Similarly, quasi-static stability predictions when the redundancy variable was set to γ=1.5π are shown in Figure 5.29.

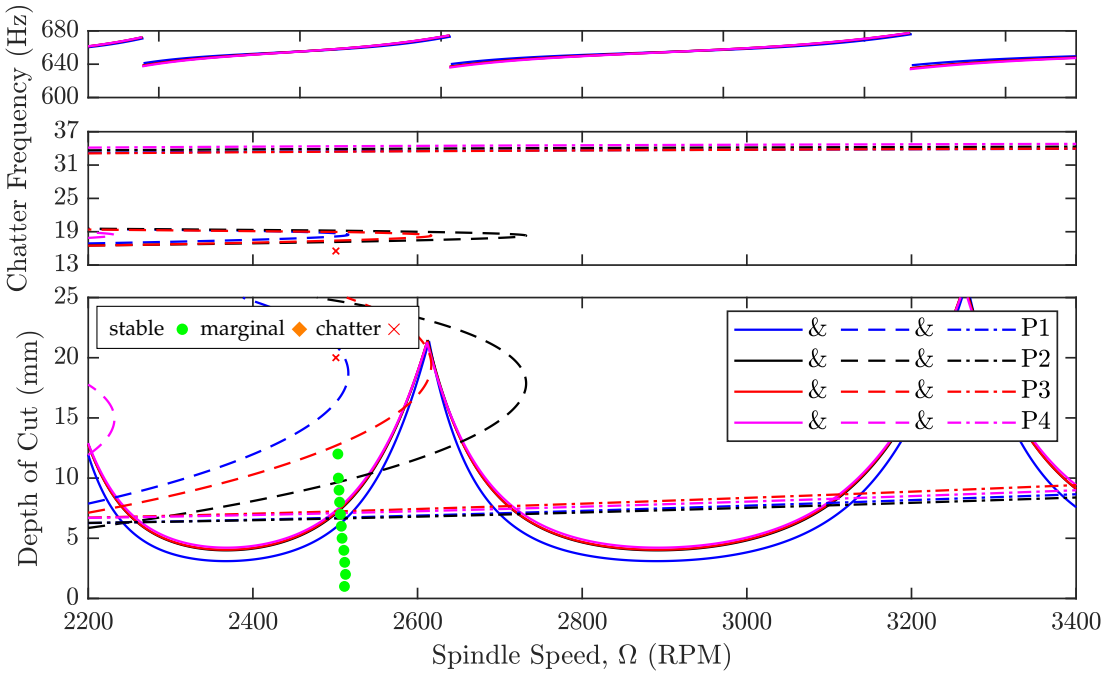

FIGURE 5.29: The high spindle speed regenerative stability predictions at all tap tested poses when γ=1.5π; solid lines: tool holder-spindle shaft mode, dashed lines: most flexible structural robot mode & dashed dot lines: structural robot mode around 35 Hz

Stability predictions for tool-spindle shaft mode showed similarity with Figure 5.28 in terms of lobe location and behaviour at the limiting depth of cut. On the other hand, stability predictions obtained from the most flexible structural robot mode at 14-15 Hz depicted strong dependency on the configuration of the robot. The N=0 lobes coming from the structural robot mode was observed to curve back. This was due to another closely spaced robot mode, having slightly higher natural frequency but lower magnitude. It was causing a secondary stability boundary on top of the most flexible structural mode and therefore curving the N=0 lobe. N=0 lobes corresponding to the robot mode around 35 Hz were observed not to be as strongly dependent to robot configuration.

Tests were conducted at constant spindle speed but various depth of cuts to identify the presence of the lobe. Findings showed that, the lobe was actually located 100 RPM lower than what it was predicted, similar to the observation made in Figure 5.28. Even though, the stability lobe coming from structural modes at $P2$ predicted instability, tests were all stable up until DOC=12 mm. At DOC=20 mm, however, a low-frequency chatter was observed at 15.5 Hz. Even though low-frequency chatter agrees with majority of the stability predictions coming from the structural robot mode, the possibility of mode coupling chatter should not be eliminated for unstable tests. Mode coupling chatter was

claimed to be present in robotic milling operations in the existing literature when milling at high spindle speeds. The presence of mode coupling chatter was claimed based on the low frequency characteristics of process instability which also fit the chatter frequency identified in the test. The tests showed that the process stability was not affected by lobes corresponding to the robot mode around 35 Hz which could be due to errors in state space model identification.

This time, the redundancy variable was set to $\gamma{=}\pi$ and the quasi-static stability predictions are shown as in Figure 5.30.

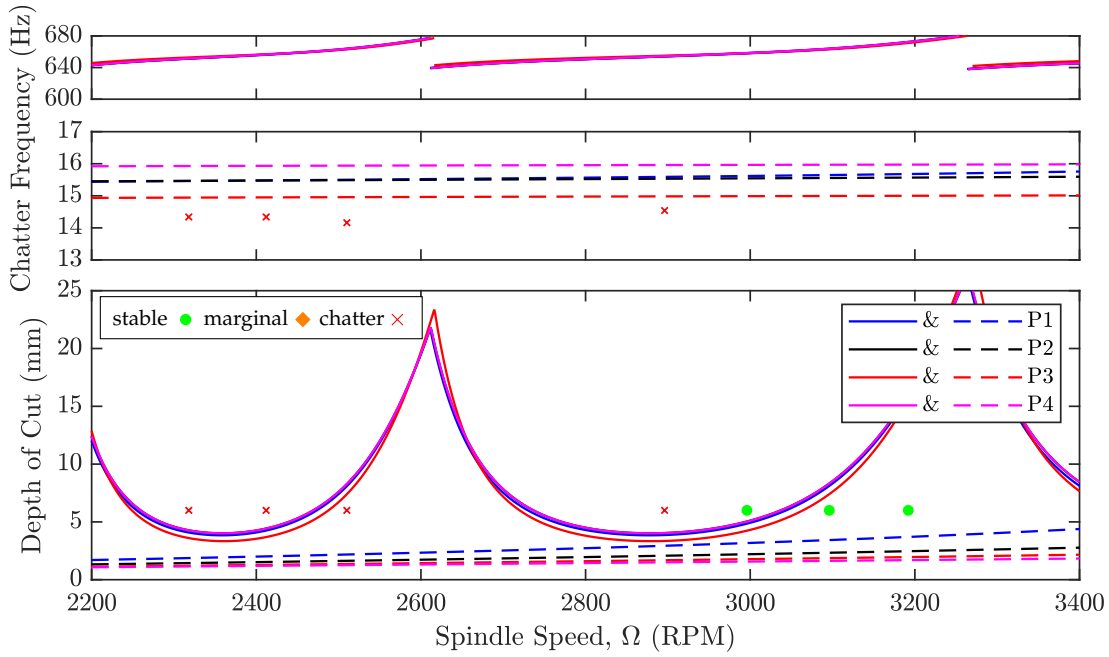

FIGURE 5.30: The high spindle speed regenerative stability predictions at all tap tested poses when $\gamma{=}\pi$; solid lines: tool holder-spindle shaft mode & dashed lines: most flexible structural robot mode

It can be seen that changing the redundancy variable strongly influenced stability predictions belonging to the most flexible robot structural mode around 14-15 Hz. Compared to Figures 5.28 and 5.29, lobes were predicted to have lower depth of cut across the same spindle speed region. The stability predictions coming from tool-spindle shaft mode at different tap testing poses showed similar behaviour; unaffected lobe locations but magnitude variations especially at lobe peaks and dips were observed.

Tests were carried out at different spindles speed while keeping the depth of cut the same. At the chosen depth of cut, all tests were expected to chatter at the structural robot mode. Findings showed that four cuts chattered close to the structural robot mode whereas three cuts resulted stable process. Unstable tests agree well with the prediction giving a chatter frequency close to the structural robot mode. The ones corresponding to the stable process, did not agree with predictions. The disagreement between the predictions and the tests could be due to various reasons such as the inaccuracies in the identified FRF and mode coupling chatter. The presence of the low frequency chatter behaviour at considerably high spindle speed with severe magnitude of vibrations suit characteristics of

mode coupling chatter as discussed in the literature [37, 152, 178, 180]. The low flexibility of serial manipulators is known to favour mode coupling chatter and could potentially be the reason of low frequency chatter giving the fact that tests did not entirely agree with the predictions.

Finally, the quasi-static stability predictions corresponding to the robot configuration when the redundancy variable was set to γ=0.5π are shown as in Figure 5.31.

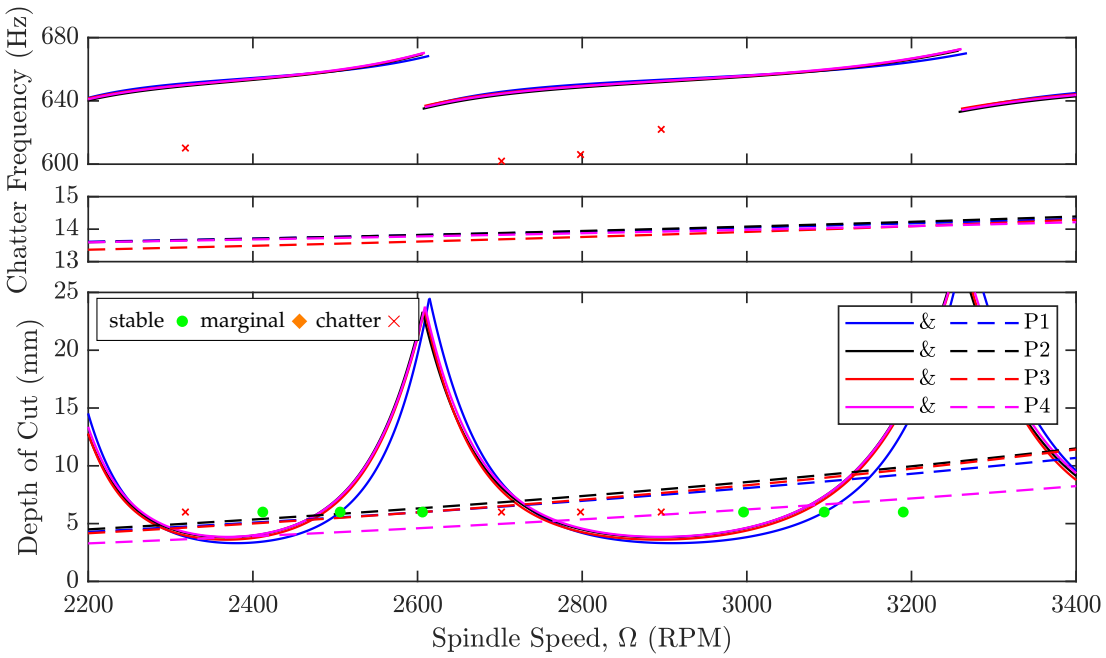

FIGURE 5.31: The high spindle speed regenerative stability predictions at all tap tested poses when γ=0.5π

As before, stability predictions at tool-spindle shaft mode showed similarity with predictions obtained at any other robot configuration obtained by altering the redundancy variable. The robot structural mode around 14-15 Hz, however, depicted similarity with Figure 5.30 with N=0 lobes passing close to the limiting depth of cut for stability predictions at the tool holder-spindle shaft mode.

Experimental tests showed that the process stability was dominated by the tool holder-spindle shaft mode even though some of the tests were predicted to be unstable by N=0 lobe boundaries of the most flexible robot structural mode. The tests predicted to be unstable happened to be very close to the N=0 lobe of the robot structural mode. Any inaccuracies in stability predictions could have contributed to the false prediction of the process stability.

5.10.3 Possible sources of errors

A quantitative disagreement between quasi-static stability predictions and tests were observed. The disagreement could be due to many factors affecting the accuracy of stability predictions. The following are possible sources errors that could have caused the disagreement;

- Throughout the experiment, the *WorkObjectFrame* was defined every time a new workpiece was clamped. *WorkObjectFrame* definition relies on the capability of operator as it requires manual set-up (3 tool tip pose measurements) and is prone to human related errors. Thus, the TCP pose with respect to workpiece could be affected by inaccuracies every time a new workpiece was clamped. The perpendicularity of the tool, radial immersion and depth of cut are the parameters that could be influenced by inconsistencies in *WorkObjectFrame*.
- The shift in the location of the stability lobes could potentially indicate that poor structural dynamics of the manipulator was affected by the contact and interaction of tool with workpiece. The contact and interaction of tool and workpiece could have possibly altered natural frequencies of modes of vibration. This could be a possible explanation for the quantitative mismatch between predicted and validated lobe location.
- The poor static rigidity of the robot could also have contributed to undercutting in radial and overcutting in axial directions (lower radial immersion and higher depth of cut). Additionally, the configuration dependent static stiffness could have also resulted variations in static deformation of the TCP. Thus, the identified process stability could have differed from what was predicted for the given machining parameters.
- The low frequency spectrum of FRF was not identified at the tool tip. This meant that the identified FRFs did not describe structural dynamics at the point where the cutting process took place. FRFs being used in the low spindle speed stability predictions hence, could incorporate inaccuracies in stability predictions.
- Manipulator dynamics at low frequencies were found to demonstrate non-linearities especially at mode peaks. Additionally, cross-FRFs were observed to partially disobey the reciprocity assumption utilised in the state space model. Considering the non-linearities and dissimilarity of cross-FRFs, the state space model might not have represented structural dynamics accurately causing inaccuracies in the stability predictions.
- The cutting force coefficients used in stability predictions were for the tool with same geometry and number of flutes but different helix angle (25°) at 1300 RPM for the same material. The helix angle and the spindle speed at which coefficients were identified could have an impact on the accuracy of the stability predictions.
- The poor TCP pose accuracy of the robot could have caused inaccuracies in the radial immersion and depth of cut of the tool throughout the tests. Changes in the radial immersion and depth of cut could have caused mismatch between stability predictions and test findings.
- Application of the mechanistic model of cutting forces to machining acetal copolymer could also introduce inaccuracies in prediction and hence stability of cutting forces.

Besides, it is known that helix angle could potentially effect the magnitude of cutting force coefficients; K_{tc} and K_{rc} [219]. Using cutting force coefficients identified with a similar tool but with a different helix angle could also cause inaccuracies in stability predictions.

5.10.4 Summary

The summary of robotic milling tests are presented as below;

- The low spindle speed process stability was found to be dominated by the most flexible, low frequency structural mode. This mode was slightly affected by the manipulator configuration alteration as a result of the tool translation along the cutting trajectory. The extent to which FRFs were influenced however, was observed to depend on the choice of manipulator configuration and the length of tool translation. Thus, low spindle speed stability boundaries were found to be marginally influenced based on variations observed in FRFs. However, cutting tests depicted that there was a quantitative mismatch between predicted and validated stability boundaries.
- The high spindle speed stability boundaries were found to be dominated by multiple modes; tool holder-spindle assembly mode around 650 Hz, most flexible structural robot around 12-15 Hz and structural robot mode at 35 Hz. The identified tool holder-spindle shaft mode was observed to show minor dependency on the manipulator configuration variation as a result of tool translation along the cutting trajectory. The stability predictions coming from tool holder-spindle assembly mode were observed to yield slight variations in the limiting depth of cut along the cutting trajectory. However, the $N = 0$ lobe belonging to structural robot showed stronger dependency. The cutting tests chattered at low and high frequencies depending on the choice of spindle speed and depth of cut. A quantitative mismatch was observed between the predicted and identified stability boundaries. The mismatch could be due to experimental factors or mode coupling chatter mechanism as per the claims in literature. On the other hand, instability due to the stability boundaries belonging to the structural robot at 35 Hz was not encountered in the cutting test.

5.11 Effect of continuously varying structural dynamics on the stability

The effect of manipulator configuration variation as a result of the tool tip translation along the cutting trajectory on the process stability was concluded to be substantial by cutting tests. However, alteration of the redundancy variable even at a single 5-DOF pose was observed to cause more significant structural dynamics variations which could result in further variations in the process stability. Hence, managing the redundancy variable could enable process stability control by selectively choosing robot configurations during machining. In addition to that, continuously sweeping through different robot configurations during cutting could also enable chatter stabilisation and/or avoidance.

On this basis, the functional and kinematic redundancy of ABB IRB 6640 205/2.75 around the axis of rotation of tool was utilised to controllably alter its configuration, and therefore its dynamics, as the tool translated along a straight cutting trajectory. The robot was continuously configured starting from the redundancy variable γ=2π progressing to γ=1.5π, π and 0.5π at last. As before, two spindle speed regions were considered to test viability of the hypothesis; low & high spindle speed regions. Machining parameters were kept the same as in Table 5.1. The transition between redundancy variables to alter the robot configuration was ruled by the TCP pose rotation velocity which was 6000 $^\circ/sec$ for both spindle speed regions. This was to ensure quickest variation of structural dynamics of the robot even though it wasn't practically achievable. The actual rotational velocity, however, got saturated and limited by the controller based on the magnitude of Cartesian feed of tool tip.

Note that, while cutting, accelerometers located on the spindle holder were also rotated in harmony with the TCP orientation. This meant that accelerometer axes were also rotated together with the robot TCP orientation. For this reason, acceleration data from both accelerometers was analysed and compared for chatter identification.

5.11.1 Low spindle speed region

For low spindle speed tests, spindle speed was kept at 270 RPM and depth of cut was altered to investigate the effect of varying dynamics on the process stability. To rotate the TCP pose, the cutting length (50 mm) was divided into sections where robot had a defined redundancy variable across the cut as shown in Figure 5.32.

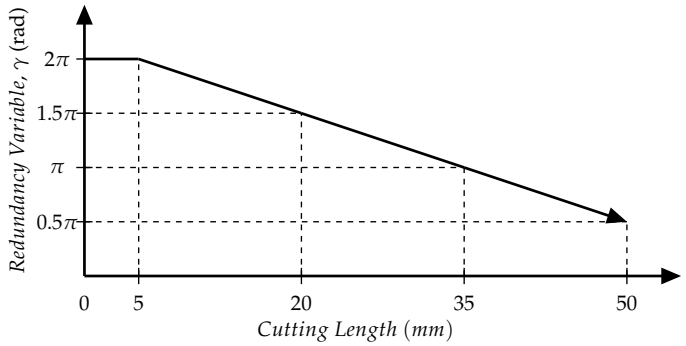

FIGURE 5.32: Transition between redundancy variables across the cutting length at low speeds

Having defined the cutting trajectory for the robot, quasi-static stability predictions at $P1$ and validations for the low spindle speed tests are depicted in Figure 5.33 (the findings at $P2$ can be found in Appendix I).

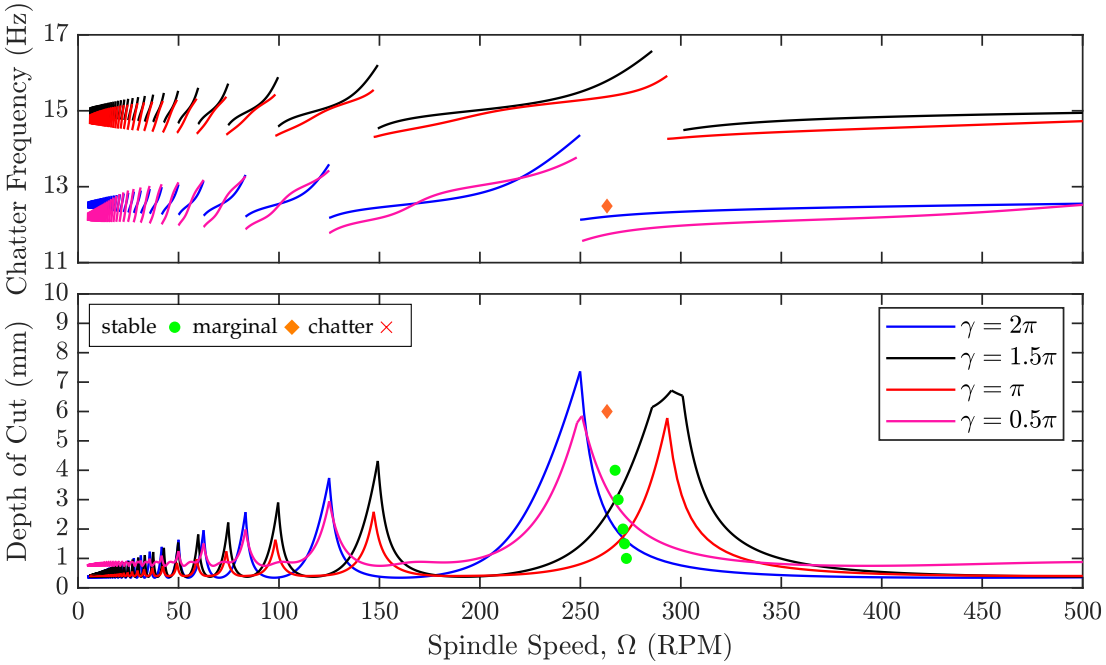

FIGURE 5.33: The low-spindle speed stability predictions at $P1$ for all redundancy variables, γ

As expected, at low spindle speeds, the dominant structural mode dominated the process stability. Altering redundancy variable at the same tap testing pose, $P1$, was observed to shift stability lobes in spindle speed spectrum. This was due to frequency shift in the natural frequency of most flexible structural mode as seen in Figure 5.15. The stability variation observed was larger than that obtained by simply keeping the redundancy variable same and translating the tool tip as in Figures 5.26 and 5.27. This implied that altering redundancy variable, γ had a greater impact on the structural mode compared to simply translating the tool tip with constant redundancy variable. This was due to the relatively more significant manipulator configuration variation. The tests showed that the process stability was found out to be stable except for at 6 mm DOC. The FFT of acceleration data from both accelerometers are depicted as in Figure 5.34 for 4 mm DOC.

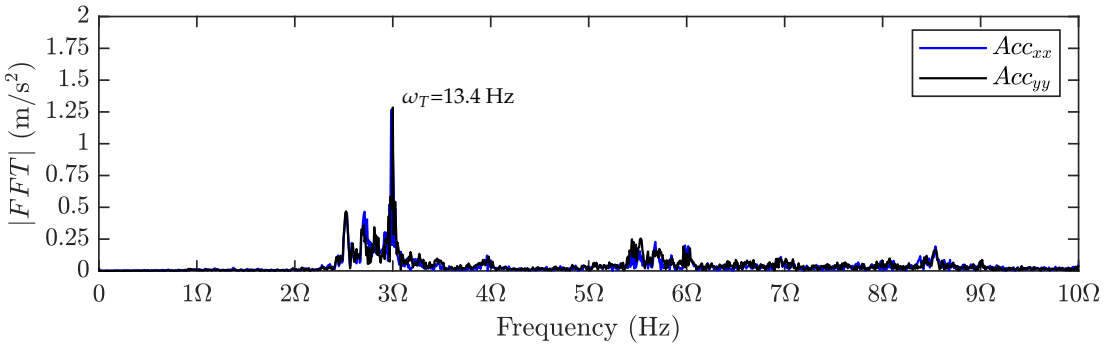

FIGURE 5.34: The FFT of acceleration data while the robot reconfigured itself through the cut at low-spindle speed at 4 mm DOC

It can be seen that dominant frequency was the tooth passing frequency at ω_T=13.4 Hz for both acceleration data (which agreed with the the tooth passing frequency identified from hall effect sensor 13.4 Hz). Hence, at 4 mm DOC, the process was concluded to be stable even though it was predicted to be unstable. Nevertheless, taking the potential uncertainties arising in predictions into account, the process being found out to be stable at 4 mm DOC could not be accepted as a strong indication of chatter stabilisation.

For completeness, the FFT of acceleration data from both accelerometers are depicted as in Figure 5.35 for 6 mm DOC as below.

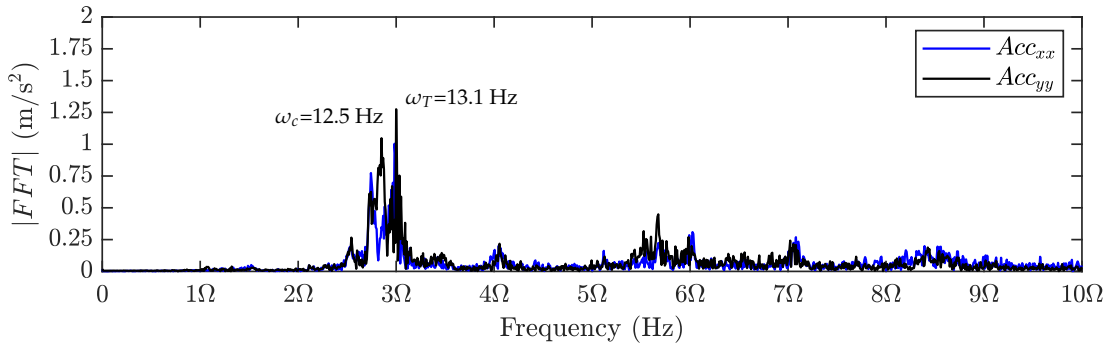

FIGURE 5.35: The FFT of acceleration data while the robot reconfigured itself through the cut at low-spindle speed at 6 mm DOC

Findings showed that there was a competing peak at ω_c=12.5 Hz which could be referred as chatter frequency besides the tooth passing frequency ω_T=3Ω=13.1 Hz. Even the magnitude of peak was slightly smaller than that of tooth passing frequency, they were comparable. Also, the magnitude of peaks could be affected by the choice of steady state region of the cutting process while analysing test data. Hence, the stability of the process was deduced to be marginal.

5.11.2 High spindle speed region

At high spindle speed region, a single spindle speed was tested at 2700 RPM and depth of cut was altered in pursuit of examining the influence of varying dynamics on the process stability. In this respect, the cutting length was divided into sections to allow transition between redundancy variables, γ, across the cutting length as in Figure 5.36 analogous to Figure 5.6.

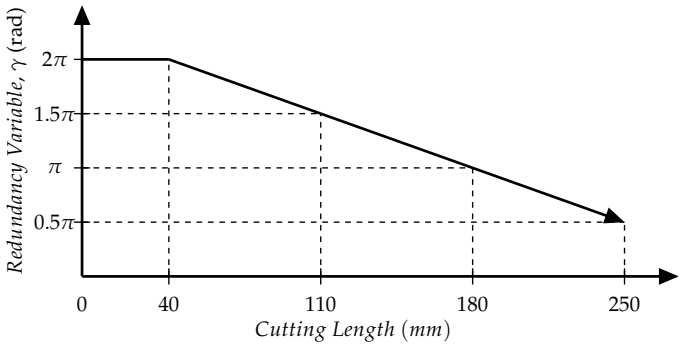

FIGURE 5.36: Transition between redundancy variables across the cutting length at high speeds

The tests were carried out across the length of the rectangle workpiece between $P3$ and $P4$. Like previously, quasi-static stability predictions at $P3$ and validations are depicted in Figure 5.37 (the findings at $P4$ can also be found in Appendix I).

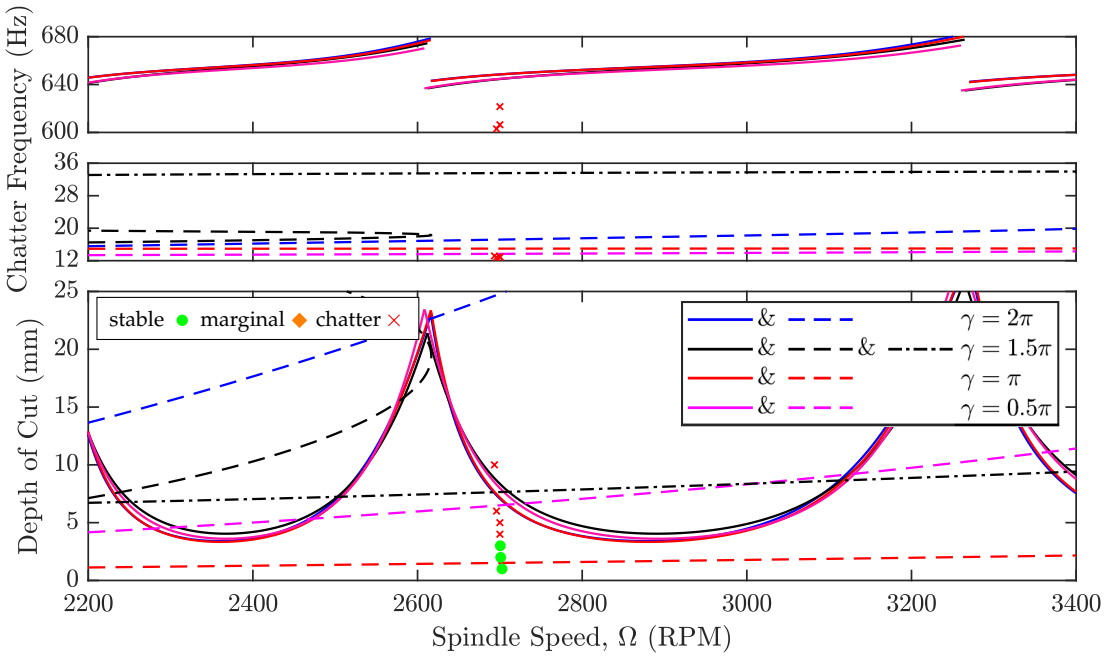

FIGURE 5.37: The high-spindle speed stability predictions at $P3$ for all redundancy variables, γ

In the region considered, the process stability was found to strongly depend on the N=0 lobe of most flexible configuration dependent structural robot mode around 14-15 Hz. The extent of configuration variation achieved by altering the redundancy variable, γ across

the cut resulted in the stability boundary and hence, chatter frequencies to shift between structural and tool-spindle assembly modes in the predictions. This means, based on the choice of machining parameters, the robot configuration determines stability limits and which mode of vibration dominates the process stability.

In tests, the process stability was found to be stable until 3 mm DOC. Thereafter, the process was found out to chatter at two different frequencies which corresponded to most flexible structural robot mode and tool holder-spindle shaft mode as shown in Figure 5.37. Findings supported predictions on the configuration dependent stability boundaries and chatter frequency shift due to the configuration variation of the robot across the cut. Note that, the chatter frequency from the mode around 35 Hz didn't appear in tests as per underlined before. The FFT of acceleration data from both accelerometers were plotted for more detailed analysis of chatter frequencies at 5 mm DOC in Figure 5.38.

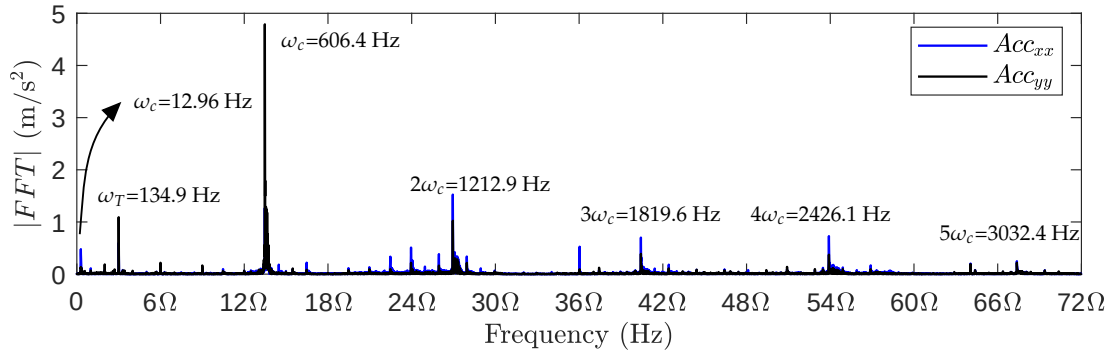

FIGURE 5.38: The FFT of acceleration data from both accelerometers while the robot reconfigures itself through the cut at high-spindle speed at 5 mm DOC

The frequency content of acceleration data revealed chatter frequency at 606.4 Hz was the dominant frequency within the process compared to forced vibrations observed at tooth passing frequency at 134.9 Hz. The harmonics of chatter frequency at 606.4 Hz were also clearly present up until its 4^{th} harmonic. In addition to that, a low frequency chatter frequency was observed at 12.97 Hz which came from most flexible structural mode of the robot. Chatter frequencies clearly depicted that the process was unstable and instability was caused by different modes of vibrations in the system.

In order to investigate how the instability developed and which modes of vibration dominate the stability while the redundancy variable was altered, the time varying frequency content of the process was analysed in spectrogram. The spectrogram was based on short-time Fourier transform of one of acceleration data when cutting at 5 mm DOC and was shown in Figure 5.39. Note that, vertical black lines represent approximate location of the robot with a specific redundancy variable, γ, across the cutting length as per Figure 5.36 and cutting time.

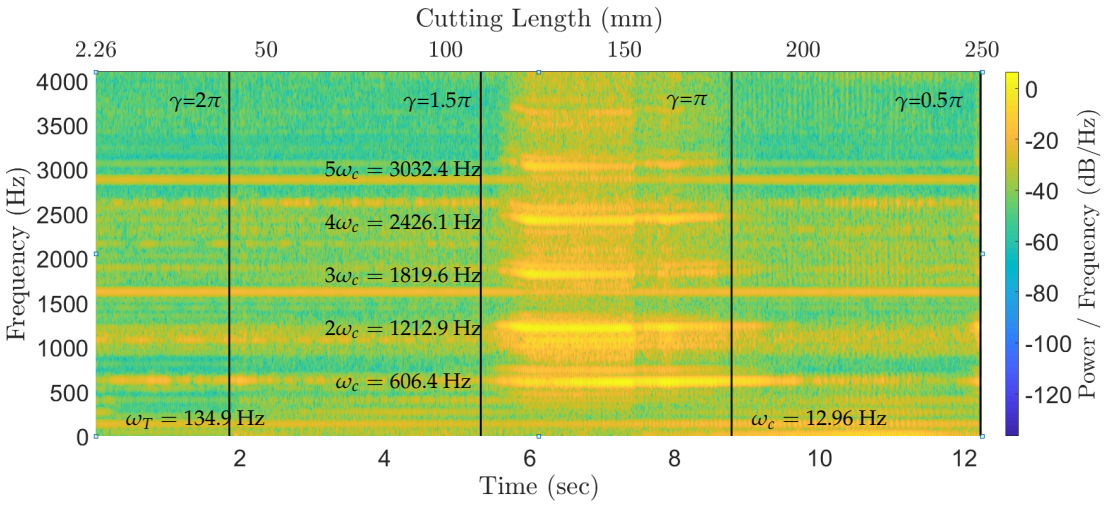

FIGURE 5.39: The spectrogram of the acceleration data while the robot reconfigures itself through the cut at high-spindle speed at 5 mm DOC

It could be seen that the process was stable between configurations with redundancy variable, γ=$[2\pi, 1.5\pi]$ which agreed with the predictions as in Figure 5.37. As the redundancy variable was altered from γ=1.5π to π, the process was observed to chatter around tool holder-spindle shaft mode at 606.4 Hz. The process chattered around the tool holder-spindle shaft mode even though predictions stated the process to be stable for tool holder-spindle shaft mode but unstable for robot structural mode. It should be noted that, experimentally identified stability lobes were 100 RPM shifted in spindle speed domain compared to the predictions. Therefore, instability around the tool-spindle mode actually agreed with experimentally identified lobes. Also, predictions depicted that the transition between redundancy variables slightly altered the stability boundary coming from the tool holder-spindle shaft mode as in Figure 5.37. This explains the stability transition from stable to unstable at tool holder-spindle shaft mode observed in the spectrogram. The process chattered (at 12.96 Hz) around most flexible structural robot mode when the tool tip was approximately 150 mm (around 7.3^{th} seconds) in the cut which also agreed with predictions. The redundancy variable γ=π onwards, the instability was dominated by structural robot mode chattering at a low frequency. The predictions agreed with frequency content in spectrogram where the process stability was predicted to be dominated by the N=0 lobe of most flexible structural robot mode between γ=$[\pi, 0.5\pi]$.

Altogether, predictions and tests were found to agree fairly with each other however, no trace of chatter stabilisation was found. This could be due to the TCP rotation velocity not being quick enough to vary structural dynamics and acquire chatter stabilisation. However, it is possible to control the configuration dependent N=0 lobe of most flexible structural robot mode by utilising the redundancy variable. In this way, at selective spindle speeds, low stability boundaries coming from most flexible structural robot mode could be enhanced by shifting the stability dependency to the tool holder-spindle shaft mode. By doing so, the detrimental low frequency chatter could also be avoided within that region.

5.12 Relation of static stiffness to regenerative stability

This section explores whether it is possible to optimise manipulator configurations to enhance the minimum limiting depth of cut directly from a static stiffness model of the robot, as modelled in Chapter 4. Such an approach would have the obvious advantage of not requiring a full dynamic model of the robot to optimise the process stability.

In Section 5.10, based on the choice of spindle speed, there were two candidates for critical (minimum) depth of cut due to MDOF structural dynamics of the manipulator. It was shown that low frequency structural mode dominated the stability in low spindle speed region whereas tool holder-spindle shaft mode dominated the high spindle speed region. For this reason, minimum depth of cut predictions for marginal stability obtained for low and high spindle regions are referred as $b_{c,low}$ and $b_{c,high}$ and shown in Figure 5.40.

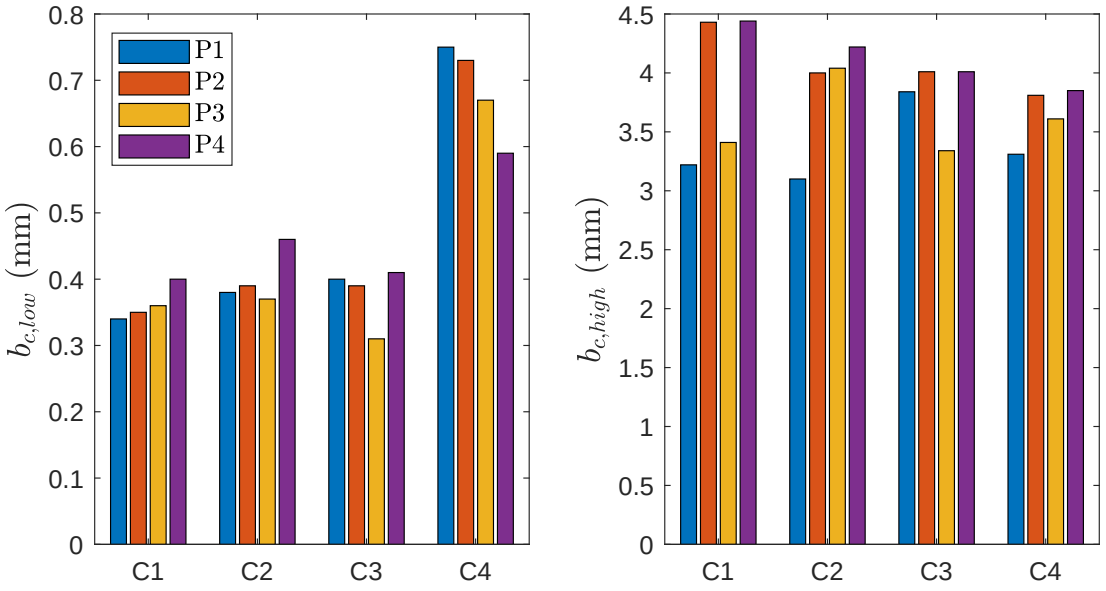

FIGURE 5.40: The minimum limiting depth of cut predictions by quasi-static zero frequency regenerative chatter approach

At low spindle speeds, $b_{c,low}$ was observed to be highest for manipulator configuration C4 among all tap testing poses (highlighted by a red circle) whereas a trend could not be observed in $b_{c,high}$ for high spindle speeds. This suggested that the manipulator configuration C4 certainly had an improved structural dynamics against regenerative chatter compared to other configurations. Hence, a question arises, whether the $b_{c,low}$ at manipulator configuration C4 can be related to static stiffness of the manipulator.

In this context, Cartesian compliance of the manipulator was analysed at all tap testing poses. Owing the fact that, regenerative chatter mechanism is known to be mainly affected by vibrations in the orthogonal direction of the axis of rotation of tool (X_{Base} and Y_{Base}), top left 2×2 entities of Cartesian stiffness matrix (left hand side of Equation 5.3) were considered. Cartesian compliance matrix can also be regarded as Frequency Response Function (FRF) of the structure at zero frequency, it can be visualised as;

$$\begin{bmatrix} c_{xx} & c_{xy} \\ c_{yx} & c_{yy} \end{bmatrix} = \begin{bmatrix} FRF_{xx}(0) & FRF_{xy}(0) \\ FRF_{yx}(0) & FRF_{yy}(0) \end{bmatrix} \tag{5.3}$$

In order to compare static compliance and minimum limiting depth of cut, direct compliance terms (c_{xx} & c_{yy}) were compared due to their dominant effect on the stability as highlighted by the oriented frequency response function in [200]. The comparison of direct compliance parameter predictions of manipulator configurations at all tap testing poses is illustrated in Figure 5.41.

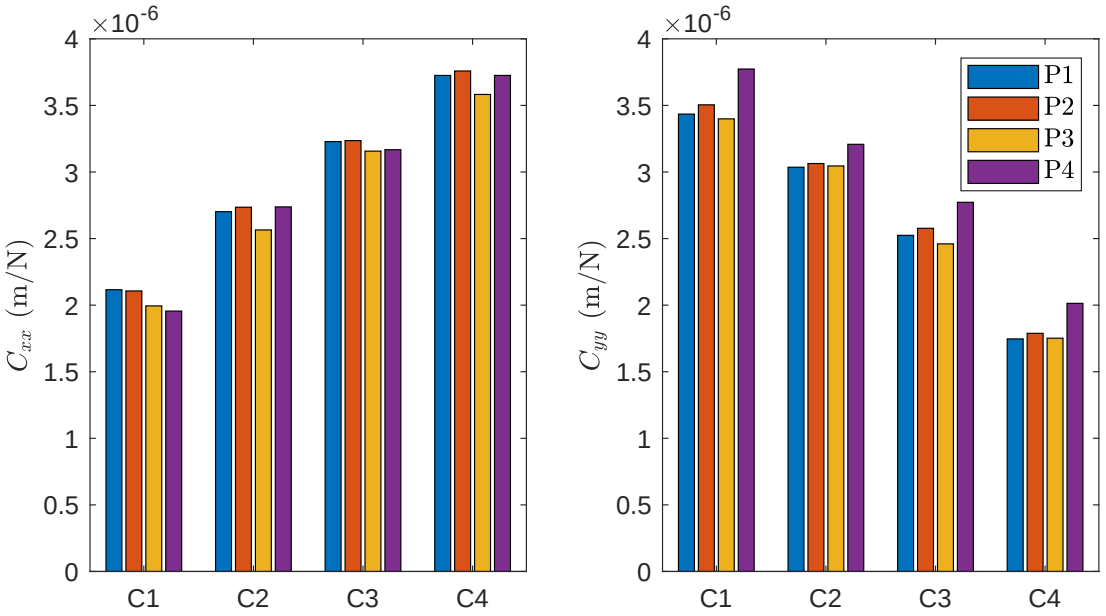

FIGURE 5.41: The compliance predictions by the manipulator stiffness model at the tap testing locations for each redundancy variable

The prediction for the compliance parameter c_{xx} was observed to gradually increase from manipulator configuration C1 to C4 whereas no trend was observed among the manipulator configurations having same redundancy parameter but different tap testing poses. However, c_{yy} was observed not only to decrease gradually from manipulator configuration C1 to C4 but also the manipulator configurations at P4 was found out to have the highest c_{yy} among the rest of tap testing poses.

Considering the behaviour of compliance predictions, however, there is no apparent relation between the static compliance (or stiffness) of the manipulator with the process stability. Even though a trend can be seen in the static compliance between robot configurations, it can not be related to a dynamic phenomenon which depends on machining parameters and dynamic characteristics of the system. Hence, the deployment of Cartesian compliance matrix to predict and optimise limiting stability boundaries is not feasible.

5.13 Discussion

Quasi-static stability predictions and cutting tests revealed that the process stability was affected by the manipulator configuration in low and high spindle speed regions. The degree of variation in the process stability was found to be related to the extent to which manipulator configuration was altered. The more the manipulator configuration was altered, the more the stability was affected.

Keeping the redundancy variable the same and only translating TCP was observed to yield slight stability boundary and location alterations in low and high spindle speeds. In low spindle speeds, the variation in minimum limiting depth of cut was negligible. In high spindle speeds, predictions indicated larger minimum limiting depth of cut variation as in [36, 155], while the lobe locations stayed the same. Nevertheless, no shift in the stability was observed during cutting tests in both low and high spindle speed regions. The identifiability of stability alterations, however, might have been obstructed by factors detailed in Section 5.10.3.

Overall, findings indicated that keeping the redundancy variable same and only translating TCP causes insignificant stability alterations due to the minor manipulator alteration as TCP translated 50-250 mm along the trajectory. Imperceptibility of any stability alteration in tests implied that the serial industrial manipulator behaved like a machine tool in milling as also noted in [34], in particular at high spindle speeds, along the considered cutting trajectories. This means that there is no need for a cumbersome modelling and identification of structural dynamic model of the manipulator, if cutting trajectories are relatively short. As such, an impact testing could provide enough information to ensure the choice of machining parameters would stay in stable zone.

Manipulator configurations with different redundancy variables revealed an entirely different scenario. Cutting tests and predictions justified that the N=0 lobe of structural mode altered significantly based on the manipulator configuration. Such an alteration of the N=0 lobe of structural mode gave birth to an opportunity of unveiling regions in the SLD that were previously unstable and hence, opportunities for chatter avoidance (as in Figure 5.28 compared to Figures 5.30 and 5.31). The manipulator configuration can be optimised by choosing an appropriate redundancy variable to make sure the N=0 lobe of structural mode diverges as fast as possible. Thus, previously unstable SLD regions would be uncovered in which the stability would be dominated by tool holder-spindle shaft mode. The strong dependency of stability boundaries coming from structural mode on the manipulator configuration can be utilised to enhance limits of robotic milling in the spindle speed region chosen for tests as illustrated in Figure 5.42 for stability predictions at P1.

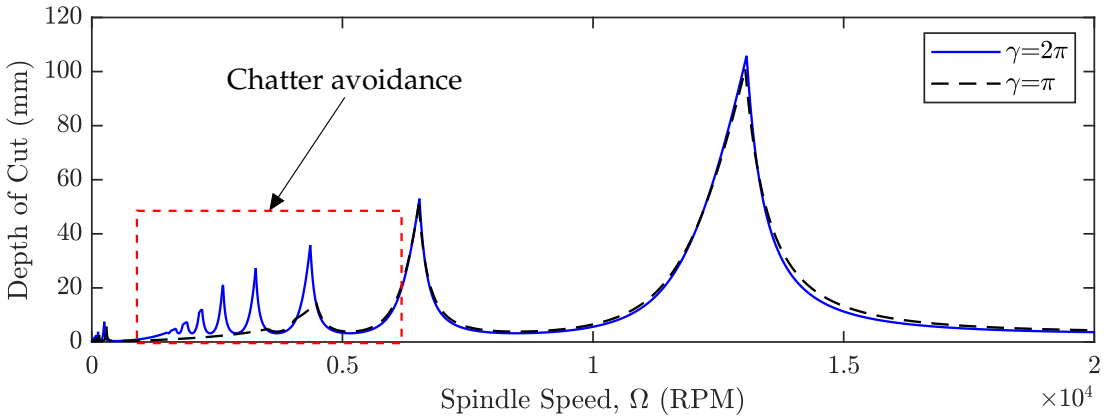

FIGURE 5.42: The manipulator configuration optimisation by controlling the redundancy variable to enhance robotic milling stability

Experimental findings motivated the possibility of achieving larger structural dynamics variation and hence, stability variation by not only translating TCP but also utilising the redundancy variable. In this context, the hypothesis, in which the effect of deployment of continuously varying structural dynamics of manipulator on the process stability characteristics was investigated with controlling the redundancy variable.

In the low spindle region, the manipulator configuration variation resulted in the natural frequency of dominant structural mode to slightly vary. The changes in natural frequency resulted the location of stability boundaries to shift in stability predictions. In this way, similar to chatter stabilisation based on continuous spindle speed variation, chatter stabilisation and avoidance were aimed by structural dynamics variation. Such a significant variation in the process stability was a great opportunity to investigate the effect of continuously varying structural dynamics on the process stability. However, the hypothesis was found inconclusive based on cutting tests; machining parameters were found to be insufficient to examine the hypothesis. Cutting tests could have been extensively carried out with a variety of spindle speeds and depth of cuts instead of a single spindle speed and a number of depth of cuts. Similarly, keeping the rotation velocity of TCP pose the same could also have had an effect on the stability, however, experimental findings were not enough to explore it in depth.

In high spindle speed region, quasi static stability predictions indicated that the stability of process could greatly vary based on the manipulator configuration. The stability predictions coming from tool holder-spindle shaft mode were observed to yield stability boundary variations as in [136, 137] which were validated with cutting tests too. However, stability predictions coming from most flexible structural mode greatly dominated the spindle speed region under consideration. The cutting tests revealed that process was first stable, then chattered at high frequency around tool holder-spindle shaft mode and then, at low frequency around most flexible structural mode. A chatter frequency shift from high to low frequency detrimental vibrations was experimentally observed, however, didn't unveil any chatter suppression and/or avoidance characteristics. In particular, the appearance of chatter suppression might have been related to the rotation velocity of TCP pose as in low spindle speeds. Having only tested a single rotation velocity throughout the tests might have hindered the identifiability of any chatter stabilisation effects. Higher the rotation velocity could possibly cause quicker stability alterations but without enough

number of tests, it is not possible to validate the hypothesis. In addition to that, the choice of spindle speed and depth of cut could have also varied to allow more extensive investigation of the hypothesis. Hence, the hypothesis can be said to be inconclusive at high spindle speed region too.

All in all, stability predictions and cutting tests revealed that there was a quantitative mismatch which could be due to various factors as listed in Section 5.10.3. The onset of low frequency chatter vibrations as well as the mismatch of stability predictions and tests around the N=0 lobe of most flexible structural mode motivated the presence of un-modelled effects, such as mode coupling chatter vibrations. The mode coupling mechanism in milling would be investigated in the next chapter.

5.14 Chapter summary

In this chapter, a robotic milling trial was designed and implemented in pursuit of validating regenerative stability predictions at low and high spindle speeds. Additionally, the hypothesis of chatter stabilisation by controlling configuration dependent dynamics of the robot was investigated.

First, an appropriate material was chosen to be used in the robotic milling trial that would increase the identifiability of regenerative stability boundaries that are usually very low. Then, geometric dimensions of spindle, tool holder and tool were defined that would enable computation of TCP kinematics. Having complete geometric model of the robot, its kinematic performance was analysed over the machining table based on computing Kinetostatic Conditioning Index (KCI). KCI of all manipulator configurations was found out by taking into account the redundancy of the robot around axis of rotation of tool. In this way, the location of workpiece was determined where the manipulator was most dexterous. Additionally, four redundancy variables were selected that do not encounter any singularities across cutting trajectories. These redundancy variables were aimed to be used to continuously vary configuration dependent structural dynamics of the manipulator for deployment of the hypothesis of chatter stabilisation.

The experimental set-up and machining parameters used in cutting tests were detailed which were essential in computation of stability predictions. After that, the experimental impact testing was conducted. This was to identify structural dynamics of the manipulator at the chosen redundancy variables and tap testing poses. Then, MDOF state space model of robot structural dynamics was obtained from experimentally identified FRFs which was aimed to be utilised for zero frequency stability predictions. Having identified the state space model, the procedure for chatter identification was depicted in which a microphone and accelerometers were used for cross validating the findings.

The quasi-static stability predictions were, then, computed based on chosen machining parameters. First, stability predictions with and without cross-FRF terms were compared in low and high spindle speeds to justify the importance of mode coupling on the stability. Then, stability predictions for manipulator configurations were computed for manipulator configurations that involve only tool tip translation. The findings depicted that, at low spindle speeds, configuration dependent robot modes dominate the process stability and cross-FRFs play an important role in the accuracy of stability predictions. The experimentally identified stability lobes were found to be located at slightly lower spindle speeds. It was shown that predicted and identified stability boundaries did not depend

on the manipulator configuration alteration as a result of the TCP translation along the cutting trajectory. Nevertheless, the choice of the redundancy parameter could play an important role on stability boundaries. At high spindle region, stability predictions were influenced by both structural robot and tool holder-spindle shaft modes. The N=0 lobes coming from most flexible robot structural modes were found out to be still dependent on the robot configuration (predominantly to redundancy variable) and influenced the process stability at chosen spindle speeds. Nevertheless, N=0 lobe corresponding to robot structural modes was observed to rise slowly but steadily at higher spindle speed regions and process stability tends to depend on higher modes of vibrations such as tool-spindle assembly mode. Most importantly, at high spindle speeds, an appropriate choice of robot configuration was proven to avoid the detrimental and low frequency chatter coming from configuration dependent structural modes of vibration (chatter avoidance). The choice of redundancy variable was shown to improve stability limits by ruling the rate of divergence of N=0 lobe of structural robot mode, unveiling stable regions, which were previously unstable in the SLD. In this way, chatter avoidance was achieved enhancing stability of robotic milling operation.

Finally, the hypothesis of chatter stabilisation by deployment of configuration dependent dynamics of the robot by continuously altering the redundancy variable was investigated. Dynamics of structure was varied by continuously configuring the robot around axis of rotation of tool by controlling the redundancy variable across the trajectory. The stability predictions depicted that, at low spindle speeds, the redundancy variables altered the location of stability lobes in spindle speed domain due to configuration dependent robot structural modes. The tests, however, were found to be insufficient to conclude the presence of chatter stabilisation. At high spindle speeds, the process stability was observed to depend on configuration dependent N=0 lobe of robot structural as well as tool-spindle assembly modes. Altering redundancy variable was predicted and observed to alter stability boundaries coming from tool-spindle assembly mode. Continuously altering the redundancy variable caused chatter frequencies to shift from high frequency tool holder-spindle shaft mode to structural robot mode. In this respect, the effect of manipulator configuration on the process stability was proven, however, no trace of chatter stabilisation was encountered. The speed of changing dynamics, TCP rotation velocity, could be the main factor affecting the degree of chatter stabilisation in both low and high spindle speeds. Besides, static stiffness predictions were aimed to be used to predict the stability of process. The findings indicated that it is not possible to use static part of the FRF to predict the process stability, which is a dynamic phenomenon.

On the whole, regenerative stability predictions and experimental validations agreed fairly with each other. Nevertheless, the appearance of low frequency chatter could be related to mode coupling chatter as per the claims in [37, 152, 178–180] at machining parameters where regenerative chatter stability predictions did not match with tests. Even though the mismatch between regenerative chatter stability predictions and experimental validations could be assigned to various inaccuracies, this doesn't justify the absence of mode coupling chatter mechanism in milling. The process could actually be stable with regards to mode coupling chatter mechanism for machining parameters used and there could be un-modelled effects contributing to the mismatch of theory and experiment. For this reason, no clear signs and conclusions were reached based on the presence of mode coupling chatter in the robotic milling tests. Therefore, in the next chapter, the mode coupling chatter mechanism was developed for milling operations in order to investigate

and possibly validate whether the mode coupling chatter mechanism could appear in robotic machining applications.

5.15 Summary of contributions to knowledge

In this chapter, the following contribution is made to knowledge:

- The quasi-static predictions and cutting tests indicated that structural robot modes depend more strongly on manipulator configuration than local modes such as tool holder-spindle shaft mode. It was shown that larger structural dynamics variation could be achieved by utilising the redundancy variable than only translating TCP pose along the cutting trajectory. In the tests, the N=0 lobe of most flexible structural robot mode was controlled by managing the redundancy variable which was shown to significantly vary in the spindle speed region considered. Managing manipulator configuration by the redundancy variable enabled controlling the divergence of the N=0 lobe of most flexible structural robot mode. In this way, an optimum manipulator configuration could be chosen that enables fastest convergence of the N=0 lobe to unveil regions of SLD that were unstable for another robot configuration. Hence, the stability of robotic milling operations could be improved in moderate spindle speeds by selecting an optimum redundancy variable to carry out the cutting operation.

Chapter 6

Mode coupling chatter in milling

In this chapter, presence of mode coupling chatter in milling is investigated. The theory of zero frequency mode coupling chatter mechanism is redefined with classical eigenvalue approach and a new approach based on solving the stability on modal directions is proposed. Following that, the theory is extended to cover the multi frequency approach. Stability boundary predictions for both zero and multi frequency approaches are computed for each manipulator configuration and validated with cutting tests. Along with that, regenerative and mode coupling chatter mechanisms are compared to better understand which chatter mechanism is present in milling tests.

6.1 Introduction

In the Chapter 5, quasi-static zero frequency regenerative chatter predictions and experimentally identified stability of the robotic milling tests were found to have a significant mismatch across different spindle speed regimes. Particularly in high spindle speed regime, predicted and experimentally identified stability boundaries as well as chatter frequencies were not matching. To an extent, the disagreement between theory and experiment could be explained by potential errors within robotic cutting tests as described in Section 5.10.3, however there could be other un-modelled effects involved affecting the stability mechanism too. Notably, the onset of low-frequency severe chatter vibrations at relatively high spindle speeds had same features of mode coupling chatter vibrations as in the literature [37, 177–179]. For this reason, one possibility of the onset of low frequency chatter vibrations is mode coupling chatter vibrations. Additionally, the process could be stable in terms of mode coupling chatter mechanism at regions satisfying regenerative stability mechanism as well. Hence, a further investigation was required to investigate the chatter mechanism observed within robotic milling tests with theory supported validations for mode coupling chatter mechanism in milling.

For this reason, this chapter explores whether the mode coupling chatter mechanism is present in milling operations alongside regenerative chatter mechanism or not. In the existing literature, two different types of self-excited chatter mechanisms were reported to be present in robotic milling operations; regenerative and mode coupling chatter. While regenerative chatter stability boundaries were predicted and validated at various cutting parameters (spindle speed and depth of cut) [34, 137, 155], stability boundaries for mode coupling chatter were not defined in the literature. Instead, low frequency chatter vibrations at relatively high spindle speeds were claimed to be mode coupling chatter mechanism [37, 177–179]. For a more rigorous way of validating the presence of

mode coupling chatter in milling, stability boundaries need to be computed and validated. Owing to the fact that they are different types of self-excited chatter mechanisms, an ambiguity arises whether only one or both types of mechanisms appear at different cutting parameters in milling.

The process stability in machining operations is dominated by presence of self-excited vibrations which arise as a result of the instability in varying dynamic chip thickness. While the most common type, regenerative chatter [199], happens as a result of dynamic chip generation by vibrations imprinted on current and previously cut chip surface, there also exists another type of self-excited instability for specific machining scenarios. These machining scenarios involve the tool cutting a new surface at all times without being influenced by delayed vibrations of the tool-workpiece one revolution before, as opposed to regenerative chatter mechanism [171]. Hence, dynamic chip thickness variations are only due to current vibrations of the tool-workpiece. The instability of such type of self-excited vibrations is called mode coupling chatter. Mode coupling chatter can only occur for systems with multiple degrees of freedom where chatter vibrations in the system degrees of freedom differ in magnitude and phase. The coupling of modes of vibration is the main reason for instability [177]. In the literature, mode coupling chatter is claimed to happen when serial industrial robots are used as machine tools in milling operations [37, 152, 175, 179, 181]. The appearance of low frequency, severe & unstable vibrations is claimed to be mode coupling chatter and low frequency flexible structural modes of vibrations are held responsible for this kind of instability. Having noted similar characteristics in the stability of robotic milling tests in Chapter 5, which may not be explained by regenerative chatter mechanism, constitutes the motivation to investigate the possibility of mode coupling chatter mechanism in milling.

In this chapter, mode coupling chatter is explored in milling operations in order to enlighten the mismatch in zero frequency regenerative chatter predictions and experimentally identified stability of robotic milling tests in Chapter 5. The rest of the chapter is organised as follows; the theory of mode coupling for a multi degree of freedom system along two orthogonal directions is described for milling operations in Section 6.2. The theory covers zero and multi frequency solutions of the stability problem as well as regular and highly varied helix and pitch end mill tools. In Section 6.3, quasi-static zero frequency mode coupling chatter predictions are analysed, compared with regenerative chatter predictions and validated with robotic milling tests in low and high spindle speed region. The quasi-static multi frequency mode coupling chatter predictions are computed and validated with robotic milling tests in low and high spindle speed region in Section 6.4. The effect of cutting process on tool holder-spindle shaft mode and hence process stability is discussed in Section 6.5. The findings are discussed in Section 6.6, the chapter summary is outlined in Section 6.7 and contributions are listed in Section 6.8.

6.2 Theory

In this section, the theory of mode coupling chatter mechanism in milling is described in zero and multi frequency approaches. The zero frequency approach developed in [182] is adapted and zero frequency stability is developed and solved in modal directions. Mode coupling chatter mechanism is also extended to cover multi frequency approach and unconventional end mill tools to further investigate its behaviour.

The following two assumptions are the main conditions that were previously emphasised for mode coupling chatter to happen in milling according to [37, 176, 177, 182];

1. System dynamics must be represented by at least two degrees of freedom, and they must have different modal directions.
2. The dynamic chip thickness must be only dependent on current waves on the chip surface. In other words, previous undulations on the chip surface should be zero ($v(t - T_k(b_a))$=0).

The first assumption is fairly valid in practice, because of the asymmetrical geometry of the machine tool (or serial manipulator) structure. Modes of vibrations could come from the machine tool, spindle shaft, tool etc. and could have various dynamic properties depending on the geometric structure, contact interface, clamping properties etc.

On the other hand, the second assumption is against the nature of milling operation. In milling, the tool with multiple teeth rotates and cutting takes place as a result of the relative linear feed between the tool and the workpiece. Contrary to thread turning or boring operations, the tool always cuts previously machined surface in milling as it follows the tool path. Surface undulations left by the previous tooth are always present on the surface currently being machined. As a result, it is not possible to have a milling scenario where undulations left by the previous tooth are simply zero as opposed to thread cutting in turning and boring. This clearly suggests that one of the main assumptions where dynamic chip thickness in unaffected by regeneration does not hold for milling. Nevertheless, leaving the above incongruity between dynamic chip thickness assumption and nature of the milling operation to aside, undulations left by the previous teeth on surface of the chip are assumed to be negligible (zero). Thus, the behaviour and properties of the phenomenon proposed as mode coupling chatter in milling is aimed to be explored which is schematically depicted as in Figure 6.1.

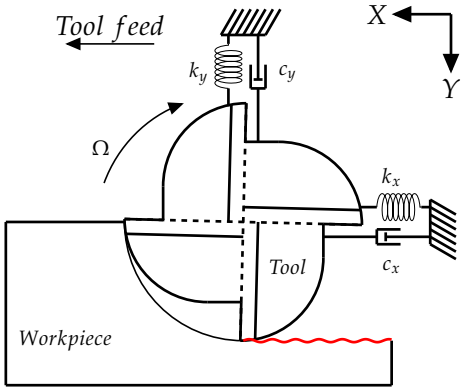

FIGURE 6.1: Mode coupling vibrations in milling operation

The milling operation is assumed to reach steady state and system structural dynamics to be represented by 2 DOF. Dynamic chip thickness is assumed to depend on current vibrations only and total dynamic chip thickness for mode coupling chatter in milling is expressed as,

$$h(\phi_k(b_a, t)) = (h_0(\phi_k(b_a, t)) - v(t))g(\phi_k(b_a, t)) \tag{6.1}$$

The above equation is reduced from Equation 3.41 where undulations left by the previous tooth were assumed to be zero. As before, the static part of chip thickness is ignored as it doesn't contribute to the stability of dynamic chip variations. Hence, the dynamic part of chip thickness becomes,

$$h(\phi_k(b_a,t)) = (x(t)\sin(\phi_k(b_a,t)) + y(t)\cos(\phi_k(b_a,t)))g(\phi_k(b_a,t)) \tag{6.2}$$

For milling, equations relating the instantaneous immersion angle (Equation 3.45), the gradient of helix (Equation 3.46), dynamic tangential and radial cutting forces (Equations 3.47 and 3.48) and its corresponding components in X and Y directions (Equations 3.49 and 3.50) are as described in regenerative chatter mechanism. Hence, total dynamic cutting force in X and Y directions is represented as,

$$\begin{bmatrix} F_x(t) \\ F_y(t) \end{bmatrix} = \frac{1}{2}K_{tc}\sum_{k=1}^{K}\int_{b_a=0}^{b}[A_T(\phi_k(b_a,t))]\begin{bmatrix} x(t) \\ y(t) \end{bmatrix} db_a \tag{6.3}$$

where the matrix $A_T(\phi_k(b_a,t))$ is directional dynamic milling force coefficient matrix in time domain and represented in Equation 3.52. Taking Fourier Transform of Equation 6.3 yields,

$$\begin{bmatrix} F_x(j\omega) \\ F_y(j\omega) \end{bmatrix} = \frac{1}{2}K_{tc}\sum_{k=1}^{K}\int_{b_a=0}^{b}\mathcal{F}\Big([A_T(\phi_k(b_a,t))]\begin{bmatrix} x(t) \\ y(t) \end{bmatrix}\Big) db_a \tag{6.4}$$

where Fourier Expansion of directional dynamic milling coefficient matrix $[A_T(\phi_k(b_a,t))]$ is shown in Equation 3.55. Henceforth, Equation 6.4 becomes,

$$\begin{bmatrix} F_x(j\omega) \\ F_y(j\omega) \end{bmatrix} = \frac{1}{2}K_{tc}\sum_{k=1}^{K}\int_{b_a=0}^{b}\sum_{r=-\infty}^{\infty}e^{jr(\phi_{k0}+\beta_k b_a)}[A_F(r)]\mathcal{F}\Big(\begin{bmatrix} x(t) \\ y(t) \end{bmatrix}e^{jr\Omega t}\Big) db_a \tag{6.5}$$

With the application of shift theorem, vibrations are converted into frequency domain as in [203] and Equation 6.5 turns into,

$$\begin{bmatrix} F_x(j\omega) \\ F_y(j\omega) \end{bmatrix} = \frac{1}{2}K_{tc}\sum_{k=1}^{K}\int_{b_a=0}^{b}\sum_{r=-\infty}^{\infty}e^{jr(\phi_{k0}+\beta_k b_a)}[A_F(r)]\begin{bmatrix} X(j\omega-jr\Omega) \\ Y(j\omega-jr\Omega) \end{bmatrix} db_a \tag{6.6}$$

As before, assuming the combined tool-workpiece structural dynamics ($FRF(j\omega)$) to be linear time-invariant, Equation 6.6 becomes,

$$\begin{bmatrix} X(j\omega) \\ Y(j\omega) \end{bmatrix} = \frac{1}{2}K_{tc}\sum_{k=1}^{K}\int_{b_a=0}^{b}\sum_{r=-\infty}^{\infty}e^{jr(\phi_{k0}+\beta_k b_a)}[A_F(r)][FRF(j\omega)]\begin{bmatrix} X(j\omega-jr\Omega) \\ Y(j\omega-jr\Omega) \end{bmatrix} db_a. \tag{6.7}$$

The combined tool-workpiece structural dynamics ($FRF(j\omega)$) and frequency domain directional dynamic milling coefficient matrix are represented as in Equations 3.60 and 3.61. The stability of Equation 6.7 can be obtained in two approaches which are classified based on the approximation of directional dynamic milling force coefficient matrix; zero and multi frequency approach.

6.2.1 Zero frequency approach

Zero frequency approximation for mode coupling chatter in milling considers the static part of directional dynamic milling force coefficient matrix $[A_F(r)]$ and can be solved in two ways; converting it into classical eigenvalue problem and solving the equations of motions in modal directions X and Y. Both approaches are described as in Sections 6.2.1.1 and 6.2.1.2.

6.2.1.1 Classical eigenvalue problem

If only the static part of directional dynamic milling force coefficient matrix $[A_F(r)]$ is considered ($r = 0$), then Equation 6.7 is reduced to;

$$\begin{bmatrix} X(j\omega) \\ Y(j\omega) \end{bmatrix} = \frac{1}{2} K_{tc} \sum_{k=1}^{K} \int_{b_a=0}^{b} [A_F(0)][FRF(j\omega)] \begin{bmatrix} X(j\omega) \\ Y(j\omega) \end{bmatrix} db_a \tag{6.8}$$

Further simplifications can be made due to independence of the equation to depth of cut and number of teeth as;

$$\begin{bmatrix} X(j\omega) \\ Y(j\omega) \end{bmatrix} = \frac{K}{2} b K_{tc} \begin{bmatrix} A_{xx}(0) & A_{xy}(0) \\ A_{yx}(0) & A_{yy}(0) \end{bmatrix} \begin{bmatrix} FRF_{xx}(j\omega) & FRF_{xy}(j\omega) \\ FRF_{yx}(j\omega) & FRF_{yy}(j\omega) \end{bmatrix} \begin{bmatrix} X(j\omega) \\ Y(j\omega) \end{bmatrix} \tag{6.9}$$

As it can be seen above, consideration of the static part of directional dynamic milling force coefficient matrix ignores the effect of helix angle and pitch of teeth giving a mean approximation for dynamic cutting force. The static parts of individual terms in directional dynamic milling force coefficient matrix are shown in Equation 3.65. Considering the critical process stability, the roots of the characteristic equation is obtained from the determinant of Equation 6.9 as;

$$det\Big(I - \frac{K}{2} b K_{tc} \begin{bmatrix} A_{xx}(0) & A_{xy}(0) \\ A_{yx}(0) & A_{yy}(0) \end{bmatrix} \begin{bmatrix} FRF_{xx}(j\omega) & FRF_{xy}(j\omega) \\ FRF_{yx}(j\omega) & FRF_{yy}(j\omega) \end{bmatrix} \Big) = 0 \tag{6.10}$$

The eigenvalue of the characteristic equation is,

$$\lambda = -\frac{K}{2} b K_{tc} \tag{6.11}$$

Defining Φ to be the product of directional dynamic milling force coefficient and combined tool-workpiece structural dynamics matrices, determinant in Equation 6.10 gives the following relationship;

$$(\Phi_{1,1}\Phi_{2,2} - \Phi_{1,2}\Phi_{2,1})\lambda^2 + \lambda(\Phi_{1,1} + \Phi_{2,2}) + 1 = 0 \tag{6.12}$$

The solution for above quadratic equations gives two solutions, $\lambda_{1,2}$,

$$\lambda_{1,2} = \frac{-(\Phi_{1,1} + \Phi_{2,2}) \pm \sqrt{(\Phi_{1,1} + \Phi_{2,2})^2 - 4(\Phi_{1,1}\Phi_{2,2} - \Phi_{1,2}\Phi_{2,1})}}{2(\Phi_{1,1}\Phi_{2,2} - \Phi_{1,2}\Phi_{2,1})} = \lambda_{RE} + j\lambda_{Im} \tag{6.13}$$

Due to the nature of $FRF(j\omega)$, both solutions for $\lambda_{1,2}$ are complex numbers. Substituting, λ into Equation 6.11 delivers;

$$b_{lim1,2} = \frac{-2(\lambda_{RE} + j\lambda_{Im})_{1,2}}{KK_{tc}} \tag{6.14}$$

In order for depth of cut b_{lim} to be an admissible solution, it has to be a positive real number with zero imaginary part. For this reason, depth of cut in Equation 6.14 is only valid for chatter frequencies which makes the imaginary part of eigenvalues λ_{Im} zero at the same time resulting in a negative real part of eigenvalues λ_{Re}. Having satisfied these conditions, the admissible positive real solution for depth of cut is,

$$b_{lim1,2} = \frac{-2(\lambda_{RE})_{1,2}}{KK_{tc}} \tag{6.15}$$

In order to obtain a valid solution for depth of cut b_{lim}, a specified range of chatter frequencies should be scanned for a possible admissible solution by 1D optimisation algorithm. Note that, limiting depth of cut for zero frequency mode coupling in milling does not depend on spindle speed; the chatter frequency is not associated to spindle speed due to the absence of delay term T_k. This means that the smallest stability boundary will dominate the stability of process for any given spindle speed.

6.2.1.2 Solving in modal directions

Let us consider Equation 6.3 in orthogonal directions of modes of vibrations, X and Y directions as in Figure 6.1;

$$\begin{bmatrix} m_x\ddot{x}(t) + c_x\dot{x}(t) + k_x x(t) \\ m_y\ddot{y}(t) + c_y\dot{y}(t) + k_y y(t) \end{bmatrix} = \frac{1}{2}K_{tc}\sum_{k=1}^{K}\int_{b_a=0}^{b}[A_T(\phi(b_a,t))]\begin{bmatrix} x(t) \\ y(t) \end{bmatrix} db_a \tag{6.16}$$

Oscillations in each direction $X(j\omega)$ and $Y(j\omega)$ are assumed to be harmonic with a phase difference, Θ, between them. Hence, displacements, velocities and accelerations in modal directions can be represented in the form of,

$$\begin{aligned} x(t) &= A_x e^{(\sigma+j\omega)t} & y(t) &= A_y e^{(\sigma t + j(\omega t - \Theta))} \\ \dot{x}(t) &= A_x(\sigma + j\omega)e^{(\sigma+j\omega)t} & \dot{y}(t) &= A_y(\sigma + j\omega)e^{(\sigma t + j(\omega t - \Theta))} \\ \ddot{x}(t) &= A_x(\sigma^2 - \omega^2)e^{(\sigma+j\omega)t} & \ddot{y}(t) &= A_y(\sigma^2 - \omega^2)e^{(\sigma t + j(\omega t - \Theta))} \end{aligned}$$

Here, both modes of vibration are allowed to oscillate sinusoidally and exponentially grow. For critical stability, let $\sigma = 0$ and substitute displacements, velocities and accelerations in each direction into Equation 6.16. The equations of motion in each direction can be represented as;

$$\begin{bmatrix} A_x(k_x - \omega^2 m_x + jc_x\omega) \\ A_y(k_y - \omega^2 m_y + jc_y\omega)e^{-j\Theta} \end{bmatrix} = \frac{1}{2}K_{tc}\sum_{k=1}^{K}\int_{b_a=0}^{b}[A_T(\phi(b_a,t))]\begin{bmatrix} A_x \\ A_y e^{-j\Theta} \end{bmatrix} db_a \tag{6.17}$$

Let us define the ratio of amplitudes of modes of vibrations as $P = \frac{A_x}{A_y}$. By substituting Fourier Expansion of directional dynamic milling force coefficient matrix (as in Equations

3.55 and 3.61), Equation 6.17 becomes;

$$P(k_x - \omega^2 m_x + jc_x\omega) = \frac{1}{2}K_{tc}\sum_{k=1}^{K}\int_{b_a=0}^{b}\sum_{r=-\infty}^{\infty}[PA_{xx}(r) + A_{xy}(r)e^{-j\Theta}]e^{jr(\phi_{k0}+\beta_k b_a)}e^{-jr\Omega t}db_a \tag{6.18a}$$

$$(k_y - \omega^2 m_y + jc_y\omega)e^{-j\Theta} = \frac{1}{2}K_{tc}\sum_{k=1}^{K}\int_{b_a=0}^{b}\sum_{r=-\infty}^{\infty}[PA_{yx}(r) + A_{yy}(r)e^{-j\Theta}]e^{jr(\phi_{k0}+\beta_k b_a)}e^{-jr\Omega t}db_a \tag{6.18b}$$

Equations 6.18a and 6.18b can only be solved by considering the static part of directional dynamic milling force coefficient matrix. Setting ($r = 0$) results;

$$P(k_x - \omega^2 m_x + jc_x\omega) = \frac{1}{2}K_{tc}\sum_{k=1}^{K}\int_{b_a=0}^{b}[PA_{xx}(0) + A_{xy}(0)e^{-j\Theta}]db_a \tag{6.19a}$$

$$(k_y - \omega^2 m_y + jc_y\omega)e^{-j\Theta} = \frac{1}{2}K_{tc}\sum_{k=1}^{K}\int_{b_a=0}^{b}[PA_{yx}(0) + A_{yy}(0)e^{-j\Theta}]db_a \tag{6.19b}$$

Since equations of motions do not depend on number of teeth and depth of cut any more, the summation across number of teeth and integral can be simplified straightforward. Dividing Equation 6.19b by $e^{-j\Theta}$ and substituting $e^{\pm j\Theta} = \cos(\Theta) \pm j\sin(\Theta)$ to both equations give;

$$P(k_x - \omega^2 m_x + jc_x\omega) = \frac{K}{2}K_{tc}b[PA_{xx}(0) + A_{xy}(0)(\cos(\Theta) - j\sin(\Theta))] \tag{6.20a}$$

$$(k_y - \omega^2 m_y + jc_y\omega) = \frac{K}{2}K_{tc}b[PA_{yx}(0)(\cos(\Theta) + j\sin(\Theta)) + A_{yy}(0)] \tag{6.20b}$$

Collecting real and imaginary part of each equation,

$$P(k_x - \omega^2 m_x) = \frac{K}{2}K_{tc}b[PA_{xx}(0) + A_{xy}(0)\cos(\Theta)] \tag{6.21a}$$

$$Pc_x\omega = \frac{K}{2}K_{tc}b[-A_{xy}(0)\sin(\Theta)] \tag{6.21b}$$

$$k_y - \omega^2 m_y = \frac{K}{2}K_{tc}b[PA_{yx}(0)\cos(\Theta) + A_{yy}(0)] \tag{6.21c}$$

$$c_y\omega = \frac{K}{2}K_{tc}b[PA_{yx}(0)\sin(\Theta)] \tag{6.21d}$$

Dividing Equation 6.21b by Equation 6.21d gives;

$$\frac{Pc_x}{c_y} = \frac{-A_{xy}(0)}{pA_{yx}(0)} \tag{6.22}$$

Therefore, the amplitude ratio of the oscillations in X to Y directions is;

$$P = \sqrt{\frac{-c_y A_{xy}(0)}{c_x A_{yx}(0)}} \tag{6.23}$$

Dividing Equation 6.21a by Equation 6.21c gives;

$$\frac{P(k_x - \omega^2 m_x)}{k_y - \omega^2 m_y} = \frac{PA_{xx}(0) + A_{xy}(0)\cos(\Theta)}{PA_{yx}(0)\cos(\Theta) + A_{yy}(0)} \tag{6.24}$$

Rearranging the above equation to find out the phase angle between oscillations in X to Y directions gives;

$$\cos(\Theta) = \frac{(k_y - \omega^2 m_y)PA_{xx}(0) - P(k_x - \omega^2 m_x)A_{yy}(0)}{P^2(k_x - \omega^2 m_x)A_{yx}(0) - (k_y - \omega^2 m_y)A_{xy}(0)} \tag{6.25}$$

Having the amplitude ratio of oscillations defined as in Equation 6.23 and the phase angle obtained for a given angular frequency ω from Equation 6.25, two possible solutions for depth of cut b_{lim} are obtained;

$$b_{lim,1} = \frac{2P\omega c_x}{KK_{tc}(-A_{xy}(0)\sin(\Theta))} \tag{6.26a}$$

$$b_{lim,2} = \frac{2(k_y - \omega^2 m_y)}{KK_{tc}(PA_{yx}(0)\cos(\Theta) + A_{yy}(0))} \tag{6.26b}$$

Equation 6.26 defines the stability boundary for the depth of cut in mode coupling in milling for both directions of orthogonal modes of vibration. Since the instability in either modal direction would cause a global instability in the process, the union of solutions of Equation 6.26 need to be found out. As such, a possible angular chatter frequency ω_c, is searched that results the same magnitude of admissible depth of cut in Equation 6.26 for modes of vibration in both directions. While chatter frequencies for admissible solutions are obtained, the corresponding phase angle and amplitude ratio are also recorded.

This concludes the zero frequency stability of mode coupling in milling across modal directions. The benefits of this approach include computation of amplitude ratio and phase angle between oscillations in X to Y directions which can not be obtained by solving stability equations in terms of eigenvalue problem. However, it should be noted that this method does not take cross-FRFs into account while determining stability boundaries which could have improved the stability prediction. The cross terms could still be incorporated to equations of motion, however, with an expense of increased computational effort. In addition, multiple modes of vibration along a single orthogonal direction are not accepted as well which, in turn, impedes the consideration of entire structural dynamics and the accuracy of stability predictions.

It is observed from Equation 6.26, the limiting depth of cut does not depend on spindle speed when the stability is computed in modal directions. This supports the behaviour of limiting depth of cut as in the classical eigenvalue approach. Hence, the process stability is dominated by the smallest limiting depth of cut for any spindle speed.

6.2.2 Multi frequency approach

In order to accurately acquire the stability boundary for low radial immersion milling operations with high intermittent cutting characteristics, better estimation of the cutting force profile is required. Henceforth, this necessitates directional dynamic milling force coefficients to be computed with a non-zero harmonic number, r. Higher the harmonics, the more accurate stability prediction with an expense of the computation power and time requirements. As opposed to zero frequency mode coupling chatter approach in milling, multi frequency approach depends on spindle speed as stated in Equation 6.7. This is due to the directional dynamic milling force coefficients are periodic at spindle pass frequency and its harmonics.

Equation 6.7 defines a relationship between vibrations in frequency domain with itself, regulated with harmonics r as appears in directional dynamic milling force coefficient. Adapting the approach from [203], rewriting ω=ω+$p\Omega$, Equation 6.7 can be expressed as;

$$\begin{bmatrix} X(j\omega + jp\Omega) \\ Y(j\omega + jp\Omega) \end{bmatrix} = \frac{1}{2} K_{tc} \sum_{k=1}^{K} \int_{b_a=0}^{b} \sum_{r=-\infty}^{\infty} e^{jr(\phi_{k0}+\beta_k b_a)} [A_F(r)] \\ [FRF(j\omega + jp\Omega)] \begin{bmatrix} X(j\omega - jr\Omega + jp\Omega) \\ Y(j\omega - jr\Omega + jp\Omega) \end{bmatrix} db_a \tag{6.27}$$

Let the harmonic number to be $r = p - q$ where p, then,

$$\begin{bmatrix} X(j\omega + jp\Omega) \\ Y(j\omega + jp\Omega) \end{bmatrix} = \frac{1}{2} K_{tc} \sum_{k=1}^{K} \int_{b_a=0}^{b} \sum_{p-q=-\infty}^{\infty} e^{j(p-q)(\phi_{k0}+\beta_k b_a)} [A_F(p-q)] \\ [FRF(j\omega + jp\Omega)] \begin{bmatrix} X(j\omega + jq\Omega) \\ Y(j\omega + jq\Omega) \end{bmatrix} db_a \tag{6.28}$$

If p represents rows and q represents the columns of a matrix where $p = -\infty, \ldots, \infty$ and $q = -\infty, \ldots, \infty$, then Equation 6.28 can be expressed in a more compact way after reverting $r = p - q$ format as;

$$\begin{bmatrix} X(j\omega) \\ Y(j\omega) \end{bmatrix}_p = \begin{bmatrix} X(j\omega + jp\Omega) \\ Y(j\omega + jp\Omega) \end{bmatrix} \tag{6.29}$$

$$[FRF(j\omega)]_{p,p} = [FRF(j\omega + jp\Omega)] \tag{6.30}$$

$$[\Psi(j\omega)]_{p,q} = \frac{1}{2} K_{tc} \sum_{k=1}^{K} \int_{b_a=0}^{b} e^{jr(\phi_{k0}+\beta_k b_a)} [A_F(r)] db_a \tag{6.31}$$

Therefore,

$$\begin{bmatrix} X(j\omega) \\ Y(j\omega) \end{bmatrix}_{p,p} = [FRF(j\omega)]_{p,p} \sum_{q=-\infty}^{\infty} [\Psi(j\omega)]_{p,q} \begin{bmatrix} X(j\omega) \\ Y(j\omega) \end{bmatrix}_{q,q} \tag{6.32}$$

The above formulation summarises multi-frequency approach in mode coupling chatter in milling which takes into account tool geometrical features such as helix angle and pitch while predicting the stability boundary.

6.3 Quasi-static zero frequency mode coupling predictions & validations

In this section, zero frequency stability boundaries of mode coupling chatter in milling is computed, validated with cutting tests and compared with regenerative stability boundaries. Machining parameters given in the Table 5.1 as well as state space model of its FRFs were used to obtain mode coupling chatter stability predictions in two spindle speed regions; low and high spindle speed regions. Chatter frequencies between 0-1000 Hz were scanned for mode coupling stability analysis. The mode coupling chatter stability of manipulator configurations across the trajectory involving tool translation was compared at the chosen redundancy parameters at $P1$, $P2$, $P3$ and $P4$.

Note that, due to the fact that zero-frequency approach for mode coupling chatter mechanism does not dependent on spindle speed, the admissible solution corresponding to smallest depth of cut is the global stability boundary for entire spindle speed spectrum.

6.3.1 Low spindle speed region

Zero frequency stability predictions were obtained and validated for the redundancy variable $\gamma = 1.5\pi$ at all tap testing poses as illustrated in Figure 6.2.

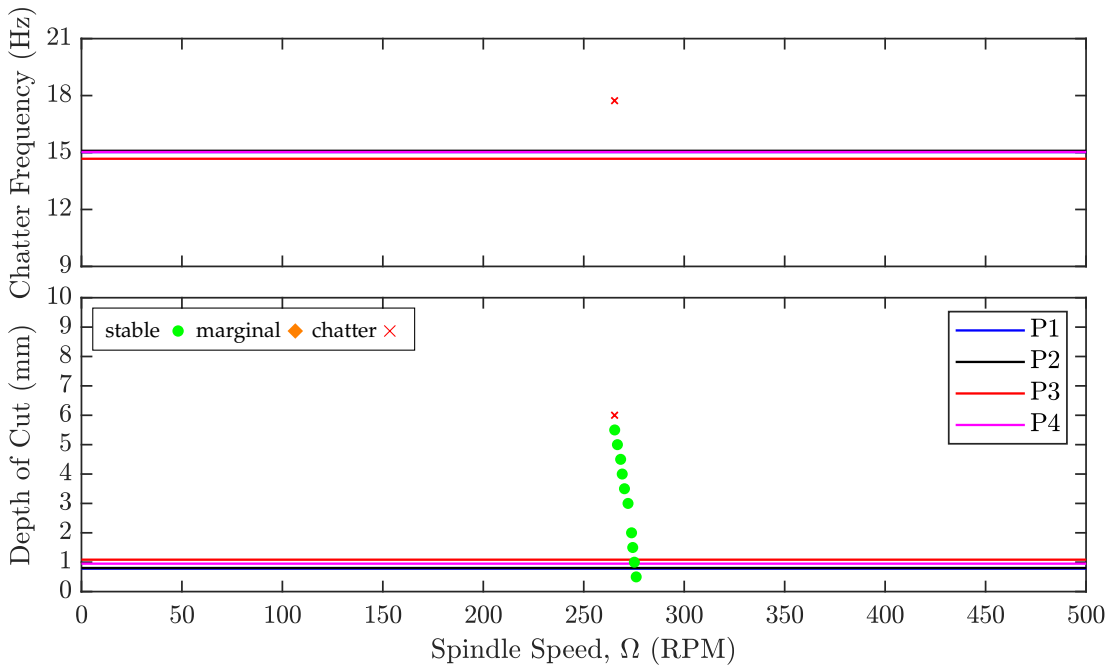

FIGURE 6.2: Low-spindle speed mode coupling stability predictions at all tap testing poses when γ=1.5π

Stability predictions were observed to vary slightly in magnitude while showing spindle speed independent behaviour at each tap testing pose. The magnitude variations were due to slightly dissimilar behaviour of structural dynamics. Stability of milling tests revealed that stability predictions for depth of cut did not hold with most of the cutting tests. While stability predictions were valid for cutting tests carried out with the smallest

two depth of cuts, cutting tests were stable up to 5.5 mm, even well above the stability boundaries. Cutting tests were stable until when chatter vibrations at approximately 18 Hz was observed at 6 mm depth of cut which was not extremely further away from chatter frequency predictions. Overall, there is a significant mismatch between predictions and most of the cutting tests.

Mode coupling chatter stability predictions and validations with experimental cutting tests are depicted for redundancy variable, $\gamma = \pi$, at all tap testing poses in Figure 6.3.

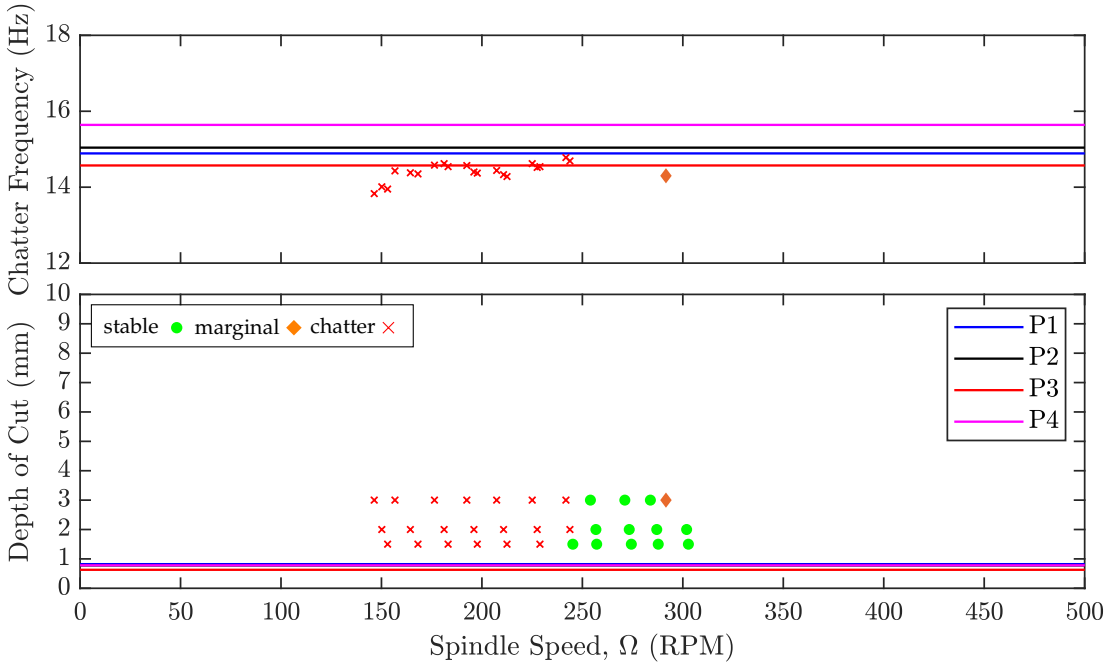

FIGURE 6.3: Low-spindle speed mode coupling stability predictions at all tap testing poses when γ=π

Mode coupling chatter stability predictions showed the same behaviour (spindle speed independence with slight magnitude variations) as in Figure 6.2. The stability of milling tests revealed that process could be stable even well above predicted stability boundaries. Cutting tests also showed that the stability depends on spindle speed as opposed to spindle speed independent characteristics of zero frequency mode coupling chatter mechanism. On the other hand, experimental chatter frequencies and predictions showed close agreement and ranges around 14 - 15 Hz.

Mode coupling and regenerative chatter stability predications were compared for the redundancy parameter, $\gamma = \pi$, at tap testing pose, $P1$. Results are depicted in Figure 6.4.

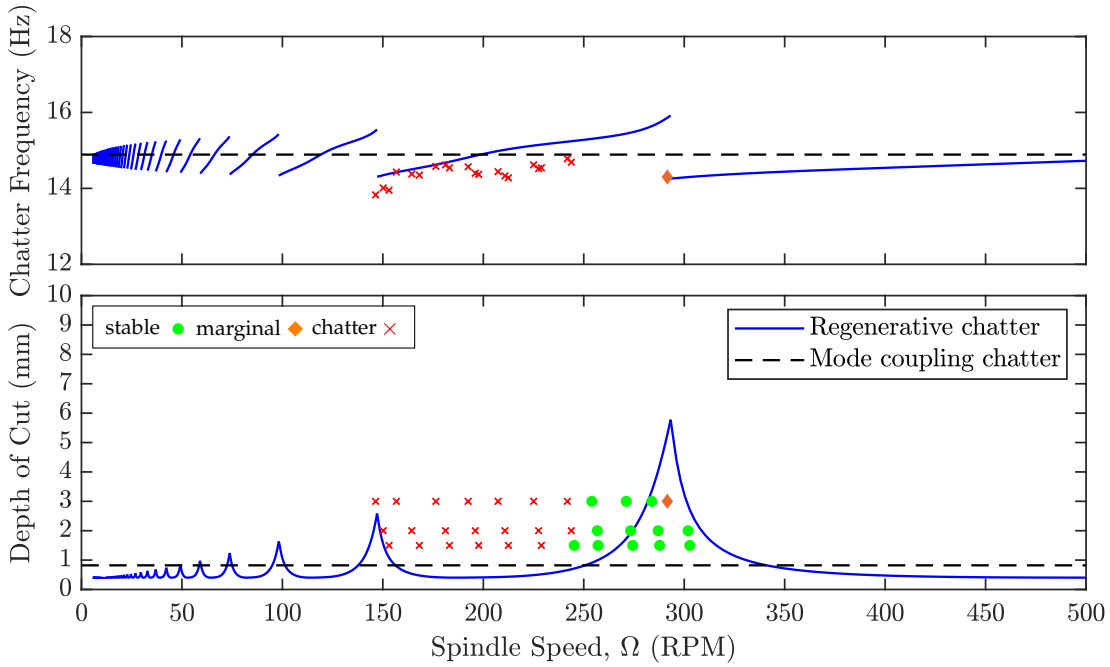

FIGURE 6.4: Comparing regenerative and mode coupling chatter predictions at low-spindle speed region when γ=π

Zero frequency regenerative chatter stability prediction was clearly observed to capture spindle speed dependent stability behaviour of milling tests. The lobbing effect of the regenerative chatter stability boundary could be associated to stable milling tests at higher depth of cuts. Even though, the spindle speed dependent behaviour of regenerative chatter stability did not perfectly fit to stability of milling tests, the stability behaviour of tests and predictions were similar. Mode coupling chatter prediction, however, does not have spindle speed dependency and did not fit to stability of cutting tests at all. On the other hand, chatter frequency predictions for both chatter mechanisms were similar to what observed in the cutting tests.

In the next section, the zero frequency mode coupling predictions were validated with cutting tests at higher spindle speeds.

6.3.2 High spindle speed region

Zero frequency mode coupling chatter stability predictions were obtained and validated with cutting tests for the redundancy variables, $\gamma = [2\pi, \pi]$, at all tap testing poses for high spindle speed region. The conformity between mode coupling stability predictions and experimental findings for the redundancy variable $\gamma = 2\pi$ is shown in Figure 6.5.

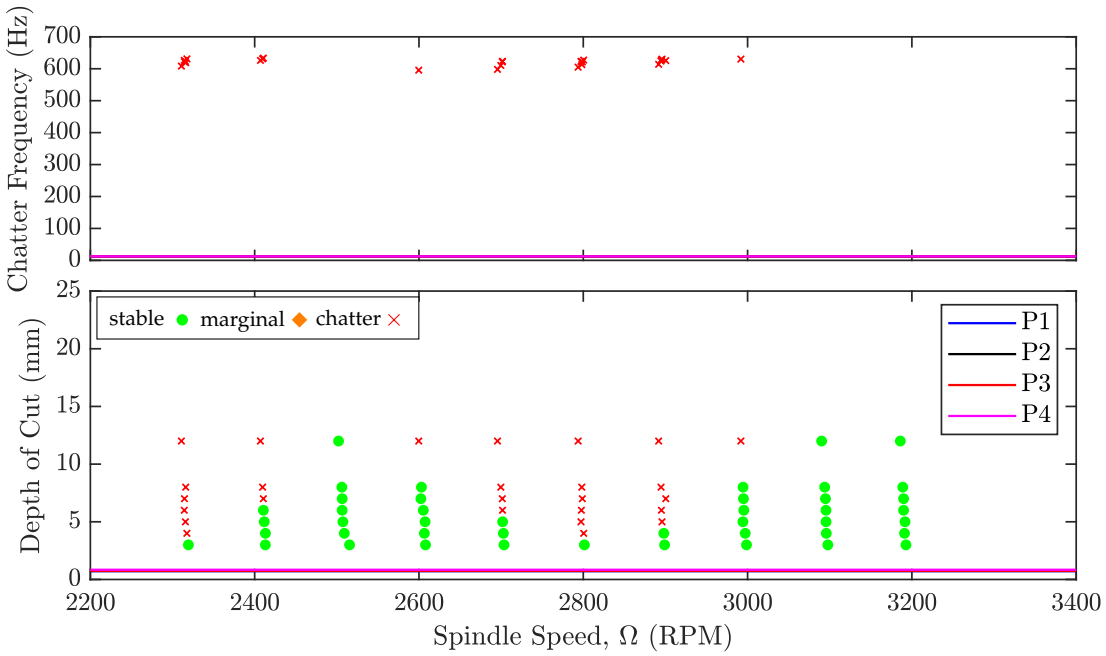

FIGURE 6.5: High spindle speed mode coupling stability predictions at all tap tested poses when γ=2π

Mode coupling chatter stability predictions and stability of milling tests showed significant mismatch. While predicted and experimentally identified minimum limiting stability boundaries for depth of cut did not agree, it was evident that stability of tests depended on spindle speed. The zero frequency mode coupling chatter approach predicted approximately 1 mm limiting depth of cut whereas cutting tests revealed that process could be stable even at 12 mm depth of cut at selective spindle speeds while the experimental minimum limiting depth of cut was between 3-4 mm. In addition, chatter frequencies identified from cutting tests were higher than that of predictions and hence, showed great divergence too. Rather than chattering at structural mode of vibration at around 12-15 Hz, the process chattered around 600-640 Hz which coincided with tool holder-spindle shaft mode of vibration.

To further investigate mode coupling and regenerative chatter behaviour, stability predictions from both mechanisms were compared and validated for the redundancy parameter, $\gamma = 2\pi$, at tap testing pose, $P1$. The results are depicted in Figure 6.6.

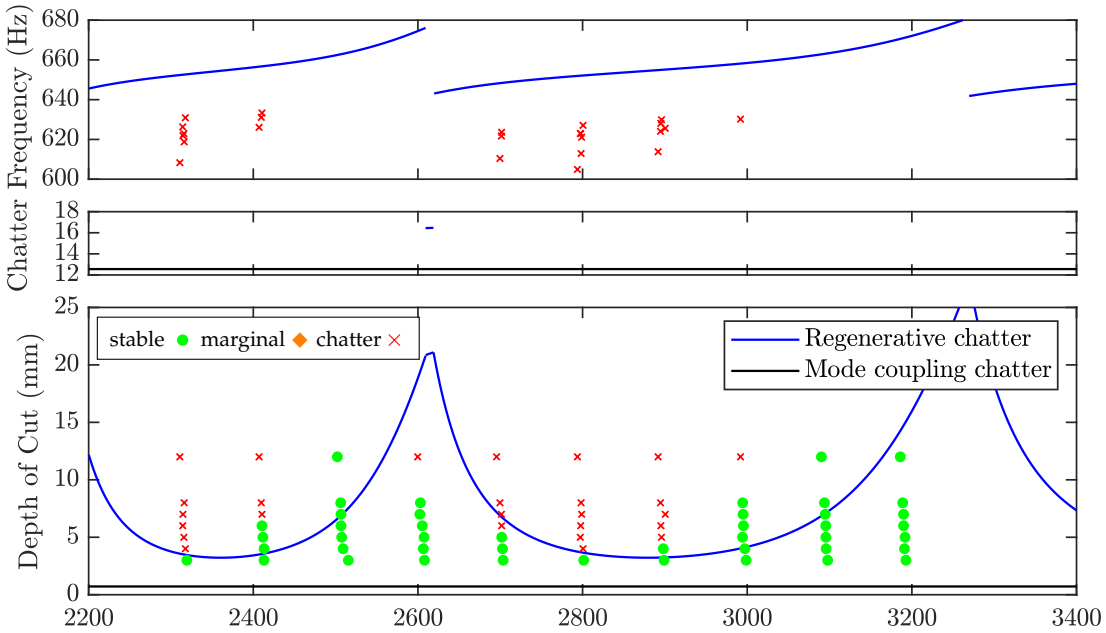

FIGURE 6.6: Comparing regenerative and mode coupling chatter predictions at high-spindle speed region when γ=2π

It can be seen that regenerative chatter stability prediction suits better to the stability of milling tests than the mode coupling chatter stability prediction. It describes the spindle speed dependency of milling tests as opposed to mode coupling chatter stability prediction. Even though regenerative chatter stability boundary and stability of milling tests did not fit perfectly, the stability behaviour was similar. This suggests, the mismatch (100 RPM shift) in the predicted regenerative stability boundary and stability of milling tests could be attributed to various factors but particularly to the influence of process on the modes of vibration of the structure as explained in Section 5.10.3. Additionally, the predicted chatter frequencies based on the regenerative chatter mechanism fairly matched to the experimentally identified chatter frequencies too.

Similarly, zero frequency mode coupling chatter stability predictions were obtained and validated with cutting tests for the redundancy variable $\gamma = \pi$. The results are illustrated in Figure 6.7.

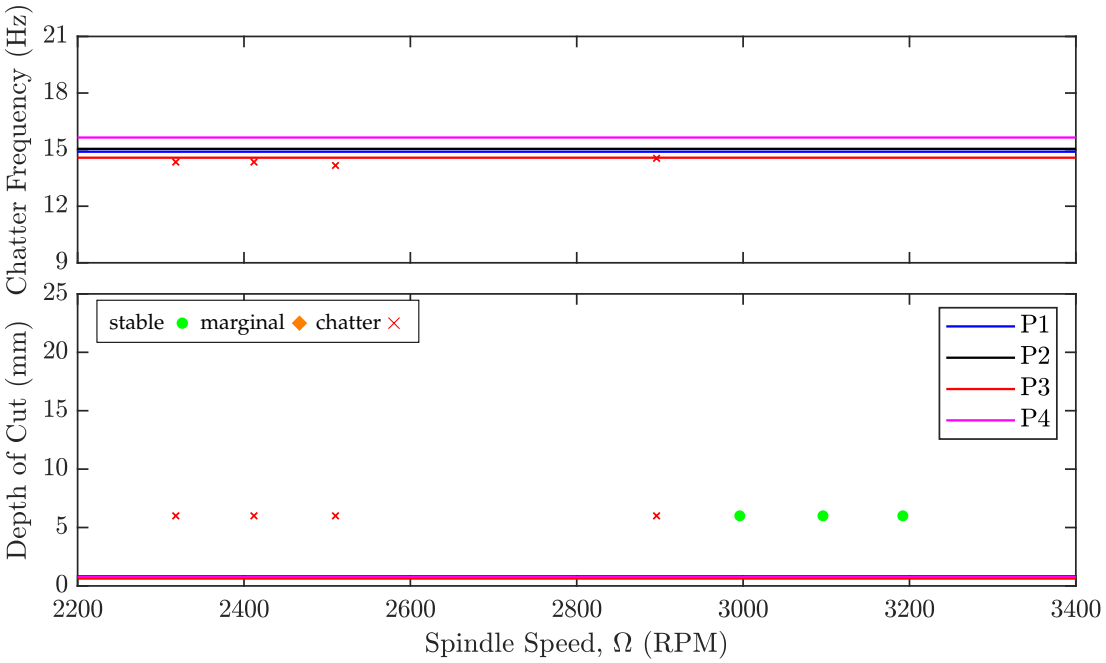

FIGURE 6.7: High spindle speed mode coupling stability predictions at all tap tested poses when γ=π

Here, stability predictions and tests seemed to disagree too. Even though, mode coupling stability boundaries were around 1 mm at each tap testing pose, cutting tests revealed that the process could be stable at selective spindle speeds around 6 mm depth of cut, which was markedly higher. Hence, cutting tests pointed out spindle speed dependency of the stability of milling tests as in Figures 6.3 and 6.5 at low and higher spindle speeds. On the other hand, identified and predicted mode coupling chatter frequency seemed to agree. The process chattered around 14-15 Hz around the most flexible structural mode of vibration as predicted.

Stability predications from both mechanisms were examined and validated for the redundancy parameter, $\gamma = \pi$, at tap testing pose, $P1$. In that, for simplicity and ease understanding, the lowest stability boundary in regenerative chatter stability predictions were plotted which was N=0 lobe coming from the most compliant structural mode. Findings are shown in Figure 6.8.

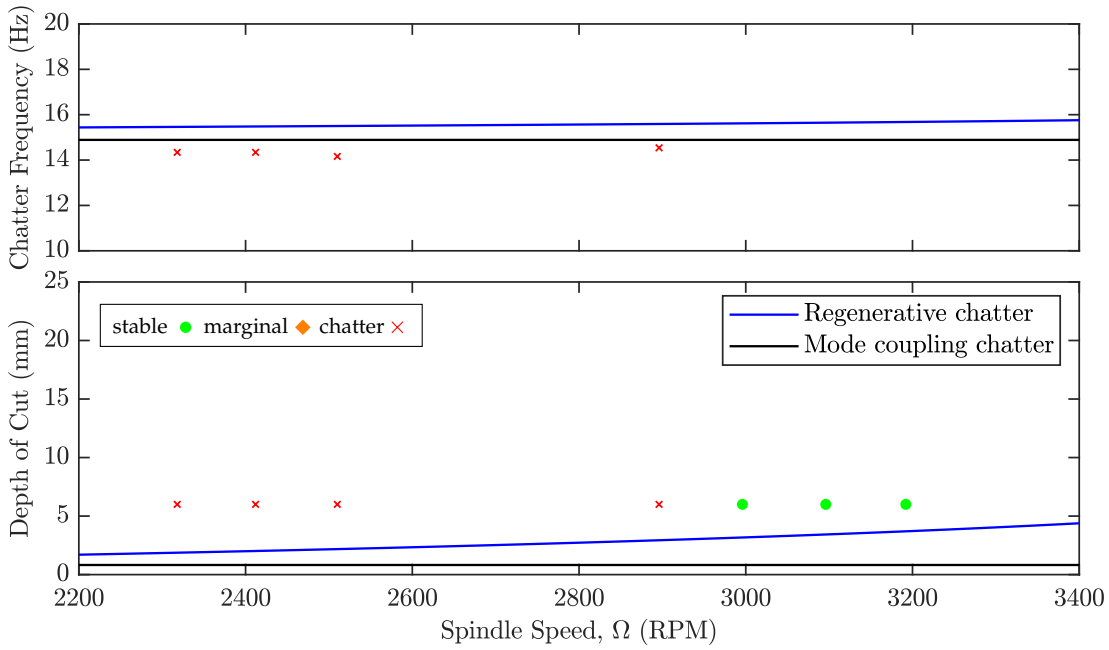

FIGURE 6.8: Comparing regenerative and mode coupling chatter predictions at high-spindle speed region when γ=π

As opposed to the spindle speed independent behaviour of mode coupling chatter stability boundary, the regenerative chatter stability boundary was observed to slightly increase at higher spindle speeds. With the slight increase, regenerative stability boundary got closer to the cutting parameters which tests were found to be stable. Even though the regenerative chatter stability boundary did not fit to the stability of milling tests, it could still describe the spindle speed dependent stability behaviour of tests. The slight mismatch between tests and regenerative chatter predictions could be due to inaccuracies coming from various sources as described in Section 5.10.3. Thus, findings suggest that regenerative chatter mechanism describes the stability of the milling tests better than zero frequency mode coupling chatter predictions.

The fact that zero frequency mode coupling approach did not consider spindle speed dependency motivated the consideration of multi frequency approach which is able to take into account the effect of spindle speed on process stability. With the aim of attaining spindle speed dependent stability predictions in mode coupling chatter mechanism, the multi frequency approach was computed and compared with the stability of cutting tests in next section.

6.4 Quasi-static multi frequency mode coupling predictions & validations

Zero frequency mode coupling chatter stability boundaries showed significant mismatch with stability characteristics identified from cutting tests. One of the main dissimilarities of predictions was the spindle speed dependency of process stability as determined with cutting tests. The zero frequency approach for predicting stability boundaries for milling seemed to be inaccurate and incapable of predicting spindle speed dependency of the process stability. For this reason, multi frequency approach which takes into account spindle speed is considered in this section. For validation purposes, multi frequency solution for low and high spindle speeds are computed by considering machining parameters in Table 5.1 and Section 6.2.2 with the tool helix angle taken into account. The number of harmonics used was altering based on the choice of spindle speed for selected maximum frequency as in [203]. The results are presented for the redundancy variables $\gamma = [\pi, 2\pi]$ at all tap testing poses and validated with cutting tests respectively.

6.4.1 Low spindle speed region

Multi frequency stability predictions and the stability of cutting tests for redundancy variable $\gamma = \pi$ are illustrated at low spindle speed region in Figure 6.9.

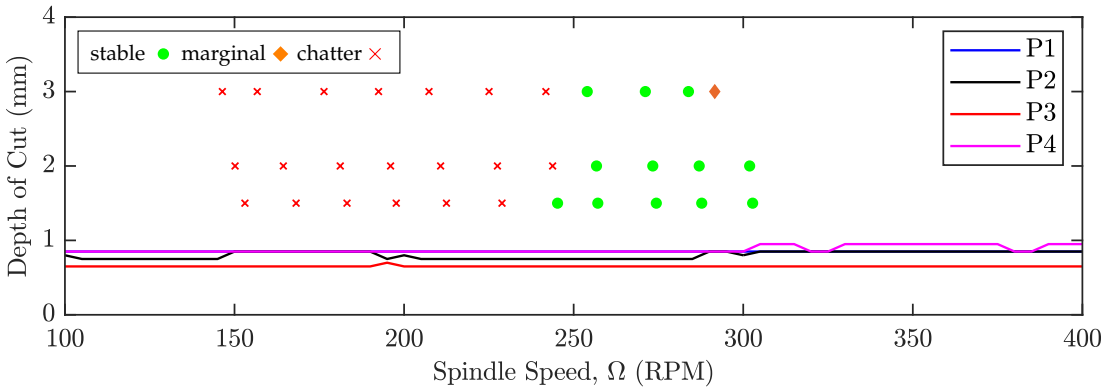

FIGURE 6.9: The multi frequency mode coupling stability predictions at all tap tested poses when γ=π at low spindle speeds

Multi frequency mode coupling chatter predictions were observed to possess spindle dependency as a result of consideration of the harmonics of spindle pass frequency. However, stability boundaries were not greatly affected to match with identified stability characteristics of cutting tests. The spindle speed dependency of stability predictions was not strong enough compared to that of identified from cutting tests. Chatter frequencies, on the other hand, could not be estimated straight away; multi frequency stability predictions result multiple possible chatter frequencies unlike zero frequency approach. Considering the magnitude of stability boundaries, chatter frequencies were expected to be similar to that in the Figure 6.3.

6.4.2 High spindle speed region

Similarly, multi frequency stability predictions and the stability of cutting tests for redundancy variable $\gamma = 2\pi$ are shown at high spindle speed region in Figure 6.10.

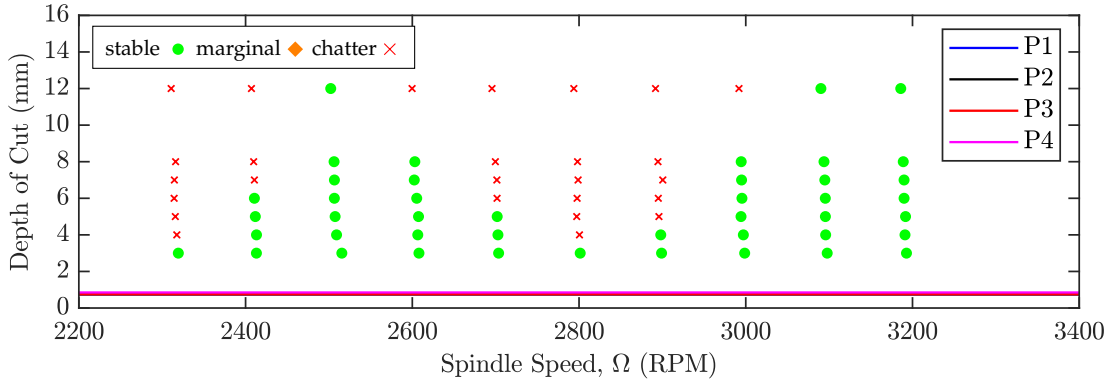

FIGURE 6.10: The high spindle speed mode coupling stability predictions at all tap tested poses when γ=2π

As opposed to low spindle speed predictions, multi frequency mode coupling predictions at the considered high spindle speed region seemed to be unaffected by spindle pass frequency harmonics, hence, did not show spindle speed dependency. The spindle speed dependent stability behaviour observed in cutting tests, as a consequence, was not fulfilled and predictions seemed not accurate enough to describe experimental stability boundary and characteristics.

6.5 Further remarks

Mode coupling chatter stability predictions in milling were not able to describe stability characteristics of tests. The spindle speed dependent stability of milling tests as well as identified chatter frequencies at high spindle speeds showed prominent disagreement. However, regenerative chatter stability predictions were observed to describe stability characteristics of tests better even though predictions were not perfectly fitting to the stability of tests. One possible explanation for the mismatch of regenerative chatter predictions and tests was the role of possible sources of errors in stability characteristics of robotic milling as described in Section 5.10.3.

Revising all possible sources of error, the effect of tool-workpiece contact (cutting process) on natural frequencies of the robot structure could explain the stability lobe location shift in regenerative chatter stability predictions. The natural frequency of a mode of vibration is related to the location of stability regions by Equation 6.33 [200],

$$\Omega_{Best} = \frac{60 f_n}{(N+1)K} \tag{6.33}$$

where, f_n (Hz) represents the natural frequency of mode of vibration and Ω_{Best} defines best spindle speeds (spindle speed where a stable region is located) for the considered lobe number, N.

With the aim of enlightening stability location shift observed in high spindle speed tests, the effect of natural frequency shift of tool holder-spindle shaft mode of vibration on the location of stability boundaries was considered. Natural frequency shift of the mode was estimated by comparing the predicted and identified chatter frequencies; the difference between predicted and identified chatter frequencies was assumed to represent natural frequency shift of the mode of vibration. Having identified the shift in natural frequency, the affected natural frequency is predicted and stability lobe locations are computed based on Equation 6.33.

Machining parameters, which caused instability at 4 mm depth of cut at 2317.5 and 2800.5 RPM spindle speeds over N=4 and N=3 lobes were chosen respectively. At these machining parameters, predicted chatter frequencies were at 652 and 651 Hz, which were 22-24 Hz higher than identified chatter frequencies at 630.9 and 627.1 Hz. Assuming that the identified tool holder-spindle shaft mode (around 655 Hz) was lowered an average of 23 Hz due to the tool-workpiece interaction to 632 Hz (tests chattered at lower frequencies than predictions), shifted lobe locations were predicted to be at 2528 and 3160 RPM based on Equation 6.33. The predicted shifted lobe locations (2528 and 3160 RPM) were actually matching to the identified stability of robotic milling tests as in Figure 6.6. This showed that effect of tool-workpiece contact (cutting process) on natural frequencies of the mode could surely explain such a large quantitative mismatch of predicted regenerative stabilities boundaries and tests.

It should not be forgotten that other sources of errors such as slight variations in tool orientation, form error, TCP pose accuracy, material properties and slight non-linearities in the dynamic model could also cause alterations in stability boundary predictions too. However, considering the fact that these variations were insignificant compared to corresponding machining parameters (TCP pose inaccuracy or form error was much smaller than axial and radial engagement of the tool), their effect on stability boundaries were expected to be relatively small. Nevertheless, above remarks suggest that even though robotic milling is subject to many sources of errors, the most striking one is the extent of effect of tool-workpiece contact on natural frequencies of robot structural modes of vibration.

6.6 Discussion

Quasi-static zero frequency mode coupling chatter predictions and stability of robotic milling tests showed a prominent mismatch. The mismatch extended from low to high spindle speed region even though chatter frequencies showed close agreement in low spindle speed region. Stability predictions did not show spindle speed dependency but experimentally identified stability characteristics indicated that the stability depended strongly on spindle speed. The comparison of regenerative and mode coupling stability boundaries revealed that the stability of milling tests could be better explained by regenerative chatter mechanism. Regenerative stability boundaries were able to describe the spindle speed dependent behaviour of milling tests at high and low spindle speed regions. In an attempt to model the spindle speed dependency and increase the accuracy of stability predictions, multi frequency approach was computed. However, the spindle speed dependency of predictions were not strong enough to explain experimental findings in both low and high spindle speeds.

The immediate implication of the significant disagreement between theory and experiment is the hypothesis of appearance of un-modelled effects related with mode coupling chatter is incorrect, for the considered machining scenario - milling. The disagreement justifies that mode coupling chatter is not present in milling operations. This is mainly due to the false assumption which states that dynamic chip thickness depends only on current normal vibration on the chip surface in milling. Instead, stability predictions from both chatter mechanism indicated that dynamic chip thickness depends not only current undulations but also undulations left by the previous tooth on the surface of chip. This indisputable and evident disagreement between milling tests and mode coupling chatter stability predictions, in fact, implies the extent of inaccuracies in regenerative stability predictions. In particular, it suggests that the onset of low frequency vibrations could all be attributed to inaccuracies in regenerative chatter stability predictions. These inaccuracies could come from the aspects as listed in Section 5.10.3, in particular, the effect of cutting process on structural dynamics of the manipulator at the tool tip. The reason why the location of the stability lobes in low and high spindle speeds were shifted, could easily be associated to natural frequency of modes of vibration through regenerative chatter theory as described in Section 6.5. The agreement of predictions in shifted stability lobe locations with stability of tests indicated the extent of the effect of tool-workpiece contact (cutting process) on structural dynamics of serial robots. Such a significant alteration in natural frequency is not common in machine tools and could affect application of robots in machining operations resulting in difficulties in predicting the stability of robotic milling.

It seems like there is a misunderstanding of mode coupling chatter mechanism in the literature. The origin of mode coupling chatter leans on to unstable vibrations while machining a new surface at all time such as thread cutting operations. Hence, mode coupling chatter principles can not be applied to milling operations in which the tool always cuts previously cut surface. The findings of this chapter support the invalidity and infeasibility of mode coupling chatter in milling and apply to machining with any machine tools, including machining robots.

All in all, findings indicate that mode coupling chatter is not possible in milling. The robotic milling is subject to many sources of inaccuracies that could cause a mismatch of regenerative stability predictions and the stability of cutting tests. Nevertheless, regenerative chatter mechanism is the only chatter mechanism in milling, including robotic milling operations too.

6.7 Chapter summary

In this chapter, mode coupling chatter mechanism in milling was developed and used to predict mode coupling chatter stability boundaries for the robotic milling trial explained in Chapter 5. The main assumptions in mode coupling chatter mechanism were; dynamic chip thickness does not depend on undulations imprinted on the surface of chip by the previous tooth and structural dynamics should possess multi degrees of freedom (MDOF) with different modal directions.

First, the theory of mode coupling chatter mechanism was developed and a generalised equation of the mechanism was established. The zero frequency approach based on solving the characteristic equation by classical eigenvalue problem was revised as defined in the literature. Next, a new zero frequency approach was proposed which is based on solving the stability on modal directions of structural dynamics of the system. The zero frequency approach was then extended to cover multi frequency solution by taking into account non-zero harmonic number to describe directional dynamics milling force coefficients. In this respect, the accuracy of mode coupling chatter predictions was aimed to be increased by allowing predictions to take into account the effect of spindle speed. In addition to this, multi frequency approach also takes into account irregular pitch and helix angle of end mill tools on stability predictions.

Zero frequency mode coupling stability predictions were then compared with the stability of robotic milling tests. The stability of tests was in great mismatch with mode coupling chatter predictions. The most striking disagreements were stability boundaries and spindle speed dependency between predictions and tests. The predicted stability boundaries in low and high spindle speeds showed great disagreement with the experiment. The zero frequency regenerative and mode coupling chatter stability predictions were compared in low and high spindle speeds. The comparison revealed that spindle speed dependency of the experimentally identified process stability can be certainly explained by regenerative chatter mechanism. The mode coupling chatter mechanism failed to address such a behaviour as well as the dependency of stability characteristics to more than one mode of vibration as revealed by the appearance of low and high chatter frequencies in tests.

In an attempt to improve stability predictions, multi frequency approach was computed and predictions were compared with the stability of cutting tests. The stability predictions showed slight spindle speed dependency in low spindle speed region however, not in high spindle speed region. Nevertheless, the spindle speed dependency of predictions was not strong enough to match milling tests. A deeper analysis revealed that the mismatch between regenerative chatter stability predictions and tests could be largely explained by the effect of cutting process on tool holder spindle shaft mode.

All in all, findings indicated that mode coupling chatter in milling is not possible. The assumption of dynamic chip thickness not depending on undulations imprinted on the surface of chip by the previous tooth is not correct in milling. Hence, the onset of appearance of low frequency chatter vibrations and the mismatch in regenerative chatter predictions to the experiment can not be due to the mode coupling chatter mechanism. This implies that regenerative chatter mechanism is the only chatter mechanism in milling operations.

6.8 Summary of contributions to knowledge

Throughout the chapter, the following contributions are made to knowledge;

- Zero frequency mode coupling chatter mechanism in milling was developed and solved in modal directions. The developed approach was used to compute two additional parameters; phase angle and amplitude ratio. Mode coupling chatter in milling was also extended and solved based on multi frequency approach which takes into account regular and highly varied helix and pitch end mill tools. In this way, spindle speed dependency of mode coupling chatter predictions could also be explored.
- In the literature, a validation between stability boundaries and cutting tests is missing for mode coupling chatter mechanism in milling. This caused an ambiguity of the chatter mechanism appearing in robotic milling operations. In this chapter, mode coupling chatter stability boundaries were computed, validated with tests and compared to regenerative chatter stability predictions. It was concluded that there was a significant mismatch between stability predictions and cutting tests. The comparison of mode coupling chatter with regenerative chatter stability predictions revealed that regenerative chatter mechanism could explain the stability behaviour of cutting tests more effectively. Also, mode coupling chatter stability predictions were not able to predict fundamental characteristics of cutting tests such as spindle speed dependency, chatter frequency shift from low to high frequencies due to the underlying assumptions in the theory. This means that mode coupling chatter does not exist in milling operations.

Chapter 7

Conclusions

In this chapter, summary of the thesis, conclusions, contributions to the knowledge and publications are outlined.

7.1 Summary of the thesis

Application of serial industrial robots to machining operations could provide large workspace, versatility with high dexterity and low cost compared to conventional machine tools. However, their current design and manufacturing purpose are to do repetitive tasks - not conducting machining operations. They suffer from low pose accuracy and due their architectural structure, they tend to have poor and configuration dependent dynamics. Poor and configuration dependent dynamics cause relatively large forced vibrations, early onset of self-excited chatter vibrations and configuration dependent process stability. For this reason, the thesis was organised to investigate static stiffness and structural dynamics of serial industrial robots on dynamics of machining operations; machine tool chatter. In this way, stability boundaries for robotic machining operations could be enhanced and ambiguity in the literature regarding the chatter mechanism either being regenerative or mode coupling chatter could be enlightened.

In this context, in Chapter 1, an introduction to modern manufacturing technologies was given and importance of machining processes (subtractive technologies) within the manufacturing sector was explained. Pros and cons of Computer Numerical Controlled (CNC) machine tools in manufacturing end products were examined and the motivation of utilising serial industrial robots as machine tools was discussed. Structural dynamics of both serial industrial robots and machine tools were compared and the implications of similarities and dissimilarities on process stability were outlined. Based on the initial considerations, possible research directions of the thesis were elaborated and thesis structure was described.

Following the initial research directions, the state of art in robotic machining was presented by reviewing the literature in Chapter 2. Overview of errors in robotic machining applications was discussed and the importance of modelling of manipulators was underlined to compensate these errors. In this manner, the literature in static stiffness modelling and identification of serial and parallel manipulators was outlined revealing advantages and disadvantages of modelling techniques. Next, the state of art structural dynamic modelling and identification techniques of manipulators were discussed and examined based on their prediction accuracy. Lastly, chatter mechanisms appearing in robotic machining operations were revealed, highlighting the ambiguity in observed chatter characteristics.

In Chapter 3, theoretical background and terminology for "robotics" and "machine tool dynamics" were defined. First, geometrical modelling and kinematics of serial industrial robots were defined. The theory behind forward, inverse and differential kinematics of serial manipulators was introduced that was utilised later on for stiffness modelling and identification as well as the robotic machining trial. Types of redundancies and causation of singularities as well as quantification of closeness to singularities were discussed. Following that, analytical derivations of the regenerative chatter mechanism in turning and milling operations were defined to enable computation of stability boundaries for the robotic machining trial. Lastly, self-excited vibration mechanism in thread cutting operations known as, mode coupling chatter, was analytically defined based on the previously established knowledge. This was to give deeper insight into the mode coupling chatter mechanism and enlighten the ambiguity in observed chatter mechanism in the existing literature for robotic milling operations. Hence, the chatter mechanism could be extended to milling operations with the aim of distinguishing and validating regenerative and mode coupling chatter mechanisms.

In Chapter 4, Conservative Congruence Transformation (CCT) without link flexibility based on Virtual Joint Model (VJM) was adapted to describe static stiffness modelling of the serial industrial manipulator, ABB IRB 6640 205/2.75. The theory underlying stiffness modelling technique was described. *Complementary stiffness matrix* was then minimised to reduce CCT to conventional stiffness modelling for joint compliance parameter identification. The joint compliance identification preliminary design was shown and simulated in a virtual environment to replicate the experimental procedure. In this way, joint compliance parameter identification accuracy and the factors affecting the identification accuracy were investigated to optimise and determine procedures and parameters to be applied in the experiment. In the experiment, manipulator geometrical model was calibrated, joint compliance parameters were computed and VJM stiffness model was validated experimentally by the linearity test. Finally, direct Cartesian compliance parameters c_{xx} and c_{yy} were optimised by utilising kinematic and functional redundancy of the robot around the axis of rotation of tool over the machining table. In this context, the capability of manipulator stiffness parameters being improved was investigated and magnitude variations were underlined.

In Chapter 5, the effect of continuously varying structural dynamics on the process stability was investigated with robotic milling trials. After choosing the workpiece material and defining spindle and tool dimensions, kinematic performance of the manipulator was analysed based on KCI index. The analysis was shown to be beneficial for locating the workpiece on the machining table and choosing redundancy variables to control the manipulator configuration. Following structural dynamics identification of manipulator configurations at tap testing poses, quasi-static stability predictions were computed and validated for cutting tests, which were carried out while keeping the redundancy variable constant. In an attempt to further cause varying structural dynamics, the redundancy variable was continuously varied as the tool translated to cut material. Stability predictions and experimental findings were investigated and regions of SLD were found that improves limits of robotic milling. Lastly, the predictability of minimum limiting stability boundary by static stiffness predictions was discussed.

In Chapter 6, the theory of mode coupling chatter mechanism in milling was developed. The characteristic equation was solved through zero frequency approach by adapting classical eigenvalue approach given in the literature. In addition, a new way of solving the

stability on modal direction was proposed for zero frequency approach. Zero frequency approach was then extended to multi frequency approach to increase the accuracy of stability predictions by allowing predictions to take into account the effect of spindle speed. The zero frequency and multi frequency mode coupling stability predictions were compared with robotic milling tests described in Chapter 5 and discussed. The zero frequency regenerative and mode coupling chatter mechanisms were compared and examined. Lastly, having given a further insight into the effect of experimental errors on regenerative stability predictions, implications of findings were discussed on the presence of mode coupling chatter in milling.

7.2 Conclusions

In this thesis, the influence of configuration dependent dynamics of the serial industrial robot, ABB IRB 6640 205/2.75 on machine tool chatter along with the existence of mode coupling chatter in milling have been investigated with robotic milling tests. The main conclusions are;

1. **The CCT based VJM manipulator stiffness model identification accuracy is affected by various theoretical, experimental and procedural factors**.

   CCT based VJM stiffness modelling is one of the most simplistic ways of describing manipulator static stiffness and involves omitting link stiffness as discussed in Section 2.3. Negligible link stiffness assumption causes misrepresentation of manipulator static stiffness behaviour and hence, intrinsic inaccuracies exist within VJM model and its identification [120]. The accuracy of identification of joint compliance parameters is strongly influenced by Complementary stiffness matrix, choice of manipulator configurations, number of manipulator configurations, magnitude of loading, displacement and loading measurement sensitivity as reported in [114, 115, 120]. Besides, in the current work, truncation of joint variables defined in the controller, Jacobian matrix (manipulator geometrical model), loading procedure and number of loading sets applied to each manipulator configuration were identified to also influence the identification accuracy. The effect of measurement noise, number of manipulator configurations, loading procedure, number of loading sets applied to each configuration and magnitude of loading on the identification accuracy were investigated in Section 4.5 to quantify and minimise their influence. With an optimal choice of procedural factors, it was shown that the identification accuracy of joint compliance parameters could be improved.

2. **Manipulator static stiffness can be optimised by utilising the kinematic and functional redundancy while complying TCP pose requirements for 5-axis milling operations**.

   6-axis industrial manipulators applied to 5-axis milling operations tend have kinematic and functional redundancy around the axis of rotation of tool. Benefiting from configuration dependent static stiffness property of the manipulator, the redundancy was utilised to improve manipulator static compliance as in [128, 129]. However, previous techniques made use Equation 3.15 and hence, inverse of Jacobian matrix to compute manipulator inverse kinematics. Even though stiffness optimisation can be achieved while avoiding from singularities, the use of inverse Jacobian introduces inaccuracies to the manipulator TCP pose. The inaccuracies in TCP pose was

addressed by computing inverse kinematics by analytical approach to ensure the accuracy of TCP pose in Section 4.7. While optimising its compliance (or stiffness) by benefiting from the redundancy, kinematic performance of the manipulator was investigated as well. This proved that manipulator static stiffness can be optimised while ensuring the TCP pose accuracy for 5-axis milling operations.

3. **The behaviour of manipulator structural dynamics depends on the manipulator configuration**.

   Serial industrial manipulators are known to have low-frequency and configuration dependent modes of vibration as reported in [34, 35, 136]. This was validated by experimental modal testing in Section 5.6 and shown that low-frequency modes of vibration change magnitude, mode shape and natural frequency based on the extent of manipulator configuration alteration. The manipulator configuration is also known to affect higher frequency modes of vibration coming from tool holder-spindle shaft and tool as reported in [35, 36, 136, 137, 155]. However, since higher frequency modes of vibrations are locally located on spindle, they are not affected as strongly as structural modes of vibration. The findings from modal testing depicted that there could be slight variations in the magnitude and natural frequency of modes in Section 5.6. The variation in structural dynamics for both structural and local modes was found to be larger when a greater extend of manipulator configuration alteration was achieved by utilising the redundancy variable.

4. **The manipulator configuration alteration achieved by varying the redundancy variable, γ, is more effective in causing stability variations than that of achieved when translating the TCP along cutting trajectory only.**

   The effect of manipulator configuration alteration on process stability as a result of tool tip translation along a cutting trajectory has been reported to be marginal in high spindle speed region [35, 36]. Quasi-static stability predictions and stability of cutting tests in Section 5.10 depicted that slight variations in predicted stability boundaries were observed in low and high spindle speed regions. In low spindle speeds, stability boundary variations were found to be small enough to be unidentifiable. In high spindle speed region, even though the predicted stability variation coming from tool holder-spindle shaft mode was identifiable, cutting tests did not show stability alteration.

   The effect of manipulator configuration alteration attained by varying the redundancy variable, however, was reported to cause larger stability variations in high spindle speed [136, 137]. Quasi-static stability predictions and stability of cutting tests in Section 5.11 revealed that the location of stability lobes changed in low spindle speeds. In high spindle speeds, $N = 0$ lobe of most flexible low frequency structural mode was observed to significantly vary and affect process stability depending on the choice of redundancy variable. In addition, stability boundaries coming from tool holder-spindle shaft mode of vibration also showed variations as in [136, 137]. In particular, magnitude of the minimum limiting depth of cut was observed to vary which was also identified with cutting tests too.

5. **The hypothesis of deployment of continuous structural dynamics variation during cutting by controlling the redundancy variable for chatter suppression in low and high spindle speeds was found to be inconclusive**.

In low spindle speeds, the hypothesis of chatter suppression was tested by benefiting from stability lobe location alteration as a result of manipulator configuration alteration by varying redundancy variable. However, the choice of cutting parameters was not enough to establish a strong evidence to validate the hypothesis.

In high spindle speeds, chatter suppression was aimed by benefiting from manipulator configuration dependency of N=0 lobe of most flexible structural robot mode and tool holder-spindle shaft mode of vibration. The tests showed no sign of chatter suppression through deployment of continuous structural dynamics variation. Even though the process stability was observed to change based on the choice of redundancy variable, no trace of chatter suppression was found out.

The hypothesis was deduced to be inconclusive due to the insufficiency of cutting tests failing to investigate the effect of various spindle speeds, depth of cuts and TCP pose rotation velocities on process stability.

6. **Mode coupling chatter mechanism does not to exist in milling operations**.

   In the existing literature, appearance of low frequency severe vibrations while milling with flexible machine tools and industrial robots at high spindle speeds was attributed to mode coupling chatter mechanism [37, 175, 177–179]. However, regenerative chatter stability boundaries were not adequately analysed before deducing the type of chatter mechanism within the process. Mode coupling chatter models used in milling were initially based on turning/ boring operation [37, 175, 178, 179] which incorrectly represented the operation as well as ignored the effect of the time delay on dynamic chip thickness. Even though mode coupling chatter model was updated to represent milling operations in [182], there were not any information about the validity of model. Additionally, stability boundaries as well as discrepancies between regenerative and mode coupling chatter mechanisms were not clearly illustrated and validated.

   In Chapter 6, zero and multi frequency mode coupling chatter mechanism were adapted based on [182], developed and validated with milling tests. The findings pointed out that mode coupling stability boundaries (zero and multi frequency) are not able to describe the spindle speed dependent process stability behaviour of cutting tests at low and high spindle speeds. In addition, stability boundaries at high spindle speeds were not matching to high frequency chatter vibrations observed in tests. The comparison between stability boundaries of regenerative and mode coupling chatter mechanism revealed that regenerative chatter mechanism was effective enough to describe the process stability even though predictions were not perfectly fitting to the stability of tests. Thus, mode coupling chatter was proved not to exist in milling operations. Note that the assumption of negligible time delay is incorrect for such an intermittent cutting process in which the tool always cuts previously machined surface.

7.3 Contributions to knowledge

1. **The N=0 stability boundary coming from the most flexible low frequency structural mode can be controlled by utilising functional and kinematic redundancy variable to unveil regions in SLD which were previously predicted as unstable regions**.

   Low stability of robotic milling operations has been an obstacle for application of industrial manipulators in milling operations. The attempts made to improve stability of robotic milling such as eddy current damper design for chatter suppression [154] and stability boundary optimisation by utilising the redundancy variable as in [136, 137] were not effective enough. In the thesis, a large region of SLD was unveiled by choosing an optimal manipulator configuration by utilising the functional and kinematic redundancy. The unveiled region in SLD could enable carrying out milling operations at larger depth of cuts across moderate to high spindle speeds while avoiding from low frequency severe chatter vibrations as illustrated in Figure 5.42. Such an enhancement in the stability of robotic milling operations has the potential to increase the impact and application of robots in machining sector.

2. **Zero frequency mode coupling chatter mechanism was developed along modal directions and extended to multi frequency for milling operations. Mode coupling chatter stability boundaries were validated with cutting tests and mode coupling chatter was concluded not to exist in milling operations**.

   Zero frequency approach in modal directions as well as multi frequency approach were developed and solved to better understand the behaviour of mode coupling chatter in milling. The work carried out extends mode coupling chatter models developed in literature with improved stability boundary predictions and validation of predictions with cutting tests. The comparison of zero and multi frequency predictions with the stability of cutting tests revealed a great mismatch. However, it was shown that stability of cutting tests could be easily explained with regenerative chatter mechanism. Thus, findings suggested that mode coupling chatter does not exist in milling operations. This enlightens the ambiguity of chatter mechanism observed especially in robotic milling operations and justifies that mode coupling in milling is impossible. Such a justification could stop the ambiguity to build up in academia and industry and help redirecting research directions on the stability of robotic milling.

3. **Design of a joint compliance identification simulation and framework to investigate and fine-tune factors affecting the identification accuracy in industrial environment**.

   Modelling the experimental design and measurement sensitivities for joint compliance parameter identification are crucial for predicting and fine-tuning the accuracy of parameters being identified experimentally. In the existing literature, there exists an approach used for identifying joint compliance parameters of an industrial robot while investigating their accuracy based on considering measurement noise and number of manipulator configurations. The procedure, however, was tested in a virtual environment with a loading that could violate the torque limits of joints and cause structural damage. The proposed framework, however, underlines a greater number of factors affecting joint compliance parameter identification accuracy and

avoids application of loads that could cause damage to the robot. Even though the proposed framework could be more cumbersome than the existing approach, a possible damage to the robot can be avoided. The proposed framework could be used in industrial environment for identifying manipulator stiffness safely and more accurately to be used for applications such as form error minimisation and compensation for machining operations. The approach can also be benchmarked to enable the user to determine the accuracy of stiffness model be applied in various environments and applications too.

4. **Optimising manipulator compliance by utilising the functional and kinematic redundancy around the axis of rotation of tool while ensuring TCP pose accuracy**.

   By the time the contribution was made, existing approaches were not making sure TCP pose accuracy while optimising manipulator stiffness (or compliance). Inaccuracies in TCP pose mean that tool tip will deviate away from ideal tool path even in unloaded conditions and cause further dimensional inaccuracies on the end product while machining. This problem is solved by utilising inverse kinematics to meet TCP pose accuracy requirements. Addressing TCP accuracy requirements with the proposed approach makes sure that the manipulator configuration and TCP pose are accurately defined while optimising its compliance. Additionally, with the proposed approach, manipulator configurations with optimum compliance can also be searched within the entire parameter space of the redundant DOF to make sure the chosen configurations are optimum globally. Having possible dimensional inaccuracies coming from the manipulator optimisation eliminated, it is more effective to minimise the compliance of the manipulator along the selective direction. The proposed approach, however, can only optimise the selective compliance parameters at a time. This means manipulator compliance along a single selected direction can be optimised if the type of applied loading is known (force or torque). Nevertheless, optimised manipulator configurations with minimised compliance across TCP trajectory can reduce static deflection of TCP at a single direction at a time. Such an approach could be easily applied to software packages being used in industry for robotic applications requiring high pose accuracy (such as robotic waterjet cutting). In this way, static deflection of the manipulator can be minimised without affecting cutting trajectories.

5. **Extension of 1-DOF Multi Frequency Analysis (MFA) for variable helix and pitch tools developed by [203] to 2-DOF to consider the effect of radial vibrations on regenerative stability**.

   In the existing literature, there exists 2-DOF multi frequency regenerative chatter mechanism model but for regular end mills with straight flutes in [26, 202]. However, it is not suitable to model the stability of milling with end mill tools having non-uniform pitch and highly varied helix angles. This was addressed by approaches proposed in [203, 220] that describes the stability in 1-DOF. Thus, a 2-DOF multi frequency regenerative chatter mechanism model for end mill tools with non-uniform pitch and highly varied helix angles was developed based on [203]. The 2-DOF MFA for variable helix and pitch tools has the potential to increase accuracy of stability predictions for MDOF machine tool structures. The proposed approach also takes into account structural mode coupling between modes of vibration which could improve the stability predictions for manufacturing with tighter tolerances.

7.4 Publications

Findings of the thesis were published and presented in the conference proceedings. The following are the published conference proceedings that can be found in the literature;

1. H. Celikag, N. D. Sims, and E. Ozturk. *"Cartesian Stiffness Optimization for Serial Arm Robots"* In. vol. 77. Procedia CIRP. 2018, pp. 566-569. [130]
2. H. Celikag, N. D. Sims, and E. Ozturk. *"Chatter Suppression in Robotic Milling by Control of Configuration Dependent Dynamics"* In. vol. 82. Procedia CIRP. 2019, pp 521-526. [221]

7.5 Future work

Throughout the thesis, structural static and dynamic properties of industrial manipulators were investigated and their relation to stability of robotic machining operations was examined. The work done could be further expanded based on findings of the thesis in order to enhance capabilities of robotic machining operations.

Regarding structural statics of industrial manipulators, manipulator static stiffness identification, modelling and optimisation were considered throughout the thesis.

In order to identify joint compliance parameters of an industrial manipulator, a simulation was implemented to imitate the experimental set-up and investigate the factors affecting joint compliance parameter identification accuracy. The simulation utilised a measure of performance index that was based on standard deviation of identified parameters after a statistical analysis to determine the identification accuracy. However, the proposed performance index may not be the most effective way of quantifying identification accuracy. Instead, the difference between corresponding deflection of initially defined and identified joint compliance parameters of manipulator stiffness model under a theoretically applied loading could have been used as a measure of identification accuracy. The identification accuracy of joint compliance parameters would then be represented by a physical parameter (static deflection error between a theoretical and identified manipulator stiffness model) rather than a non-physical parameter. In this way, the interpretation of simulation results could be used as a guidance to adjust identification accuracy based on the industrial environment and requirements where it would be used for (machining operation, material handling etc).

Poor manipulator static stiffness is known to result in large static deflection under cutting forces. In order to minimise static deviation (form error), kinematic and functional redundancy could be utilised to optimise manipulator TCP stiffness/ compliance. The proposed approach considers optimisation of manipulator compliance matrix by utilising a single compliance parameter at a time. Such an approach is certainly not suitable and effective enough in an industrial environment to minimise form errors for robotic milling operations. This is due to the fact that static deviation in any direction depends on more than one Cartesian compliance parameter as well as the magnitude and direction of loading. An objective function to consider multiple Cartesian compliance parameters (as in [128, 132]) could enable a better optimisation but it would not still make sure that manipulator configurations are optimised in selective directions. In addition to the consideration of direction of loading (as in [131, 132]), the magnitude of loading should also be taken into account to optimise the manipulator compliance/ stiffness. Considering all, the

optimisation should be based on static TCP deviation rather than manipulator compliance to minimise static TCP deviation. Thus, instead of manipulator compliance optimisation, TCP deformation optimisation should be aimed in single or multiple directions. The proposed theory behind Cartesian compliance optimisation could be expanded easily for deformation optimisation. Deformation optimisation would necessitate Cartesian compliance/ stiffness matrix together with loading vector defining the magnitude and direction of loading to predict and optimise static TCP deviation (form error). In this way, manipulator configurations could be better optimised to minimise form errors for any 5-axis robotic machining operation. Such an approach could deliver more effective form error minimisation for any robotic operation (material handling, machining etc.) and could enable visualisation of form errors before carrying out operations. Such an advantage is crucial for visualising form error and making sure the end product would satisfy dimensional accuracy requirements.

The deformation (deflection) optimisation has the potential to further minimise the form error in robotic machining operations without necessitating any additional equipment or hardware that could be costly. Provided that the process stability is ensured, form error could be minimised based on optimising the manipulator configurations without altering the 5-axis cutting trajectories. Form error compensation techniques could also be applied (online or offline) to compensate minimised form errors as a second step after deformation optimisation. Deformation optimisation and form error compensation, together, could help machining robots to satisfy dimensional accuracy and tolerance constraints. Such an improvement would definitely increase the application of robots in the manufacturing industry. However, deformation optimisation does not improve the performance of robots in metal cutting operations. This is because the low process stability is the main factor that impedes the feasibility of robotic machining operations rather than the form error. Hence, the poor structural dynamics of robots is the limiting factor.

Regarding structural dynamics, the work done throughout the thesis (as well as in the literature) suggested that the stability of robotic milling is low and configuration dependent. However, the kinematic and functional redundancy could be utilised to optimise the stability of robotic milling operations. It was shown that stability boundaries in low spindle speed region is very low but strongly dependent on the manipulator configuration. In high spindle speed region, stability boundaries are relatively higher with marginal dependency on the manipulator configuration. Even though it seems more plausible to machine at higher spindle speed region, stability boundaries are still relatively low for metal machining operations compared to a machine tool.

In the thesis, the deployment of continuously varying structural dynamics was investigated to improve stability of robotic milling and achieve chatter suppression. However, even though stability predictions showed a great potential chatter suppression characteristics, cutting tests were found to be inconclusive. While altering the manipulator configuration to achieve continuously varying structural dynamics in robotic milling tests, only one TCP rotation velocity was assigned to rotate the TCP pose. In addition to that, only one spindle speed was utilised in both low and high spindle speed regions with different depth of cuts to validate the hypothesis of chatter suppression. The milling tests were found to be inconclusive with no trace of chatter suppression (or stabilisation) possibly due to the choice of cutting parameters. Instead, a variety of TCP rotation velocity, spindle speeds and depth of cuts should have been carried out to completely validate the hypothesis of chatter stabilisation. A faster TCP rotation velocity could result in quicker

shift of chatter frequencies and result in more apparent and effective chatter suppression. An effective chatter suppression has the potential to increase the stability of robotic machining operations and allow carrying out milling operations in a larger set of machining parameters with higher productivity. The benefit of this approach is that the kinematic and functional redundancy can be used for any operation that necessitates 5-axis (DOFs) cutting trajectories (or less).

In order to further enhance the stability of robotic machining operations, tuned mass dampers could also be utilised to damp selective modes of vibration. Knowing that low frequency structural robot modes could affect the moderate-high spindle speed spectrum of the SLD, tuned mass dampers can be used to damp these low frequency modes. This could enable further control over stability boundaries coming from structural modes and unveil larger regions where machining operations could be carried out without chatter vibrations. However, it should not be forgotten that structural robot modes are configuration dependent. In order to achieve effective damping of structural modes, natural frequency of the tuned mass damper would also need to be adjustable based on the manipulator configuration. A structural dynamic model of the manipulator could be used to predict natural frequency of the most flexible structural mode to adjust natural frequency of the tuned mass damper by online or offline methods. However, the natural frequency shift of structural modes could be large as a result of considerable structural alterations of the manipulator configuration during machining. This could limit the working envelope of machining operations as tuned mass damper could not be adjusted to match such a large natural frequency shift of structural mode. Nevertheless, utilisation of tuned mass dampers has the potential to further improve the stability of robotic machining operations.

Moving towards machining metal parts with industrial robots, the most striking obstacle would be the process stability. Even though chatter suppression or dynamic optimisations are possibly increase stability limits, they might not be sufficient to apply robots for high productivity metal machining. For this reason, a further research is required to improve manipulator structural dynamics with a particular attention could be given to joint dynamics. Joints are known to be the most flexible components and not designed to handle dynamic loading. Thus, identifying and modelling dynamic characteristics of joints could play an crucial role.

Lastly, the revised current theory of mode coupling chatter mechanism in thread cutting operations in turning and boring was spotted to possess some drawbacks. These drawbacks include inapplicability of cross-FRFs terms and multi modes of vibration in each modal (or orthogonal) direction into the equations. Hence, a more comprehensive theory for mode coupling chatter mechanism in thread cutting (thread boring and turning) operations needs to be developed to enable better understanding of the chatter mechanism and more accurate prediction of stability boundaries. In this way, mode coupling chatter theory can be made more applicable in an industrial environment.

Appendix A

End effector device

The end effector device attached onto the end effector of ABB IRB 6640 205/2.75 is presented in Figure A.1;

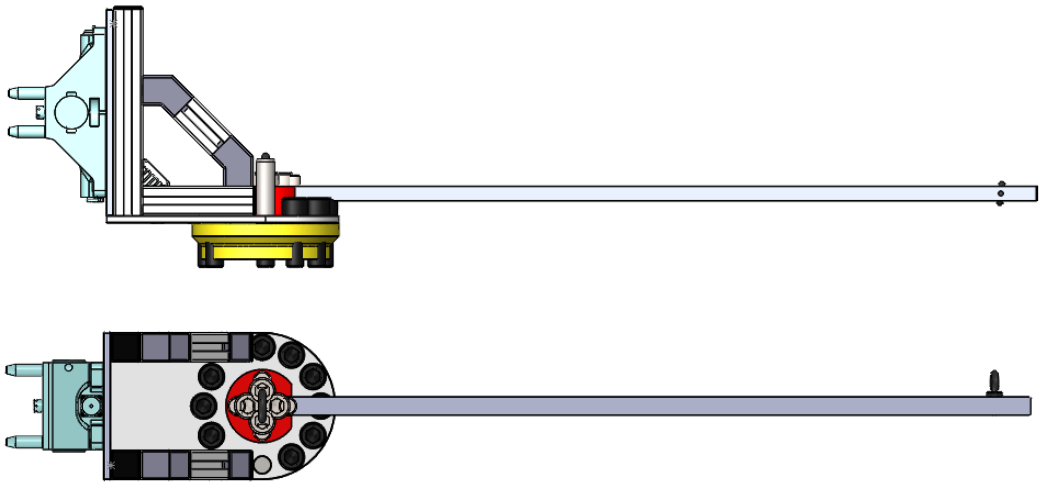

FIGURE A.1: The top and front views of the end effector device together with TMAC

The end effector device acted as an attachment to accommodate the TMAC for taking TCP pose measurements before and after application of loading. Additionally, it was used to apply forces to the manipulator that are aligned with its *Base Frame* as well as apply a torque around the end effector pose.

Appendix B

Random loading applied in joint compliance identification

For joint compliance identification of ABB IRB 6640 205/2.75, the plates were hanged onto the weight baskets that were suspended with a string and pulley. In this way, tension was aimed to be applied to the end effector to load the manipulator. The random loading procedure used in the experiment makes use of the random assignment of the weights to be suspended. The total loading applied to each weight basket along the *Base Frame* axes are given as below.

Loading number	Mass hanged along axes		
	$+X_{Base}$	$-Y_{Base}$	$-Z_{Base}$
1	65	20	40
2	5	65	50
3	10	80	10
4	0	55	80
5	30	50	55
6	80	15	35
7	55	60	5
8	40	40	25
9	35	0	70
10	20	45	0
11	45	25	20
12	75	10	15
13	25	70	30
14	70	5	60
15	60	35	75
16	15	75	65
17	50	30	45

TABLE B.1: The masses applied to each weight basket that was used to apply a tension along the specified axes

Appendix C

Bill of Materials for Scaffolds

Table C.1 outlines the bill of materials used to build the scaffolds in the joint stiffness identification experiment.

Product	Profile	Length (or Angle)	Quantity
Strut Profile	40x40	73 mm	2
	40x40	1920 mm	5
	40x40	2000 mm	2
	40x40	360 mm	4
	40x40	400 mm	4
	40x40	1000 mm	6
	40x40	960 mm	5
	40x40	500 mm	7
	40x40	600 mm	10
	40x40	220 mm	5
	40x40	766 mm	4
	40x40	427 mm	4
	40x40	300 mm	4
	40x40	1200 mm	5
	40x40	1280 mm	2
	40x40	280 mm	2
	40x40	150 mm	2
	40x40	1920 mm	1
Connector	40x40	45 °	20
Gusset	40x40	-	70
Clamping Lever	-	-	16
Sliding Element	-	-	20
T-Nut	10MB	-	100
Cap Cover	40x80	-	20
Foundation Kit	-	-	20
Cap Cover	40x40	-	40
Gusset	40x80	-	30

TABLE C.1: The bill of materials used to build the scaffolds

Appendix D

Details of SADE and findings

Self Adaptive Differential Evolution is an extension of Differential Evolution (DE) where in its foundation, it generates a better population of the possible solutions for the optimisation problem in an iterative manner based on comparing the assigned measure of quality (cost) between the population in the previous and current generations [222]. What differentiates SADE from DE is that it adapts its hyper-parameters by using the knowledge developed through exploration and identification of the problem being optimised to improve the performance.

The chosen link lengths and offsets to be optimised were parametrised into 6-dimensional parameter vectors of DH parameters within a population having fixed upper and lower bounds. Every 6-dimensional parameter vector was used to create a trial DH kinematic model for the manipulator and for the given 5 sets of joint variables, the forward kinematics of the kinematic model was compared with the measured TCP pose (the remaining measured TCP pose left for validating the model). Robot configurations used in the optimisation procedure are listed in Table D.1.

Joint Variable (°)	q_1	q_2	q_3	q_4	q_5	q_6
Configuration 1	-9	8.5	-61	13	76.5	-25
Configuration 2	14	16	-44	28	16	-40
Configuration 3	45	-20	14	80	0	-93
Configuration 4	58	-33	23	-19	97	38
Configuration 5	70	-38	15	80	-49	-124

TABLE D.1: The manipulator configurations used for kinematic calibration

The total error coming from all configurations were summed to give a scalar measure for the quality. The *Cost* of the SADE is given below,

$$Cost = \frac{1}{5}\sum_{z=1}^{5} Error_z \tag{D.1}$$

where $Error_z$ is the mismatch between modelled and measured TCP pose,

$$Error_z = \frac{3}{RL_z^M} tr({}^{Err}T_z^T \times {}^{Err}T_z) \tag{D.2}$$

where RL_z^M is the reach length of the modelled manipulator and ${}^{Err}T$ is given by,

$$ {}^{Err}T = ({}^{Exp}T_z^{-1} \times {}^{M}T_z) - I \tag{D.3}$$

where ${}^{M}T_z$ and ${}^{Exp}T_z$ are the modelled and measured TCP poses. SADE was run for 450 generations until the minimum *Cost* of the current population converged. The minimum *Cost* over the number of generations computed is represented in Figure D.1.

Even if the minimum *Cost* seems to be converged around 150 generations, the fluctuations were observed until 250 generations. Nevertheless, SADE was run until 450 generation to make sure the obtained solution is a global solution for the problem being optimised. Another aspect to consider is that, even though the minimum *Cost* converged, the parameters being optimised might still vary as a result of their weak influence on the *Cost*.

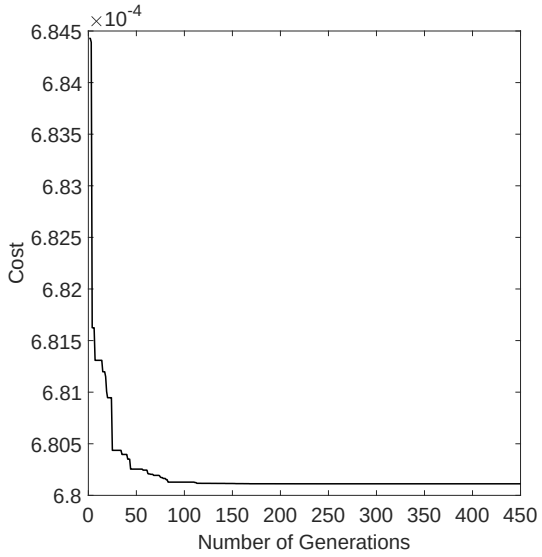

FIGURE D.1: The minimum cost versus number of generations implemented in SADE

The optimised link lengths and offsets over the number of generations are also depicted as in Figure D.2.

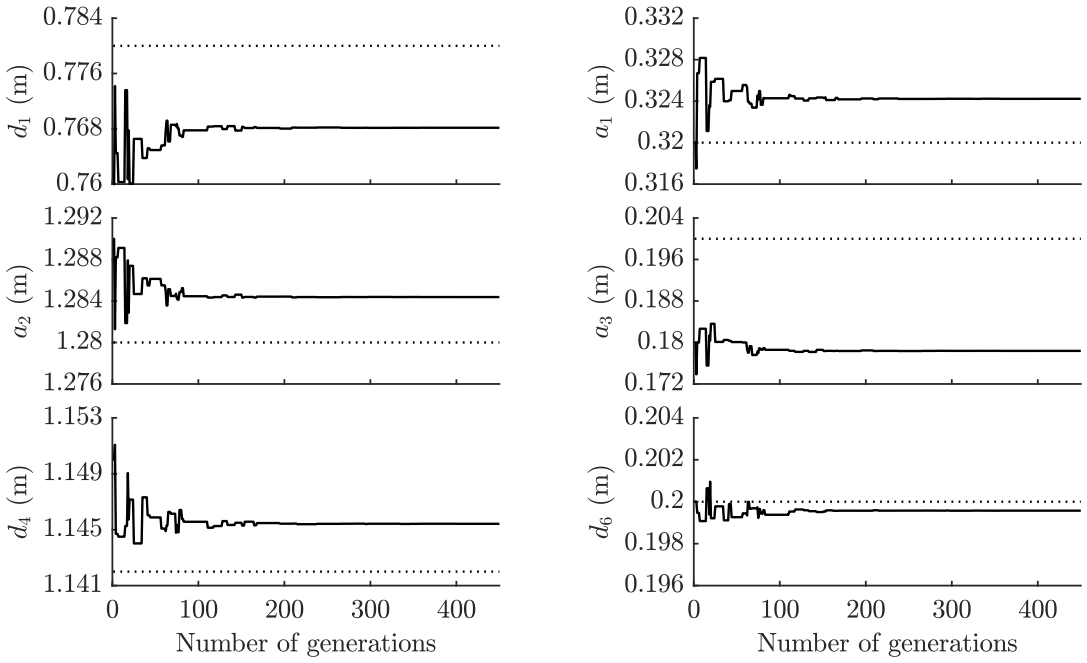

FIGURE D.2: The comparison between the optimised and nominal DH parameters versus the number of generations implemented in SADE. Solid line represents the evolution of the optimised DH parameter, Dashed line represents its corresponding nominal value

The optimised link lengths and offsets clearly indicate that the SADE converged for the number of generations implemented. It could also be seen that some of the parameters diverged slightly from their corresponding nominal values. This supports that manipulator link length and offset dimensions could possibly vary from one manipulator to another due to manufacturing, assembly, etc tolerances.

Appendix E

Manipulator configurations used for joint compliance identification

The joint variables used to configure the serial industrial manipulator, ABB IRB 6640 205/2.75, into the suitable configurations are given as below.

Joint Variable (°)	q_1	q_2	q_3	q_4	q_5	q_6	KCI %
Configuration 1	55	-5	50	60	-75	-30	56.6
Configuration 2	60	0	45	-120	85	140	59.1
Configuration 3	60	5	45	-120	85	140	58.8
Configuration 4	60	5	50	-120	85	140	59.0
Configuration 5	60	10	50	-120	85	150	58.7
Configuration 6	60	10	50	60	-95	-20	60.7
Configuration 7	60	10	55	-120	85	150	58.7
Configuration 8	60	15	50	-120	95	-190	60.4
Configuration 9	60	15	55	-120	85	150	58.5
Configuration 10	60	15	55	60	-95	-20	60.3
Configuration 11	40	5	50	40	-85	-30	56.3

TABLE E.1: The manipulator configurations used for joint compliance parameter identification

Appendix F

Tool trajectories

Two sizes of workpieces were designed; square and rectangular plates as in Figure F.1.

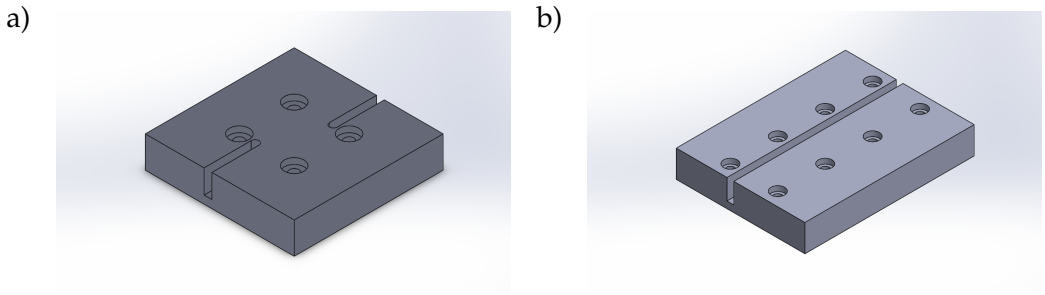

FIGURE F.1: Acetal Co-polymer workpieces in CAD a) Square plate b) Rectangle plate

Square workpiece was used for low spindle speed cuts as it requires short trajectories whereas rectangular plate was high speed spindle cuts. The dimensions of both plates, locations of slots etc. are given in Appendix H.

The set of straight trajectories designed are as shown in Figure F.2.

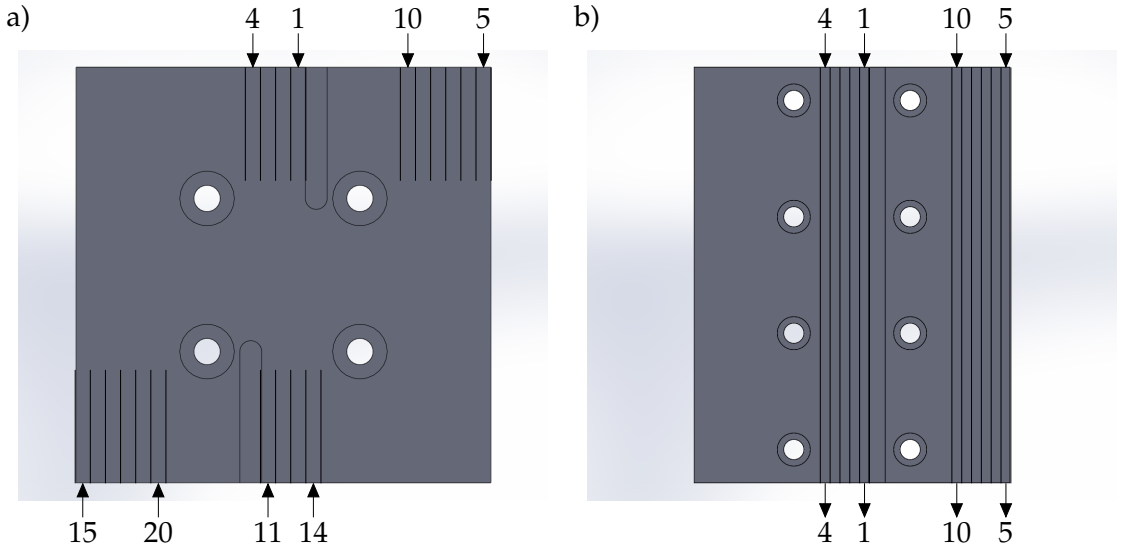

FIGURE F.2: Tool trajectories on Acetal Co-polymer a) Square plate b) Rectangle plate

The number of tool trajectories were set to be 10 in each side of the square plate. The plate was rotated 180° to make use of the material at the opposite side as shown in Figure F.2a. On the other hand, rectangular plate was set to accommodate 10 tool trajectories in total which run along the length of the plate as in Figure F.2b. The order of tool trajectories that commanded to cut are listed on both plates.

Appendix G

Identified Work Object Frames

Identified workobject frames T_{WObj} for square and rectangle Aceltal Co-polymer workpieces are shown below respectively.

$$ {}^{Sq}T_{WObj} = \begin{bmatrix} 0.9998 & 0.0173 & -0.0035 & 1.0167 \\ -0.0173 & 0.9998 & 0.0002 & -1.434 \\ 0.0035 & -0.0001 & 1.0000 & 0.5908 \\ 0 & 0 & 0 & 1 \end{bmatrix} \tag{G.1} $$

$$ {}^{Re}T_{WObj} = \begin{bmatrix} 0.9999 & 0.0156 & -0.0029 & 0.9871 \\ -0.0156 & 0.9999 & 0.0023 & -1.433 \\ 0.0029 & -0.0023 & 1.0000 & 0.5912 \\ 0 & 0 & 0 & 1 \end{bmatrix} \tag{G.2} $$

Appendix H

Workpiece dimensions

H.1 Square plate

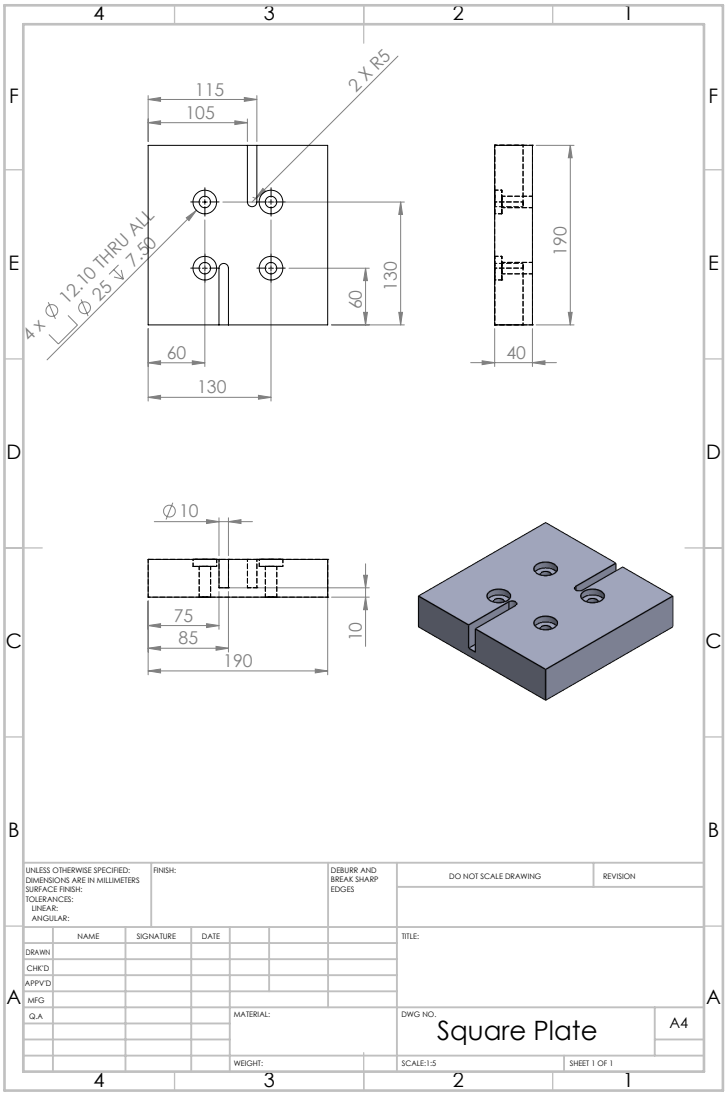

FIGURE H.1: Square plate engineering drawing

H.2 Rectangle plate

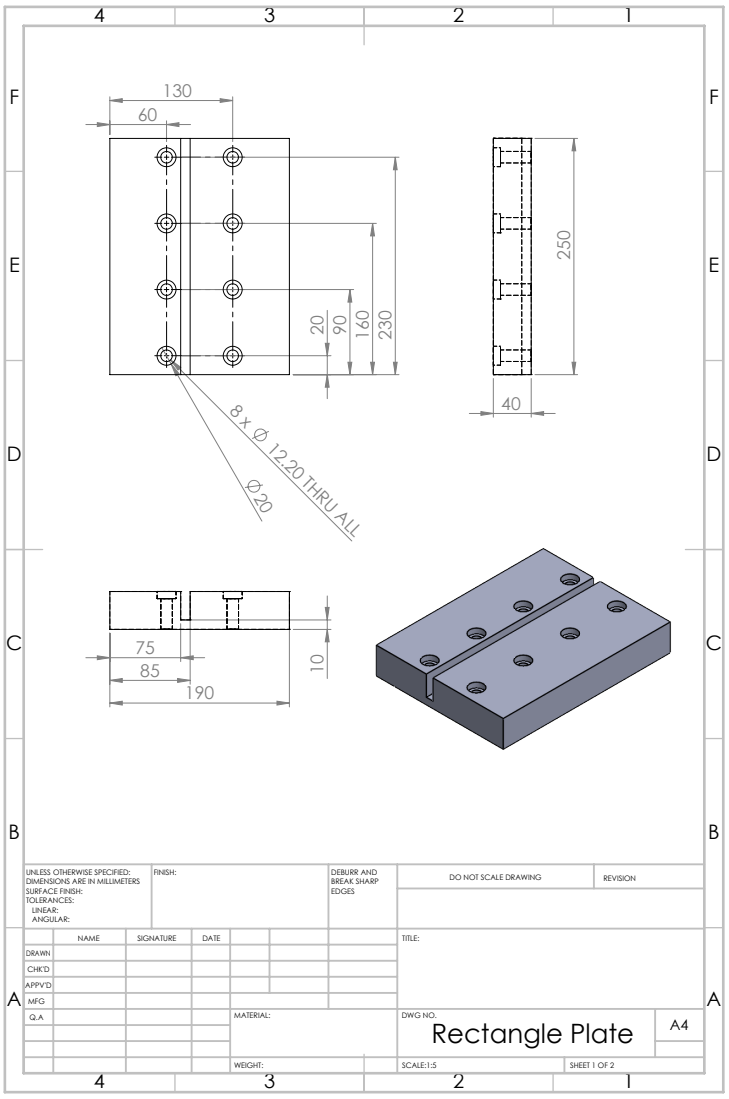

FIGURE H.2: Rectangle plate engineering drawing

Appendix I

Stability predictions for chatter stabilisation

I.1 Low spindle speed - P2

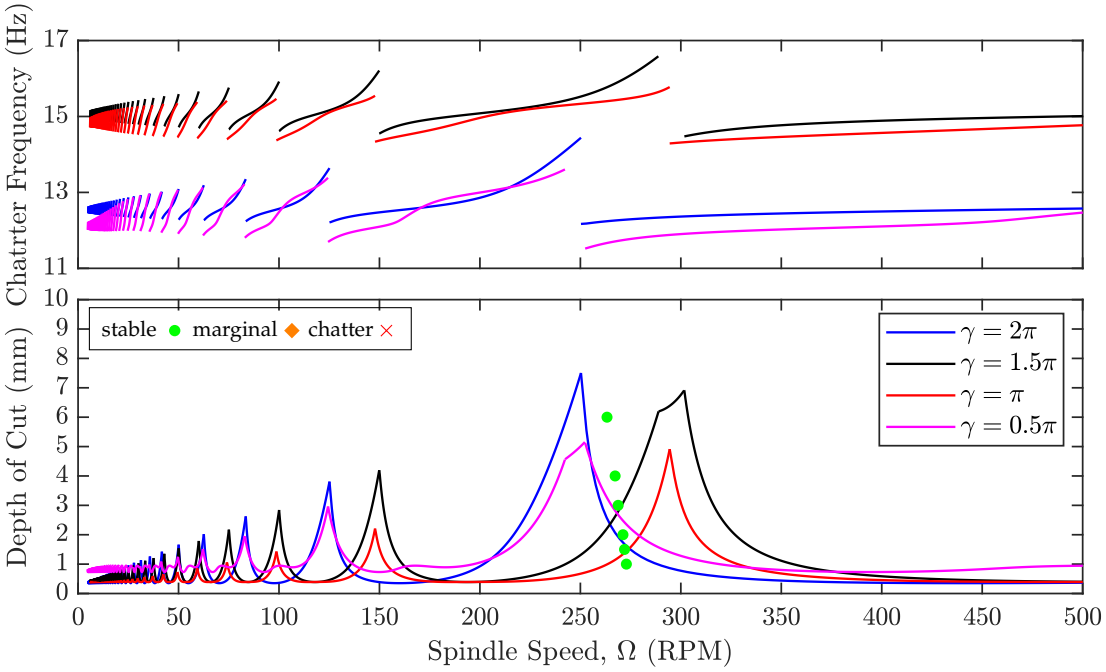

FIGURE I.1: The low-spindle speed stability predictions at *P*2 for all redundancy variables, γ

I.2 High spindle speed - P4

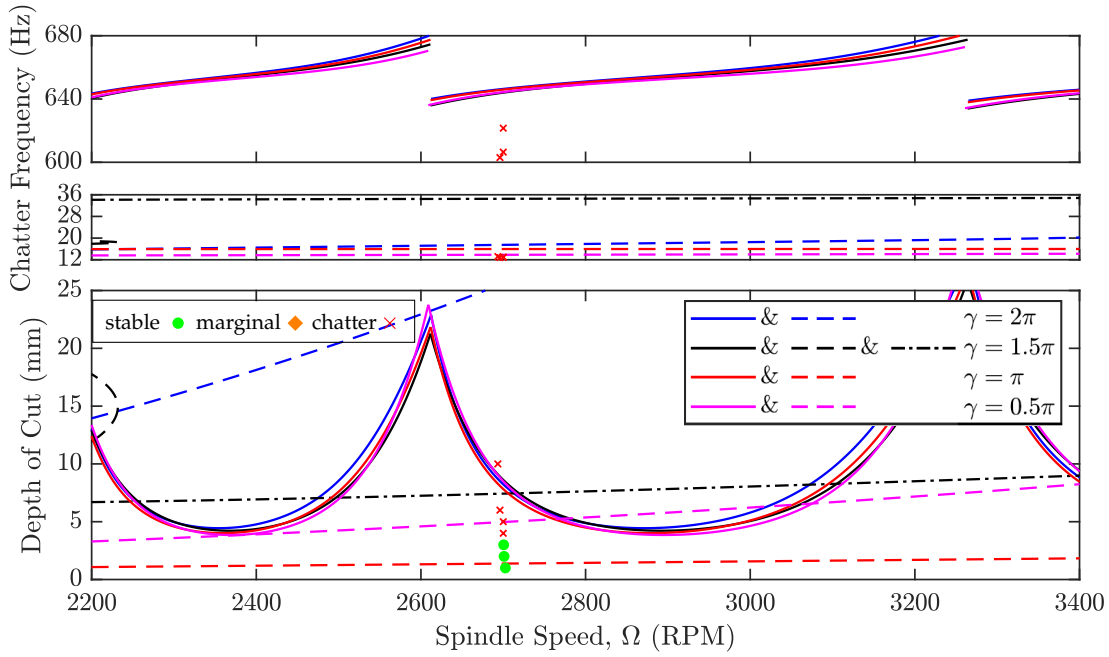

FIGURE I.2: The high-spindle speed stability predictions at *P*4 for all redundancy variables, γ

References

[1] C. Roser. *"Faster, Better, Cheaper" in the History of Manufacturing*. CRC Press, 2017.

[2] M. P. Groover. *Fundamentals of Modern Manufacturing: Materials, Processes, and Systems*. John Wiley & Sons, Inc, 2007.

[3] Z. Zhu et al. "A review of hybrid manufacturing processes – state of the art and future perspectives". In: *International Journal of Computer Integrated Manufacturing* 26 (2013), pp. 596–615.

[4] W. Zhu et al. "An off-line programming system for robotic drilling in aerospace manufacturing". In: *The International Journal of Advanced Manufacturing Technology* 68 (2013), pp. 2535–2545.

[5] Hae-Sung Yoon et al. "A comparison of energy consumption in bulk forming, subtractive, and additive processes: review and case study". In: *International Journal of Precision Engineering and Manufacturing-Green Technology* 1 (2014), pp. 261–279.

[6] B. T. Araghi et al. "Investigation into a new hybrid forming process: Incremental sheet forming combined with stretch forming". In: *CIRP Annals* 58 (2009), pp. 225–228.

[7] R. Anitha, S. Arunachalam, and P. Radhakrishnan. "Critical parameters influencing the quality of prototypes in fused deposition modelling". In: *Journal of Materials Processing Technology* 118 (2001), pp. 385–388.

[8] Ferry P. W. Melchels, Jan Feijen, and Dirk W. Grijpmaa. "A review on stereolithography and its applications in biomedical engineering". In: *Biomaterials* 4 (2010), pp. 6121–6130.

[9] Peter Heinl et al. "Cellular Ti–6Al–4V structures with interconnected macro porosity for bone implants fabricated by selective electron beam melting". In: *Acta Biomaterialia* 4 (2008), pp. 1536–1544.

[10] J. P. Krutha et al. "Selective laser melting of iron-based powder". In: *Journal of Materials Processing Technology* 149 (2004), pp. 616–622.

[11] Jessica M. Williams et al. "Bone tissue engineering using polycaprolactone scaffolds fabricated via selective laser sintering". In: *Biomaterials* 26 (2005), pp. 4817–4827.

[12] I. Gibson, D. W. Rosen, and B. Stucker. *Additive Manufacturing Technologies: Rapid Prototyping to Direct Digital Manufacturing*. Springer, 2010.

[13] O. Abdulhameed and A. Al-Ahmari abd W. Ameen. "Additive manufacturing: Challenges, trends, and applications". In: *Advances in Mechanical Engineering* 11 (2019), pp. 1–27.

[14] Amit Bandyopadhyay and Susmita Bose. *Additive Manufacturing*. CRC Press, 2016.

[15] H. A. El-Hofy. *Fundamentals of Machining Processes: Conventional and Nonconventional Processes*. CRC Press, 2014.

[16] T. Childs et al. *Metal Machining: Theory and Applicaitons*. Arnold, 2000.

[17] Bert Lauwers et al. "Hybrid processes in manufacturing". In: *CIRP Annals* 63 (2014), pp. 561–583.

[18] S. Z. Chavoshi and X. Luo. “Hybrid micro-machining processes: A review”. In: *Precision Engineering* 41 (2015), pp. 1–23.
[19] H. Liand et al. “Experimental Research of Al6061 on Ultrasonic Vibration Assisted Micro-Milling”. In: vol. 6. 2013, pp. 561–564.
[20] Tong Hao, Wang Yang, and Li Yong. “Vibration-assisted servo scanning 3D micro EDM”. In: *Journal of Micromechanics and Microengineering* 18 (2008).
[21] H. Ding, N. Shen, and Y. C. Shin. “Thermal and mechanical modeling analysis of laser-assisted micro-milling of difficult-to-machine alloys”. In: *Journal of Materials Processing Technology* 212 (2012), pp. 601–613.
[22] V. Tangwarodomnukun et al. “An investigation of hybrid laser–waterjet ablation of silicon substrates”. In: *International Journal of Machine Tools and Manufacture* 56 (2012), pp. 39–49.
[23] Y. Koren et al. “Reconfigurable manufacturing systems”. In: *CIRP Annals* 48 (1999), pp. 527–540.
[24] Y. Yamane et al. “Measuring and cutting a propeller for a ship by an articulated robot”. In: *Journal of the Japan Society for Precision Engineering* 57 (1991), pp. 1387–1392.
[25] K. Shirase et al. “Articulated robot application in end milling of sculptured surface”. In: *JSME International Journal Ser. C, Dynamics, Control, Robotics, Design and Manufacturing* 39 (1996), pp. 308–316.
[26] Y. Altintas. *Manufacturing Automation: Metal Cutting Mechanics, Machine Tool Vibrations, and CNC Design*. Cambridge University Press, 2012.
[27] G. W. Long and J. R. Lemon. “Structural Dynamics in Machine-Tool Chatter: Contribution to Machine-Tool Chatter Research — 2”. In: *Journal of Engineering for Industry* 87 (1965), pp. 455–463.
[28] M. Law et al. “Position-dependent dynamics and stability of serial-parallel kinematic machines”. In: *CIRP Annals - Manufacturing Technology* 62 (2013), pp. 375–378.
[29] M. Law and S. Ihlenfeld. “A frequency-based substructuring approach to efficiently model position-dependent dynamics in machine tools”. In: *Journal of Multi-body Dynamics* 229 (2015), pp. 304–317.
[30] M. Law et al. “Position-dependent dynamics and stability of serial-parallel kinematic machines”. In: *CIRP Annals* 62 (2013), pp. 375–378.
[31] M. H. N. Widiyatro, D. G. Ford, and C. Pislaru. “Evaluating the structural dynamics of a vertical milling machine”. In: *WIT Transactions on Engineering Sciences* 44 (2003), pp. 421–430.
[32] Mohit Law. “Position-dependent dynamics and stability of machine tools”. PhD thesis. Vancouver: The University of British Colombia, Aug. 2013.
[33] L. T. Tunc and J. Barnfather. “Investigation of hexapod robot dynamics and its effects in milling”. In: 2014.
[34] M. Cordes, W. Hintze, and Y. Altintas. “Chatter stability in robotic milling”. In: *Robotics and Computer Integrated Manufacturing* 55 (2019), pp. 11–18.
[35] D. Hao et al. “Experimental study of stability prediction for high-speed robotic milling of aluminum”. In: *Journal of Vibration and Control* (2019), pp. 1–12.
[36] S. Mejri et al. “Dynamic characterization of machining robot and stability analysis”. In: *The International Journal of Advanced Manufacturing Technology* 82 (2016), pp. 351–359.
[37] L. Cen and S. N. Melkote. “CCT-based mode coupling chatter avoidance in robotic milling”. In: *Journal of Manufacturing Processes* 29 (2017), pp. 50–61.

[38] Shimon Y. Nof. *Handbook of Industrial Robotics*. John Wiley & Sons, Inc, 1999.
[39] B. Siciliano and O. Khatib. *Handbook of Robotics*. Springer, 2008.
[40] L. N. Lopez de Lacalle and A. Lamikiz. *Machine Tools for High Performance Machining*. Springer-Verlag London Limited, 2009.
[41] A. H. Slocum. *Precision Machine Design*. Prince-Hall, Inc, 1992.
[42] U. Schneider et al. "Improving robotic machining accuracy through experimental error investigation and modular compensation". In: *The International Journal of Advanced Manufacturing Technology* 85 (2014), pp. 3–15.
[43] S. H. Kim et al. "Robotic machininig: a review of recent progress". In: *International Journal of Precision Engineering and Manufacturing* 20 (2019), pp. 1629–1642.
[44] Y. T. Oh. "Influence of the joint angular characteristics on the accuracy of industrial robots". In: *Industrial Robot: An Internaltional Journal* 38 (2011), pp. 406–418.
[45] X. Yang et al. "A minimal kinematic model for serial robot calibrationusing POE formula". In: *Robotics and Computer-Integrated Manufacturing* 30 (2014), pp. 326–334.
[46] J. H. Jang, S. H. Kim, and Y. K. Kwak. "Calibration of geometric and non-geometric errors of an industrial robot". In: *Robotica* 19 (2001), pp. 311–321.
[47] A. Nubiola and I. A. Bonev. "Absolute calibration of an ABB IRB 1600 robot using a laser tracker". In: *Robotics and Computer-Integrated Manufacturing* 29 (2013), pp. 236–245.
[48] M. Cordes and W. Hintze. "Offline simulation of path deviation due to joint compliance and hysteresis for robot machining". In: *The International Journal of Advanced Manufacturing Technology* 90 (2017), pp. 1075–7083.
[49] M. Ruderman, F. Hoffmann, and T. Bertram. "Modeling and identification of elastic robot joints with hysteresis and backlash". In: *IEEE Transactions on Industrial Electronics* 56 (2009), pp. 3840–3847.
[50] M. N. Nevmerzhitskiy et al. "Friction model of industrial robot joint with temperature correction by example of KUKA KR10". In: *Journal of Robotics* 2019 (2019).
[51] C. Gong, J. Yuan, and J. Ni. "Nongeometric error identification and compensation for robotic system by inverse calibration". In: *International Journal of Machine Tools and Manufacture* 40 (2000), pp. 2119–2137.
[52] J. Zhou, H. Nyugen, and H. Kang. "Simultaneous identification of joint compliance and kinematic parameters of industrial robots". In: *International Journal of Precision Engineering and Manufacturing* 15 (2014), pp. 2257–2264.
[53] A. Klimchik et al. "Compliance error compensation technique for parallel robotscomposed of non-perfect serial chains". In: *Robotics and Computer-Integrated Manufacturing* 29 (2013), pp. 385–393.
[54] I. Tyapin, K. B. Kaldastad, and G. Hovland. "Off-line path correction of robotic face milling using static tool force and robot stiffness". In: 2015 IEEE/RSJ International Conference on Intelligent Robots and Systems (IROS). 2015, pp. 5506–5511.
[55] Y. Chen and J. E. McInroy. "Decoupled control of flexure-jointed hexapods using estimated joint-space mass-inertia matrix". In: *IEEE Transactions on Control Systems Technology* 12 (2004), pp. 413–421.
[56] U. Heisel, F. Richter, and K. H. Wurst. "Thermal behaviour of industrial robots and possibilities for error compensation". In: *CIRP Annals* 46 (1997), pp. 283–286.
[57] V. Robin, L. SSabourin, and G. Gogu. "Optimization of a robotized cell with redundant architecture". In: *Robotics and Computer-Integrated Manufacturing* 27 (2011), pp. 13–21.

[58] P.S. Shiakolas, K.L. Conrad, and T.C. Yih. "On the accuracy, repeatability, and degree of influence of kinematics parameters for industrial robots". In: *International Journal of Modelling and Simulation* 22 (2002), pp. 245–254.
[59] C. Moller et al. "Enhanced absolute accuracy of an industrial milling robot using stereo camera system". In: vol. 26. 2016.
[60] Peter Corke. *HRobotics, Vision and Control: Fundamental Algorithms in Matlab*. Springer, 2011.
[61] Shabbir Kurbanhusen Mustafa et al. "A geometrical approach for online error compensation of industrial manipulators". In: 2010, pp. 738–743.
[62] J. F. Brethe et al. "Determination of the repeatability of a Kuka robot using the stochastic ellipsoid approach". In: 2006, pp. 4339–4344.
[63] Y. Chen and F. Dong. "Robot machining: recent development and future research issues". In: *The International Journal of Advanced Manufacturing Technology* 66 (2013), pp. 1489–1497.
[64] Francesco Leali et al. "A workcell calibration method for enhancing accuracy in robot machining of aerospace parts". In: *The International Journal of Advanced Manufacturing Technology* 85 (2016), pp. 47–55.
[65] A. Verl et al. "Robots in machining". In: *CIRP Annals - Manufacturing Technology* 68 (2019), pp. 799–822.
[66] M. F. Zaeh. "Improvement of the machining accuracy of milling robots". In: *Production Engineering* 8 (2014), pp. 737–744.
[67] S. Matsuoka et al. "High-speed end milling of an articulated robot and its characteristics". In: *Production Engineering* 95 (1999), pp. 83–89.
[68] G. Wang et al. "Dynamic cutting force modeling and experimental study of industrial robotic boring". In: *The International Journal of Advanced Manufacturing Technology* 86 (2016), pp. 179–190.
[69] Guifeng Wang et al. "Early chatter identification of robotic boring process using measured force of dynamometer". In: *The International Journal of Advanced Manufacturing Technology* 94 (2018), pp. 1243–1252.
[70] S. Bi and J. Liang. "Robotic drilling system for titanium structures". In: *The International Journal of Advanced Manufacturing Technology* 54 (2011), pp. 767–774.
[71] T. Olsson et al. "Cost-efficient drilling using industrial robots with high-bandwidth force feedback". In: *Robotics and Computer-Integrated Manufacturing* 26 (2010), pp. 24–38.
[72] N. Miller et al. "Development of automated real-timedata acquisition system for robotic weldquality monitoring". In: *Mechatronics* 12 (2002), pp. 1259–1269.
[73] H. N. M. Shah et al. "An experiment of detection and localization in tooth saw shape for butt joint using KUKA welding robot". In: *The International Journal of Advanced Manufacturing Technology* 97 (2018), pp. 3153–3162.
[74] Y. Hu et al. "Mechanism and experimental investigation of ultra high pressure water jet on rubber cutting". In: *The International Journal of Precision Engineering and Manufacturing* 15 (2014), pp. 1973–1978.
[75] F. Rafieian, B. Hazel, and Z. Liu. "Vibro-impact dynamics of material removal in a robotic grinding process". In: *Robotics and Computer-Integrated Manufacturing* 73 (2014), pp. 949–972.
[76] A. M. Tahvilian et al. "Experimental and finite element analysis of temperature and energy partition to the workpiece while grinding with a flexible robot". In: *Journal of Materials Processing Technology* 213 (2013), pp. 2292–2303.

[77] J. A. Dieste et al. “Automatic grinding and polishing using spherical robot”. In: vol. 63. Procedia Engineering. 2013, pp. 938–946.

[78] M. Slamani, S. Gauthier, and J. Chatelain. “A study of the combined effects of machining parameterson cutting force components during high speed robotictrimming of CFRPs”. In: *Measurement* 59 (2015), pp. 268–283.

[79] G. Ziliani, A. Visioli, and G. Legnani. “A mechatronic approach for robotic deburring”. In: *Mechatronics* 17 (2007), pp. 431–441.

[80] L. Feng-yun and L. Tian-sheng. “Development of a robot system for complex surfaces polishing based on CL data”. In: *The International Journal of Advanced Manufacturing Technology* 26 (2005), pp. 1132–1137.

[81] F. Nagata et al. “Robotic sanding system for new designed furniturewith free-formed surface”. In: *Robotics and Computer-Integrated Manufacturing* 23 (2007), pp. 371–379.

[82] A. Pashkevich, D. chablat, and P. Wenger. “Stiffness analysis of overconstrained parallel manipulators”. In: *Mechanism and Machine Theory* 44 (2009), pp. 966–982.

[83] S. H. Kim and B. K. Min. “Joint compliance error compensation for robot manipulator using body frame”. In: *International Journal of Precision Engineering and Manufacturing* (2020).

[84] W. Wang, R. N. K. Loh, and E. Y. Gu. “Passive compliance versus active compliance in robot-based automated assembly systems”. In: *Industrial Robot* 25 (1998), pp. 48–57.

[85] M. H. Ang and G. B. Andeen. “Specifying and achieving passive compliance based on manipulator structure”. In: *IEEE Transactions on Robotics and Automation* 11 (1995), pp. 504–515.

[86] M. T. Mason. “Compliance and force control for computer controlled manipulators”. In: *IEEE Transations on Systems, Man, and Cybernetics* 11 (1981), pp. 418–432.

[87] D. Chakarov. “Study of the passive compliance of parallel manipulators”. In: *Mechanism and Machine Theory* 37 (1999), pp. 373–389.

[88] N. Ciblak and H. Lipkin. “Synthesis of Cartesian stiffness for robotic applications”. In: vol. 3. Proceedings 1999 IEEE International Conference on Robotics and Automation. 1999, pp. 2147–2152.

[89] M. Ruggiu. “Cartesian stiffness matrix mapping of a translational parallel mechanism with elastic joints”. In: *International Journal of Advanced Robotic Systems* 9 (2012).

[90] H. Zhang et al. “Machining with flexible manipulator: toward improving robotic machining performance”. In: International Conference on Advanced Intelligent Mechatronics. 2005, pp. 1127–1132.

[91] C. Corradini and J. C. Fauroux. “Evaluation of a 4-Degree of Freedom Parallel Manipulator Stiffness”. In: Proceedings of the 11th World Congress in Mechanism and Machine Science. 2003.

[92] B. C. Bouzgarrou et al. “Rigidity analysis of T3R1 parallel robot with uncoupled kinematics”. In: vol. 5. Proceedings of the 35th International symposium on Robotics. 2004, pp. 5–10.

[93] M. Farid and S. A. Lukasiewicz. “Dynamic modeling of spatial manipulators with flexible links and joints”. In: *Computers and Structures* 75 (2000), pp. 419–437.

[94] G. Piras, W. L. Cleghorn, and J. K. Mills. “Dynamic finite-element analysis of a planar high-speed, high-precision parallel manipulator with flexible links”. In: *Mechanism and Machine Theory* 40 (2005), pp. 849–862.

[95] C. S. Long, J. A. Snyman, and A. A. Groenwold. "Optimal structural design of a planar parallel platform for machining". In: *Applied Mathematical Modelling* 27 (2003), pp. 581–609.
[96] A. Klimchik, A. Pashkevich, and D. Chablat. "CAD-based approach for identification ofelasto-static parameters of robotic manipulators". In: *Finite Elements in Analysis and Design* 75 (2013), pp. 19–30.
[97] R. Rizk et al. "A comparative stiffness analysis of a reconfigurable parallel machine with three or four degrees of mobility". In: *Journal of Machine Engineering* 6 (2006), pp. 45–55.
[98] B. S. El-Khasawneh and P. M. Ferreira. "Computation of stiffness and stiffness bounds for parallel link manipulators". In: *International Journal of Machine Tools & Manufacture* 39 (1999), pp. 321–342.
[99] C. A. Felippa. "A historical outline of matrix structural analysis: a play in three acts". In: *Computers and Structures* 79 (2001), pp. 1313–1324.
[100] P. Nagarajan. *Matrix Methods of Structural Analysis*. CRC Press, 2018.
[101] A. Ghali and A. M. Neville. *Structural Analysis A Unified Classical Approach and Matrix Approach*. CRC Press, 2017.
[102] D. Deblaise, X. Hernot, and P. Maurine. "A systematic analytical method for PKM stiffness matrix calculation". In: Proceedings of the 2006 IEEE International Conference on Robotics and Automation. 2006, pp. 4213–4219.
[103] C. M. Clinton, G. Zhang, and A. J. Wavering. "Stiffness modelling of a Steward-Platform-Based milling machine". In: *Transaction of the North AmericaManufacturing Research Institution of SME* 115 (1997), pp. 335–340.
[104] T. Huang, X. Zhao, and D. J. Whitehouse. "Stiffness estimation of a tripod-based parallel kinematic machine". In: *IEEE Transactions on Robotics and Automation* 18 (2002), pp. 50–58.
[105] A. Klimchick, A. Pashkevich, and D. Chablat. "Fundamentals of manipulator stiffness modeling using matrix structural analysis". In: *Mechanism and Machine Theory* 133 (2019), pp. 365–394.
[106] C. Gosselin and D. Zhang. "Stiffness analysis of parallel mechanisms using a lumped model". In: *International Journal of Robotics and Automation* 17 (2002), pp. 377–382.
[107] J. K. Salisbury. "Active stiffness control of a manipulator in Cartesian coordinates". In: 19th IEEE Conference on Decision and Control including the Symposium on Adaptive Processes. 1980, pp. 87–97.
[108] C. Gosselin. "Stiffness mapping for parallel manipulators". In: *IEEE Transactions on Robotics and Automation* 6 (1990), pp. 377–382.
[109] E. Abele, M. Weigold, and S. Rothenbucher. "Modeling and identification of an industrial robot for machining applications". In: *CIRP Annals* 56 (2007), pp. 387–390.
[110] N. R. Slavkovic, D. S. Milutinovic, and M. M. Glavonjic. "A method for off-line compensation of cutting force-induced errors in robotic machining by tool path modification". In: *The International Journal of Advanced Manufacturing Technology* 70 (2014), pp. 2083–2093.
[111] E. Abele, S. Rothenbucher, and M. Weigold. "Cartesian compliance model for industrial robots using virtual joints". In: *Prod. Eng. Res. Devel* 2 (2008), pp. 339–343.
[112] I. Kao and C. Ngo. "Properties of the grasp stiffness matrix and conservative control strategies". In: *The International Journal of Robotics Research* 18 (1999), pp. 159–167.

[113] S. F. Chen and I. Kao. "Conservative congruence transformation for joint and cartesian stiffness matrices of robotic hands and fingers". In: *The International Journal of Robotics Research* 19 (2000), pp. 835–847.

[114] G. Alici and B. Shirinzadeh. "Enhanced stiffness modeling, identification and characterization for robot manipulators". In: *IEEE Transactions on Robotics* 21 (2005), pp. 554–564.

[115] C. Dumas et al. "Joint stiffness identification of six-revolute industrial serial robots". In: *Robotics and Computer-Integrated Manufacturing* 27 (2011), pp. 881–888.

[116] A. Klimchick et al. "Identification of geometrical and elastostatic parameters of heavy industrial robots". In: vol. 18. 2013 IEEE International Conference on Robotics and Automation (ICRA). 2013, pp. 3707–3714.

[117] A. Klimchick et al. "Modelling of the gravity compensators in robotic manufacturing cells". In: vol. 46. 7th IFAC Conference on Manufacturing Modelling, Management,and Control. 2013, pp. 790–795.

[118] A. Klimchick, E. Magid, and A. Pashkevich. "Design of experiments for elastostatic calibration of heavy industrial robots with kinematic parallelogram and gravity compensator". In: vol. 49. IFAC-Papers OnLine. 2016, pp. 967–972.

[119] A. Klimchick et al. "Calibration of industrial robots with pneumatic gravity compensators". In: 2017 IEEE International Conference on Advanced Intelligent Mechatronics (AIM). 2017, pp. 285–290.

[120] A. Klimchik et al. "Identification of the manipualtor stiffness model parameters in industrial environment". In: *Mechanism and Machine Theory* 90 (2015), pp. 1–22.

[121] A. Pashkevich, A. Klimchick, and D. Chablat. "Enhanced stiffness modeling of manipulators with passive joints". In: *Mechanism and Machine Theory* 46 (2011), pp. 662–679.

[122] A. Olabi et al. "Improving the accuracy of industrial robots by offline compensation of joints errors". In: IFAC-PapersOnLine. 2012, pp. 492–497.

[123] Ilya Tyapin, Geir Hovland, and Torgny Brogardh. "Method for estimating combined controller, joint and link stiffnesses of an industrial robot". In: 2014, pp. 1–6.

[124] A. Klimchik et al. "Compliance error compensation technique for parallel robots composed of non-perfect serial chains". In: *Robotics and Computer-Integrated Manufacturing* 29 (2013), pp. 385–393.

[125] A. Ajoudani, N. G. Tsagarakis, and A. Bicchi. "On the role of robot configuration in Cartesian stiffness control". In: IEEE International Conference on Robotics and Automation (ICRA). 2015, pp. 1010–1016.

[126] J. Chen et al. "Stiffness analysis and optimization of a novel cable-driven anthropomorphic arm manipulator". In: IEEE 10th International Conference on Industrial Informatics. 2012, pp. 746–751.

[127] W. Owen, E. Croft, and B. Benhabib. "Stiffness optimization for two-armed robotic sculpting". In: *Industrial Robot* 35 (2008), pp. 46–57.

[128] Y. Guo, H. Dong, and Y. Ke. "Stiffness-oriented posture optimization in robotic machining applications". In: *Robotics and Computer-Integrated Manufacturing* 35 (2015), pp. 69–76.

[129] Y. Lin, H. Zhao, and H. Ding. "Posture optimization methodology of 6R industrial robots for machining using performace evaluation indexes". In: *Robotics and Computer - Integrated Manufacturing* 48 (2017), pp. 59–72.

[130] H. Celikag, N. D. Sims, and E. Ozturk. "Cartesian stiffness optimization for serial arm robots". In: vol. 77. Procedia CIRP. 2018, pp. 566–569.

[131] J. Jiao et al. “Processing configuration off-line optimization for functionally redundant robotic drilling tasks”. In: *Robotics and Autonomous Systems* 110 (2018), pp. 112–123.
[132] G. Xiong, Y. Ding, and L. Zhu. “Stiffness-based pose optimization of an industrial robot for five-axis milling”. In: *Robotics and Computer-Integrated Manufacturing* 55 (2019), pp. 19–28.
[133] Yang Lin, Huan Zhao, and Han Ding. “Spindle configuration analysis and optimization considering the deformation in robotic machining applications”. In: *Robotics and Computer - Integrated Manufacturing* 54 (2018), pp. 83–95.
[134] N. Shen et al. “A practical method of improving hole position accuracy in the robotic drilling process”. In: *The International Journal of Advanced Manufacturing Technology* 96 (2018), 2973–2987.
[135] S.H.H. Zargarbashi, W. Khan, and J. Angeles. “Posture optimization in robot-assisted machining operations”. In: *Mechanism and Machine Theory* 51 (2012), pp. 74–86.
[136] S. Mousavi et al. “Dynamic modeling and stability prediction in robotic machining”. In: *The International Journal of Advanced Manufacturing Technology* 88 (2017), pp. 3053–3065.
[137] Said Mousavi et al. “Stability optimization in robotic milling through the control of functional redundacies”. In: *Robotics and Computer-Integrated Manufacturing* 50 (2017), pp. 181–192.
[138] R. N. Jazar. *Theory of Applied Robotics*. Springer, 2010.
[139] W. Khalil and E. Dombre. *Modelling, Identification & Control of Robots*. Kogan Page Science, 2004.
[140] J. Wu, J. Wang, and Z. You. “An overview of dynamic parameter identification of robots”. In: *Robotics and Computer-Integrated Manufacturing* 26 (2010), pp. 414–419.
[141] J. Jin and N. Gans. “Parameter identification for industrial robots with a fast and robust trajectory design approach”. In: *Robotics and Computer-Integrated Manufacturing* 31 (2015), pp. 21–29.
[142] M. Brunot et al. “An improved instrumental variable method for industrial robot model identification”. In: *Control Engineering Practice* 74 (2018), pp. 107–117.
[143] B. Subudhi and A. S. Morris. “Dynamic modelling, simulation and control of a manipulator with flexible links and joints”. In: *Robotics and Autonomous Systems* 41 (2002), pp. 257–270.
[144] A. Janot, P. O. Vandanjon, and M. Gautier. “An instrumental variable approach for rigid industrial robots identification”. In: *Control Engineering Practice* 25 (2014), pp. 85–101.
[145] R. H. Cannon and J. E. Schmitz. “Initial Experiments on the End-Point Control of a Flexible One-Link Robot”. In: *The International Journal of Robotics Research* 3 (1984), pp. 62–75.
[146] W. J. Book. “Recursive lagrangian dynamics of flexible manipulator arms via transformation matrices”. In: *IFAC Proceedings Volumes* 16 (1983), pp. 5–17.
[147] M. O. Tokhi, Z. Mohamed, and M. H. Shaheed. “Dynamic Modelling of a Flexible Manipulator System Incorporating Payload: Theory and Experiments”. In: *Journal of Low Frequency Noise, Vibration and Active Control* 19 (2000), pp. 209–229.
[148] J. M. Martins et al. “Approaches for dynamic modelling of flexible manipulator systems”. In: *IEE Proceedings - Control Theory and Applications* 150 (2003), pp. 401–411.

[149] H. N. Huynh, E. R. Lorphevre, and O. Verlinden. "Report of Robotic Machining Measurements Using a Stäubli TX200 Robot: Application to Milling". In: vol. 5B. Proceedings of the ASME 2017 International Design Engineering Technical Conferences, Computers, and Information in Engineering Conference. 2017.

[150] F. He, Y. Liu, and K. Liu. "A chatter-free path optimization algorithm based on stiffness orientation method in robotic milling". In: *The International Journal of Advanced Manufacturing Technology* 101 (2018), pp. 2739–2750.

[151] Said Mousavi et al. "Control of a Multi Degrees Functional Redundancies Robotic Cell for Optimization of the Machining Stability". In: vol. 58. Procedia CIRP. 2017, pp. 269–274.

[152] L. Yuan et al. "Mode coupling chatter suppression for robotic machining using semi-active magnetorheological elastomers absorber". In: *Mechanical Systems and Signal Processing* 117 (2019), pp. 221–237.

[153] C. Chen et al. "Posture-dependent stability prediction of a milling industrial robot based on inverse distance weighted method". In: vol. 17. Procedia Manufacturing. 2018, pp. 993–1000.

[154] F. Chen and H. Zhao. "Design of eddy current dampers for vibration suppression in robotic milling". In: *Advances in Mechanical Engineering* 10 (2018), pp. 1–15.

[155] J. Li et al. "Effect of the cutter path and the workpiece clamping position on the stability of the robotic milling system". In: *The International Journal of Advanced Manufacturing Technology* 89 (2017), pp. 2919–2933.

[156] M. Leonesio et al. "Vibration analysis of robotic milling tasks". In: vol. 67. Procedia CIRP. 2018, pp. 262–267.

[157] C. F. Bisu et al. "Dynamic behavior analysis for a six axis industrial machining robot". In: *Advanced Materials Research* 423 (2011), pp. 65–76.

[158] L. T. Tunc and J. Shaw. "Experimental study on investigation of dynamics of hexapod robot for mobile machining". In: *The International Journal of Advanced Manufacturing Technology* 84 (2016), pp. 817–830.

[159] L. T. Tunc and D. Stoddart. "Tool path pattern and feed direction selection in robotic milling for increased chatter-free material removal rate". In: *The International Journal of Advanced Manufacturing Technology* 89 (2017), pp. 2907–2918.

[160] F. W. Taylor. *On the art of cutting metals*. American Society of Mechanical Engineers, 1906.

[161] R. N. Arnold. "The mechanism of tool vibration in the cutting of steel". In: *Proceedings of the Institution of Mechanical Engineers* 154 (1946), pp. 261–284.

[162] R. S. Hann. "Metal cutting chatter and its elimination". In: *Transations ASME* 75 (1953), pp. 1073–1080.

[163] S. Doi and S. Kato. "Chatter vibration of lathe tools". In: *Transations ASME* 78 (1956), pp. 1127–1134.

[164] S. A. Tobias and W. Fishwick. "Theory of regenerative machine tool chatter I". In: *The Engineer* 1 (1958), pp. 199–203.

[165] S. A. Tobias. "Machine tool vibration research". In: *International Journal of Machine Tool Design and Research* 1 (1961), pp. 1–14.

[166] F. Koenigsberger and J. Tlusty. *Machine Tool Structures*. Pergamon Press, 1970.

[167] F. Koenigsberger and J. Tlusty. *Machine Tool Structures - Vol I: Stability agaisnt chatter*. Pergamon Press, 1967.

[168] S. A. Tobias. *Machine-Tool Vibration*. Blackie & Son LTD, 1965.

[169] G. Quintana. "Chatter in machining processes: A review". In: *International Journal of Machine Tools & Manufacture* 51 (2011), pp. 363–376.

[170] G. Wang et al. “Chatter mechanism and stability analysis of robotic boring”. In: *The International Journal of Advanced Manufacturing Technology* 91 (2017), pp. 411–421.
[171] B. Stone. *Chatter and Machine Tools*. Springer, 2014.
[172] A. Iturrospe, V. Atxa, and J. M. Abete. “State-space analysis of mode-coupling in orthogonal metal cutting under wave regeneration”. In: *International Journal of Machine Tools and Manufacture* 47 (2007), pp. 1583–1592.
[173] X. Badiola et al. “State-space analysis of mode-coupling workpiece chatter”. In: *The International Journal of Advanced Manufacturing Technology* 103 (2019), pp. 2773–2781.
[174] Y. Guo et al. “Vibration analysis and asuppression in robotic boring process”. In: *International Journal of Machine Tools & Manufacture* 101 (2016), pp. 102–110.
[175] L. Yuan et al. “A review on chatter in robotic machining process regarding both regenerative and mode coupling mechanism”. In: *IEEE/ASME Transactions on Mechatronics* 23 (2018), pp. 2240–2251.
[176] A. Gasparetto. “A system theory approach to mode coupling chatter in machining”. In: *Journal of Dynamic Systems, Measurement and Control* 120 (1998), pp. 545–547.
[177] Alessandro Gasparetto. “Eigenvalue analysis of mode-coupling chatter for machine-tool stabilization”. In: *Journal of Vibration and Sound* 7 (2001), pp. 181–197.
[178] Z. Pan et al. “Chatter analysis of robotic machining process”. In: *Journal of Materials Processing Technology* 173 (2006), pp. 301–309.
[179] O. Gienke et al. “Mode coupling chatter prediction and avoidance in robotic machining process”. In: *The International Journal of Advanced Manufacturing Technology* 104 (2019), pp. 2103–2116.
[180] L. Cen et al. “A method for mode coupling chatter detection and suppression in robotic milling”. In: *Journal of Manufacturing and Engineering* 140 (2018), pp. 2739–2750.
[181] F. He et al. “Three-dimensional stability analysis of robotic machining process”. In: *Industrial Robot: the international journal of robotics research and application* (2019).
[182] T. Hayasaka nad A. Ito and E. Shamoto. “Generalized design method of highly-varied-helix end mills for suppression of regenerative chatter in peripheral milling”. In: *Precision Engineering* 48 (2017), pp. 45–59.
[183] A. Yilmaz, E. Al-Regib, and J. Ni. “Machine tool chatter suppression by multi-level random spindle speed variation”. In: *Journal of Manufacturing Science and Engineering* 124 (2002), pp. 208–216.
[184] J. Ni E. Al-Regib and S. Lee. “Programming spindle speed variation for machine tool chatter suppression”. In: *International Journal of Machine Tools and Manufacture* 43 (2003), pp. 1229–1240.
[185] *Robots and robotic devices — Vocabulary*. Standard. International Organization for Standardization, 2012.
[186] L. Sciavicco and B. Siciliano. *Modelling and Control of Robot Manipulators*. Springer, 2000.
[187] S. M. Megahed. “Inverse kinematics of spherical wrist robot arms: analysis and simulation”. In: *Journal of Intelligent and Robotic Systems* 5 (1992), pp. 211–227.
[188] ABB Robotics. *IRB 6640 CAD Models*. 2019. URL: `https://new.abb.com/products/robotics/fr/robots-industriels/irb-6640/irb-6640-cad` (visited on 04/12/2019).
[189] G. Gogu. *Structural Synthesis of Parallel Robots*. Springer, 1989.
[190] J. Denavit and R. S. Hartenberg. “A kinematic notation for lower-pair mechanisms based on matrices”. In: *The Americal Society of Mechanical Engineering* (1955), pp. 215–221.

[191] J. J. Craig. *Introduction to Robotics: Mechanics and Control*. Pearson, 2005.
[192] L. W. Tsai. *Robot Analysis: The Mechanics of Serial and Parallel Manipualtors*. John Wiley & Sons, Inc, 1999.
[193] D. L. Pieper. "The Kinematics of Manipulators Under Computer Control". PhD thesis. Stanford University, 1968.
[194] R. P. Paul and H. Zhang. "Computationally efficient kinematics for manipulators with spherical wrists based on the homogeneous transformation representation". In: *The International Journal of Robotics Research* 5 (1986), pp. 32–44.
[195] G. Legnani et al. "The "point of isotropy" and other properties of serial and parallel manipulators". In: *Mechanism and Machine Theory* 45 (2010), pp. 1407–1423.
[196] W. A. Khan and J. Angeles. "The kinetostatic optimization of robotic manipulators: The inverse and the direct problems". In: *The Journal of Mechanical Design* 128 (2006), pp. 168–178.
[197] J. Angeles. *Fundamentals of Robotic Mechanical Systems*. Springer, 2007.
[198] S. A. Tobias and W. Fishwick. "A theory of regenerative chatter". In: *The Engineer* 205 (1958), pp. 139–239.
[199] M. Wiercigroch and E. Budak. "Sources of nonlinearities, chatter generation and suppression in metal cutting". In: *Philosophical Transactions of the Royal Society of London. Series A: Mathematical, Physical and Engineering Sciences* 359 (2001), pp. 663–693.
[200] T. L. Schmitz and K. S. Smith. *Machining Dynamics*. Springer US, 2009.
[201] Y. Altintas and E. Budak. "Analytical prediction of stability lobes in milling". In: *CIRP Annals* 44 (1995), pp. 357–362.
[202] S. D. Merdol and Y. Altintas. "Multi frequency solution of chatter stability for low immersion milling". In: *Journal of Manufacturing Science and Engineering* 126 (2004), pp. 459–466.
[203] N. Sims. "Multi-frequency chatter analysis using the shift theorem". In: *Procidia IUTAM* 22 (2017), pp. 3–9.
[204] T. Insperger and G. Stephan. "Semi-discretization method for delayed systems". In: *International Journal of Numerical Methods in Engineering* 55 (2002), pp. 503–518.
[205] Y. Ding et al. "A full-discretization method for prediction of milling stability". In: *International Journal of Machine Tools and Manufacture* 50 (2010), pp. 502–509.
[206] J. Munoa et al. "Chatter suppression techniques in metal cutting". In: *CIRP Annals - Manufacturing Technology* 65 (2016), pp. 785–808.
[207] N. S. Nise. *Control Systems Engineering*. John Wiley & Sons, Inc, 2011.
[208] Leica Geosystems. *Leica Absolute Tracker AT 401 Brochure*. 2010. URL: `http://w3.leica-geosystems.com/downloads123/m1/metrology/AT401/brochures/Leica%20Absolute%20Tracker%20AT401_brochure_en.pdf` (visited on 01/17/2020).
[209] K. Subrin et al. "New redundant architectures in machininig: serial and parallel robots". In: vol. 63. Procedia Engineering. 2013, pp. 158–166.
[210] J. C. C. Rubio, T. H. Panzera, and F. Scarpa. "Machining behaviour of three high-performance engineering plastics". In: *Journal of Engineering Manufacture* 229 (2015), pp. 28–37.
[211] C. A. Harper. *Modern Plastics Handbook*. McGraw-Hill, 2000.
[212] M. Chanda and K. R. Salil. *Plastic Technology Handbook*. CRC Press, 2006.
[213] M. E. Merchant. "Mechanics of the metal cutting process. I. orthogonal cutting and a type 2 chip". In: *Journal of Applied Physics* 16 (1945), pp. 267–275.
[214] M. E. Merchant. "Mechanics of the metal cutting process. II. plasticity conditions in orthogonal cutting". In: *Journal of Applied Physics* 16 (1944), pp. 318–324.

[215] E. Budak, Y. Altintas, and E. J. A. Armarego. “Prediction of milling force coefficients from orthogonal cutting data”. In: *Journal of Manufacturing Science and Engineering* 118 (1996), pp. 216–224.

[216] L. Urena, E. Ozturk, and N. Sims. “Stability of variable helix milling: model validation using scaled experiments”. In: vol. 77. 8th CIRP Conference on High Performance Cutting (HPC 2018). 2018, pp. 449–452.

[217] L. Urena, E. Ozturk, and N. Sims. “Convergence analysis of the multi-frequency approach around a variable-helix instability island”. In: vol. 82. 17th CIRP Conference on Modelling of Machining Operations. 2019, pp. 279–284.

[218] SDT Tools. *Matlab SDT Toolbox*. 2020. URL: `https://www.sdtools.com/` (visited on 11/27/2020).

[219] E. Ozturk, L. T. Tunc, and E. Budak. “Investigation of lead and tilt angle effects in 5-axis ball-end milling processes”. In: *International Journal of Machine Tools and Manufacture* 49 (2009), pp. 1053–1062.

[220] A. Otto et al. “Stability of milling with non-uniform pitch and variable helix Tools”. In: *International Journal of Advanced Manufacturing Technology* 89 (2017), pp. 2613–2625.

[221] H. Celikag, N. D. Sims, and E. Ozturk. “Chatter suppression in robotic milling by control of configuration dependent dynamics”. In: vol. 82. Procedia CIRP. 2019, pp. 521–526.

[222] K. Worden and G. Manson. “On the identification of hysteretic systems. Part I: Fitness landscapes and evolutionary identification”. In: *Mechanical Systems and Signal Processing* 29 (2012), pp. 201–212.